Inorganic Chemistry Laboratory

Department of Chemistry

University of Oxford

Methanol conversion to hydrocarbons via acidic catalysts

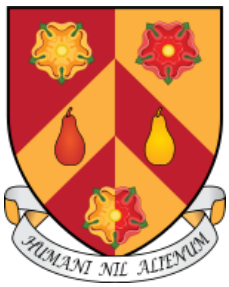

Bonan Liu

Wolfson College

University of Oxford

Supervisor: Professor Peter P. Edwards FRS

A thesis submitted in partial fulfillment of

the requirements for the degree of

Doctor of Philosophy in Inorganic Chemistry

2016

Table of contents

Acknowledgements

Already has been engraved deeply, practiced for hundred times, in my mind ever since the first day at Oxford, all those words below explained what supported my study during the past five years.

A first appreciation is given to my parents, who have devoted their luxury youth to the catalysis since 1980s, and in deed I was jealous of my ‘brothers’ which are a group of their designed, well-industrial-applied catalysts, once upon a time. Here a great lucky in my life is I can understand what they are doing, and how important their contributions are, by the end of my study at Oxford. Since then, catalysis is a label and an honor of my family.

Many important persons in my life gave me knowledge, among all of them, Professor Peter. P. Edwards FRS is a most special, respectable one. A dreamful experience of studying and researching under his supervision, and a spirit of ‘science should be applied’, will go with me in all my lifetime, not only as my ‘life motto’, but also will have affected more persons related to this area. As a great scientist, who has defined and contributed to many important chemical science areas, such as superconductivity, hydrogen storage and etc., Peter is always very keen to explore new areas; his great passion into petro-chemistry catalyzed by zeolites, sparked the relevant researches at Oxford, and is the most important motivation for our KOPRC group. Many thanks for his great encouragement in every monument of truth, extreme patience on my long-time study, and especially for his catalysis on my life!

Dr. Tiancun Xiao is a guiding light in my world, who has changed a lot of my life, not only in the perspective of science, but also in the perspective of how to be successful in my cases. With his help, I always obtain more than I expected with gradually built-up experiences, and more importantly, a strong confidence from him.

Dr. Vladimir Kuznetsov, Dr. Daniel Slocombe and Dr. Sergio Gonzalez, all helped my study at different periods, with their great patience, and of course a strong passion on the related studies. Their experiences, skills and talent gave me a lifetime memorable impression, which will be part of the motivation in my academic life.

It is my great luck and pleasure to have those lovely 'classmates', Mr. Xian Du, Ms. Afrah Aldawsari, Dr. Alex Vai, Mr. Zhaoxi Zhang, Mr. Yiwen Fang and Mr. Xiangyu Jie, who became part of my life at Oxford Chemistry, and are best friends in my life. Here I sincerely wish their future success in the related areas, and I am sure their contributions will make our life much better.

I would also like to appreciate our colleague, sponsors and best friends from KACST (Saudi Arabia), Professor Hamid AlMegren, and Dr. Mohammed AlKinany, who always stand behind our group members for a best support. The KOPRC Forum held annually, is a finalistic experience for my academic life, which is also the arts built by them and Peter and Tiancun.

Here flowers should be given to Ms. Linda Webb who is our best office secretary (Peter's assistant), for her very careful help and organizing works in the last 5 years, and she is one of the most important person for me in the group.

During the past five years, my lovely family at Oxford, Wolfson College gave me a

lot of beautiful memories. Most importantly, the college has considered my special situation of depression, and allowed me to stay and live in the college for 5 years, which greatly helped my life and supported my researches.

A final thanks to the ‘topic’ that is a series of studies based on ‘methanol catalytic conversions over zeolite catalysts’. Methanol as the most important intermediate product from coal, not only gives us energy with ‘methanol-to-gasoline’, but also gives us important chemicals with ‘methanol-to-aromatics’ as well as ‘methanol-to-olefins’. I am so lucky to see those sciences become applied, for a better life of our human being. I have great confidence on those coming days that will have a sustainable energy utilization, non-emission waste treatment, and a green chemistry for recycling of materials!

For the spirit of “*Science should be applied!*”

—Bonan

16/08/2016 Wolfson College, Oxford, UK

Table for abbreviations

**Note: Common abbreviations are explained for frequently used concepts, their full name have been explained when they are employed for the first time. After creating an abbreviation, it is thereafter used in the following contents of the thesis. The listed table is for a convenience of quick reference.*

Common technical abbreviations

FT-IR spectroscopy: Frontier-Transformed Infrared Spectroscopy

MTH: Methanol-to-hydrocarbons (including MTA, MTO and MTG)

MTA: Methanol-to-aromatics

MTG: Methanol-to-gasoline

MTO: Methanol-to-olefins

MW: Microwave

NH_3-TPD: Ammonia Temperature-programed-desorption

NMR: Nuclear Magnetic Resonance CP: Cross-Polarization

TGA: Thermogravimetry analysis

WHSV: Weight-Hourly-Space-Velocity

XRD: X-ray Diffraction

Zeolite and catalyst full names

ZSM-5: Zeolite Socony Mobil–5 (framework type MFI)

SAPO-34: Silico-Alumino-Phosphate-34 (framework type CHA)

MCM-22: Mobil-Composition-of-Matter-22 (framework type MWW)

H-zeolite, e.g. H-ZSM-5 demonstrates that the zeolite has already been pre-activated from NH_4-zeolite to acidic form, 'H' means proton.

Micro/Nano in front of zeolite means the particle size is micro or nano.

Meso-ZSM-5 employed in Chapter 5 is ZSM-5 zeolite that has mesoporous structures. In Chapter 5 (Fig. 5.7, page 213), we simply separated different nano ZSM-5 zeolites by their Si/Al ratio, so they are marked as 'ZEO46', 'ZEO60' and 'ZEO160', respectively.

Example of 'naming a sample'

Adjectives are employed for further sample specifications, an example is given in the below for "5h coked top Ind ZSM-5 25":

'5h' represents the reaction time length, i.e. 5 hours during which the sample is tested;

'coked' indicates that the sample has coke deposits obtained in the MTH reactions;

'top' demonstrates that the sample is taken from the top part of the catalyst bed, where the catalyst bed is set vertically inside the reactor;

'Ind' means the ZSM-5 sample is an industry catalyst;

'25' is the Si/Al ratio of the zeolite

Abstract of thesis

Methanol has long been advanced as a high-energy-density, widely-obtained (from non-oil sources such as coal, and biomass) material with potential as a replacement for the limitedly-distributed, finite-in-current-storage oil resources.

Given the fact that effective methanol conversion has been observed over the acidic, zeolite based catalytic materials, e.g. H-ZSM-5, since the 1970s, it is almost certain that extra catalytic properties, such as an enhanced C-H bond activation, govern by the introduced non-zeolitic promoters, e.g. metal oxide species, could further modify the reaction pathways, with potentially-achievable, lower energy costs, higher selectivity (or yields) to many valuable hydrocarbon products (e.g. olefins) and other benefits. On the other hand, a big step is to successful convert the laboratory achievements, e.g. a selected good performance zeolite sample, into the larger-scale applications. Such a process requires the involvement of catalyst binders, and when zeolite particle comes to the nano-scale, the corporation of binder phases, e.g. Al_2O_3, with the parent nano zeolite plays the most important role in determining the following methanol conversion. Another critical issue is the binder-incorporated, shaped zeolite catalysts would be better tested in larger reactors which are not often seen in the regular laboratory, and the scale-up also increases the research budgets. It should be mentioned that catalyst deactivation is another crucial limitation in this research area; particularly, the reaction formed cokes especially the higher-density, and deeply dehydrogenated graphitized compounds deopsiting deeply inside the zeolite cavities/channels give many difficulties not only in the effective methanol conversion but also in detecting and measuring their quantity and compositions.

This thesis aims to help in solving the above mentioned challenges in an effective methanol catalytic conversion, and can be accordingly divided into 3 aspects: 1) a method to further improve the C-H bond activations for higher olefin and aromatic yields, via modification of H-ZSM-5 (Si/Al=25, industrial) with MoO_3 promoters, prepared at a lower-than-usual temperature of 400 ^oC (routinely 500 ^oC or higher temperatures are employed for the calcination of metal oxide modified zeolites); 2) an attempt to scale up the laboratory methanol-to-hydrocarbon reaction, obtained over Al_2O_3 incorporated nano H-ZSM-5 samples (the parent nano zeolites have Si/Al ratios of 20, 60 and 120), with a customized larger fixed-bed reactor that allows catalyst loadings of 20g packed in the shaped forms; 3) a technique based on microwave perturbation measurements in a resonant cavity, inside which coked zeolite samples are analyzed, and different coking levels as well as coke compositions are evaluated based on the sample dielectric loss values that can be calculated from the measured perturbation data.

Our efforts herein are made for the soul of "*Science should be applied*", for a sustainable future, in a great certain to be sparked by the utilization of methanol in the industries.

Chapter 1 Introduction

General background

It has been a long time since the fossil-energy-powered industrial revolution started to change our daily lives. Nowadays, one critical issue is that fossil resources, notably, coal, oil, and natural gas, contributing extensively for our energy and material consumptions, are finite gifts from the earth. Development of new energy types, such as solar power, as well as some other new technologies to improve and extend the lifetime of fossil resources, like the recent advances in shale gas production, seem to only contribute to a limited extent as a solution, especially when there are restrictions caused by the socio-political, geographic and other issues. [1]

The intrinsic advantages of traditional fossil resources rely not only on their efficiency but also their universality. Correspondingly, oil has historically been put on a more important footing than the other two resources, as it enables the most efficient way to produce transportation fuels (gasoline & diesel) for internal-combustion engines. It is also the major raw material of the petrochemical and fine-chemical products. By contrast, coal reserves as sources of certain feedstocks have been somehow ignored for decades, except in oil-poor countries and areas with huge coal storages, such as China and India. [2] Technical issues, and significant environmental problems greatly restrict the application of coal resources, and here a breakthrough requires multiple and environmentally-efficient utilization of materials that can be easily obtained from coal reserves.

A rational way to utilize and upgrade the coal resources starts with the so-called "coal gasification technology", followed by a water-gas-shift process to further adjust the ratio between CO and H_2 in the produced syngas (syngas is mainly composed of H_2 and CO). [3] The resultant syngas can be directly converted into many types of fuels and materials through the Fischer–Tropsch (F-T) process, or via methanol platform which further increases the variety in products. [4] Fig. 1.1 illustrates the current approaches through which coal can be converted into various types of energy and materials including most of the important petrochemical products.

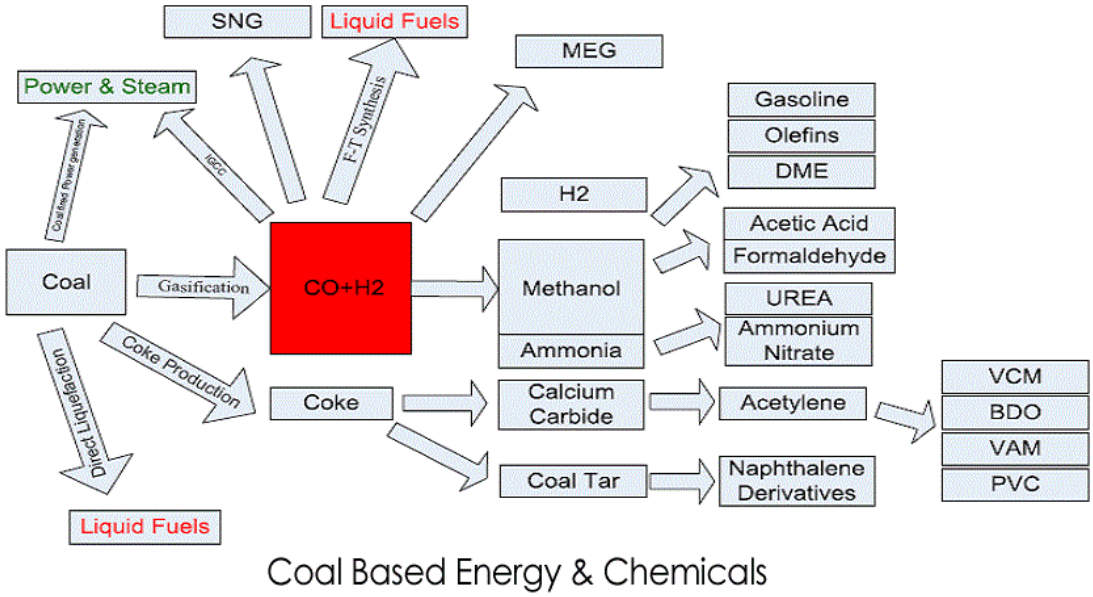

Fig.1.1 The Coal-Based Energy & Chemicals, where syngas ($CO+H_2$) plays a unique, important role as the key intermediate product, normally formed from upstream coal gasification, and methanol as a direct product from syngas is another important platform product. [5]

Here methanol is a direct downstream product from syngas, which can also be produced with natural gas alternatively. [6] On the other hand, production from biomass-to-methanol (a new approach) also possesses certain efficiencies, thus can be

expected to be extensively adopted in the future. [7] Methanol itself is also a good energy carrier, [1] and has been employed to blend with the conventional fuels. [8] The increase in the variety of products via a methanol platform is based on the fact that methanol can be converted into hydrocarbons, through a so called Methanol-to-Hydrocarbons (MTH) approach, achieved over acidic zeolite based catalysts. The main outputs include light olefins, alkanes and particularly high value aromatics (Fig. 1.2). One advantage that may surpass the more straightforward 'F-T' approach is the higher yield of aromatics, such as benzene, toluene and xylenes (BTX), which are theoretically the main products of MTH reaction. [1, 9]

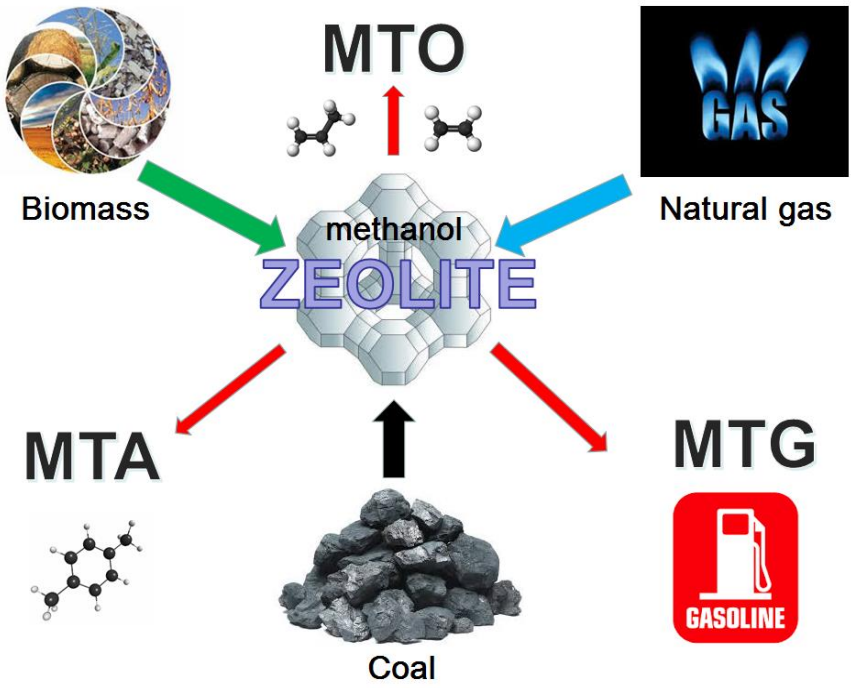

Fig.1.2 Methanol as an important intermediate materials can be obtained from both conventional fossil resources (e.g. coal and natural gas) and newly developed biomass materials, and subsequently converted into valuable products including gasoline boiling range hydrocarbons (Methanol-to-Gasoline, denoted as 'MTG'), high quality aromatics (Methanol-to-Aromatics, denoted as 'MTA'), as well as light gas olefins (Methanol-to-Olefins, denoted as 'MTO'). [9]

Aim and objectives of this thesis study

There are increasing interests in the rational utilization of methanol, as efficient methanol catalytic conversion to a variety of products builds up a platform that links various forms of energy materials forwards a future sustainable development. [1, 9] However, for any such ‘methanol success’, there are many problems which require scientific advances. Major challenges in relevant industries require further reducing the process energy cost (e.g. the heat consumed and dissipated in the high temperature reactions) and selective improvement on the yield of desired products, such as propylene and BTX (Benzene, Toluene and Xylenes) that are of great industrial value. On the other hand, most researches have mainly focused on zeolite developments, and their laboratory tests only possess limited applicability to the larger scale industrial applications. [10, 11] From the point of view of catalyst deactivation, carbon formation over catalyst (e.g. cokes deposited over zeolite) significantly reduces the potential economic benefits due to the need for replenishment of catalysts, this happens not only in methanol zeolite conversion but also in many other reactions based on hydrocarbon transformations over acidic zeolites. There have been many attempts made to improve the catalyst coke resistance, in such, a more reliable, rapid and comprehensive detecting method of the complex coke compositions is called for. [12]

The 3 projects included in this thesis have targeted on the above mentioned issues as illustrated schematically in the below (Fig. 1.3). These are:

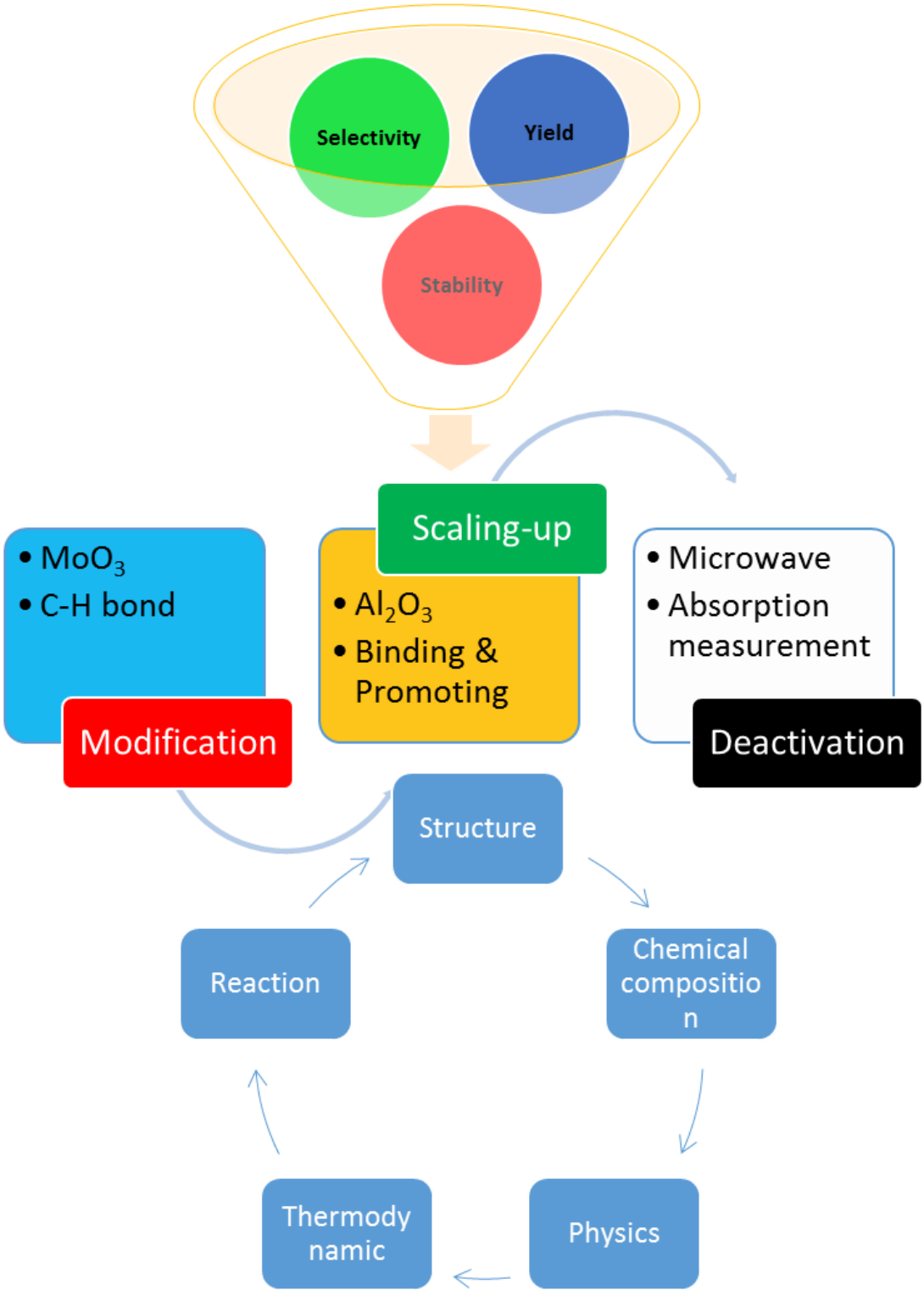

Fig.1.3 Overview of projects in this thesis

1) *Modification of H-ZSM-5 catalyst through doping MoO_3 promoters at a lower-than-usual temperature (this is for catalyst calcination to achieve a desired distribution of MoO_3 in the zeolite structure), with the resulting catalysts also being tested at the same temperature.* The employed 400 ℃ is apparently lower than the temperatures used by the catalyst calcinations of previous studies (routinely 500/550 ℃ is used for the calcination of metal oxide loaded zeolite catalyst as the transportation of metal oxide in zeolite system is driven by the calcination temperature) [9, 13-15] thus effectively reduced the energy cost. Reaction temperature was also set as 400 ℃ (no higher than this is to maintain the obtained MoO_3 distribution to a maximum extent) for the highest yield of aromatics (reaction temperature below this may suppress the aromatics production). We propose that the employed 400 ℃ temperature and other conditions in catalyst preparation and MTH reaction have helped to tailor the distribution of Mo species in the H-ZSM-5 zeolite system, balancing the promoted catalytic activity (Mo promoters help to dissociate the C-H bond) [13] with the intrinsic zeolite acidity, and may improve the MTH catalytic performance.
2) *The scale-up of MTH reaction catalyzed by nano H-ZSM-5 based catalysts which are structured into cylindrical rod shape in an industrial form with the help of Al_2O_3 binders.* The project aims to reduce the difference between laboratory experiments and industrial applications for successful lab-selected samples. Additionally, we will also illustrate other catalytic features that may be introduced for an enhanced catalytic performance of nano H-ZSM-5 zeolites.

3) *Coke analysis via microwave-based approaches for a rapid and more comprehensive measurement in terms of full-sample-body-penetration and therefore volumetric tests.* Microwave absorption that occurs in a resonant cavity has been found to be highly sensitive for detecting and quantifying various levels of coke deposition on acidic zeolite catalysts. The measurement is volumetric (full sample penetrated) and reflects the integrated, overall coke deposition of a sample. A variety of coked zeolites obtained from different MTH reactions will be examined.

Further discussions into the mechanisms and theories, as well as the relevant background knowledges of these three studies are given in the following sections.

1.1Methanol–to–Hydrocarbons: Mechanism

Debates on MTH chemistry, regarding its detailed pathways, have continued since the first series of investigations in the 1970s. A critical focus remains on how the catalytic process is obtained.

It has been widely accepted that methylbenzenes play a major catalytic role as a ‘scaffold’ in the MTH reaction, onto which the activated methyl groups (by zeolite acidic sites) are continuously added (alkylation), and from which light olefins are subsequently released (de-alkylation) to form the primary products. Those ‘scaffold’ species (e.g. methylbenzenes) allowing the subsequent C-C bond formation via alkylation/de-alkylation steps are denoted as catalytic ‘hydrocarbon pool’ in the literatures. [14, 16] It should be noted that although co-feeding in methylbenzenes with methanol greatly improves the yield of olefins and other hydrocarbon products, the methylbenzene species do not exhibit similar catalytic/reactive behavior when reacted alone. For instance, it was found that toluene, when reacted alone, was nearly inert under the conditions the same as co-feeding in with methanol, and only tiny amounts of benzene and xylenes were obtained in an H-ZSM-5 system. A proposed explanation for this has been the intra-transformation between different methylbenzenes (benzene, toluene, xylenes and tri-methylbenzenes) as another typical chemistry but mainly happens in the later stage of the MTH reaction. [17] In 2003, Haw et.al summarized some important historical proposals that had unique impacts on the development of the current Hydrocarbon-Pool MTH mechanism (Fig.1.4). [16]

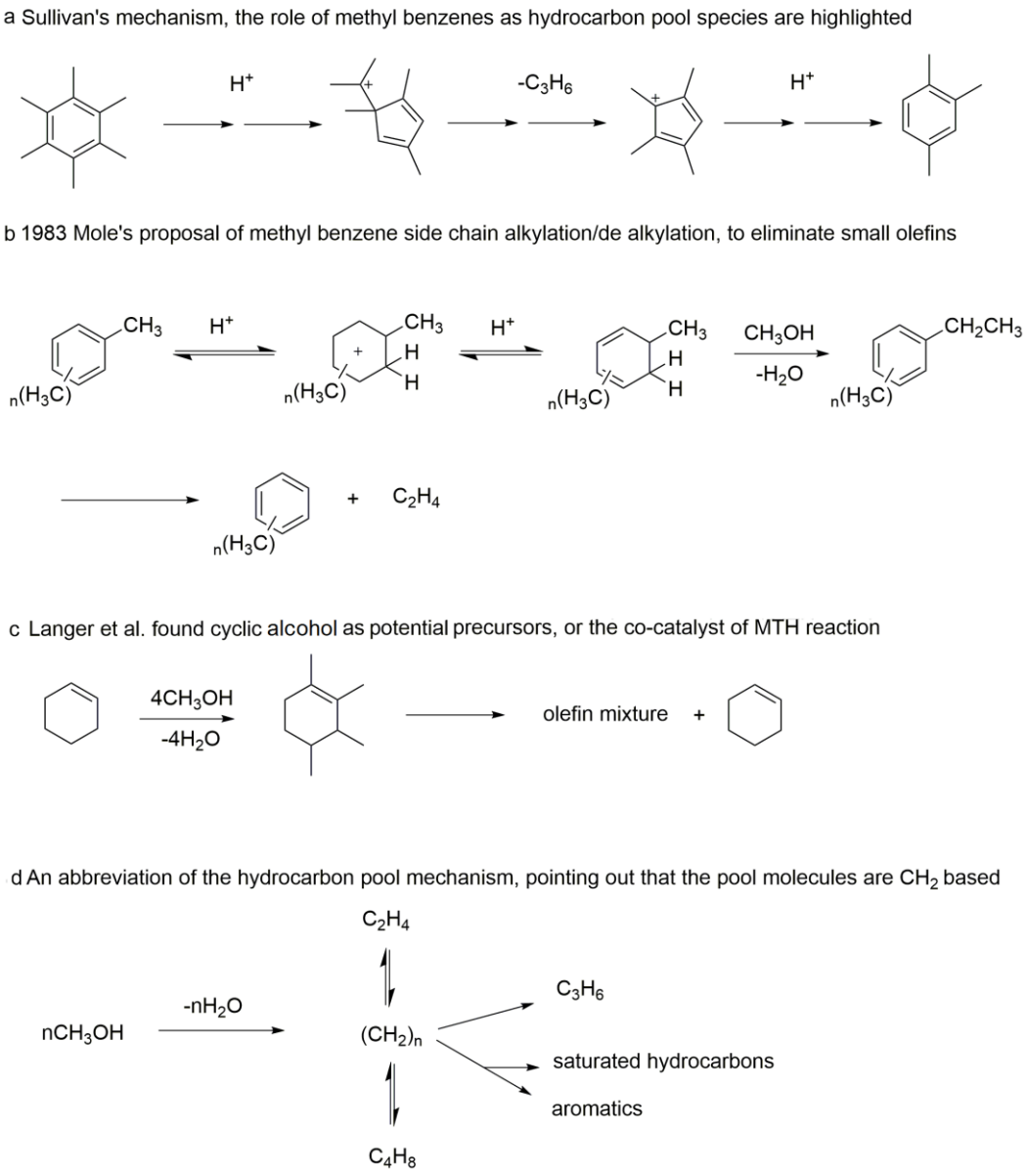

Fig. 1.4 Schematic illustration of the evolution of Hydrocarbon-Pool mechanism, with four early proposals that possess important influence in shaping the current thinking, where the important catalytic role of potentially existed hydrocarbon-pool species (e.g. methylbenzenes) in MTH reaction is highlighted: a) Sullivan's paring mechanism, demonstrated in 1961, which is an early attempt to explain the olefin formation by methylbenzene transformation (ring contraction/expansion). [18] b) In 1983, Mole proposed his hydrocarbon pool hypothesis of methylbenzene side-chain alkylation. [19] c) Langer et al. pointed out that co-feeding in cyclic alcohol species (cyclo-hexanol) with methanol effectively reduced the induction period of catalytic MTH process. [20] d) An abbreviation of the hydrocarbon pool mechanism proposed by Kolboe. [21, 22]

***Note**: This figure has been slightly adjusted (only the mechanisms are listed in a year-ascending order) from the most classic work in MTH research of Haw et.al, [16] leaving the full details of the original equations (negligible errors do exist, e.g. in equation a, more details*

about the formation of carbenium ions, and the ring contraction/expansion are missed). The formation of hydrocarbon pool molecules (e.g. aromatics) was not explained, which is still under the debate until today. The above scenarios only focused on the important role of hydrocarbon pools for their contributions to primary olefin formation via continuous methylation/dealkylations.

Explorations on MTH mechanism have never been stopped. However, it was not until Morten et al. found that ethylene formation could be mechanistically separated from the formation of higher alkenes in H-ZSM-5 catalysed MTH reaction, that researchers started to pay more attention to the essential role of other reaction pathways parallel to the methylbenzene-based Hydrocarbon-Pool mechanism. [23] In the case that only methylbenzenes perform as hydrocarbon pool molecules, C_2-C_4 olefins are mainly formed as a result of the de-alkylation of methylbenzenes. In Morten et al.'s work, it was noticed that, for H-ZSM-5, ethylene appeared to be formed exclusively in the above mechanism, from xylenes and tri-methylbenzenes (only from methylbenzene molecules, as a result of the alkyl group eliminations); however, evidences from ^{13}C isotope labelling tests indicated that propylene and higher alkenes (not only the light olefins), in a significant extent, were also formed from alkene methylation and product intra conversions (e.g. larger molecules crack into smaller fragments). It seems that there are two parallel routes to form the alkenes in the H-ZSM-5 catalysed MTH reaction, and methylbenzenes are not the only hydrocarbon pools to accelerate the methanol consumption. This finding also separates the route of ethylene formation from other alkenes (it seems that only methylbenzene based hydrocarbon pool contributes to the ethylene yield), and is of great importance for adjusting the product ratio between ethylene/propylene. The idea of alkene expanding via methylation and adding up small C_nH_m units has already been

employed by the early MTH mechanisms [16] and reported in some juvenile hydrocarbon pool hypothesises. [19]

In 2007, Bjørgen et al. drew a 'dual pathway' MTH scheme based on their works in the H-ZSM-5 system, which indicate that both methylbenzenes and primary alkenes are effective hydrocarbon pools that catalyse the MTH reaction, in sharp contrast to the previous findings in the H-SAPO-34 and H-Beta systems. [24]

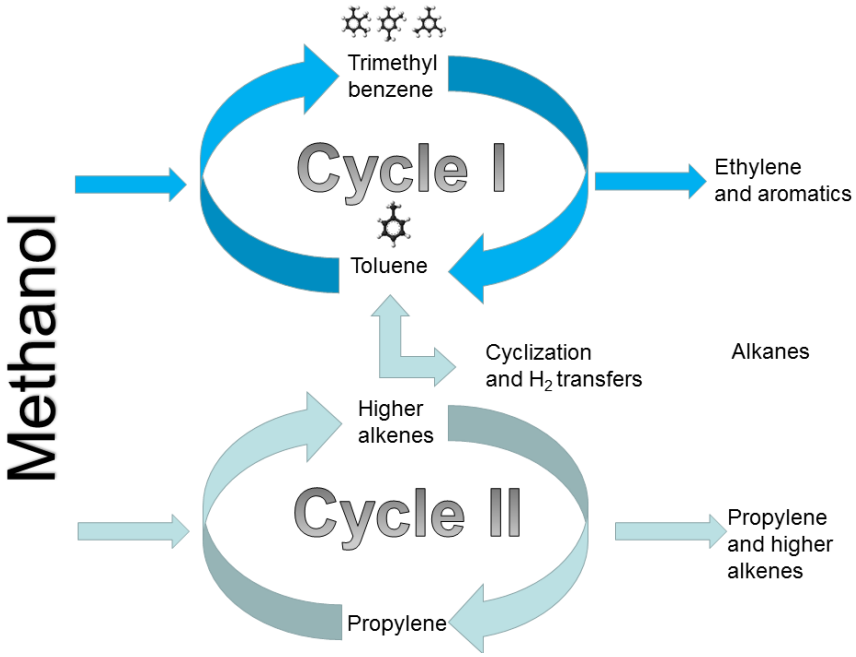

Fig 1.5 Represented 'dual pathway' mechanism for MTH reactions, adapted from [24]

As illustrated in the above Fig. 1.5, two cycles constitute the 'dual pathway' mechanism, processing in a parallel way. Cycle I is the methylbenzene route, in which alkyl groups are eliminated from tri-methylbenzene molecules to form ethylene and other olefins. On the other hand, toluene can be converted back into tri-methylbenzene to complete the cycle. Particularly, for H-ZSM-5 catalysed methanol conversion, it was found tri-methylbenzene is the most active hydrocarbon pool molecule, from which ethylene is exclusively formed. In Cycle II, propylene and

higher alkenes are formed through alkene methylation to a significant extent. Accompanied cracking and hydrogen transfers also yield alkanes and cyclic compounds which finally convert into aromatics.

It should be noted that, although viewed as proceeding in a parallel way, the two cycles are not completely independent. [24] Theoretically, there is no newly formed benzene ring structure in the Cycle I (this cycle does yield aromatics, but does not provide new cyclic structures), as it is defined as a simple alkylation/de-alkylation cycle. However, there is a continuous yield of aromatics during the MTH reaction, as Bjørgen noted, hence there must be corresponding aromatization steps in the Cycle II. In fact, ring structures can be formed by cyclization of higher alkenes, and subsequently converted into aromatics by dehydrogenation (hydrogen transfer), both of these two chemistries have been assigned to the Cycle II. Therefore, it seems that the Cycle I cannot proceed without the Cycle II, at least for H-ZSM-5. Interestingly, evidences from that research also show ethylene methylation only contributes limitedly in the formation of propylene and higher alkenes. This implies propylene is mainly from de-alkylation of methylbenzenes in the Cycle I, or cracking of larger molecules in the Cycle II. If methanol can be activated in some conditions, as Bjørgen suspected, cycle II would proceed solely, although it has never been confirmed yet.

Recent studies have revised the ‘dual pathway’ MTH mechanism based on further specification of different hydrocarbon pools, according to which Cycle II is explained as an ‘olefin carbon pool’ based process (Fig. 1.6) [25] Here the researchers used a more specified word ‘olefin’ rather than the word ‘alkene’ as the latter signifies a

larger family of compounds.

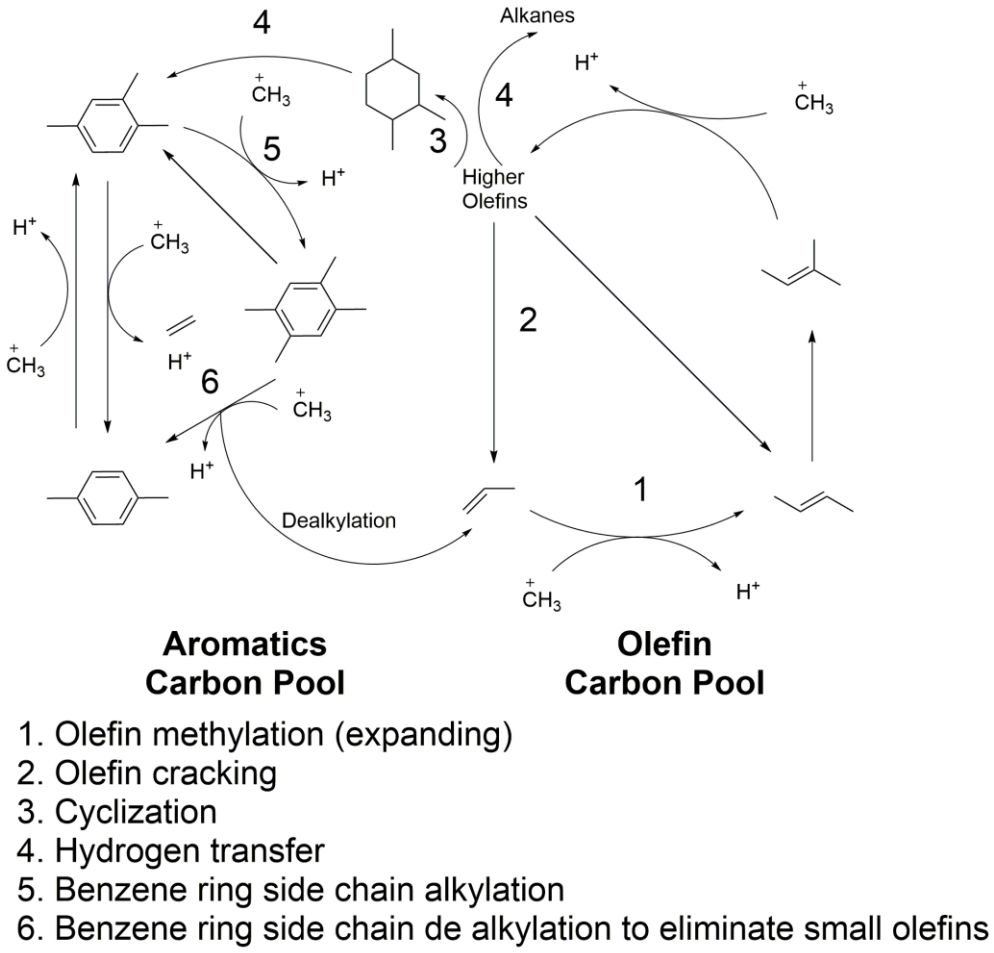

Fig 1.6 Revised MTH 'dual pathway' mechanism, based on an aromatic carbon pool and an olefin carbon pool. The figure is adapted from [25]

In the above scheme, the aromatics carbon pool mainly yields gaseous olefins and methylbenzenes, while the olefin carbon pool promotes the expansion of small olefins. The accompanied steps (2-4) included in the Cycle II play an essential role to maintain the reaction process. Higher olefins crack to yield light olefins in a significant extent although ethylene formation is more or less independent from this approach. Importantly, cyclization steps produce new ring structures, which could be subsequently converted to aromatics by series of hydrogen transfers (this also yields alkanes as well as H_2).

Here the zeolite Brønsted acid sites are essential to activate the hydrocarbon molecules and structures involved in the reaction scheme, by donating protons which help to charge and thence dissociate the chemical bonds. However, the exact mechanism of bond dissociations, e.g. the disconnection of a C=C bond in an olefin structure is still under debate. It has to be noted that the final product distribution of MTH is complex contributions of each component reaction step and is also greatly affected by the exact reaction thermodynamic conditions. [9, 14-16]

It has been clearly pointed out in the above 'dual pathway' mechanism that both methylbenzenes and olefins could be the effective catalytic centres in the MTH reaction. Questions may arise from the point that how those initial hydrocarbon pool molecules are formed when there is methanol only. It seems that without the hydrocarbon pools methanol cannot be effectively converted, but the hydrocarbon pools have to be formed from methanol. The origin of the organic species initially catalyzed the methanol conversion is still in debate, a large number of researchers believe they are impurities in the reaction feedstock, or exist as deposits in a continuously working system. [9, 14, 26] As Song et al. suggested, it is nearly impossible to avoid the incorporation of organic impurities into the MTH system, they could be brought into the system from the feedstock (even reagent standard methanol contains tiny amount of other organics), or, generated from the last run of reaction. Surprisingly, even in tiny amounts, these organic catalysts greatly promote the methanol conversion, and once the reaction is initiated, it supplies more organic catalysts (methylbenzenes and olefins that promote the reaction).[26]

1.2 Catalyst scaling up and binders

1.2.1 Catalyst shaping for scaling up

Progress in catalysis study has been, and is always being pushed forwards by an ultimate purpose of successful applications in industry; in essence, how a lab-designed catalyst can be effectively converted into an optimized industrial form is uniquely important.

Rarely *pure* zeolites are employed solely in large scale applications (e.g. reactions in an industrial plant), particularly for the concerns such as reduced catalytic activity, limited mechanical strength, unsatisfied hydrothermal stability, resulted system blocking, irregular temperature control and etc. Industrial catalysts are considerably more complex in constitution. They are normally blended, mechanically-shaped mixtures, composed of the main zeolitic catalyst components, and/or supports, co-catalysts, binders, and other additives with different specific functions. As a result, the catalyst preparation (manufacture) is further complicated. [3, 10, 11, 27]

Rational catalyst design does not require the scaled-up products (i.e. industrial catalysts) to have catalytic performance (e.g., the conversion rate of reactant) as good as the laboratory selected samples. On the contrary, technical features such as long term stability, anti-coking behaviour and particularly improved mechanical strength become ever more crucial. [10, 11] Here the development steps of a zeolite based commercial catalyst applied in petrochemical industries are schematically illustrated

in the below Fig. 1.7. [10]

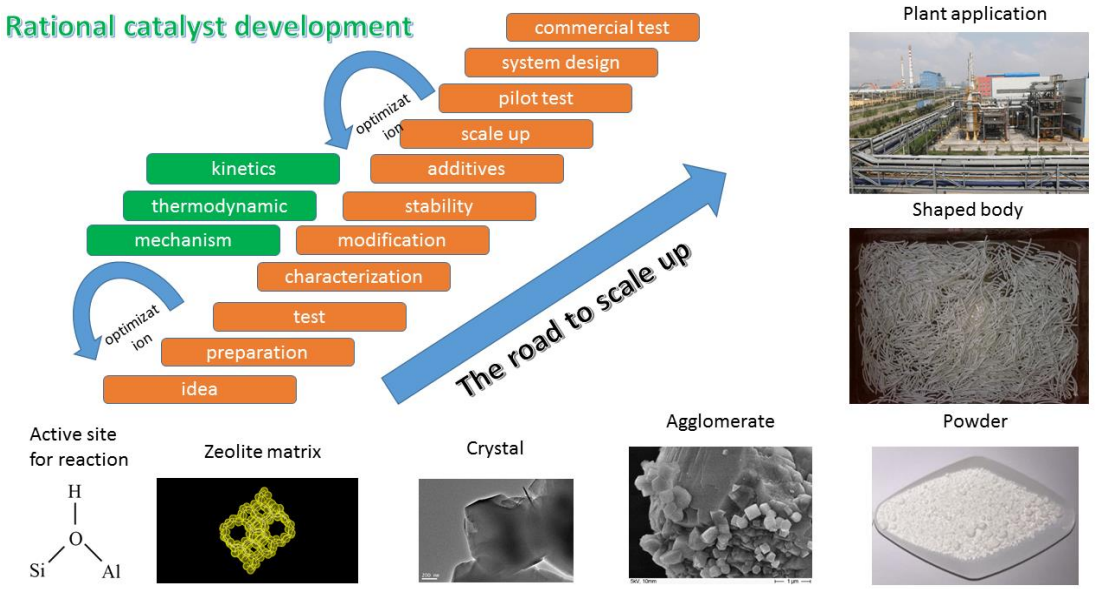

Fig. 1.7 Represented zeolite-based catalyst rational design, in the form of a story 'from laboratory to factory'. The whole process started with the reactant converted at an active site in the catalyst framework, and finally ended up with the expected production in plant applications. In this road to successfully scale up the designed catalyst, 3 main stages are generally involved, denoted as 'lab design', 'pilot test' and 'commercial test', in which 'backwards' modifications on catalyst compositions and structures are always necessary, and all adjustments should be based on series of re-screening works (tests in laboratory, pilot plants and even in real industrial plant) for a finally optimized catalytic performance.

Thus there is a long road from a single zeolite active site to tons of industrial catalysts! For zeolite catalyzed hydrocarbon conversions Brønsted acid sites are essential, as they activate the chemical bond (e.g. C-H bond) dissociations. [3, 14, 15] Those active acid sites, chemically consisted of a Si-OH-Al structure, are part of the zeolite framework. Zeolite crystals are built up with the framework unit cells, and subsequently form into agglomerates. Those zeolite powders, when shown under microscope, are agglomerates of numerous of crystallites. In most cases, lab zeolite

catalyst research will end up by the powder phase samples, as zeolite powder is not only a good acidic catalyst but also a gifted support for other catalytic promoters (here a simple couple of zeolite body plus metal oxide promoters could be a good lab-developed catalyst for many reactions). This is due to the large surface area and porous space as intrinsic properties of aluminosilicate materials. [3, 10, 11, 15] However, powder zeolite samples cannot meet the harsh conditions found in industrial plant reactions, therefore their desired form are normally mixtures made into a designed shape with additives or fillers to provide enhanced mechanical strength. Zeolite particles are hard to bind with each other, and therefore binders should be employed. Powders (zeolite and binder) are firstly compacted dry, then mixed in liquid phase (water is normally employed) to form a primary slurry/gel phase. The next step is a shaping process mechanically, often followed by higher temperature calcinations to model the catalyst-binder mixture into the designed shape with the required physical and chemical properties, as well as certain level of hydrothermal stability. The quality of shaped zeolite catalyst is mainly dictated by 3 things: 1) The physicochemical characteristics of the original zeolite material; 2) the binder blended with and its potential impacts on the zeolite; 3) the mixing and preparing conditions which induce the interactions between the constituent zeolite and binders. [3, 10, 11]

1.2.2 Binders for zeolite catalysts

Commonly used binders for zeolite catalyst are aluminum-silicon based species, such as alumina, silica, alumina oxide, natural clays, and their precursors or derivate. [11]

Those materials and their resultants after preparation possess high melting points and are, therefore, highly stable under most industrial operating conditions. [3] Another important feature of those binders is that they simply bind the zeolite particles together, with (hopefully) limited influence on their original chemical properties (in fact, in most cases binders just positively improve the catalyst performance). [10, 11] Hargreaves has succinctly summarized the commonly observed effects as a result of the introduction of binders, and categorized them into 6 major points: 1) Possible anti-coking property, 2) Entrapment of poisons, 3) Transportation of chemicals (e.g. metal cations can be exchanged between the binder matrix and the zeolite framework), 4) Improved thermal stabilities and catalytic behavior, 5) Modification on the system porosity, as well as 6) Improvement of the physical durability (various of shaping forms). [11]

In this project, our interests mainly focus on the alumina based binders (e.g. Al_2O_3) which are commonly used for zeolite catalyst shaping. In the early time H-ZSM-5 investigations, Chang and Shihabi (1985) noticed that Alumina insertion from a binder matrix (α-Al_2O_3) into zeolite framework, and the improved catalytic properties in 4 individual reactions including n-hexane cracking, propylene oligomerization, lube hydro-dewaxing, and particularly methanol to hydrocarbons. [28] The resulting enhanced catalytic performances in the investigated 4 reactions, were all attributed to new acid sites formed as a result of the aluminum ion migration from the binder matrix into the zeolite framework, which complements the ongoing reaction-consumed catalytic sites. Particularly, those newly formed Al active sites

(new acidic centres) were noted to be truly intra-zeolitic, and could be separated from the new alumino-silicate phase formed at the zeolite grain boundaries.

Notably, those Al precursors, although might be quite close in the chemical compositions and/or prepared via similar procedures, often transform into different binder phases, which exhibit distinguished functions in the same reaction. Normally, the difference is made through calcination, in which the precursor oxide or oxyhydroxide is dehydrated to form the functional Al sites. The highest temperature (up to 1473 K) gives α-Al_2O_3, which can be transformed from lower temperature prepared Al_2O_3 analogs. However, if the desired product is γ-Al_2O_3, which is the most commonly used 'transition-alumina' catalyst binder/support, boehmite, an oxyhydroxide precursor, should be calcined at a much lower temperature, say below 723 K. Other analogs of Al_2O_3 can also be formed with variety mainly in the calcination temperatures. The transitions between different Al-O based binders are illustrated as below (Fig. 1.8): [3]

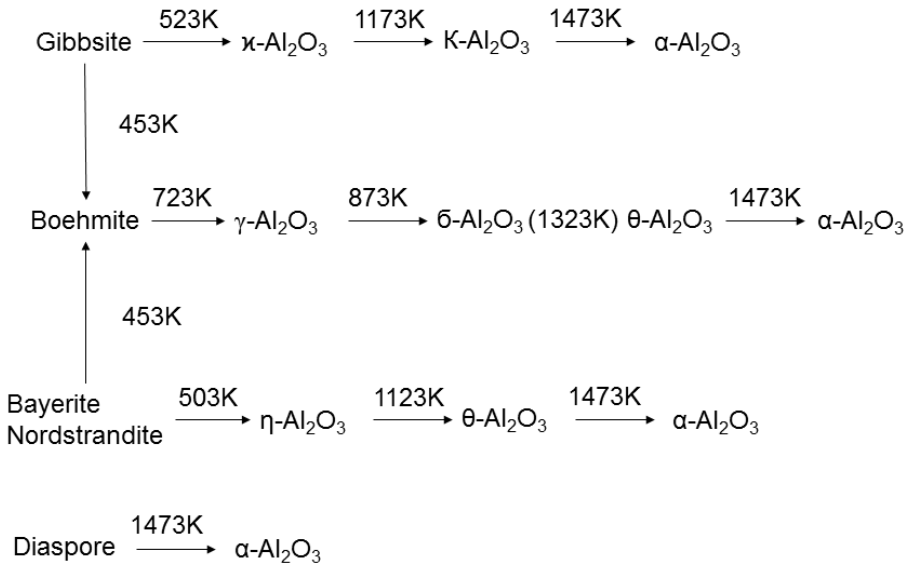

Fig. 1.8 Representation of the aluminas transition as a result of different temperatures

For the scaling up of MTH reaction catalyzed by nano H-ZSM-5 zeolites, as described in the later Chapter 4, we employed Boehmite (AlOOH) as binder precursor, which converts into γ- Al_2O_3 phase after calcination in a temperature range of 573 – 873 K. [3, 11, 29] When bound with H-ZSM-5, it brought about many advantages, such as increased olefin yields and restricted coke formation. The formed γ-Al_2O_3 was found to possess important co-catalytic functions which help to adjust the product distribution in a variety of hydrocarbon transformations, by its extra Lewis acidity, as well as a partial neutralization effect on the zeolite Brønsted acid sites. [30] The resulted loss on Brønsted acid sites mildly mitigated the reaction rate while the introduced Al Lewis acid sites also leaded to enhanced hydrogen abstraction, both of which have been considered to effectively slow down the coke formation in MTH reaction. Furthermore, it was also noted that Al in the prepared catalyst played a role as coke depot, which also effectively extended the catalyst lifetime. [30]

1.2.3 Effects on the material porosity

Recent research has focused on the changes of zeolite porosity as a result of introducing the binder phases. Those zeolites before modification normally possess some intrinsic hierarchy in porosity [10, 31, 32]

The hierarchy of a porous material, e.g. zeolite, is not a simply complication of the pores; in contrast, before a material is defined as hierarchical, each level of porosity within it should have a distinct function, and possess certain levels of ordinance. As is pointed out by Ramírez, the functionality of distinguished porous systems is the

differentiating feature of hierarchical materials with respect to a disordered porous material. Besides, the connectivity between different pores is also important. [32] Pure zeolite structure normally possesses hierarchy (e.g. the well-organized two channel systems in an H-ZSM-5 structure), unless there is strictly only one type of zeolite micropores. Fragmentation of zeolite crystals into small nano pieces generates mesopores connecting the already existed micropores, thus, brings in extra hierarchy. Inner crystal mesopores and some larger pores crossing the micropores possess similar effects as the inter-crystalline mesopores; this is because the micropores are also well connected. The increased mass transfer ability leads to some superior performances of the hierarchically structured zeolite, thus, have been employed to improve the catalytic performance of many zeolite promoted reactions. [32]

Introducing binder phase into the catalyst body brings in a new porous system, which is totally different from the one in parent zeolite. The resulted changes may generate, or further increase the hierarchy of the already existed porous system. [32] In a Methanol-to-Hydrocarbon research by Ramírez and others, many types of binders/precursors including silica, alumina, clay and their deviants have been blended with hierarchically structured H-ZSM-5 zeolites, by physical mixing, extrusion and millings. [27] The observed catalysis shows that binder effects can, without optimization, match or even exceed those of hierarchically structuring the porosity of MFI (ZSM-5) crystals. The introduced binder phase may possess extra macro-porosity leading to improved mass transfer properties of the prepared technical bodies.

1.2.4 Necessity of a ‘customized’ larger system

In most of the above mentioned works, although the catalysts have been made into an industrial (technical) form, they were not tested in really ‘scaled up’ conditions. Limitations are possibly due to the shortage of budgets available, and it is difficult to set up a larger size reactor system inside the laboratories. In many cases, some important works were undertaken in the regular lab conditions, and only small amounts of catalyst were tested. Furthermore, the shaped catalysts had to be grounded back into the powder form before the catalytic performance test which is a real retrogression, although by such treatments the interactions between the binder phase and parent zeolite might be better illustrated. [10, 11, 32]

In our work on Al-H-ZSM-5 to be reported here, we have given the catalytic tests a ‘scaled up’ application, by designing and building up an amplified fixed-bed reactor system for the catalyst performance tests. The customized, enlarged reactor allows at least 20 grams of prepared catalyst in a real rod shape (prepared with Al binders) to be tested at a much higher pressure (6bar) than the commonly employed atmosphere pressure. Besides, as nano-sized zeolites were not commonly employed in the related researches, [10, 11, 15, 28, 32] we particularly chose a family of superior nano H-ZSM-5 zeolites as the original parent zeolites for shaping modifications and their intrinsic catalytic performances were also measured for comparisons.

1.3 Coke formation in the MTH reaction

1.3.1 General discussions on coking models

Generally, coke formation in catalytic hydrocarbon transformations is a dehydrogenation process in which hydrogen is lost thermodynamically from the deposited organic products that cannot be moved out from the system timely. [12] However, the exact route varies among different reaction types, and for Methanol-to-Hydrocarbon reaction, the mechanism behind is even more complex than normal dehydrogenation of organics, which is based on a recent decades developed Hydrocarbon-Pool mechanism: the organic species as impurities in the methanol feedstock promote the initial formation of methylbenzenes/olefins which catalyse the later stage reactions that yield olefins, aromatics and other products; [26] on the other hand, through series of intra-conversions (hydrogen transfers) driven by the reaction conditions more aromatics and aliphatic species are formed, which finally convert into condensed poly-aromatics, and eventually, into graphitic species (they have been considered as the final status of cokes). [9, 33, 34]

It has been generally accepted that coke induced zeolite deactivation proceeds both inside and outside of the zeolite cavities/channels, but varies in two different models. [35] In most cases, the limited cavity/channel space has somehow restricted the geometry of carbonaceous deposits, inside which most of the methylene-chloride-soluble (MCS), lower molecular weight coke species (smaller, less condensed carbonaceous deposits, normally can be dissolved in methylene

chloride) are formed. [35, 36] Those are simple aromatic species, in which a large proportion are trapped inside the zeolite cavities/channels, and display a ‘pre-graphite’ status, which can be explained as a failure in the hydrogen-loss molecular expanding; [12] for instance, if a poly-methylbenzene molecule fails to expand its aromatic ring structure during the MTH reaction and is trapped inside the zeolite inner space due to the restricted product transportation, it will become part of the coke deposits. Notably, these MCS, smaller and less-dehydrogenated aromatics also perform as the catalytic centres (hydrocarbon pools) during the methanol conversion, [9, 16, 33, 34, 37] and multiple evidences of their existence have been achieved by dissolving the zeolite framework to liberate the inner cokes. [12, 16, 33, 35, 37, 38]

On the other hand, the larger space on zeolite surface enables molecule-expanded and further condensed coke species to be formed and gradually build up, which also leads to the deactivation of zeolite catalyst by blocking the cavity/channel openings from outside and inhibits the reaction mass transportations to a greater extent. Those external cokes, as a result of further aromatization and hydrogen deficiency, are mainly deeply-graphitized poly-aromatics showing poor solubility in methylene chloride (methylene chloride insoluble, MCI). [35, 38] They are electro-microscopy visually (TEM) shown in the form of either black particles (small amount), or an envelope shape covering the zeolite crystals which remains an empty mould after zeolite framework solubilisation. [12, 35, 38]

Great researching interests have been paid to the above mentioned two coke types for their distributions in the reaction. Normally, this is mainly decided by the reaction

conditions, e.g. the temperature employed. For instance, previous MTH studies showed that at 375^{o}C coke formation over H-ZSM-5 was primarily internal, while at 475 ^{o}C coke deposition was mainly external. [39, 40] Here the faster mass transportation at higher temperatures may promote the generation of coke precursors so as their diffusion to outside of zeolite cavities/channels. The outside zeolite surface, with less limitation on molecular expanding, gives the best chance for previously formed coke species to expand their structures via secondary reactions in terms of alkylation, oligomerization, aromatization and etc. [12, 16, 34, 35, 37]

Herein, a comprehensive model of coke evolution that combines the above two models can be described for MTH reaction. Firstly, those smaller single-aromatic-ring methylbenzene molecules (MCS), which are formed inside the zeolite cavities/channels since the early time of MTH reaction, perform as catalytic centres to accelerate the reaction. Once the reaction has been greatly progressed and reached a steady rate, the spreading and deposition of poly-aromatics and further condensed graphitic species (MCI) on the external zeolite surface is an intrinsic solution for the reaction system to avoid deactivation by emptying the potential cavity/channel blocking stuffs. Here the limited zeolite inner space cannot afford the volume of large reaction products, so later formed expanded molecules (coke components or precursors) will be principally dispersed onto the external zeolite surface by intra-reaction diffusion and gas transportation. The outer coke species covering the zeolite body can be further stabilized by dehydrogenation and finally stop the reaction process by blocking the mass transportations from outside, on the other hand, coke

species in the zeolite cavities/channels also reduce the number of catalytic sites and kill the reaction from inside.

Interestingly, by step pulsing quantified methanol molecules into the reacting system, methylbenzenes were observed as precursors to the further graphitized coke species, as detected by the Laser-Raman technique. [41] Later studies increased the dose to a normal methanol-to-olefin reaction standard, and detected condensed poly-aromatics formed as further step coke species. [42] These findings well supported the above assumptions on coking models.

Here the role of those non-aromatic species in coke formation cannot be ignored, although it might be not as important as the aromatics. Typically, the major components/precursors of coke formed in MTH reaction are mainly aromatics (in most cases they are poly-aromatics), these chemicals are more favoured by the thermodynamics, not only in MTH reaction but also in all other acid zeolite catalysed hydrocarbon transformations, and therefore are important intermediates of the deeper graphitized coke species. [12-14, 37] However, it has been found that deactivation of small-pore zeolite catalysed hydrocarbon reactions, particularly at lower temperatures (below 350 ^{o}C), is often attributed to those non-aromatic species. [12] Olefinic and aliphatic species take important portions in the non-aromatic cokes, and they are considered as the earlier stage adsorbed compounds on the zeolite surface blocking the cavity openings and precursors to the aromatics. [12-14, 16]

1.3.2 Coke inner migration

Given the fact that a large portion of zeolite Brønsted acid sites are located inside the zeolite cavities/channels, [43] it has been noted that the first sign of possible coke/precursor accumulation often emerges at the zeolite crystal edges, which has been observed even at the initial period of the reaction. [44] In the work of Mores et al., confocal fluorescence microscope in an upright configuration was employed and they managed to capture the formation of coke molecules and their precursors inside the zeolite grains (Fig.1.9). It was found that fluorescence-marked methylbenzenes (important components/precursors of coke deposits) were firstly built up at the zeolite crystal edges, and this was the case for both H-ZSM-5 and H-SAPO-34 catalyzed MTO reactions. The captured fluorescence patterns also show that the accumulation of methylbenzenes gradually moved inwards to the zeolite crystal cores (the research focused on the coke inner migrations). However for H-ZSM-5 catalyst, the inner migration of coke species halted much earlier, whereas for H-SAPO-34 there was a gradually progressed process, and by the end of reaction the inner space of H-SAPO-34 cavity was fully filled with the methylbenzenes. [44]

One most possible explanation for the coke accumulation starting at the zeolite crystal edges would be a priority to have the first contact with the reactant feedstock for those zeolite edge regions, much earlier than the cavity/channel inner areas. Therefore, it is reasonable to imagine a faster product / coke precursor deposition firstly occurs at those sites near zeolite edges, and particularly, at where those cavity/channel openings locate. Here, the inner migration of ‘coke frontline’ is

possibly driven by two forces: 1) As more catalytic sites (Brønsted acid sites) are needed for the chemical steps such as methanol dissociation, product dehydrogenation, and aromatization, etc., cokes gradually build up inside the zeolite cavities/channels as the inner catalytic sites are fully occupied by the reactant, intermediates and products. 2) Coke formation is a condensation process that often ends up with molecule-expanded, larger size chemical structures, where geometry limitation has forced it to move either inwards to the deeper space inside cavity/channel, or to the outside zeolite surface.

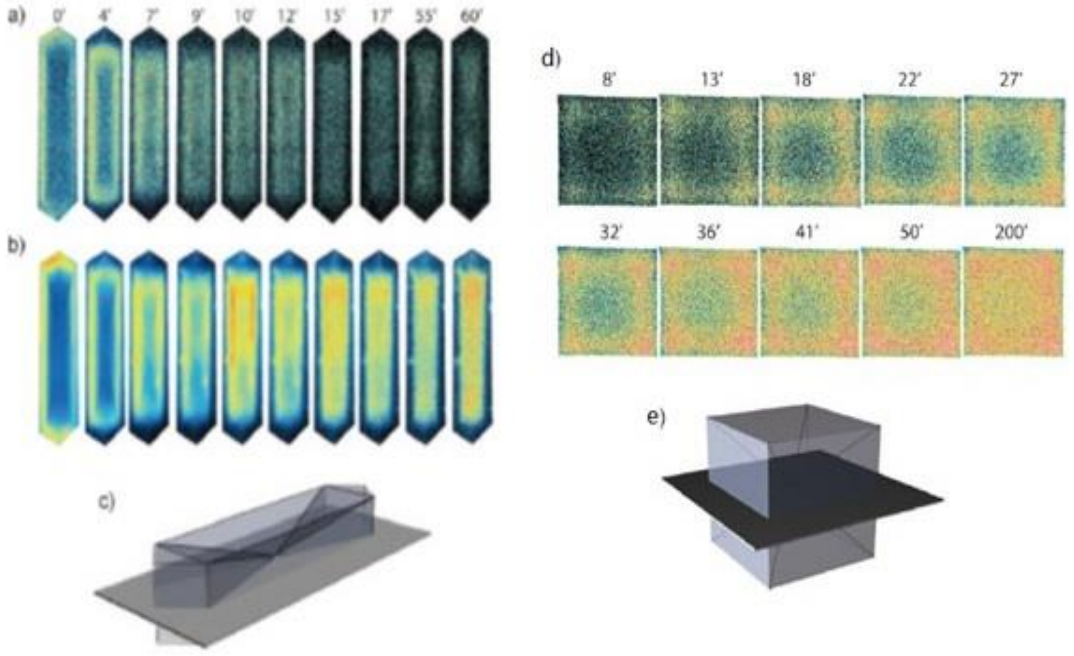

Fig.1.9 Confocal fluorescence microscope images of H-ZSM-5 crystal during MTO reactions at 660 K with time-on-stream (numbers represent reaction minutes), and achieved with laser excitation at a) 488nm (penetration 510-550 nm), and b) 561 nm (penetration 565-635 nm), respectively. c) Schematic representation of the H-ZSM-5 slice at which the confocal fluorescence measurements were performed. d) Confocal fluorescence microscope images of H-SAPO-34 crystal during MTO reactions at 660 K with time-on-stream (numbers represent reaction minutes) achieved with laser excitation at 561nm (penetration 565-635 nm). e) Schematic representation of the H-SAPO-34 slice at which the confocal fluorescence measurements were performed.[44]

In the above examples, as the channel diameters of H-ZSM-5 are relatively uniform and much smaller (approximately 5 Å), there is not much space for the coke building up inside, whereas the larger inner space allows the H-SAPO-34 cavity to store more coke species inside, with expanded coke structures. It should be noted that here the volume of coke storage is not directly correlated to the coke tolerance of zeolite; in contrast, due to the uniformly distributed channel sizes, H-ZSM-5 possesses much better coke resistance in real reactions. Chemicals in larger-than-the-channel-diameter size are hardly formed inside H-ZSM-5 channels, which greatly reduces the chance of channel blocking caused by coke accumulation. [9] For H-SAPO-34, the smaller cavity opening and a much larger cavity space makes it difficult to move those large coke species to the outside space once they are formed inside the cavities, thus, would finally lead to the un-avoidable catalyst deactivation in a shorter time. [9, 15, 45]

1.3.3 Coke outer accumulation

Coke formation starting at the zeolite edges has been further confirmed in the works of Nordvang et al. [46] Their findings reveal that fast formation of aromatic molecules (e.g. methylbenzenes) at the periphery of H-ZSM-5 crystals is the main reason for the coke coverage over the zeolite body. We could imagine the building up of simple aromatics, and subsequent poly-aromatics formation as well as the resulted extension of superficial carbonaceous structure, finally reach a ‘network’ of carbons, which processes thermodynamically during the external coke formations. Instead of a monolayer of carbons, coke accumulation over zeolite surface could be multilayers,

where the formed ‘networks’ of carbons are structurally built up as the reaction proceeds, and finally a ‘pre-graphite’ status would be achieved. [12] Notably, owing to the thermodynamics and the reaction mechanism, [9, 13, 14] dehydrogenation is un-avoidable for most of the hydrocarbons deposited. Therefore, more SP^2 carbons are formed due to the loss of hydrogen. Compounds such as aliphatic or olefins with sp^3 carbons dominating in molecule structure will be continuously consumed, and converted into the sp^2 carbonaceous compounds. Layers of hex-atomic ring structure, without any doubt, are favored in the above process, and often the graphitized cokes play a terminal role in most of the reactions. [12]

On the other hand, we should not ignore the role of small fractions of light hydrocarbons, e.g. the light olefins with a much better transportability in the reaction, for their contribution to the poly-aromatics formation. Previous studies have observed the conversion of olefins into methyl-benzenes, e.g. xylene, at the zeolite external surface, [47] and these single-ring aromatics (e.g. methylbenzenes) are the basic units to build a poly-aromatic structure. The MTH mechanism also implies the potential contribution of olefin aromatization in external coke formation, as the relevant chemical processes are thermodynamically favored under the reaction conditions. [9, 12, 14]

The coke building-up in terms of layered poly-aromatics (graphitized carbons [12]), positioned vertically and covered the H-ZSM-5 zeolite channel openings is schematically presented in Fig. 1.10. Here we also show the TEM images of a coke covered post-run industrial H-ZSM-5 (micrometer crystallite size, Si/Al = 25,

WENFENG, BEIJING, CN), obtained from 300 mins MTH reaction (400 ^{o}C, atmosphere pressure, WHSV of 2h^{-1}).

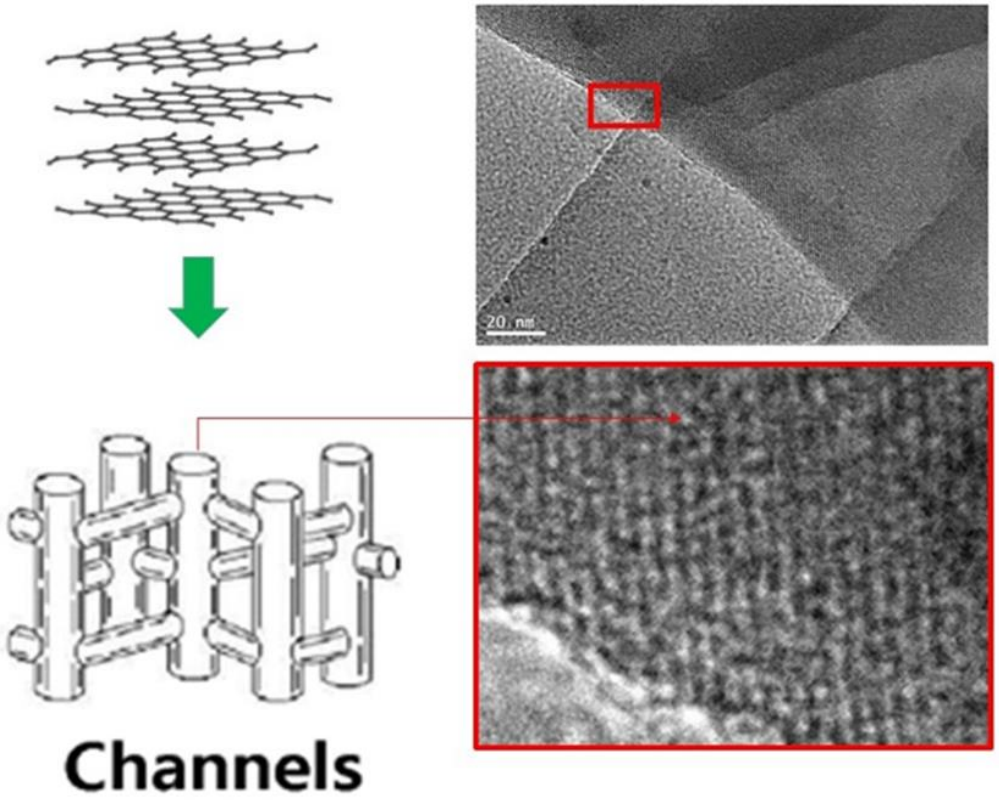

Fig.1.10 Schematic representation of layers of carbon structure (graphitized) building up over the zeolite surface, in a vertical position over the zeolite channel openings based on a TEM images of a coked industrial H-ZSM-5 zeolite (Si/Al =25, micro-sized crystallite), reacted in MTH reaction under the conditions of 400 ^{o}C, atmosphere pressure, WHSV of 2.0 h^{-1}, and reacted for 300 mins.

These transmission electron microscopy (TEM) pictures were undertaken using a JEM-3000F microscope (300kV). The catalyst samples were dispersed in ethanol and baked out in vacuum after transferring onto the carbon coated copper grids.

It is obviously shown that the coverage of superficial carbonaceous species is reflected by the blacking zones covering the originally transparent zeolite crystallite. The amplified vision of selected areas shows pore blockings at the zeolite edges.

Questions may come from the fact that Brønsted acid sites that are necessary for coke formation in a great portion locate inside the zeolite cavity/channel. [43] It is

hard to confirm the catalytic behavior of those surface Si-OH (silanol) groups that are typical terminal structures of the zeolite framework, for their contributions to the hydrocarbon conversions, as they only possess limited acid strength. [9, 14, 15, 43] However, considering there is a rapid mass transportation process during the reaction, the precursors of the external cokes may be activated inside the zeolite cavities/channels and then transported to the zeolite surface and finally stabilized. In fact, external cokes accounts for a great portion in the total coke amount, which has been examined by Bibby et al. [48] They noticed that in a MTH reaction over H-ZSM-5, the coke volume had exceeded the concomitant decrease in channel volume, therefore, there must have been coke deposited on the external zeolite surfaces. Surprisingly, the estimated inner cokes only took about 20wt% in the total coke amount.

1.4 Microwave absorption of carbon

1.4.1 General background

Microwaves lie between infrared rays and radiowaves in the electromagnetic (EM) spectrum. They are EM waves of 0.001-1 m in wavelength, corresponding to frequencies between 300 and 0.3 GHz. [49] The existence of microwave was firstly predicted in 1864 and then demonstrated in 1888 by Maxwell. Microwaves firstly attracted global attention in the WWII, for their special utilizations in military Radar; subsequently they came to global significance in public communications, and then

became popular for food heating in microwave ovens. [50]

In chemical science area, microwave techniques have been widely used for analytical purposes. One important application is the microwave-assisted sample preparation. Such technique is based on microwave digestion which helps to successfully mist different samples before next step analysis. [51] It has been noted that a wide range of samples can be digested, such as metallic, biological, environmental materials and even sludge, coal as well as synthetic materials. [52, 53] Instruments such as focused microwave system, [52] low-volume-sample microwave digestion system, [54] as well as continuous-flow microwave digestion system have been sequentially developed. [55]

Microwave Spectroscopy, as another important application of microwave in chemistry has been employed for decades in qualitative and quantitative analysis of materials. Not like digestion only in sample preparation, this technique directly analyses the targeted samples, and the basic idea relies on the interaction between microwave and materials, where chemical structure and relevant information can be obtained. [56] Such technique measures energy change in pure rotational transitions of polar molecules in gas phase in the presence of external MW field, providing information about molecular structure, geometry and the electronic structure of molecules. However, for coke characterization, microwave spectroscopy possesses intrinsic limitations due to the intermolecular interactions of solid coke species which suppress the rotational freedom and lead to poor signals for integration. [56, 57]

1.4.2 Fundamentals of dielectric heating

One important microwave application related to our project has been the microwave dielectric heating of materials, [58] particularly for carbonaceous species that are the major components of catalyst coke depositions [49] Such a heating process is based on the dielectric properties of the target material, and the related early researches can be dated back to the 1950s at which time the theory was soundly explained with a database of dielectric properties of common substances, foodstuffs and other materials initially established. [59] The rapid, volumetric heating by microwave effectively reduced the reaction time, and energy loss in some chemistry, therefore, soon became widely used in synthesis organic chemistry, [60] and, more in catalytic process. [61]

For a certain time, the time-reduced chemical reactions powered by MW heating were considered as a special case which was dynamically different from the case of thermal heating, and the related phenomenon was defined as ‘Microwave effect’. However, finally it has been found that chemical reactions proceeding under microwave conditions are governed by the same fundamental principles of thermodynamics and kinetics as reactions which occur under conventional thermal conditions. [62] The accelerated heating process by microwave is based on its more efficient heat transferability. In a conventional thermal heating process, energy is transferred to the core part of material through convection, conduction and radiation of heat from material surface. In comparison, microwave passes energy directly to the material inner part through interactions between material particles and the applied microwave field. Simply saying, thermal heating is transporting of thermal energy

from temperature higher point to lower point driven by the thermal gradients, and the part of energy transported is in terms of heat. Different from thermal heating, what really occurs in microwave heating is the transfer of energy from electromagnetic energy to thermal energy, thus, could be defined as a kind of energy conversion. The microwave field penetrates the full body of targeting material; therefore the transfer of energy occurs in each part of the material at the same time. [63]

Microwaves are electromagnetic waves containing both electric and magnetic fields. In a heating process, the microwave electric field applies a force on charged material particles as a result of which the charged particles start to migrate or rotate. Further polarizations of those polar particles could occur as a result of the initial movement. Here the external microwave forces applied to the charged particles are changing in direction with a rapid speed (for example, the common microwave frequency used in home and for commercial purpose is 2.45GHz), leading to heating effects due to the non-stopping assembly of molecules. For instance, the material cannot respond instantaneously to the rapid changing direction of the microwave *E*-field (the resulted migration and rotation of charged particles will not stop in this case) and this phenomenon generates heats owing to material particle frictions. [62]

The exact heating mechanism can be further specified into two models: ionic conducting and dielectric polarization depending on the material properties.

Ionic conduction, this mechanism is applicable to materials containing free ions or ionic species. Those charge ions/ionic species migrate and re-locate to form internal charge in an opposite direction to the applied external MW E-field, during which

process the resulted collision generates heat. [64] Iconic conduction has been widely applied in microwave-assisted synthesis & sintering of metal complexes. [65]

For dielectric materials, including dipoles, or those containing asymmetric charge distribution, the microwave heating undergoes dielectric polarization mechanism.

1) In the case of dipolar molecules, such as water and other polar fluids, the electric field component of the microwaves causes both permanent and induced dipoles to rotate as they try to align themselves with the rapidly alternating field (e.g. according to the normally used microwave frequency 2.45GHz, the applied field alternates 2450 million times per second). The motion of the polar molecules causes friction and energy is dissipated in the forms of heat. This phenomenon is defined as Dipolar Polarization. [49]
2) In the case of dielectric solid materials with charged particles that can move in a delimited region inside the material, a current traveling in phase with the electromagnetic field is induced. Taking the π electrons in SP^2 carbons as an example, as they cannot couple to the external alternating electric field, the induced current generates heat causing energy dissipation. This phenomenon is called Interfacial or Maxwell-Wagner Polarization. [66]

1.4.3 Measurement of material microwave-heating ability

To measure the ability of a dielectric material that can be microwave heated, a set of parameters are introduced. A dipolar material contains either permanent or induced diploes, and when placed between two electrodes acts as capacitor (energy is stored in

dipolar polarization), i.e. the material allows charge to be stored and no dc conductivity is observed between the plates. At the molecular level, this is achieved by redistribution of the electron cloud within a molecule or, relocation or rotation of the molecular dipoles, which stores energy from the applied external *E*-field. On the other hand, energy is also dissipated in terms of heat by induced frictions. [58] So the behavior of dielectric materials in a MW *E*-field involves both energy storing (charging) and dissipation (elimination in heat). The permittivity of a material, ε, is a property that describes the charge storing ability of that substance irrespective of the sample's dimensions. In practice, the extent that a microwave field interacts with a substance is quantified by the relative permittivity, or dielectric constant, ε*. It shows a measure of the ability of the dielectric material to store and absorb electric potential, quantifying the fundamental interaction between the material and the microwave *E*-field. [67] The exact definition is shown in the below:

$$\varepsilon^* = \varepsilon' - I\varepsilon''$$

Here ε' is the real part of the relative permittivity, it measures the ability of material to store electromagnetic energy through polarization corresponding to when the dipoles (or charged particles) are in phase with the alternating *E*-field. ε'', defined as dielectric loss factor, is the imaginary part of the permittivity, which expresses the efficiency of the material in converting electromagnetic energy into heat. Without doubt, for effective microwave heating a higher ε" value is necessary, where tanδ = ε"/ε', called dissipation factor or loss tangent is introduced. The tanδ value reflects the tendency and ability of a material to convert electromagnetic energy into other forms

of energy (heat in the case of microwave heating process) rather than being stored in the substance through polarization. [58, 62, 63, 67] From the change in microwave resonant frequency (Δf) and the change in bandwidth (ΔBW), we can infer the above mentioned sample dielectric properties. [68, 69]

Commonly present in the post-run deposits, carbonaceous species, or cokes, are often the main reason of catalyst deactivation, and they are also found to be excellent microwave absorbing (converting energy into heat dissipated) materials, thus, we believe that they can be 'microwave measured'. In previous work, it has been proved that the proportion of sp^2 hybridized carbons within a carbon based material could be measured with the microwave cavity perturbation technique. [68, 70] The obtained results show that microwave absorption is proportional to the sp^2 carbon content in the material and therefore their qualification and quantification could be achieved. Carbonaceous species are dielectric solids, as discussed above, and do not possess dipolar polarization since the particles are not able to rotate or migrate freely. Instead, the excellent microwave absorbing/heating ability of these carbon materials are due to the special π electrons in sp^2 carbon structures. These highly mobile electrons are free to move in delimited regions, therefore undergo Maxwell-Wagner polarization to a greater extent than the electrons in sp^3 carbons, where enhanced current could be achieved due to the movement of the electrons and therefore causes more energy dissipation in terms of heat. This dielectric loss property (i.e., ε'') of sp^2 carbon, which can be reflected by changes in microwave resonant properties (e.g., Δf and ΔBW) detected with microwave cavity perturbation technique, as we proposed, could

be utilized in the catalyst coke analysis. The unique distribution of sp^2 carbons characteristic of a particular coke compound would lead to distinguished intensity of signal obtained, therefore could be used as important evidence for further identification and quantification. [49, 68-70]

Chapter 2 Experimental methods, instruments, and fundamentals

2.1 Catalyst preparation methods

Solid catalysts can be prepared by a variety of methods, here only the approaches employed by our researches are illustrated in the contents below.

2.1.1 Impregnation

A common way to modify a porous solid state catalyst with large surface area and inner pore space, such as zeolite, is to dope with the catalytic promoters which will provide one or multiple extra functions so as to adjust the intrinsic properties of the original material. Here, the so called ‘impregnation’ means catalyst modification via ‘plating’ the original catalyst material inside another phase (e.g. solution of promoter/precursor), or, by high efficiency mechanical mixing of the original catalyst material with precursors (precursors are stable compounds in normal conditions and can be converted into corresponding promoters in the later preparation steps such as a high temperature calcination). The ultimate goal is to achieve a highly dispersed, uniformly distributed precursor/promoter phase over the original catalyst body.

One frequently used method is ‘precipitation’ impregnation, in which the precursor phase is precipitated onto the zeolite by, for instance, a sudden pH change in the mixture (solution), or by chemical reaction. However, a later filtering step is required

which normally causes unavoidable waste and pollution of water. [71]

A better method which effectively saves the solution usage, thus has been employed in series of our works is the ‘incipient wetness’ impregnation. The technique is based on a pre-calibration of the sample (i.e. zeolite) ‘solution absorbing volume’. Here the precursor/promoter concentration in a prepared solution should meet the necessary requirement that volume of solution added onto the original zeolite body can bring the exact amount of promoters to the zeolite and just change the zeolite from powder phase into a ‘incipient wetted’ look close to very dry slurry. In such a process, capillary action draws the solution into the pores, and in the case that a higher promoter loading level is required (the maximum sample solution absorbing volume × highest precursor/promoter concentration in solution cannot meet the required promoter loading amount) multiple impregnation steps can be applied. The method also brings in another important benefit, which is the step-controlled doping of precursor/promoter, for instance, the total amount of doped additives (precursors or promoters) can be directly calculated from the volume of solution drops and their concentration in solution as no solution is wasted in such a process. [72]

The next step is to dry the impregnated material and then usually calcine to further remove moisture, and particularly, to convert the precursor phase into the required promotors. The temperature employed would affect the distribution of promoters in the porous structure, where concentrations and the porous structure also play an important role in the process. [73]

2.1.2 To make the catalyst into a ‘shape’

The final step in the production of many industrial, heterogeneous catalysts is to give the catalyst a macroscopic, shaped form which can be used in the plant with improved mechanical strength, as well as much better hydrothermal stability, plus somewhat poison tolerance. [3, 73-76] This can be carried out in two ways. The desired technical form catalyst can be shaped by either high pressure compaction (e.g. in the manufacturing of pellet catalyst), or an extrusion process of the plasticized catalyst-additives mixtures. Here the plasticized form gives certain freedom of shaping, where catalyst binders (e.g. silicon, alumina and their deviants) and other additives are employed to effectively bind the powder phase zeolites, and may also play the roles like functional promoters, or co-catalysts. Again, after the mixing steps, a drying/calcination step is required to remove the moisture, and further combine the parent zeolite phase with the binder, which also support a better mechanical strength of the prepared industrial form catalyst. The exact mixing and shaping protocols and processes vary according to the different production requirements. Our work (to be described in the Chapter 4) targets the scaled up Methanol-to-Hydrocarbon reaction over technical form nano HZSM-5 zeolite (shaped into the cylindrical ‘rods’), with the help of Al_2O_3 binder in catalyst shape formation. [3, 11, 73]

2.2 Catalytic performance test

2.2.1 Fixed bed reactor system

In most heterogeneous catalyst investigations, a fixed bed reactor is the favorite choice often employed by the researchers for small-scale tests. [77-85] In such reactors (Fig. 2.1), the catalyst body is placed in a fixed bed (or packed bed) that is held between two supporting layers, which forms a kind of 'sandwich' structure.

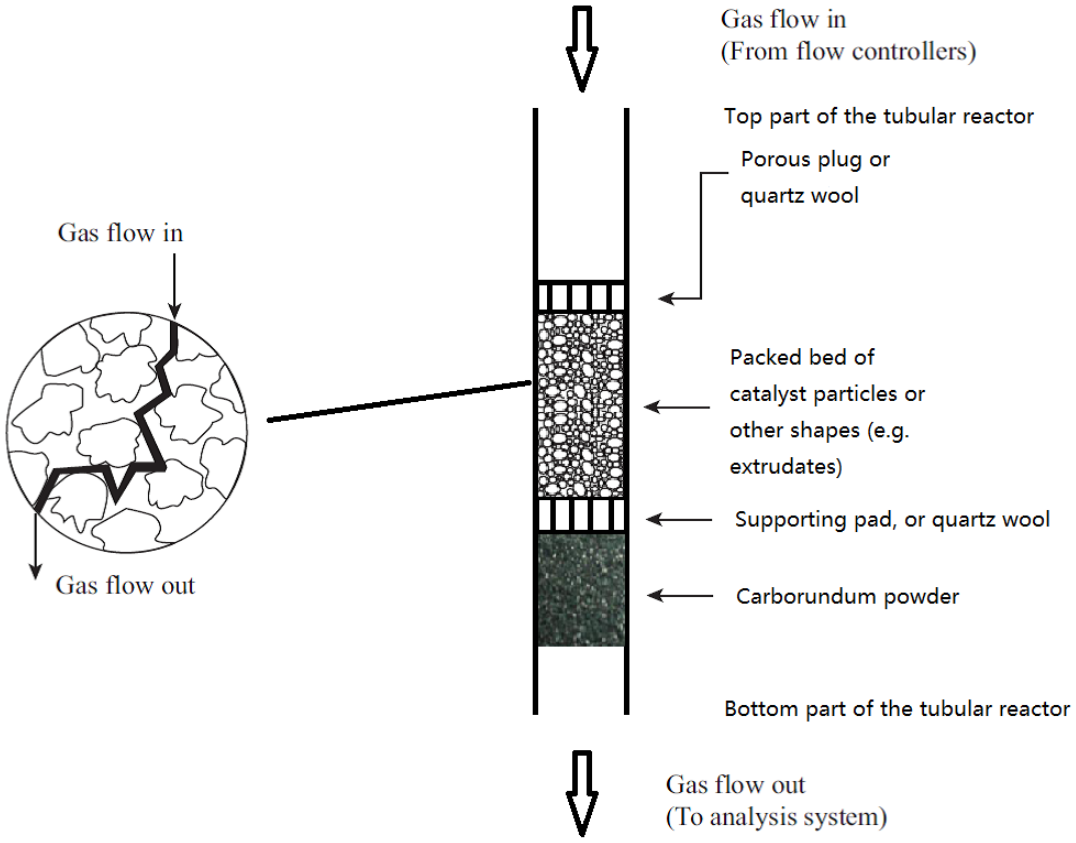

Fig. 2.1 Schematic representation of a fixed-bed tubular reactor usually for small-scale catalyst test [3]

The sandwich structure loading is designed to help ensure uniform contact of the

reactant(s) with the settled catalyst. To support the loaded catalysts (in most cases, the reactor tube is set vertically, so the catalyst weight needs to be hold), and prevent escape of the catalyst powders (this may cause downstream channel blocking), a supporting pad (in some cases quartz wool) and/or frits (e.g. silicon sand, or carborundum particles) are set just beneath the catalyst bed bottom. In many cases, the catalyst bed top is also covered by porous pad or quartz wool so that the packing of catalyst is not disturbed. One common feature of such reactors is a frequently used tubular design (the reactor is forged into a tube shape with high quality stainless steels or other materials), which is normally mounted vertically to make sure that the catalyst bed is packed as uniformly as possible and the gas flow passing through can be directed from top (beginning part of the tubular design) to bottom (end part) smoothly to ensure that the packing of the catalyst bed is not disturbed by the flow turbulence. [3]

One important thing that needs to be particularly addressed in the design of fixed bed reactor is the gas flow between the catalyst particles, which has been illustrated in Fig. 2.1 (the amplified vision shown on the left hand side). The packing of the bed must be such that the gas flows through individual catalyst particles in a highly tortuous fashion (this occurs in micro space between the catalyst particles) to ensure that there is good lateral mixing and minimal concentration gradients in the catalyst bed layer at right angles to the axis of the reactor. However, concentration gradients of reactant and product along the axis of the reactor are common phenomenon (Fig. 2.2).

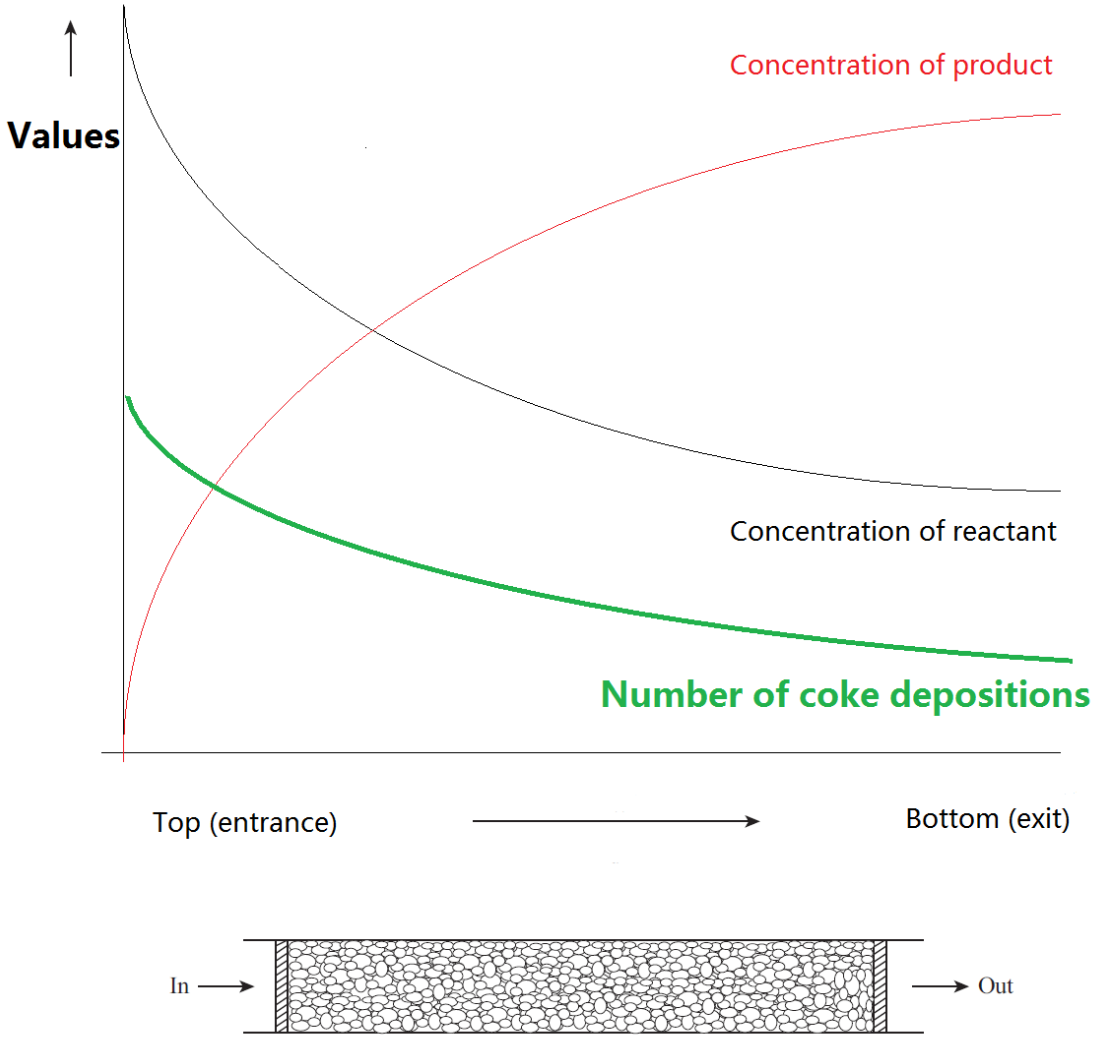

Fig. 2.2 Concentrations of product and reactant plus number of coke depositions vs. positions in a fixed bed tubular reactor [3]

In most cases, as it is the first contact with the continuous flow of reactant, the top (entrance) part of the catalyst bed possesses the highest reactant concentration. In contrast, the product concentration at the bottom of catalyst bed would be much higher than all other positions. This is because the reactant flow is gradually consumed along the catalyst bed from the top to the bottom, while more products are gradually accumulated close to the bottom by the gas flow.

For optimized mixing in the tubular reactor, the catalyst body must be significantly

smaller than the diameter of the catalyst bed (this is also the reactor inner diameter in most cases). For instance, more than 10 catalyst particles across the catalyst bed diameter are suggested, and the catalyst bed depth should be more than at least three times of the bed diameter so as the back mixing of products with reactants can be avoided. Here the pressure inside reactor is controlled by the integrated pressure maintaining system (a set of values positioned before and after the tubular reactor), and the pressure drop along catalyst bed has been minimized to a negligible scale.[3]

It should also be noted that coke accumulates along the catalyst bed when catalyst deactivation occurs, which normally shows an opposite direction to the gradient of product concentration (Fig. 2.2). The highest reactant concertation at the catalyst bed top results in the local product yield greatly accelerated, while part of the products can be transported to the bottom of catalyst bed, others would be trapped and further dehydrogenated and converted into the high density coke species. This effect reduces along the catalyst bed from top to bottom, which is not directly correlated to the product concentrations but somewhat greatly affected by the product transportability and local reaction rate (it is easy to imagine there is a faster reaction rate at the catalyst bed top due to the highest reactant concentration). [3, 12, 41, 74, 76].

The integrated catalyst test system employed in our experiments with a tubular fixed bed reactor as the core part is schematically shown in the following Fig. 2.3.

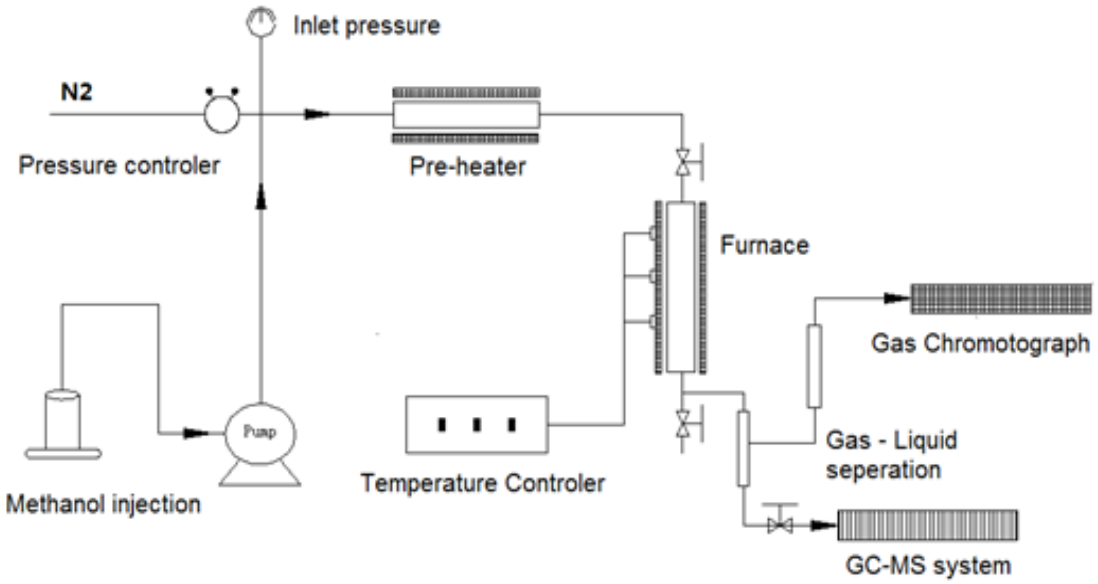

Fig. 2.3 Schematic representation of a fixed bed reactor system for catalyst performance test

Placed in a suitable furnace, with a thermocouple inserted either in direct contact with the outside walls next to the catalyst bed or inside a sleeve dived into the bed itself, the tubular fixed-bed reactor can be carefully heated with precise control on temperature ramping. Normally, before the reaction, the catalyst bed will be heated to the temperature that is required for the planned reaction and maintained at that temperature for a certain time period (e.g. 1 hour before the reactant injection) so as the catalyst is fully activated and purified (in some cases, a higher temperature may be employed which will be cooled back to the temperature that is required for reaction). Prior to the reactor, there is a pre-heater often set to temperatures between 150-200 ^{o}C (the exact setting may vary according to different experimental requirements, for methanol conversion, 150 ^{o}C is enough to get all the methanol molecules vaporized into gas phase), which allows the non-gas-phase reactant (e.g. methanol liquid) to be fully vaporized so that it can be carried into the reactor by the carrier gas (inert gas,

such as nitrogen, or helium). Liquid reactant is injected into the system with a HPLC (High Performance Liquid Chromatography) pump, and the rate of reactant injection is carefully pre-calibrated periodically. The injection rate of reactant plays an important role in controlling the Weight-Hourly-Space-Velocity (WHSV) of the reactant, which directly affect the speed of reaction and also the exact catalytic performances as well as coke accumulation. In most investigations, catalyst loading of 0.5-2.0g is recommended, and a mild WHSV of $2.0h^{-1}$ is sufficient to measure the intrinsic catalytic performance of samples. For instance, in the case that 1.0g of catalyst is loaded, a $2.0h^{-1}$ WHSV requires $2 \times 1.0g = 2.0g$ of reactant to be injected and transported to the catalyst every one hour.

All products are transported out from the reactor originally in gas phase with the help of a carrier gas, and subsequently cooled down to lower temperatures (e.g. room temperature) so as liquid and gaseous products (this is the natural phase of these chemicals at room temperature under atmosphere pressure) can be easily separated in the liquid trap. Normally, there is a cooling water system passing through the outer wall of the liquid trap, which helps to remove the heat and cool down the products to lower temperatures. Analysis of products is often carried out with a Gas-Chromatograph system, configured with multiple detectors.

The arrangement and connections of all the above components are shown in the below (Fig.2.4).

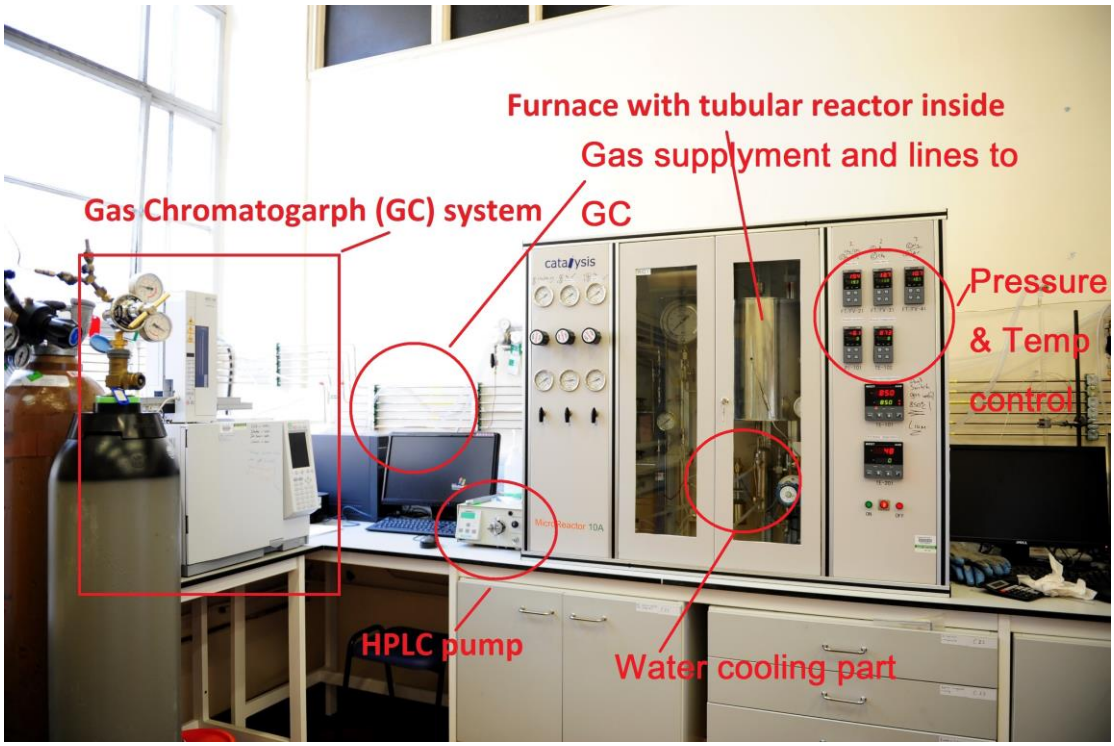

Fig. 2.4 Instrument arrangement and connections of our catalyst testing system

For gas products, in most cases, on-line monitoring of product yields during time-on-stream reaction is allowed, by sampling flow of gas mixture at time intervals (e.g. every 30 mins). Liquid products can be collected after the reaction and analyzed off-line; however, in case that the quantity of liquid is enough for on-line analysis sampling at time intervals is also available.

The post-run catalyst can be un-loaded after the reactor is cooled down to room temperature. Coke deposits in post-run catalyst sample are important for assessing catalyst performance and deactivation, and can be analyzed in many approaches, e.g. ^{13}C NMR, and Laser-Raman.

2.2.2 Gas Chromatography in catalyst test

As is mentioned above, Gas-Chromatography (GC) plays the major role in the

reaction product analysis, which directly measures the catalytic performance, e.g. conversion of reactant, and selectivity to a certain product. It is a commonly employed technique for the separation of volatile components of mixtures by differential migration through a column containing a liquid or solid stationary phase. [86] In a separation process, solutes are transported through the column with the help of a gaseous mobile phase and are detected when they are eluted.

In most cases, inert gas is employed as the mobile phase to carry the analytes passing through the column, generally nitrogen or helium, supplied from a cylinder via pressure and mass flow controls. It should be noticed that it is better to use two different inert gases for reactor carrier gas, and GC column carrier gas, respectively. The GC carrier gas (mobile phase in instrument) will not interact with the injected sample, and there is even no need for it to be detected. On the other hand, the inert gas employed as reactor carrier gas will be present in the reactor effluent (it will not interact with the reactant and reaction products) with the product mixture, thus can be used as internal standard for product quantification, and normally its quantity is an already known figure which has been predetermined before the reaction (it also requires a good GC signal response of the carrier gas in this case, for an accurate calculation). [86, 87]

Column property is uniquely important for an efficient separation of analytes. GC columns are either long, narrow, capillary tubes, [88-90] with the stationary phase coated onto the inside wall, [91] or tubes with materials packed inside. [92-95] The most important feature of stationary phase is a high boiling point, according to which,

thermo-stable liquids, waxes or solid sorbents (e.g. zeolite) are good materials. [96-98]

Successful separation of different analytes also requires relatively high temperatures inside the column, where a thermostatically-controlled oven that is maintained at a steady temperature or programmed to increase temperature progressively during a separation is normally employed.

Optimized GC column separation is a combination of suitable instrumental settings (e.g. a right carrier gas flowing rate, and an efficient temperature-ramping program) with proper column choice. In practice, separation of different analytes in a column is based on their distribution ratios between the mobile phase and stationary phase. During a chromatographic separation, there is a continuous transfer (exchange) of analyte species back and forth between the mobile and stationary phase by the process of non-stopping sorption and desorption. These are inversely proportional to the volatilities of analytes, which are determined by their partial vapor pressures and hence their boiling points. As a result, different analytes elute from the column in an order of increasing boiling point, otherwise, there might be specific interactions between particular analyte and the stationary phase which also affects the elution time. [89, 90, 97, 98] Instead of elution time (a single time point when an analyte elutes out), the exact separation is characterized by the retention time of analyte, which is the time length taken by an analyte to pass through the column. [86, 87]

Here the retention time, t_R, is defined as: [86]

$$t_R = t_M (1+k)$$

where t_M (the dead time) is the time taken by a non-retained solute to pass through the column, and *k*, the retention factor, is a value in direct proportion to the distribution ratio (D) of an analyte.

The distribution ratio, D, can be worked out with the formula below: [86]

$$D = C_S/C_M$$

where Cs is the total analyte concentration in the stationary phase, and correspondingly, C_M is the total analyte concentration in the mobile phase, achieved by a timeless exchange in theory (this is an intrinsic property of the analyte). It should be noted that a non-retained solute migrates at the same velocity as the mobile phase, thus, possessing a distribution ratio and retention factor of zero; also $t_R = t_M$. Any analyte with D and *k* values higher than zero are proportionately retarded in the GC column, resulted in longer retention time than the t_M. An efficient separation requires a *k* value smaller than 20, otherwise there will be an unacceptably long retention time. More detailed information and fundamental explanations can be found in text books. [86, 87]

The detection of analytes is based on a process, in which the GC carrier-gas carrying an analyte passes through a detector that responds to changes in a bulk physical property, such as its thermal conductivity, or to a specific property of the injected analytes themselves, such as their ability to be ionized. The detector responses are recorded and converted into digital signals. In practice, during a chromatographic analysis (separation + detection), individual analyte develops a symmetrical or Gaussian concentration profile in the direction of flow of the mobile

phase. For efficient and accurate chromatographic separation, the profiles, in terms of peaks or bands, should be clearly separated in the results, where quantification of analytes can be achieved by mathematical integration of the profiles. Normally, the integrated peaks are directly proportional to the amount of analyte chromatographed when working within the linear range of the detector, and are the most reliable. [87, 99-101] For the quantifications, calculations are based on previous calibrations by using pure standards. The basic work is to establish a relationship between the detector responses and the already-known concentrations of a particular analyte, and in most cases, there will be a well-developed linear trend reflected by the calibration results. [102-106] The establishing work of a calibration graph may employ an extra standard compound, as an internal standard for calculation, or, proceed without adding a standard, just by comparing signals with pre-determined analyte concentrations. The exact theories and explanations on calculation can be found in Gas-Chromatography text books or Analytical Chemistry books. [86, 87, 99, 101]

In the analysis of gas components, we have employed two common detectors, Thermal Conductivity Detector (TCD) and Flame Ionization Detector (FID). TCD (Fig. 2.5), as one of the classic types, is a basic detector made up of a heated metal block which contains a reference cell through which reference gas (normally there is pure carrier gas as reference) constantly flows, and a sample cell through which gas mixture (GC carrier gas and analytes) flows. [86, 100]

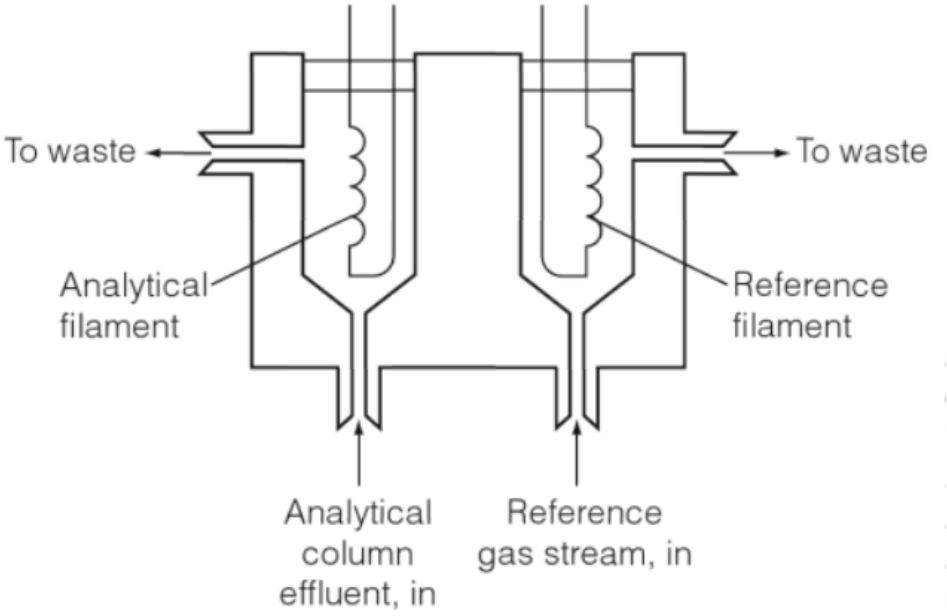

Fig. 2.5 Schematic representation of a Thermal Conductivity Detector (TCD) [86]

The core part of TCD cells is an individually heated platinum filament whose resistance depends on its temperatures, and hence the rates of heat loss from its outer surfaces which is as a function of the thermal conductivity of the gases at surroundings. When both cells are filled up with carrier gas only, there will be no difference in the filaments' resistance, and hence the *Wheatstone bridge circuit* into which they are incorporated is balanced. [86, 87, 100, 101, 107] This balance gives a base line of the detector signal. The introduction of analyte gas (normally some inorganic, non-hydrocarbon gases, such as N_2, H_2 and CO) into sample cell will break out the above balance as it changes the gas composition surrounding the filament, which leads to the difference in resistance. The out-of-balance signal is generated in the bridge circuit, and is in proportion to the introduced analyte concentration (idealy, due to the perfect separation each signaling time is only responsible to a single analyte). TCD performs well as a basic but comprehensive detector, and the only

weakness is the limited sensitivity to some organic compounds. [86, 87, 100, 101]

Organic compounds in the reaction gas effluent can be better analyzed with a Flame ionization detector (FID), which possesses much higher signal sensitivity for hydrocarbons (schematically shown in Fig. 2.6). [86, 87, 100] The signal intensity of FID is decided by the ionization of analytes in flame combustion. Gas from the column is mixed with air and hydrogen, and combusted at a small metal jet, where a DC potential (150-300 V) is applied between the burner jet (positive) and the collector electrode (negative) just above the flame. Signals are generated from the electrodes, which can be further amplified by external circuit. The electrical conductivity between the electrodes is directly affected by the ions generated from analytes combustion in flame (flame ionization). One most important feature of the FID detector is its widest linear dynamic range among all GC detectors, which makes it as the best choice for quantification of analytes. [99, 100, 108] Correspondingly, a lack of signal response to inorganics (poor combustion) also limits the application of FID, and in most cases, gas analysis employs both TCD and FID working in a parallel way. [86, 87, 100, 101, 107, 109]

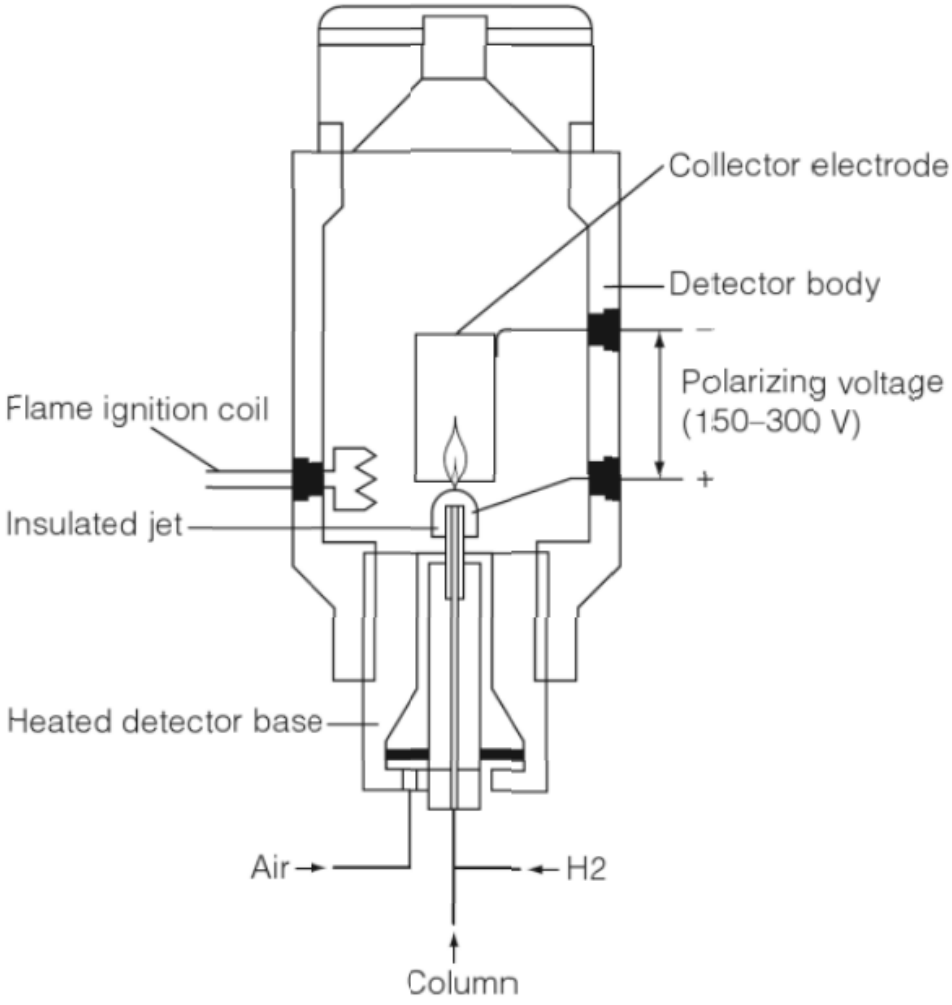

Fig. 2.6 Schematic representation of a Flame Ionization Detector (FID) [86]

Liquid product analysis in our works employed an off-line Gas Chromatography and Mass Spectrometer (GC-MS) system (also with FID installed). A mass spectrometer measures the mass-to-charge ratio (m/z) of gaseous ions, and reflects the abundance of each ionic species. As a result, measurement of the corresponding dissociated, ionized compound is available (for a single molecular, it may be broken into a molecular-mass ion, or several lower-mass fragment ions, which is characteristic of the molecular structure). [110-112] Practical measurement is calibrated against ions of already-known m/z, and to date, computer-aided database

supports a more efficient analysis process. [110-115] For GC-MS analysis, the charge employed is almost always 1, and therefore the calibrated scale is in Daltons or atomic mass units. [114] The gas phase ions of different masses (from one molecule) are separated in a low pressure condition by steps of interaction with applied external magnetic or electrical fields (simply shown by Fig. 2.7a); as a result, the pattern of detected ion signals, when displayed within a calibrated mass scale, can be achieved as a 'fingerprint' of the analyte compound, and is called a mass spectrum (the mass spectrum of toluene is presented as an example by Fig. 2.7b). Generally saying, separation of ions takes place inside a channel system governed by external electromagnetic field, the ions of a certain m/z value will have a unique path radius which can be determined if both magnetic field magnitude (B) and voltage difference (V) for region of acceleration are held in a constant. When similar ions pass through the magnetic field, they all will be deflected to the same degree and will all follow the same trajectory path. Those ions which are not selected by V and B values will collide with either side of the flight tube wall or will not pass through the slit to the detector. Here the various ionization and separation methods have beyond the research of this thesis (this is much deeper knowledge than the fundamentals of basic Gas-Chromatograph and takes a lot contents to describe in details), and can be found from the cited text books or any comprehensive analytic chemistry books, therefore, they are not included for further discussions.[110, 114, 115]

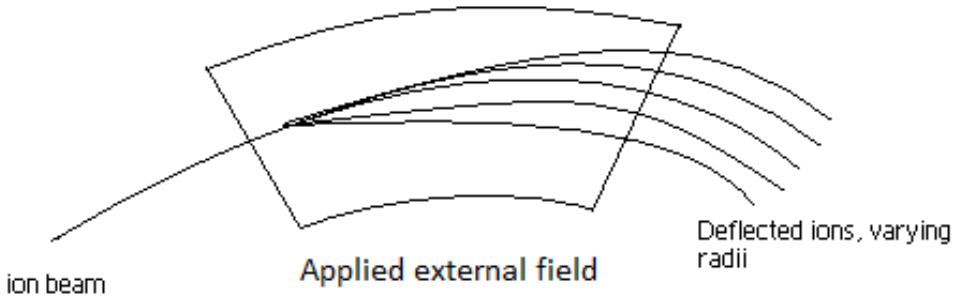

Fig. 2.7a Schematic of ion separation process by external magnetic fields,[116]

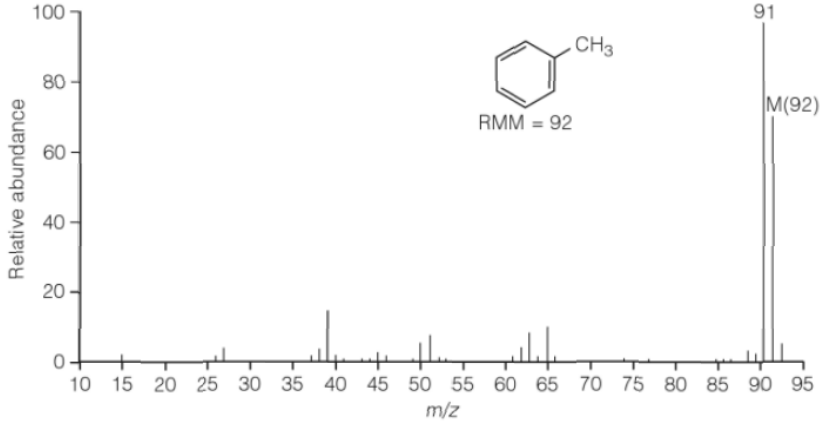

Fig. 2.7b An example of mass spectrum of toluene [86]

Modern computer-aided GC-MS system can automatically identify the ionized compound by matching the obtained mass spectrums with the preloaded database; therefore, GC-MS is also the best choice for detecting unexpected reaction products. Prior to the Mass spectrometer, separation of different analytes accomplishes in the gas chromatography, where the exact process is similar to the normal GC analysis with TCD/FID. As MS manages to identify the analyte, there is no need to match the analytes with their GC column retention times for identification, unless there is a special need for more efficient column separation. Here the MS responses corresponding to the quantity of an analyte compound can be converted into digit signals, and when combined with the gas chromatography, GC-MS profiles can be drawn for quantifications. The calculations and calibrations are similar to what have

been employed in GC analysis with FID. [87, 110] Fig. 2.8 in the below shows captured GC-MS profiles of typical oil products (diluted in acetone) in a methanol-to-hydrocarbon reaction, as a function of their GC column retention times.

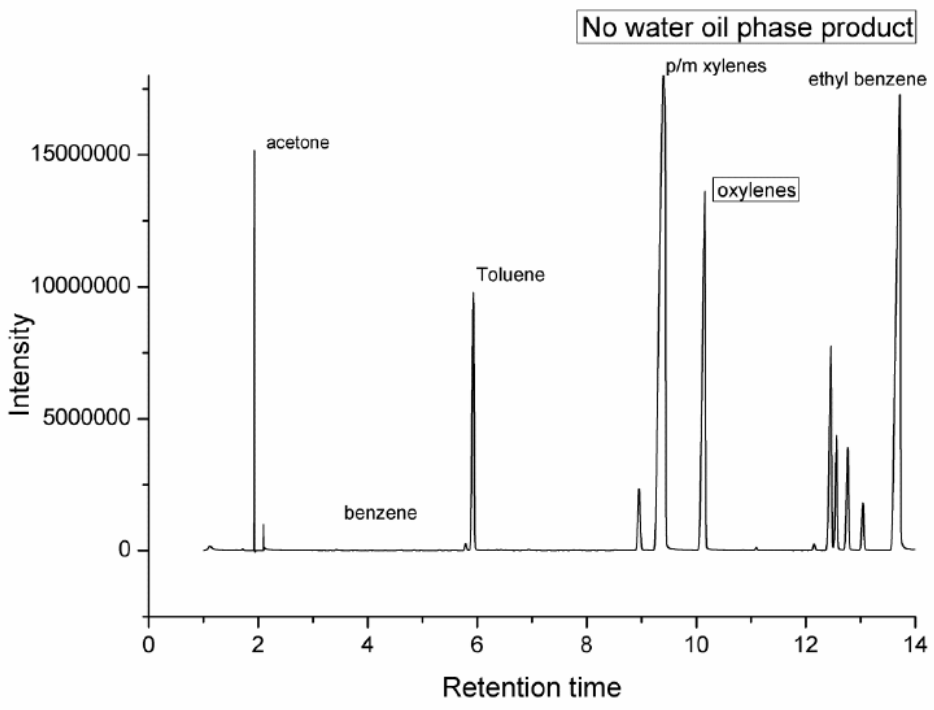

Fig. 2.8 GC-MS profiles of typical oil products achieved from a methanol-to-hydrocarbon reaction, diluted in acetone

2.2.3 Real product analysis

For discussions in this chapter, we mainly focused on the fundamentals of analysis which give a direct output of product concentrations, while the calculation methods of product yields (the main value we employed to measure the reaction performance), and methanol conversion are illustrated in the following chapters, and are subjected to different researching requirements.

Sample preparation

For gas analysis, there is no special requirement on sample treatment and all products are directly transported via a stainless steel line to the GC instrument at set time intervals, where reaction carrier gas nitrogen is employed as internal standard for gas product quantification. In the online monitoring process, we choose every 30 mins as interval between each gas sample injection, which is based on a total 27 mins analysis time (column separation + instrument cooling time). In some later works, sample injection time was changed to every 45 mins, this was for a better separation of C_2-C_4 alkanes and olefins.

Liquid products are collected at time of one hour after the reaction, with a narrow-mouth glass bottle. Before analysis, pre-treatment via still standing helps to further separate the liquid into 3 phases (wax, oil and water phase). The wax phase is closely combined with the oil (in most cases it can be dissolved), thus only two clearly separated phases can be observed in the bottle. The oil phase, on top of the water phase, consist of most of the aromatic products formed in the MTH reaction, can be carefully transported to another tube with syringe, and weighted and subsequently mixed with the internal standard compound (heptane) before the offline GC-MS analysis. The water phase is mainly made up of water, and/or methanol in tiny amount (in case the catalyst deactivation occurs at an earlier time, the un-reacted methanol possesses a certain amount in the water phase, but rarely can be observed in the oil phase). Fig.2.9 shows the collected liquid product before separation, and a schematic representation of the liquid separation via still standing treatment for

approximately 60 mins.

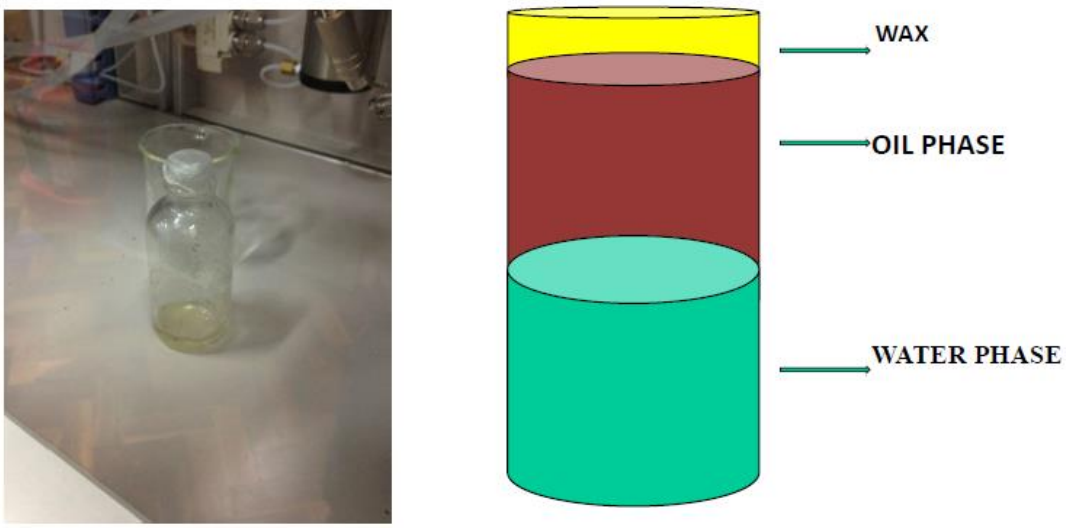

Fig. 2.9 Collected liquid product in a narrow-mouth bottle (left) and 3 layers separation of liquid products via still standing (right)

Instrument and settings

Gas product analysis carries out in a Shimadzu GC-2014 system (Fig. 2.10). For the best column separation efficiency, a RESTEK MXT-1HT column is employed and temperature-programmed heated when works. Liquid product analysis works with a Shimadzu GC-MS 2010 ultra system (Fig. 2.11), where a Shimadzu 5MS (5% dimethyl-siloxane) column is employed for analyte separation.

The instruments and operating conditions are illustrated in the below. The calibration works on best separating conditions are under the guidance of professionals from Shimadzu UK. The employed conditions allow a 30min/45min gas online monitoring, and a comprehensive analysis of liquid products.

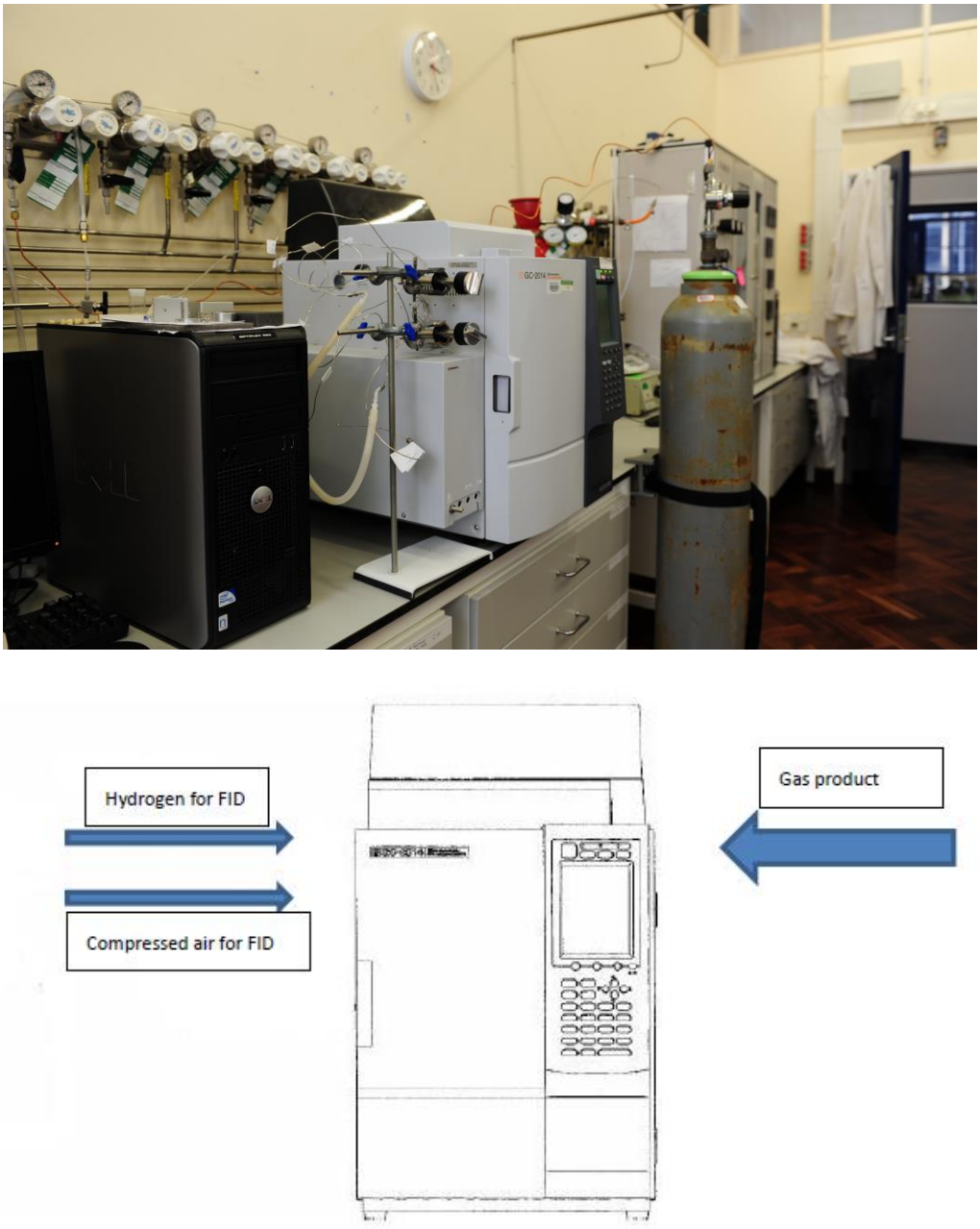

Fig. 2.10 Shimadzu Gas Chromatography 2014, with TCD and FID for gas product online monitoring (upper), and a schematic representation from the front (bottom)

Mode: Shimadzu GC-2014
Column: RESTEK MXT-1HT column (100% dimethyl poly-siloxane phase allows easy comparisons to historical data, length 5m, internal diameter 0.53 mm)
Col. Temp: 30^{o}C – 5^{o}C/min – 250^{o}C – 10min (hold)
Inj. Temp: 200^{o}C
Det. Temp: 250^{o}C
Carrier gas: He 5ml/min

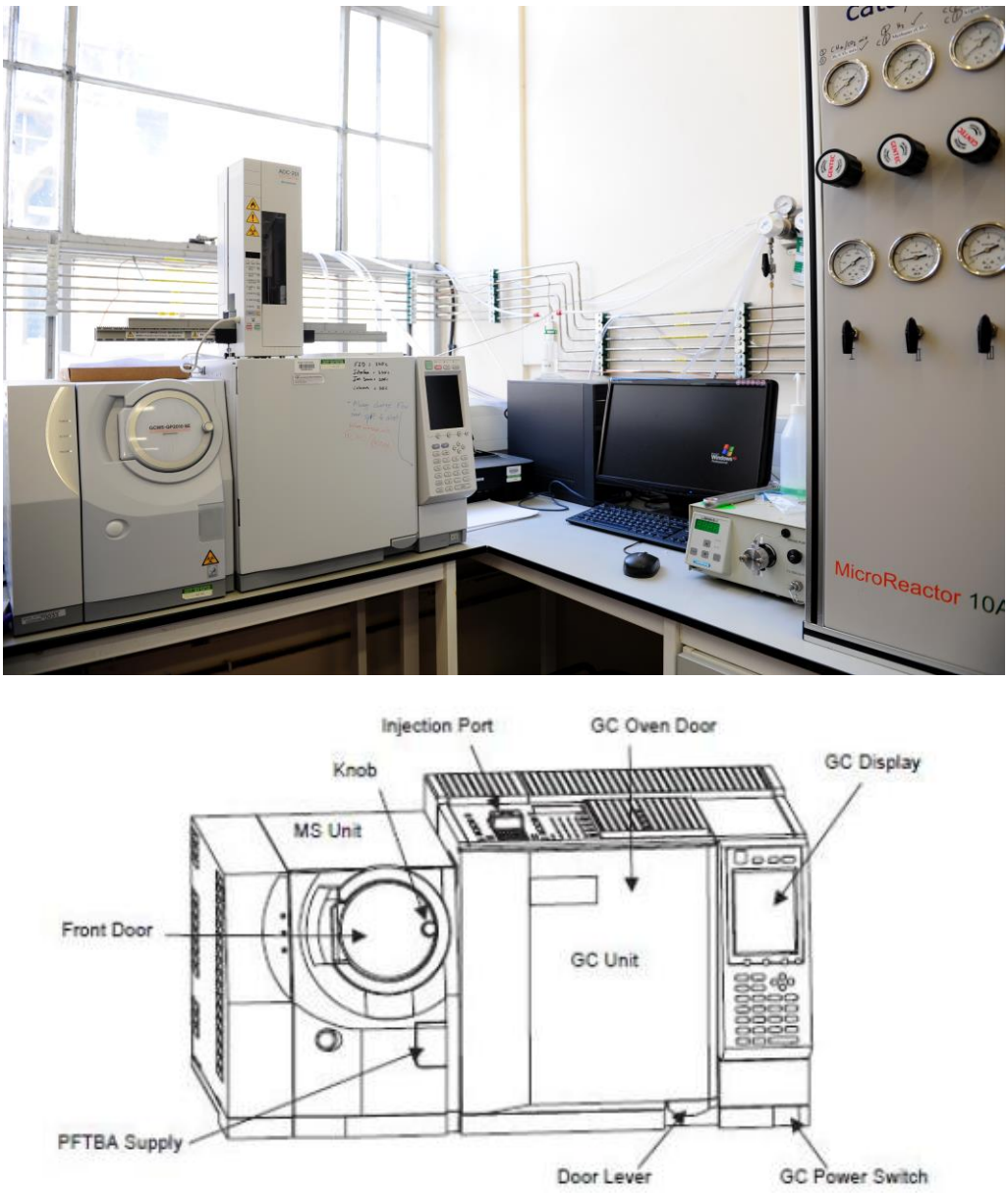

Fig. 2.11 Shimadzu Gas Chromatography – Mass Spectrometer (model GC-MS 2010 ultra) with Auto-sampler for liquid injection (all shown in the upper picture), and a schematic representation from the front view (bottom)

Mode: Shimadzu GC-MS 2010 ultra
Column: Shimadzu 5MS column (5% dimethyl-siloxane, column length 5m, internal diameter 0.25mm)
Col. Temp: 30^{o}C – 10^{o}C/min – 250^{o}C – 5min (hold)
Inj. Temp: 250^{o}C
Det. Temp: 250^{o}C
Carrier gas: He 40kpa pressure controlled flow rate at 50^{o}C
Inj. Split: direct, or 1:8 split ratio for high concentrations
Inj. Volume: 0.2Ml
Pretreatment: still standing for separation of layers

M/Z: 30-200
MS detecting time: 1min – 30min
Ion source temp: 200^{o}C
Interface temp: 250^{o}C

Calibration and quantification

Calibration work carried out with the purpose of establishing a method to detect the quantity of particular product with the GC response (normally, integrated chromatography peak area, or peak height is employed).

In our calibrations, main-product substances and internal standard are mixed in a series of designed ratios, and subsequently analyzed with GC instrument, with all chromatography peaks integrated. The work is to work out an *f* factor which helps to calculate the unknown quantity of a detected product substance, when the product substance's GC peak area, internal standard's GC peak area and the amount of internal standard employed are clear.

The basic principle is that the integrated peak area (a kind of GC detector response) is directly proportional to the amount of a substance chromatographed when working within the linear range of the detector, and considered to be the most reliable. [86, 100, 101, 114, 115] Here the *f* factor is defined as below,

$$\frac{\mathrm{M}_{\text{product}} / \mathrm{Area}_{\text{product}}}{\mathrm{M}_{\text{standard}} / \mathrm{Area}_{\text{standard}}} = \text{a constant } (f \text{ factor})$$

where M is the mass (or amount) of a substance, and only $\mathrm{M}_{\text{product}}$ in the above equation is unknown in a practical measurement, and hence can be calculated with the pre-calibrated *f* factor.

In practice, the GC instrument software automatically combined the calibration data into program (this part is done by the professionals from Shimadzu UK), and the desired product quantity therefore can be directly shown after each analysis.

2.3 Catalyst characterization methods

2.3.1 X-ray diffraction

Fundamentals

X-ray diffraction (XRD) analysis is employed to describe the crystal properties of solid state sample. The technique relies on the phenomenon that an incoming X-ray photon can be elastically scattered as a spherical wave by the electron density associated with atoms in the analyzed material. In the case that there is periodically distributed electron density, as in a crystal structure, there will be interference between the scattered waves. Although in most directions, these waves impair one another through destructive interference, however in some specific directions they do assemble constructively (shown as ‘reflections’), as is governed by the famous Bragg’s Law [74]

$$n\lambda = 2d\sin\theta$$

Here d is the spacing between diffracting planes, θ is the angle between the incident X-ray and the diffraction plane, n is the positive integer “order” of the reflection, and λ is the wavelength of the incident beam. The formula implies that it is the crystal

lattice determines the angles at which a strong scattered signal can be detected. The intensity at each Bragg angle depends on the amount of electron density in the corresponding diffraction plane.

Commonly employed methods in laboratory include single crystal diffraction, as well as powder diffractions. For single crystal experiment, the alignment of the crystal, source and detector has to be set in a critical way in order to observe reflections. The reason for that is the measurement of scattering from one particular crystal plane at a time depends on proper alignment of the crystal. In contrast, a sample in powder phase is made up of numerous very small crystallites, normally 10^{-7} to 10^{-4} mm in size, and hence allows randomly adoption of the whole range of any possible orientations. As a result, in the case that X-ray beam strikes a powder sample, which can be denoted as poly-crystallite, it will be diffracted in all potential directions in respect to the Bragg equation. [75] The benefit here is that each crystal lattice spacing can be reflected by giving rise to a cone of diffraction. The combined results creates a comprehensive analysis, thus, the powder XRD analysis is more frequently employed in solid state, especially heterogeneous catalyst studies.

The XRD analysis results are normally shown in of the form of a set of plots (pattern), which are converted from the original signals. The XRD pattern displays signal intensity as a function of the diffraction angle, 2θ. In the case of powder experiment, all reflections from different angles are present along the same axis, and normally, there will be overlapping of signals. [75] Exacting signal of individual reflection is very difficult, and in most cases, the pattern is refined as a whole rather

than separating the reflections individually, which is noted as the Ritveld method. [117]

One most important contribution of XRD pattern is that it reflects the degree of crystallinity of the catalyst, or, a doped component on/in it. On the other hand, it also estimates the size of the crystallites that may be present, and what is more, is that it also provides information about the atomic constituents of the unit cell since *d*-spacings and unit cell dimensions can be obtained. [74, 118] The identification of particular substance in XRD pattern is based on previously established and on-developing libraries of available characteristic *d*-spacings and intensities of solids. [74] Digital databases (online), such as the JCPDS (Joint Committee on Powder Diffraction Standards, from the International Centre for Diffraction Data, ICDD), [119] and ASTM (American Society for Testing and Materials, International), [120] have now included more than 80000 entries, [74] and relevant products (PDF card) can be loaded by professional software, (e.g., MDI Jade, from Materialsdata) to help in a rapid finger print matching, which has greatly saved the time for analysis. [121]

Experimental conditions

Only powder diffractions are employed in our catalyst characterizations. Before the analysis, samples are ground to fine powders with no bulky particle inside. The powders are then transported to and fulfill a customized sample holder, with the top surface of the powder pile being flat, smooth, and better as high as the holder cavity depth, so as there are no powders falling out. The XRD scanning program requires

settings of scanning range (2θ), step size and time per step (scanning rate can be calculated from these two parameters), and a spinning speed (r/min). Here the sample holder can be spun at a high rate for adoption of all possible diffractions.

2.3.2 Infrared Spectroscopy (IR)

Difference in the fundamentals between Infrared and Raman spectroscopies

Vibrational transitions in molecules cause absorption in the infrared region of the electromagnetic spectrum (Infrared spectroscopy), or, in the case of Raman spectroscopy they also scatter exciting radiation with accompanying shift in the wavelength. The obtained vibrational spectrum is characteristic of the functional groups in molecules, and the observed group frequencies are also affected by the molecular interactions, e.g., hydrogen bonding between molecules. Therefore, vibrational spectrum evidence not only evaluates the abundance of a specified functional group, but also provides information about its surrounding environment. [86, 122-125]

Infrared and Raman spectrometers include a radiation source, from where the electromagnetic beams (focused radiation) are sent to the samples, normally targeting at a single point of the sample, and a detector to measure the absorption (IR) or radiation (Raman). [86] Although both working in an ‘electromagnetic beam to sample’ model, the two approaches do vary according to the electrical features of the target molecule/structure.

Here the fundamental principle is that the electrical properties of target molecule will be changed as a result of the interactions between the molecule and incident radiation (Fig. 2.12).

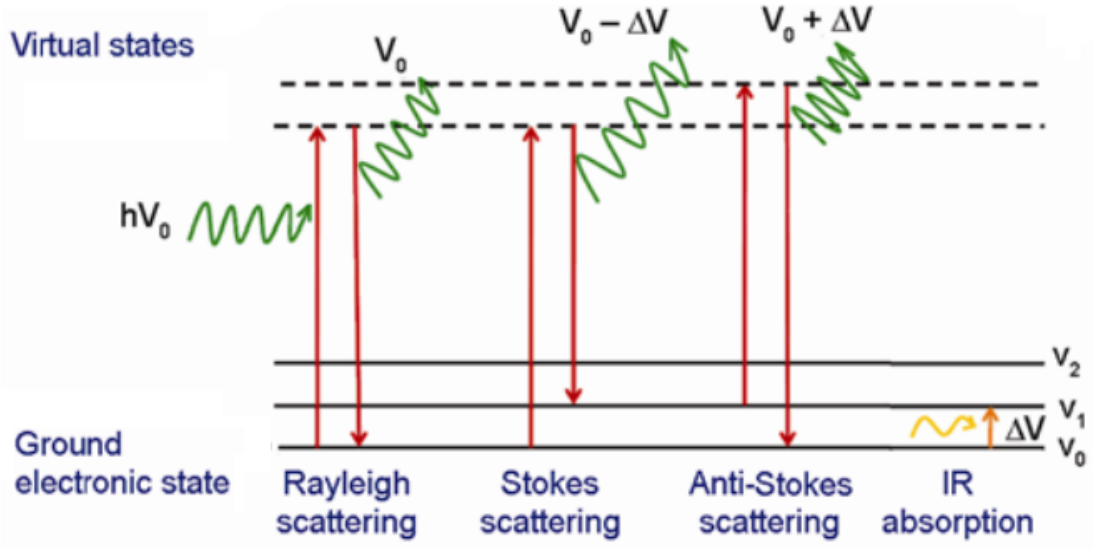

Fig. 2.12 Energy levels of transitions owing to IR absorption and Raman radiation adjusted and cited from reference [126]

Molecules contain bonds of specific spatial orientation and energy. These bonds are seldom completely rigid, and when energy is supplied from outside, they may bend, contract or stretch and these are so called ‘molecular vibrations’. For each type of vibrations, there are different energy levels characterized with vibrational quantum numbers *v*. Here when the energy required for transitions between two near vibrational status can be matched with the energy of incident radiation, absorption will occur, and the corresponding frequency of absorbed photons is within the Infrared region. [86, 123, 125-127] IR absorption only causes the transitions between different vibrational statuses within a particular electronic state of the molecule. On the other hand, there is indeed jumping from the ground electronic state to a virtual

state for a molecule, which can be induced by the incident photons on interaction with the molecule. Incident radiation can excite the molecule in ground electronic state of different vibrational status (e.g. V_0 or V_1). The excited virtual state only exists in a very short time and will release energy by scattering radiation so as to go back to the original state. The majority of the scattered radiation is of the same frequency as the incident radiation; this is known as Rayleigh or elastic scattering. However, the vibrational status of molecule may change when it comes back from the excited virtual state and as a result, the frequency of the scattered radiation is shifted to a lower or higher value in comparison with the frequency of the incident radiation, and this phenomenon is what we called 'Raman effect'. Raman scattering is an example of inelastic scattering that is affected by the different molecular vibrational statuses within the electronic state. As is demonstrated in the above Fig. 2.13, scattered radiation that takes up energy from the vibrations of the molecule gives rise to anti-Stokes signal, whereas radiation that gives energy to the vibrations of the molecule results in Stokes signal. [86, 122, 127, 128]

From the point of view in molecular symmetry, some molecules possess a dipole moment due to the charge separation. Other molecules may acquire a dipole as they are vibrating. (e.g. CH_4, the molecule has no dipole but will develop a temporary dipole as one of the C-H bonds stretches). The ability that a molecule can create a dipole in the presence of external *E* field (this *E* field is associated with the incident radiation) is described as polarizability. [86, 122] In order to have the absorption of radiation occurs in the IR region, the dipole moment of the molecule must change

during the vibration, and such vibrations are IR active. On the other hand, for Raman radiation to occur, the molecular vibration must have changed the molecular polarizability (Raman active). [86, 123, 125] In the case of real analysis, where the molecule structure may become more complex, IR and Raman complement each other, and choices are often made based on the symmetry of molecular vibrations.

For example, carbon dioxide, CO_2, has three atoms arranged in a linear set, O=C=O. The molecule does not have a dipole originally and two typical vibration models can be observed on the C-O bond in the presence of external E field: [86]

1) The antisymmetric stretch, which has one C-O bond stretching while other contracts. The carbon atom moves as well so that the centre of mass of the molecule remains stationary. Here a dipole moment and changes are induced, but the molecular polarizability does not change, hence the vibration is IR active.
2) The symmetric stretch, in which case both oxygen atoms are equidistant from the central carbon atom, but the C-O bonds lengthen and contract together. There is no diploe change but the polarizability changes hence the vibration is Raman active.

Experimental conditions of IR

The practical IR measurement carried out with an infrared spectrometer, such as the Perkin-Elmer Spectrum RX1 FT-IR spectrometer employed by the ICL department at Oxford. Before analyzed with the instrument, powder samples are added into potassium bromide (KBr) powders and the mixture is then mechanically grounded for

a better sample dispersion. Here the ratio of sample/KBr is approximately 3/997, equaling to concertation of ~0.003 wt%. The mixed powders will be compressed into a pellet form with special tools (the pressure employed in compressing is normally 10 tons and lasts for 20 seconds). A satisfied pellet sample for IR measurement should be at least semi-transparent, with no damages such like slits. Both KBr and prepared samples can absorb moistures in air, and normally the KBr can be pretreated in heated oven, while similar procedures can be applied for the prepared samples. And in other case that the measurement is undertaken with In-situ facilities, there is no need to treat sample through the above steps.

IR radiation energy transmitted through a zeolite sample is measured as a function of the wavenumber, in cm^{-1}, or wavelength, in μm. Modern type Fourier-transform IR spectrometer (a kind of non-dispersive instrument) provides immediately the whole IR spectrum of sample via a process of interference plus mathematical calculations. [127, 128] Firstly, a complex interferogram is generated by superimposition of the radiation energies of all the partial energy fluxes corresponding to the various wavelengths of the polychromatic IR light transmitted or partially absorbed. Then, the data was processed in computer with a mathematical method 'Fourier Transformation' and finally presented in the form of FT-IR spectrum which is a plot of the transmitted intensity as a function of the wavenumber (cm^{-1}). [76, 129] In most cases, the mid-IR region (4000-400 cm^{-1}) is employed, and used as the horizontal axis of the FTIR spectrum. [86]

2.3.3 Laser-Raman spectroscopy

Advantages of Raman spectrum as compared to IR

As has been discussed in the above, Raman and IR are complementary techniques due to the electrical symmetry of molecules. However, there are some cases that employing Raman provides better performances than IR in the catalyst investigations. Here we have discussed 4 cases in the below.

1) The Raman spectrum of water is much weaker than the IR spectrum, where the potential contamination due to the atmospheric moisture could be effectively avoided.
2) For analysis of organic compounds, such as hydrocarbons, vibrations of symmetrical structures, such as R-C≡C-R, which have weak intensity in the IR, exhibit strong bands in the Raman spectrum. This has been ascribed to the working theory of the technique and discussed in the above.[86]
3) Normally, the sample preparation for Raman does not need special pretreatment, as what is for IR, e.g. a mixing step with salts such as KBr is required in general FT-IR analysis.
4) One most important feature which is related to coke characterizations is that in contrast to what occurs with IR spectroscopy, symmetric modes of weakly polar bonds, such as C=C, can be well observed in terms of apparent bands in the Raman spectrum. [12] Therefore, Raman technique is more appropriate for a comprehensive analysis of coke compositions. The problems caused by strong

fluorescence interference can be avoided by using Fourier transform (FT) Raman, or, more effectively solved by changing the radiation source to Ultraviolet (UV). [12, 41]

Experimental conditions of Raman

Obtained Raman signals (scattered radiations) can be collected and converted into spectrum which has similar 'group-frequency' correlations as what is for IR. Here the difficulty is to selectively filter out the Rayleigh scattering radiation, which is of the same frequency (energy) as the incident radiation and possesses a much higher energy density than the inelastic Raman scatterings. Here a monochromator is employed to selectively remove the Rayleigh scattering radiations so that the useful Raman signals can be effectively collected (normally the intensity of Stokes is stronger than the anti-Stokes). [130]

Compared with IR, Raman sample is easier to prepare, which is in a tiny amount (normally at 10mg), supported in the form of a compressed thin layer on a transparent microscope slide.

The instrument employed for Raman measurements in this thesis is a PerkinElmer Raman Station^{TM} 400F spectrometer. Samples hold by the slide is fitted into the slot of the machine. Before analysis, the target point of laser on sample layer can be adjusted with the instrument camera and a stage controller and a clear view of sample particles should be present in the visual scope on the computer monitor so as the measuring point is accurately focused.

2.3.4 NH_3 temperature programed desorption (NH_3-TPD)

Fundamentals

In zeolite catalysis, the strength and quantity of zeolite acid sites are uniquely important, which often directly decide the catalyst performance, and hence the reaction output.

Temperature programmed desorption (TPD) of base molecules, e.g. ammonia, is a common method for quantitative analysis of zeolite acidity distribution. [131] It can measure the number of different acid sites based on their ability to capture the probe base molecules. [132-134]

Before the measurement on desorption, ammonia molecules are introduced to dehydrated zeolite at a proper temperature, where a saturation of NH_3 on the zeolite acidic sites can be achieved; and then a temperature programmed heating process is employed to have the ammonia molecules desorbed as a function of increasing the temperatures. The released ammonia can be detected and quantified with a thermal conductive detector (TCD), and the data is often presented in the form of a temperature-dependent concentration (signal intensity) curve.

Here the acid strength, amount and distribution can be obtained from the peak position, area, and shape of the desorption curve, respectively. Normally, the acid strength is reflected by the peak position on the curve, which is corresponding to the temperature that is required to desorb the ammonia. The basic idea is that stronger acid sites require higher temperatures to release the adsorbed ammonia molecules.

The peak area integrated directly shows the quantity of a certain type of acid sites in the zeolite characterized, where the shape of the entire curve has a measurement on the ratio between different acid sites.

Experimental conditions

Fig. 2.13 shows schematically the composition of a NH_3 – TPD instrument, and the steps of analysis.

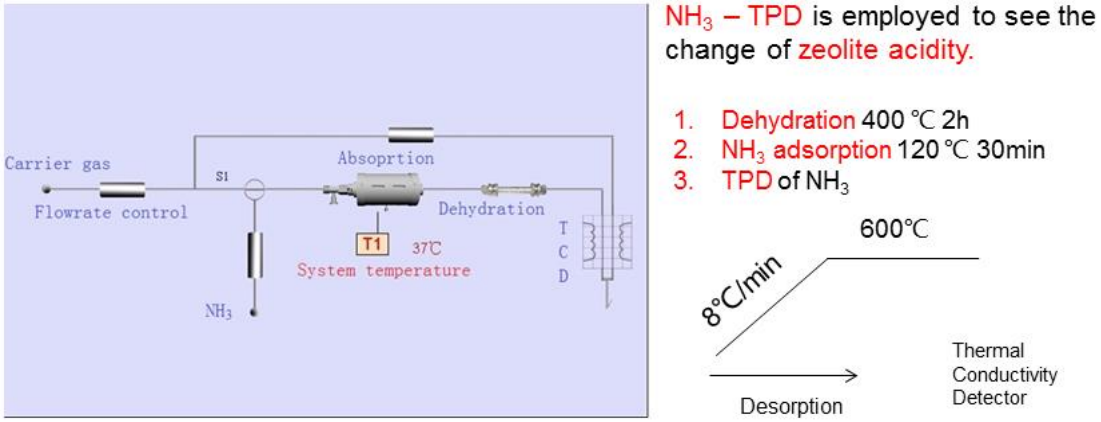

Fig. 2.13 Schematic of a NH_3 – TPD instrument, and the steps of a measurement

The NH_3-TPD analysis in this project was performed using a TP–5078 Auto TPD system (Xianquan Co. Ltd, China). In each analysis, firstly samples weighted (500mg) were carefully heated in N_2 at 300^{o}C for 2h to remove the adsorbed moisture. After the temperature dropped back to 120 ^{o}C, NH_3 adsorption (NH_3:N_2=1:3 in volume) proceeded for 30 min, and the system was subsequently cooled down to room temperature and stayed for 1h in pure N_2. The samples were then heated at a rate of 8 ^{o}C /min from room temperature to 600 ^{o}C, in which process the desorbed NH_3 was detected with a TCD.

2.3.5 Electron microscopy

General background

Electron microscopy (EM) is one of the most straightforward and powerful techniques for porous structure analysis, and has been used extensively, in many cases giving direct information about the zeolite textural properties, the surficial dispersion of catalyst promoter particles on zeolite, coke depositions, and the binding of zeolite body with binders. [31, 74, 135-138]

As has been pointed out by Professor Sir John Meurig Thomas, the EM based instruments are powerful tools in zeolite and catalyst studies, owing to many of their features that few other techniques can rival in determining the following: [74]

1) The elemental composition
2) Status of constituent atoms
3) Bond distances, in which case optimized conditions help in determination of nature of bonding and coordination of fingerprints
4) Both local and global symmetry and space groups
5) The morphology of substances
6) Nano-porosity and topological parameters of a material

Fundamentals

Scanning electron microscope (SEM) works by rastering a beam of electrons over the sample surface and determines the intensity of the backscattered electrons or

secondary electrons at different positions. As a result, surface properties such as morphology and chemical composition can be obtained. Transmission electron microscope (TEM) works with the electrons transmitted and diffracted. When the electron wave passes through the sample, the interaction between electrons and the sample leads to changes in the amplitude and phase of the electron wave. The overall change is decided by the sample thickness (density) and composition. As a result, direct image of the porous structure can be observed. For instance, regions with higher porosity appear as a brighter area in TEM image due to the lower mass density. [135]

Experimental conditions

In our project, SEM and TEM images are employed for understanding of the follows:

1) The particle size of different samples
2) The morphology of sample particles
3) The surface dispersion of metal oxide promoters on zeolite
4) Coke distributions on the zeolite surface
5) The boundary between zeolite crystallites and the binder phase

For SEM, sample preparation is relatively easy. A zeolite powder sample can be simply affixed to be observed up on an appropriately sized sample holder. Here, as the measurements take place in high vacuum conditions, only low vapor pressure adhesives (such as special carbon-based cements) are used to paste the very small powders. And wearing gloves are important to avoid the transfer of skin organics

which may eventually contaminate the microscope. For TEM, in most cases, our samples are dispersed in ethanol and baked out in vacuum after transferring onto the carbon coated copper grids.

Here the operation of SEM and TEM were carried out by professionals from other departments (e.g. the department of materials at the University of Oxford) as joint work of the projects, and the exact procedures in measurement and optimizations of images have beyond the knowledge of this thesis, thus are not discussed in details. The instrument information and a simple description on measurement for different samples are included in the later chapters and responsible to individual projects.

2.3.6 Thermal analysis on coked catalysts

Thermal methods have been widely used in catalyst study to determine both phase changes as a function of temperature and the unknown quantities introduced by the reaction. [75] In our project, we mainly employ Thermogravimetric Analysis (TGA) for the quantification of coke species formed on/in zeolites. TGA measures the change in weight of a sample, as it is heated (temperature-programmed) in air or a special gas, as a function of temperature. Here the sample weight change could be either caused by evaporation or sublimation, or, by chemical reactions corresponding to the employed temperatures (e.g. in coke analysis, carbonaceous species are burned in air flow). Providing the compositions of coke species are already-known with the help of other characterizations, their concentrations (wt%) in post-reaction sample can be directly read from the TGA results. [12, 75]

In some cases, TGA result is accompanied by the corresponding Derivative-Thermogravimetry (DTG) result, which plays a role as the TGA index, also presented in the form of a temperature-dependent curve. Here the DTG shows the time derivative (rate) of weight loss against temperature, which is characteristic of the composition of material measured in the experimental conditions. [139]

Experimental conditions

In series of our projects, a SDT Q600 (TA instruments) thermogravimetric analyser was used to measure the coke content over the used catalysts. Normally, the coke amount (in wt%) is determined by weight loss during temperature programmed calcination in air from 20 to 1120 ^{o}C (temp. ramp 10 ^{o}C /min). 50mg of spent sample was used each time. The exact steps for measurement may change in different chapters of this thesis.

2.3.7 Solid state nuclear magnetic resonance (NMR)

Solid state NMR plays a uniquely important role in catalyst study, and particularly, it has been widely employed as an essential part in the zeolite characterizations. [74, 76, 140-142]

Fundamentals

Generally, NMR spectroscopy is based on the net absorption of energy in radiofrequency region of the electromagnetic spectrum by the nuclei of those elements that have spin angular momentum and a magnetic moment. For the nuclei of

a particular element, characteristic absorption, or resonance frequencies, and other spectral features enable the identification of their different chemical environments, and hence the molecular structure (***basic principle***). A half-integral or integral spin quantum number is assigned to the nuclei that possess spin angular moment and generate a magnetic moment. This number determines the number of orientations in space that can be adopted by the spinning nuclei when subjected to an external magnetic field. (***nuclear spin***). It should be noted that electrons also possess spin angular momentum, and a corresponding magnetic moment which affects the magnitude of the external magnetic field experienced by nuclei (***electron spin***). Nuclei of a particular element that are in different chemical environments within the same molecule experience slightly different applied magnetic field strength due to the shielding and de-shielding effects of the nearby electrons. As a result, their resonance frequencies differ, and can be reflected by a series of characteristic chemical shifts (***chemical shift***). On the other hand, the spin states of one group of nuclei can affect the magnetic field experienced by neighboring groups through intervening bonds in the molecule in such a way that the absorption peaks of each group are split into a number of components. And this effect provides useful information for spectral interpretations (***spin-spin coupling***). [86, 140, 143, 144]

A NMR spectrometer has combined all the above theories to selectively interrogate one type of nuclei at one time, e.g. ^{27}Al, and convert the obtained absorption data into an NMR spectrum. By progressively sweeping the applied magnetic field at a fixed radiofrequency, or changing frequency at a fixed field, sample resonances can be

recorded in terms of a series of sharp absorption peaks as a function of the frequencies. Here the application of Fourier transform (FT) spectrometers enables all the obtained spectral information, originally in the form of a time-dependent interferogram, to be converted into a spectrum mathematically. The obtained spectrum shows all nuclei of a particular element that are in different chemical environments, and separate them by the characteristic chemical shifts, where peak area of a special nucleus is in proportion to its abundance in the substance. Generally, the NMR spectrometer is made up of a superconducting solenoid or electromagnet to supply an efficient, stable and uniform magnetic field, a transmitter to generate the appropriate radiofrequencies, and a detector to capture the signals (***working theory***). [86, 140, 143]

In contrast to liquid phase NMR, the bands of solid state NMR tend to be very broad, this is due to the incomplete averaging of the external magnetic field owing to the shielding created by other nuclei in the sample (***chemical shift anisotropy***). [75, 145, 146] In order to introduce the molecular tumbling which occurs in the liquid phase (e.g. solution) and which creates an averaged magnetic field, the solid sample can be spun at the so-called magic angle of $54^{o}44'$. The spinning inhibits the chemical shift anisotropy provided the spinning frequency is close to the frequency spread of the signal (***magic angle spinning, MAS-NMR***). However, it also takes longer time to obtain the MAS NMR spectra due to the slow spin relaxation. For spin-$^{1}/_{2}$ nuclei, e.g. silica, the relaxation time is normally 120-600s between pulses. [75, 140, 143]

In the case that a particular type of nuclei in sample possess a poor abundance, such as ^{13}C nuclei in catalyst cokes (the sample is not exchanged with ^{13}C before analysis),

the cross polarization technique (***CP-NMR***) can be employed. With a complex pulse sequence, the CP technique manages to transfer the polarization from a nucleus in high abundance (normally hydrogen, other cases employed phosphorus and aluminium) to another nucleus, hence enhances its signal response. [75, 143] However, CP-NMR is not always the best solution, such as in the case of deeper dehydrogenated coked catalyst, a poor abundance of hydrogen makes it difficult to obtain the ^{13}C NMR signal even with the CP technique. [12]

Experimental conditions

Our samples are sent to the professional NMR team in Durham University (EPSRC) for measurement. For coke analysis, ^{13}C nuclei are employed, while ^{29}Si, and ^{27}Al nuclei are employed in the catalyst structure study (zeolites, and binder-incorporated samples). The exact experimental conditions vary in the following chapters.

2.3.8 Brunauer, Emmett and Teller (BET) analysis

Fundamentals

Brunauer, Emmett and Teller (BET) analysis is based on the physical adsorption of gas molecules on material surface, and thus measures the specific surface area of a material, sometimes information about the porous volumes can also be obtained. [147]

As an extension of Langmuir theory, which is a theory for monolayer molecular adsorption, BET theory works on multilayer adsorption with the following

hypotheses:

1) Gas molecules can be physically adsorbed by a solid in layers infinitely

2) There is no interaction between each adsorption layers

3) The Langmuir theory here is suitable to each layer

Here is a complex derivation of formula, and the resulted BET equation is

$$\frac{1}{\left[V_a\left(\frac{P_0}{P}-1\right)\right]}=\frac{C-1}{V_mC}\times\frac{P}{P_0}+\frac{1}{V_mC}$$

Va **=** volume of gas adsorbed at standard temperature and pressure, in ***ml***;

Vm = volume of gas adsorbed at standard temperature and pressure, to support a monolayer absorption over the sample surface, in ***ml***;

P = partial vapour pressure of adsorbate in equilibrium with the surface at temperature of -196 ^{o}C (governed by liquid nitrogen), in ***Pa***;

P_0 = adsorbate gas saturation pressure, in ***Pa***;

C = BET constant related to adsorption enthalpy.

And finally the BET surface area can be given by [147-150]

$$S_{total}=\frac{V_mN_A\sigma}{22414}\times10^{-18}$$

$$S_{BET}=\frac{S_{total}}{m}$$

S_{total} = surface area of sample, measured in m^2;

S_{BET} = normalized surface area of sample, measured in m^2/g;

N_A = Avogadro constant ($6.022\times10^{23}mol^{-1}$);

σ = effective cross sectional area of a adsorbed molecule, in nm^2 (for nitrogen

adsorbate, the value is ***162 nm^2***);

m = sample mass, in ***g***;

22414: volume of 1 mole of the adsorbate gas at standard temperature and pressure with negligible difference from the ideal conditions, in ***ml***;

10^{-18}: exponentiation to convert ***nm^2*** to ***m^2***.

It should be noted that the in most cases, computer-assisted system will give a direct result mathematically.

Experimental conditions

Here the sample will be pretreated to remove the adsorbed gases and moisture before the analysis via a ‘degassing” process, normally by purging the sample material in a flowing stream of inert, dry and clean gas, or through cycles of desorption and adsorption. [148-150]

The exact BET measurements in our projects were undertaken with the help of professionals from Qingdao Lianxin Chemistry, Co. Ltd (China). Data presented in the Chapter 3 (MoO_3/H-ZSM-5 samples) were obtained with a Micromeritics Gemini VI BET surface area analyzer. Sample surface area was calculated from adsorption data at p/p_0 =0.05 and the total volume of sample was measured at p/p_0 =0.995. Surface area of sample in the Chapter 4 (Al_2O_3/nano-H-ZSM-5 samples) was measured with a JW-BK132f surface area analyzer (Beijing JWGB, China). Results were calculated from adsorption data at relative pressure p/p_0 = 0.003-0.05 as had been suggested for the very fine zeolite powders.

Chapter 3 Methanol-to-Hydrocarbons (MTH) reaction over MoO_3/H-ZSM-5 catalysts prepared via lower temperature calcination

3.1 Introduction

3.1.1 Dual MTH mechanism for olefin formation over H-ZSM-5

The generally accepted MTH mechanism has been based on a so called 'Hydrocarbon Pool' (HP) route in which those poly-methylbenzenes are proved to be the major reaction intermediates and particularly the co-catalytic centres, working with the zeolite Brønsted acid sites, and promoting the reaction by series of side chain alkylation and de-alkylation steps. [21, 22] However, the exact reaction mechanism appears rather different for H-ZSM-5 as compared to that for other zeolites (e.g. H-SAPO-34), as a methylation process of previously formed olefins, as well as the subsequent product intra-conversions (e.g. cracking of larger molecules) also perform as a parallel route to the above HP mechanism (There is a 'dual-pathway' mechanism for MTH reaction over H-ZSM-5). Interestingly, this route only contributes to the formation of C_3^+ olefins, whereas ethylene formation is mechanistically not involved (relevant background knowledge can be found in Chapter 1). [151] We note that this special MTH mechanism, exclusively working for the H-ZSM-5 zeolite, could be a

potential tool to adjust the MTH olefin product distribution, e.g. the ratio between propylene and ethylene, as well as some other related catalytic properties.

3.1.2 Tailoring the MTH olefin production with MoO_3/H-ZSM-5

This represents a rational way to precisely enhance the C-H bond activation of hydrocarbons which determines the efficiency of the above mentioned 'olefin methylation' and also promotes the aromatization steps that lead to a higher yield of aromatics in a variety of hydrocarbon transformations. In this case, we place our trust on the MoO_3/H-ZSM-5 catalyst which was previously extensively employed for methane aromatization. [13, 152-157] One reason that has been advanced is the greatly promoted C-H bond activation for CH_4 and other hydrocarbons involved in such reaction, governed by the molybdenum carbides (formed from MoO_3 by reduction with CH_4) working as catalytic promoter to H-ZSM-5. [158]

For such type of catalyst, the spatial location and distribution of any MoO_3 or other Mo-based species in H-ZSM-5 structure exclusively depend on the conditions employed in the catalyst preparation, especially the calcination temperature and the employed amount of MoO_3. [159] A relatively low calcination temperature (e.g. 300^{o}C) is sufficient for the decomposition of ammonium hepta-molybdate (the precursor of MoO_3, denoted as AHM) into MoO_3 molecular entities on the H-ZSM-5 zeolite surface. [152, 155, 156, 159, 160] Temperatures in the range of 350-400 ^{o}C, are known to initiate the processes of MoO_3 species sublimation and also the

beginnings of MoO_3 diffusion into the H-ZSM-5 channels. [161] It was noted that temperatures of 500 ^oC or higher are required for the MoO_3 species to be completely transported into the H-ZSM-5 channels via surface migration in gas phase. [159] And at these temperatures (500 ^oC or higher), $(Mo_2O_5)^{2+}$ dimer structures could be effectively formed within the zeolite channels, and subsequently reduced by CH_4 to form the catalytically active molybdenum carbides (MoC_x), which is pronounced to be the basis of the promoted C-H bond activation in a MoO_3/H-ZSM-5 catalyzed methane conversion. However, formation of such $(Mo_2O_5)^{2+}$ or molybdenum carbide species within the H-ZSM-5 channels also unavoidably reduces the intrinsic Brønsted acidity of the zeolite, which degrades the zeolite catalytic performance as acidic protons (H^+) are essential for most of the hydrocarbon catalytic conversions.[9]

It seems for an optimized catalytic behavior of the MoO_3/H-ZSM-5 catalyst, we should find the correct balance between the amount of the Mo catalytic sites inside the zeolite channels, and the reserved or retained zeolite Brønsted acidity. This is very difficult for high temperature methane conversions, as normally 700 ^oC is required and there is usually a complete Mo migration into the H-ZSM-5 channels (even the catalyst preparation temperature is much lower than 700 ^oC, the Mo distribution will be secondly adjusted by the reaction temperature) which inevitably leads to more severe loss on the intrinsic zeolite Brønsted acidity (most of the zeolite Brønsted acid are located inside the cavities/channels). [162] By contrast, effective methanol conversion over zeolite catalysts could be undertaken in a temperature range of 350-450 ^oC, which is much lower than the requirement for methane conversion, and

even the normally required calcination temperature for metal oxide loaded zeolite catalyst (500 ^{o}C or higher). [9, 13-15] This has greatly attracted our interests to employ a lower temperature, for both MoO_3/H-ZSM-5 catalyst preparation and the later methanol conversion (the same reaction temperature as for the catalyst preparation will have negligible influence on the preparation achieved zeolite Mo distribution during the reaction), which may help to tailor the distribution of Mo active sites in H-ZSM-5 system for our desired balance between the Mo catalytic properties and the retention of the intrinsic zeolite Brønsted acidity.

In this investigation, we prepared a group of MoO_3/H-ZSM-5 catalysts (the loading level of MoO_3 changes among different samples) via calcinations specifically at 400 ^{o}C, and the later catalyst tests in MTH reaction were also carried out at this same temperature (400 ^{o}C). The research takes advantage of the fact, from earlier studies, together with an examination of MoO_3 vapor pressure studies, that such a lower temperature for catalyst calcination and MTH reaction could lead to the MoO_3 being primarily located on the zeolite surface, where the migration of MoO_3 into zeolite channels is more controllable with its loading level; thus, the Mo species distribution in zeolite structure could be more effectively tailored, with sufficient Mo catalytic sites formed inside the H-ZSM-5 channels to promote a more efficient C-H activation, whilst also maintaining the required zeolite channel inner Brønsted acidity at a proper level for effective methanol conversions. [43, 159, 162]

3.2 Experimental conditions

3.2.1 Preparation of Catalyst

Three MoO_3/H-ZSM-5 (Si/Al=25) samples of different MoO_3 loading levels (5wt%, 7.5wt%, and 10wt%) were prepared via incipient wetness impregnation using aqueous solution of ammonium hepta-molybdate (Sigma, USP specifications), followed by dehydration at 100 ^oC for 24h in a drying cabinet and subsequent calcination at 400 ^oC for 5h in a conventional oven (in air). For comparison, a 7.5wt% MoO_3 H-ZSM-5 sample was also prepared via 500 ^oC calcination. The H-ZSM-5 is supplied by WENFENG Co. Ltd (China).

3.2.2 Characterization methods

The resulted distribution of Mo species and zeolite structure changes were analyzed with X-Ray Powder diffraction (XRD), Fourier-Transform Infrared (FT-IR) spectroscopy and Laser Raman spectroscopy. Ammonium temperature-programmed desorption (NH_3-TPD) was employed to evaluate the amount of zeolite acid sites. With the help of Brunauer-Emmett-Teller (BET) analysis and Scanning Electron Microscope (SEM), the surface properties and morphology of the prepared catalysts were also examined. Transmission Electron Microscope (TEM) measurements were applied to assess the zeolite surface Mo species and coke depositions. Coke amount was also calculated with the results from Thermogravimetric analysis (TGA).

XRD data was obtained with a PANalytical X'Pert PRO diffractometer using Cu

Kα1 radiation, the scanned diffraction angle ranged from 5° to 35° (2θ) with a scan rate of 0.8° / min.

FT-IR data were collected using a Perkin-Elmer Spectrum RX1 FT-IR spectrometer. Before analysis, samples were mixed with KBr powder (3 : 997 in weight), and pressed into tablets (10 tons for 20s), then dehydrated at 300 °C for 12h to remove the adsorbed moisture. The dehydrated sample tablets were kept in a vacuum condition to avoid moisture contamination, and directly measured when picked out, so as to aviod the potential influence by the zeolite adsorbed water molecules.

Laser Raman spectra were recorded by Perkin-Elmer Raman Station 400F Raman spectrometer. The powder sample was measured on a piece of optical glass.

NH_3-TPD analysis performed with TP–5078 Auto TPD system (Xianquan Co. Ltd, China). The loaded samples (500mg) were carefully pre-treated in N_2 atmosphere at 300 °C for 2h to remove the adsorbed moisture. The NH_3 adsorption (NH_3:N_2=1:3) performed at 120 °C for 30 min, and the system was then cooled down to room temperature for 1h stabilization in pure N_2. The samples were then heated at 8 °C /min from room temperature to 600 °C, the desorbed NH_3 was measured with a Thermal Conductivity Detector (TCD).

BET analysis proceeded with a Micromeritics Gemini VI BET surface area analyzer. The sample total surface area was calculated from the adsorption data at p/p_0 = 0.05 and the sample porous volume was measured at p/p_0 = 0.995.

The SEM images were captured by JEOL scanning microscope 840F (JSM840F). Sample powders were deposited onto the dust free scanning platform and trapped on

the surface with carbon-based cements. Resolution was carefully adjusted to make sure the sharp and clear edges of zeolite crystalline grains could be observed with as many as optical details of the zeolite surface. TEM measurements were undertaken with JEM-2100UHR microscope (200kV).

A SDT Q600 (TA instruments) thermogravimetric (TGA) analyzer was employed to determine the sample coke contents. The coke amount was determined by the weight loss during temperature-programmed combustion in air from 20 ^{o}C to 1120 ^{o}C (temperature ramping rate 10 ^{o}C / min). 50mg of coked sample was used in analysis.

3.2.3 Reaction design, catalyst test and calculations

Catalyst tests carried out in a computer-controlled fixed-bed reactor system (Beijing KLYT Co. Ltd, China) as shown schematically in Fig. 2.3 (chapter 2). Methanol was injected using a HPLC pump and vaporized at 150 ^{o}C before entering the reactor. Dry nitrogen (20ml/min) was used as carrier gas and internal standard for gas product quantification. The reaction took place at 400 ^{o}C under the pressure of 1 atm; typically, 1.0g of catalyst was tested each time when a methanol Weight-Hourly-Space-Velocity (WHSV) of 2h^{-1} was employed.

The gas products were directly transferred to a GC system (Shimadzu GC-2014SE) and analyzed with thermal conductivity detector (TCD) for non-hydrocarbons and flame ionized detector (FID) for hydrocarbons every 30 minutes, after methanol injection started. The gas product separation in GC system employed a RESTEK MXT-1HT column.

The liquid products were collected at 1h after the reaction, separated into water phase (water was generated in the reaction) and oil phase (hydrocarbon products) via still standing, both of which were then analyzed with an offline GC-MS system (Shimadzu GCMS-QP2010 Ultra High-end). Separation of different liquid components proceeded in a SHIM-5MS column.

Methanol conversion was calculated by comparing total methanol converted with total methanol injected (the amounts of unreacted methanol in oil phase and water phase were added together). After careful considerations and discussions with the GC technicians, we decided to present product yield rather than a selectivity value in the results. Here the observed yield of a product is in direct proportion to its product selectivity (in general, selectivity multiply by conversion giving us the product yield). Gas product yield in time-on-stream (TOS) was calculated by comparing the instantaneous methanol consumption (mol/min) of a particular gas product with the methanol injection rate (mol/min). The corresponding benzene, toluene, and xylenes (BTX) yields (obtained by the overall 5h reaction time) were calculated from the methanol consumptions of selected products (mol.) and total methanol injected (mol.). The definitions shown below are based on previous researches and have been modified to our current research. [3, 9, 99, 163-166]

$$\text{Methanol conversion (mol\%)} = \frac{[\text{methanol injected}] - [\text{methanol unreacted}]}{\text{methanol injected}}$$

$$\text{Gas product yield in TOS (mol\%)} = \frac{[\text{production of a gas product in TOS}] \times [\text{number of carbon in the gas product molecule}]}{\text{methanol injection in TOS}}$$

$$\text{Liquid product yield (mol\%)} = \frac{[\text{amount of a liquid product}] \times [\text{number of carbon in the liquid product molecule}]}{\text{methanol injected}}$$

3.3 Results and discussion

3.3.1 X-Ray Diffraction (XRD) analysis of the as-prepared catalysts

XRD patterns (Fig. 3.1 & 3.2) of the MoO_3 loaded samples, as well as the parent H-ZSM-5 are presented, and peaks located between 5^o - 25^o (2θ) correspond to the characteristic ZSM-5 crystal structures. As seen in Fig. 3.1, there is no apparent difference between the MoO_3/H-ZSM-5 samples and the parent H-ZSM-5, highlighting the important fact that only minimal (if any) change of the supporting zeolite framework was introduced by the MoO_3 modification. Particularly, we note that the two peak groups located at $2\theta = 7.5^o$ - 10^o, related to the zeolite channel structures, are also well maintained on all modified samples [167].

In earlier work, it has been reported that both high temperatures (e.g. 500 ^{o}C or higher) applied in catalyst calcination and a high Mo loading concentration (5wt% or higher for MoO_3), would lead to significant migration of the molybdenum oxide species into the H-ZSM-5 channels, which often results in the potential dealumination of zeolite framework and severe loss of the zeolite Brønsted acid sites that are mainly located inside the zeolite channels. In these cases, formation of crystalline $Al_2(MoO_4)_3$, is a typical sign of that process and this could be observed in the XRD results. [159, 168]

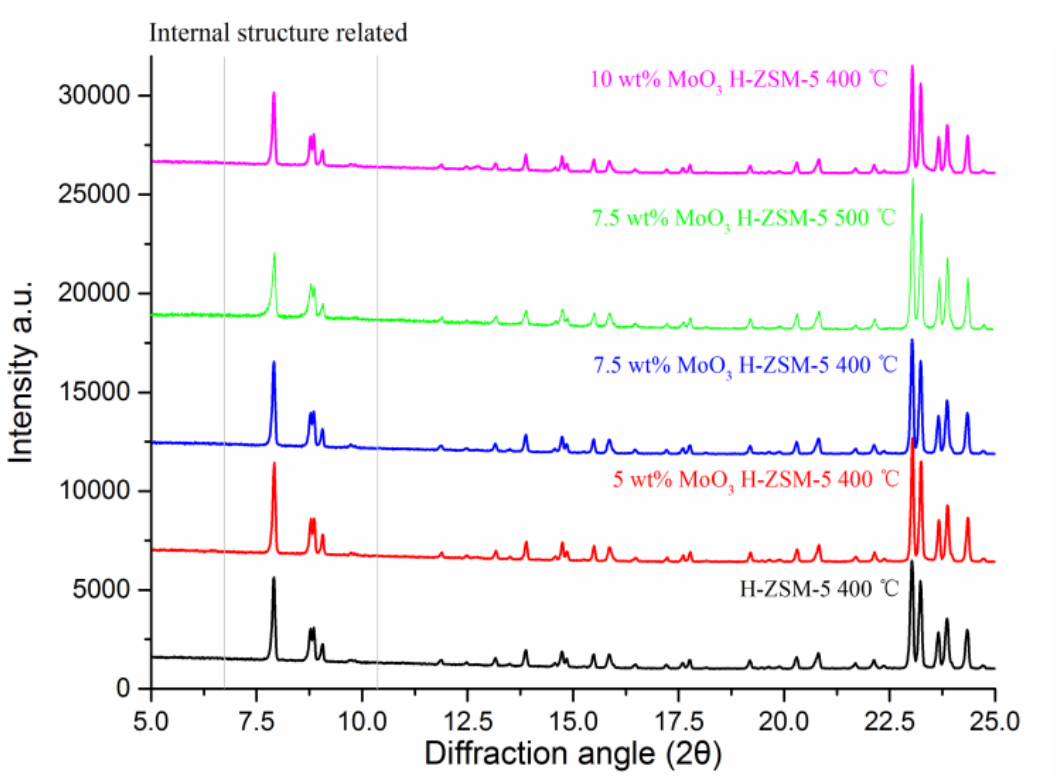

Fig. 3.1 XRD patterns (2θ = 5 – 25°) of MoO_3/H-ZSM-5 samples and parent H-ZSM-5 all prepared through 400 °C calcination (another 7.5wt% MoO_3/H-ZSM-5 sample calcined at 500 °C for comparison)

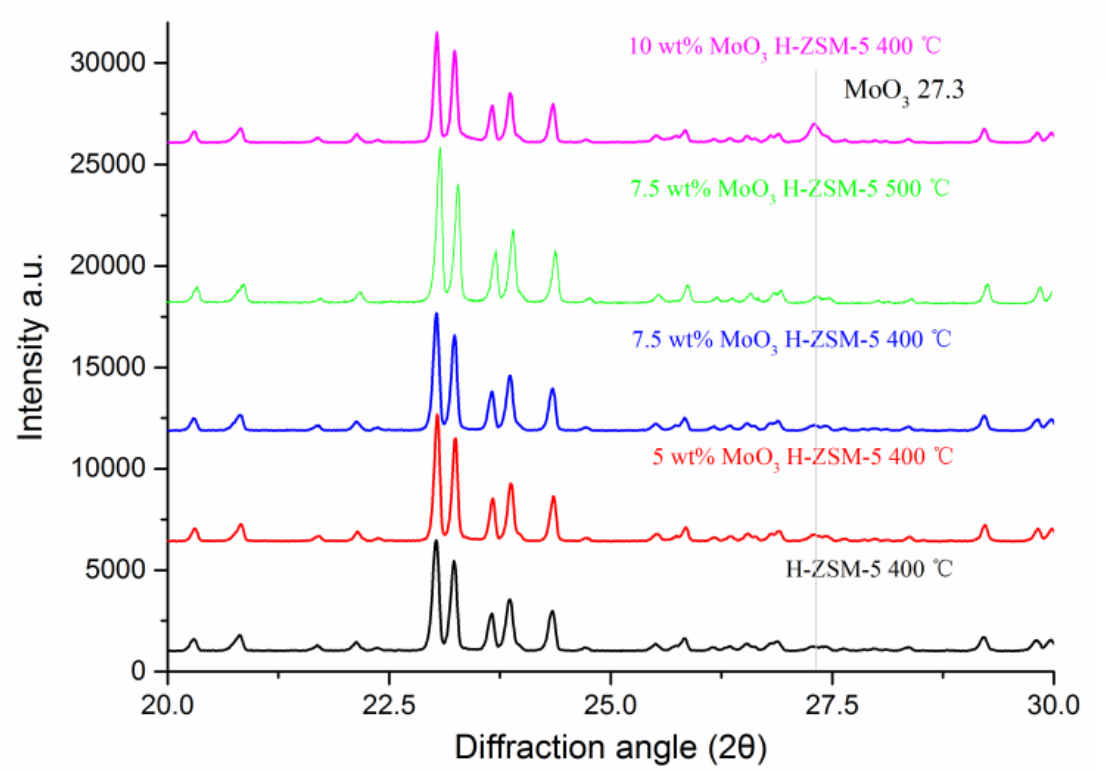

Fig. 3.2 XRD patterns (2θ = 20 – 30°) of MoO_3/H-ZSM-5 samples and parent H-ZSM-5 all prepared through 400 °C calcination (another 7.5wt% MoO_3/H-ZSM-5 sample calcined at 500 °C for comparison)

In the above XRD patterns, the 500 ^{o}C prepared 7.5wt% MoO_3/H-ZSM-5 sample has shown no detectable difference when compared with the 400 ^{o}C prepared 7.5wt% MoO_3/H-ZSM-5. Importantly, in all sample patterns, characteristic XRD diffractions arising from the crystalline $Al_2(MoO_4)_3$ are not detected. All these point out to the fact that the reported significant migration of Mo species into H-ZSM-5 channels and subsequent reaction did not occur on our samples, at least in the employed preparation conditions, and the selected H-ZSM-5 support possesses certain structural strength, which cannot be easily disrupted by the extra Mo species. However, in an expanded scan (Fig. 3.2), a small peak at $2\theta = 27.3^{o}$, assigned to the crystalline MoO_3, is observable on the 10wt% MoO_3/H-ZSM-5 sample, which has confirmed the successful decomposition of AHM precursor into our desired MoO_3 at the employed 400 ^{o}C temperature. For samples of lower MoO_3 loading levels, no peak attributed to the crystalline MoO_3 could be detected, and this implies an effective, but thin, zeolite surface dispersion of MoO_3, possibly in terms of a monolayer, which has been suggested by the previous studies (here the amount of MoO_3 molecules on zeolite surface determines in which form they are deposited). [159] Notably, a color change from white to a light lime green is also observed when the loading of MoO_3 increased, as visual evidences for the obtained zeolite surface dispersion of MoO_3 species.

3.3.2 Raman spectra

It has been reported that both MoO_3 and various other MoO_x phases (the Mo/O stoichiometry varies) could coexist on the Al_2O_3 support (another porous catalyst

support, possessing some similarity to zeolite), but for zeolite this has not been confirmed yet. [169] The Raman spectra of our prepared samples are shown in Fig. 3.3.

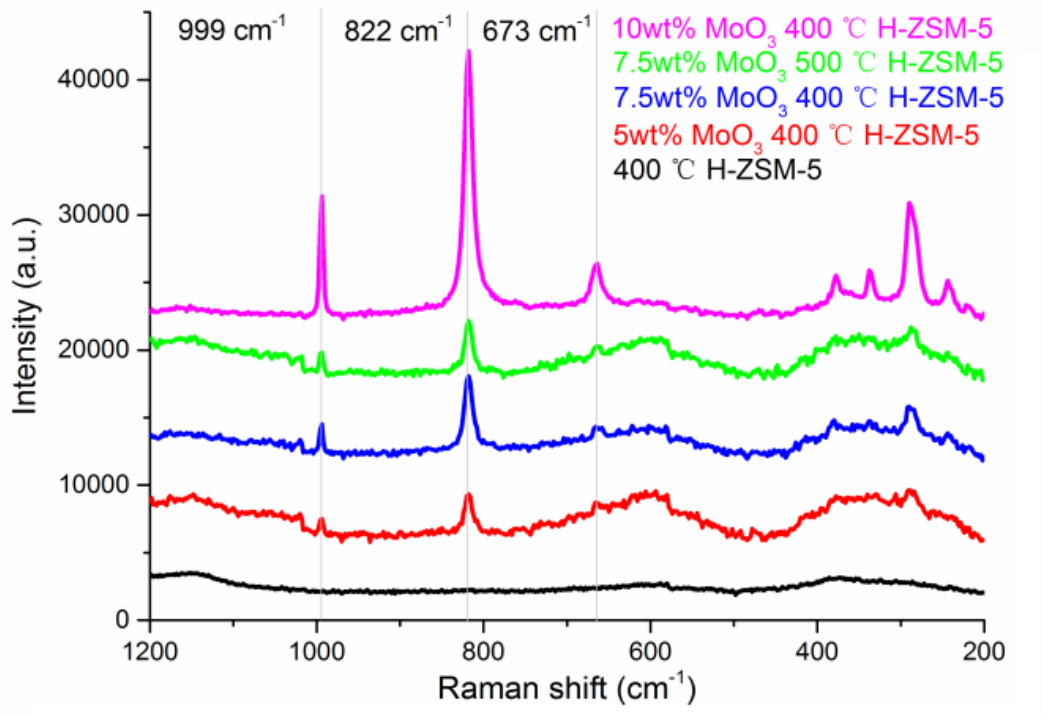

Fig. 3.3 Laser Raman spectra of the as prepared MoO_3/ZSM-5 samples and H-ZSM-5 and prepared at 400 ºC/500 º

The band at 955 cm^{-1}, arising from more complex MoO_x species is not observed. In contrast, three Raman resonance bands at 673 cm^{-1}, 822 cm^{-1}, and 999 cm^{-1} are identified for the MoO_3 structure. [169] These results confirm that there is a dominating deposition of MoO_3 achieved by our samples. According to the XRD results, it is also suggested that these Raman observable MoO_3 structures could be small clusters or oligomers of MoO_3 (these small pieces of MoO_3 spread over the zeolite surface, leading to a 'monolayer' dispersion) at lower loading levels (7.5 wt% or lower), whereas the XRD detectable "bulk" crystal phase MoO_3 would only

emerge at significantly higher loading levels (10 wt% or above). Notably, the MoO_3 Raman bands are relatively weaker for the 500 ^oC calcined 7.5 wt% MoO_3 H-ZSM-5 in comparison to the 400 ^oC calcined 7.5 wt% MoO_3 H-ZSM-5, a possible explanation would be more MoO_3 species have migrated into the zeolite channel when the calcination temperature raises.

3.3.3 Fourier Transform – Infrared (FT-IR) spectra

The FT-IR spectra of different samples are given in Fig. 3.4, targeting on the changes of zeolite hydroxyl (OH) groups.

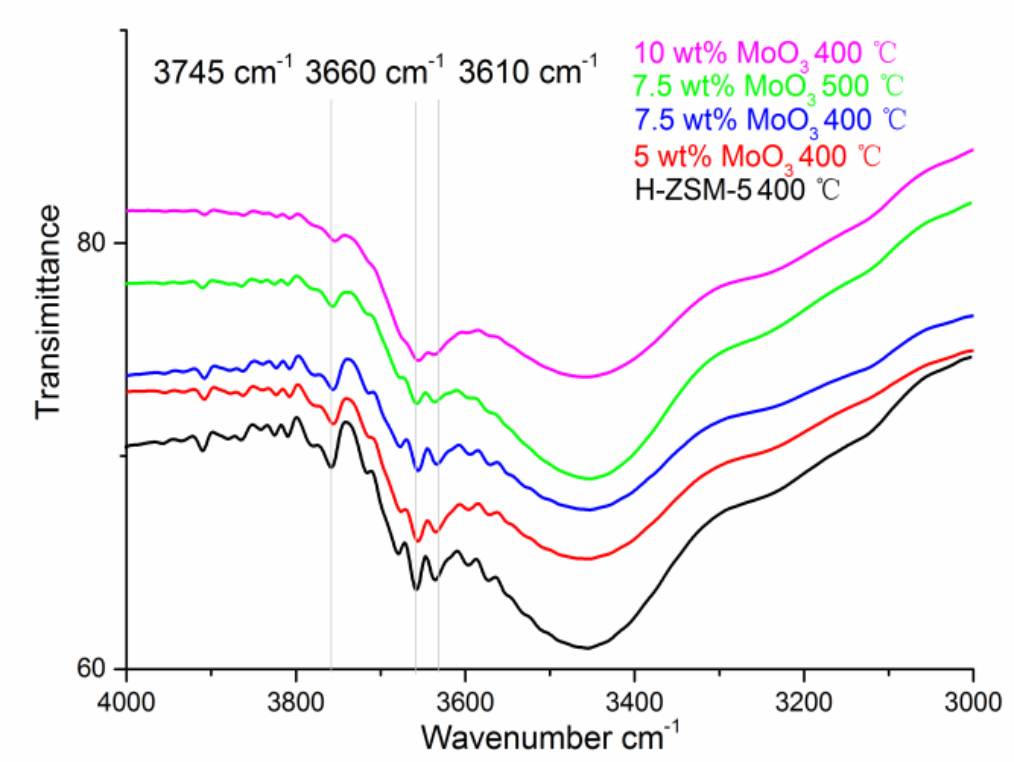

Fig. 3.4 FT-IR spectra targeting on the hydroxyl groups in different samples

The peak at 3745cm^{-1} is assigned to the O-H vibration of the silanol groups (Si-OH) mostly located on the zeolite surface; they are typically terminal structures of the zeolite crystal (the zeolite crystal growth ends at these structures).[9] These silanol

groups, although as part of the zeolite structure, only possess very weak acidity (Brønsted acidity to provide a proton in the reaction) in stark contrast to the zeolite Al-OH moiety. [170] The peak at 3660 cm^{-1} represents the zeolite extra-framework Al-OH groups with relatively weaker Brønsted acidity; the peak at 3620 cm^{-1} is assigned to the strong Brønsted acid sites those are in a Si-OH-Al structure, which is an integral part of the zeolite framework. [9] Notably, these framework Brønsted acid sites are mostly located inside the zeolite channel. [43] The migration of MoO_3 species into zeolite channels was reported to lead to a dramatic decrease of their numbers. [152, 159]

All samples are compared with the parent H-ZSM-5 which has also been calcined at 400 ^oC. Here the amount decrease of a particular OH group is reflected by a smaller absorption peak at corresponding positions in the IR spectra. On the 5wt% MoO_3/HZSM-5 sample (400 ^oC calcined), all zeolite hydroxyl groups are well preserved. Apparent loss of framework Brønsted acid sites, and extra-framework Al-OH groups, was firstly noticed on the 7.5wt% MoO_3/HZSM-5 sample (400 ^oC calcined), whereas only negligible change of Si-OH groups was observed. On the 10wt% MoO_3/HZSM-5 sample (400 ^oC calcined), apparent missing of *all* the hydroxyl groups was clearly reflected. The 7.5 wt% MoO_3/H-ZSM-5 sample (500 ^oC calcined) lost more hydroxyl groups than the 400 ^oC calcined sample, pointing out more intense interferences on zeolite structures were caused by the loaded MoO_3 species, when a higher calcination temperature was employed.

The observed FT-IR results clearly shown that the MoO_3 loading level, without

doubt, directly affects the distribution of Mo species in the zeolite structure. The loss of more Brønsted acid sites inside zeolite channels, more obviously shown on those samples with MoO_3 loading level of 7.5wt% or higher, strongly reveals an effective migration of MoO_3 into the zeolite channels, which is driven by the MoO_3 concentration to somewhat extent. The difference between 7.5wt% MoO_3 samples prepared via different temperatures, on the other hand, highlights the co-promoting effect of calcination temperature on the MoO_3 migration into zeolite channels. Notably, the Si-OH (silanol) groups were not apparently disturbed until the MoO_3 crystal emerged (on the 10wt% MoO_3/H-ZSM-5 sample), possibly due to a preference of MoO_3 species to firstly bind with the Al-OH groups, especially with the strong Brønsted acid sites. The formation of MoO_3 structure is also confirmed by FT-IR, as shown in Fig. 3.5. The bands at 1250 cm^{-1} and 1080 cm^{-1} are characteristic of the MoO_3 molecule vibrational models.[160]

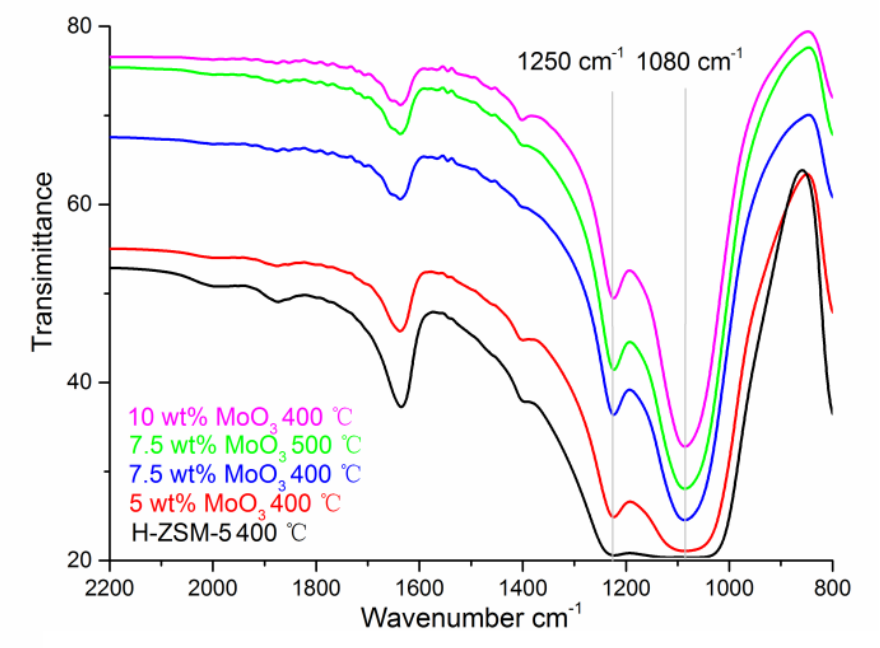

Fig. 3.5 FT-IR spectra of different samples highlighting the MoO_3 vibrations

3.3.4 NH_3 – Temperature Programmed Desorption (NH_3 – TPD)

NH_3–TPD studies are routinely used to study the acid site distribution in zeolite catalysts. [9, 159] Here the NH_3 desorption profile of original H-ZSM-5 (400 ^oC calcined) is used for standard reference, which shows 2 distinctive desorption peaks (Fig. 3.6). The desorption peak at 220 ^oC is assigned to those zeolite weak acid sites (Si-OH, extra framework Al-OH), while the peak at 450 ^oC is attributed to the strong acidic Brønsted acid sites (mainly located inside zeolite channels). [159, 171]

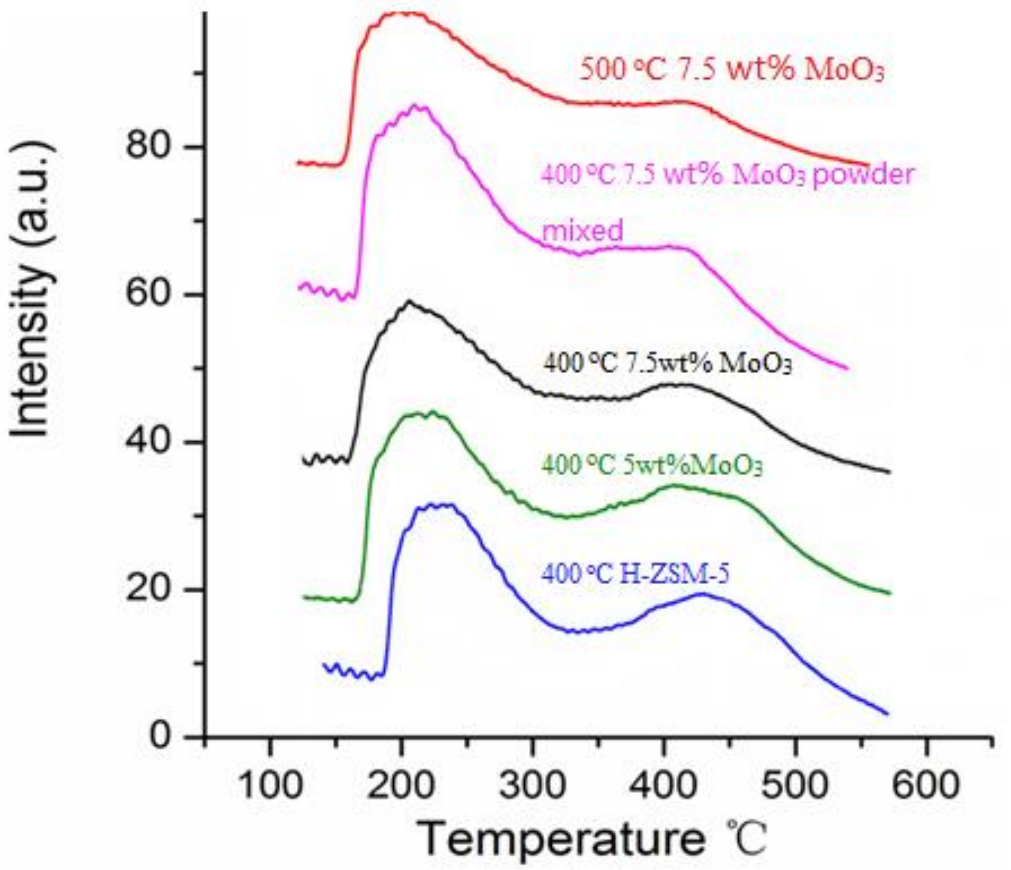

Fig. 3.6 NH_3–TPD profiles of different samples *Notice in particular the diminution of desorption peak at ca 450^oC for the higher temperature prepared (500^oC) 7.5wt % MoO_3/H-ZSM-5, and a non-impregnation, mechanical-mixing prepared 7.5wt % MoO_3/H-ZSM-5 (400^oC).

The observed changes on zeolite acidity distribution also reflect the differential MoO_3 distributions aroused by MoO_3 loading level, catalyst calcination temperature, and, particularly, the method that MoO_3 added into zeolite structure. For confirmation of these, two 7.5wt% MoO_3/H-ZSM-5 samples were prepared via incipient wetness impregnation with AHM and subsequently calcined at 400 ^oC and 500 ^oC, respectively. Another sample was prepared by mechanical mixing 7.5wt% of MoO_3 with 92.5wt% of H-ZSM-5 (room temperature overnight stirring in water, then dried at 100^oC) and subsequent calcination at 400 ^oC. The MoO_3 used in this mechanical mixture was prepared by decomposition of pure AHM at 400 ^oC to simulate the possible phenomenon that might happen in the calcination of impregnation prepared MoO_3/H-ZSM-5 samples. The selected 7.5 wt% MoO_3 doping level is based on an observed optimized catalytic process which is discussed in the following sections. In order to compare the influence by different MoO_3 loading levels, a 5wt% MoO_3/H-ZSM-5 sample, prepared via AHM impregnation and calcination at 400 ^oC, was also tested.

Comparing with the original H-ZSM-5 (400 ^oC calcined), the 7.5wt% MoO_3/H-ZSM-5 sample (made via impregnation, and 400 ^oC calcined) exhibits partial loss of the Brønsted acid sites as reflected by the subsided 450 ^oC desorption peak, whereas this change is not clearly observed on the 5wt% MoO_3/H-ZSM-5 sample (impregnation prepared, 400 ^oC calcined). This further confirms that MoO_3 loading is the major reason for the reduced zeolite Brønsted acidity. More Brønsted acid sites are lost on the mechanically prepared 7.5wt% MoO_3/H-ZSM-5 sample. Notably, for this

sample, as the transformation between AHM precursor and MoO_3 is pre-accomplished, more energy can be saved, and simply utilized by the MoO_3 migration, thus, leading to further loss of the zeolite Brønsted acidity. The most obvious loss of zeolite Brønsted acid sites is observed on the impregnation prepared 7.5wt% MoO_3/H-ZSM-5 sample which has been particularly calcined at 500 ^oC. For this, the NH_3 desorption peak at the 450 ^oC temperature becomes most apparently 'flattened'. Again, this once more reflects the fact that a higher calcination temperature greatly promotes the MoO_3 channel distribution, which is also in agreement with the previous studies [9, 34, 159]

We also note that those weak acid sites were not noticeably disrupted by the MoO_3 species since the desorption peak at 220 ^oC was well maintained for each sample. It seems that the interactions between the loaded MoO_3 species and these weak acidic hydroxyls are comparatively weak. This is also supported by the well preserved Si-OH signal in our FT-IR results.

3.3.5 Scanning Electron Microscopy (SEM)

Parent H-ZSM-5 (400 ^{o}C calcined) and the 7.5wt% MoO_3/H-ZSM-5 sample (400 ^{o}C calcined) are compared in SEM microscope (Fig. 3.7 a-d) before and after MTH reaction. Here the 400 ^{o}C prepared 7.5wt% MoO_3/H-ZSM-5 was taken as a representative example for its best catalytic performance among all the tested samples. Fig. 3.7b shows that there is no SEM observable, bulky crystal MoO_3 particle on the surface of H-ZSM-5 even at the 7.5wt% loading level. As suggested by Tessonnier et al., MoO_3 crystal once formed on the zeolite surface, often appears in a clearly defined platelet-like shape of several micro meters in length and can be easily identified by SEM. [151] The very smooth zeolite crystal surfaces, as shown in the SEM image, have revealed a uniform dispersion of Mo species over the zeolite surface. On the other hand, comparison between Fig. 3.7a and Fig. 3.7b shows that the crystal size of H-ZSM-5 did not change significantly after loading the Mo species. However, it is clearly seen that there are more cubic zeolite crystals in the SEM image of MoO_3/H-ZSM-5 while more hexagonal crystals are present in the SEM image of parent H-ZSM-5. The Mo species is considered to slightly modify the morphology and surface texture of the zeolite crystals, probably during the calcination process.

After 5h MTH reaction (400 ^{o}C, under the pressure of 1 atm, with methanol WHSV = $2h^{-1}$) both samples' crystal structures were well maintained (Fig. 3.7c and 3.7d), and there is still no observable MoO_3 crystal phase in the SEM picture of the post-reaction 7.5wt% MoO_3/H-ZSM-5 (Fig. 3.7d).

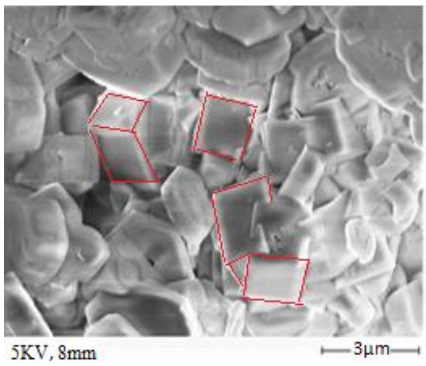

Fig. 3.7a SEM image of the parent H-ZSM-5

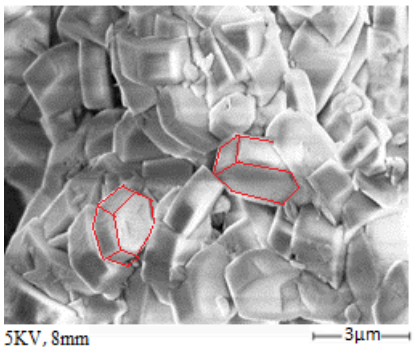

Fig. 3.7b SEM image of the H-ZSM-5 with 7.5wt% MoO_3

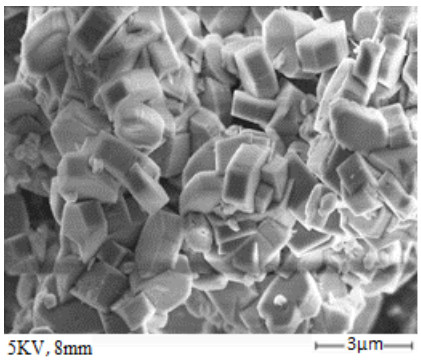

Fig. 3.7c SEM image of the parent H-ZSM-5 (after 5h MTH reaction)

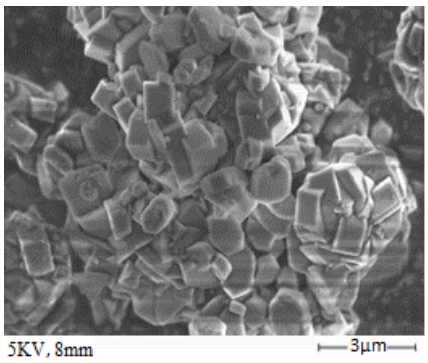

Fig. 3.7d SEM image of the H-ZSM-5 with 7.5wt% MoO_3 (after 5h MTH reaction)

3.3.6 Transmission electron microscopy (TEM)

Amplified surficial textures of MoO_3/H-ZSM-5 samples and relevant coke depositions on zeolite crystal surfaces are shown in the TEM pictures (Fig. 3.8 a-h). It should be noted that catalyst samples shown in the TEM pictures all experienced the 5h MTH reaction, with experimental conditions of: 400 ^oC, under the pressure of 1 atm, and methanol WHSV = $2h^{-1}$. Here the MoO_3 clusters (previously undetected by SEM) are clearly seen on the zeolite surface, uniformly dispersed over the zeolite surface, with no significant enlargement and possessing a somewhat uniform particle size. This is in accordance with the previously presumed 'monolayer' MoO_3 distribution on the zeolite surface, as the amplified TEM vision happens to show that all MoO_3 clusters are actually positioned on the same layer. [158, 161, 172-174] The estimated size for those MoO_3 clusters are roughly 50-200 nm in diameter. Their distribution is significantly more noticeable on 10wt%/MoO_3/H-ZSM-5 (Fig. 3.8c), with more compacted allocations on zeolite surface (Noticeably, this sample also possesses a clear MoO_3 peak in the XRD results, as shown in Fig. 3.2). Some zeolite particles appear to be connected by the MoO_3 clusters, as seen in Fig. 3.8e, pointing to the possible sintering effects (by such effect the MoO_3 clusters are re-fused and gathered to form larger crystal).

The large areas in diffusing black or grey color are due to carbon depositions on zeolite surface (coke species), which block the zeolite channels and finally lead to the deactivation of zeolite. Interestingly, these coking zones are always located close to,

or at, the MoO_3 clusters (Fig. 3.8f &3.8g). In contrast, the coking zones on the parent H-ZSM-5 are more homogeneously dispersed (Fig. 3.8d & 3.8h). A possible explanation could be the MoO_3 clusters have given rise to the formation of (or adsorb) the coke species during the MTH reaction. On the other hand, the covering MoO_3 clusters on zeolite surface may also block the zeolite channels, and thus further contribute to an early deactivation of the catalyst. It is reasonable that those surface MoO_3 sites are where the Mo species migrate into the zeolite channels. Due to the technical limitation, the inner channel Mo species are not observable. However, migration of Mo species into zeolite channel has been proposed by the reduced number of zeolite Brønsted acid sites, as shown in our NH_3-TPD and FT-IR results. The catalytic function of Mo species inside the zeolite channel, at or near the Brønsted acid sites, in promoting hydrocarbon molecular expansion, cracking, aromatics formation and coke formation have been reported previously. [175-179]

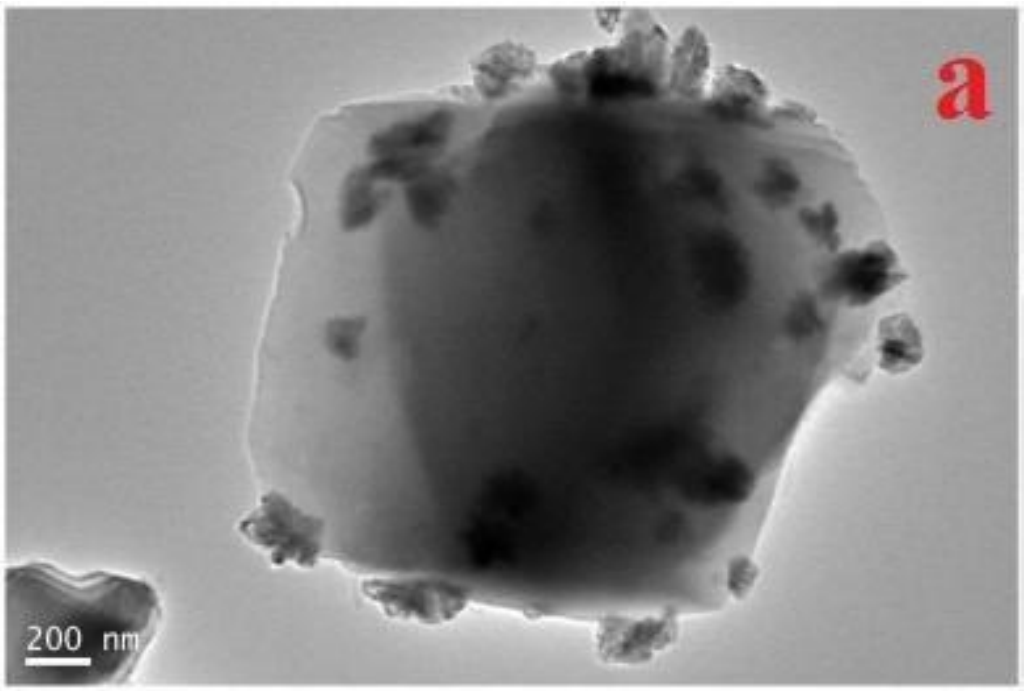

Fig. 3.8a TEM image of a post-run (5h MTH reaction, 400 ^{o}C, 1atm, WHSV= 2h^{-1}) MoO_3/H-ZSM-5 sample with a MoO_3 loading of 5wt%

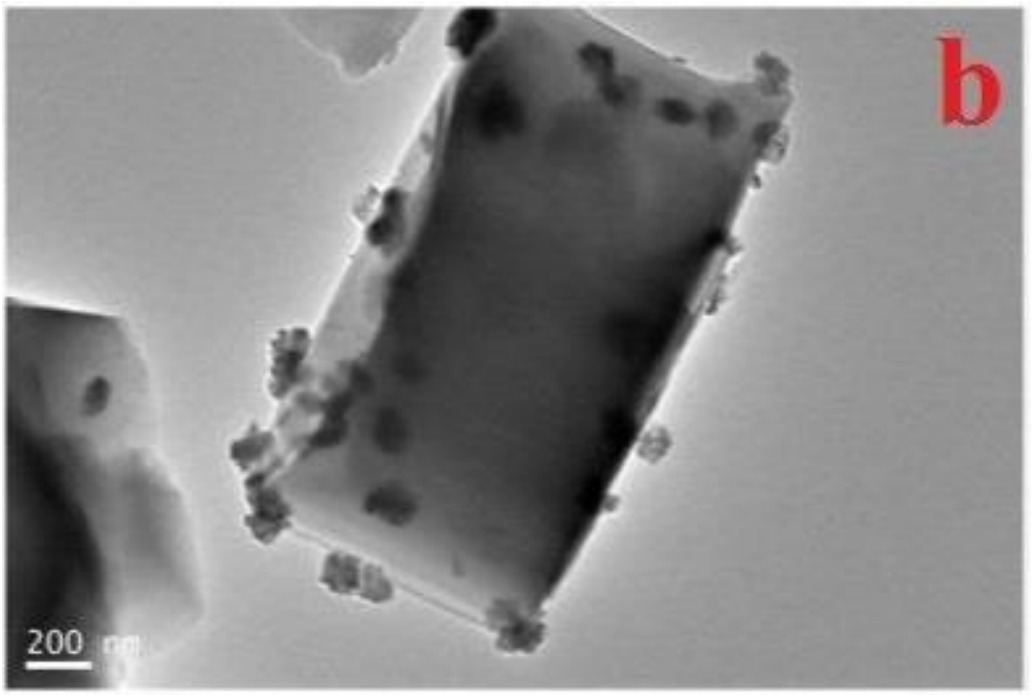

Fig. 3.8b TEM image of a post-run (5h MTH reaction, 400 ^{o}C, 1atm, WHSV= 2h^{-1}) MoO_3/H-ZSM-5 sample with a MoO_3 loading of 7.5wt%

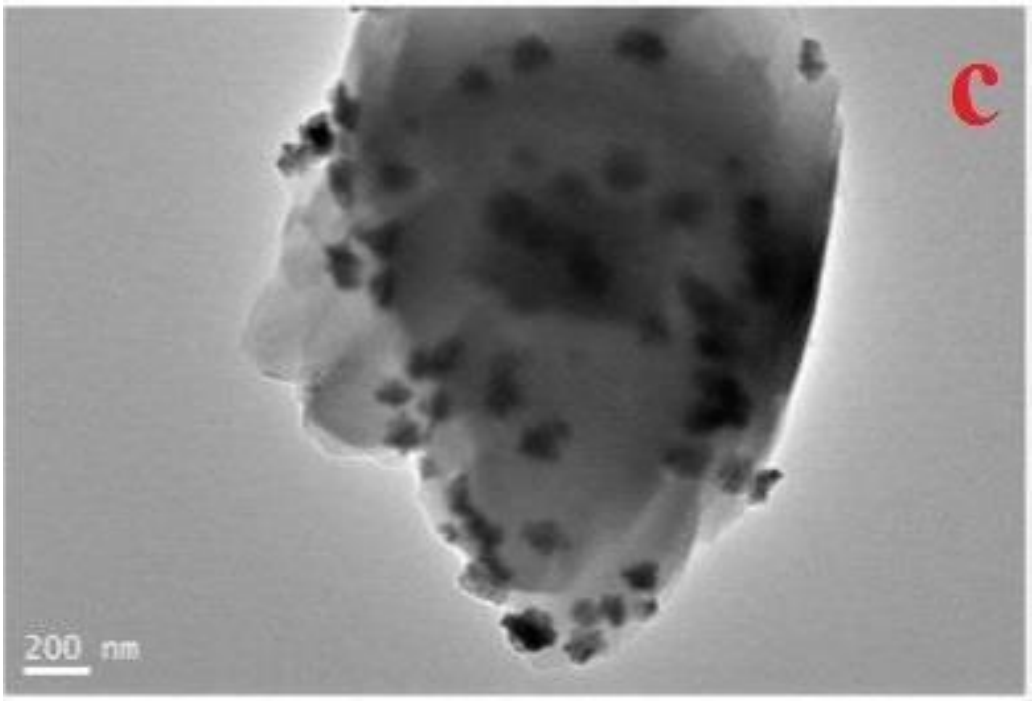

Fig. 3.8c TEM image of a post-run (5h MTH reaction, 400 ^{o}C, 1atm, WHSV= 2h^{-1}) MoO_3/H-ZSM-5 sample with a MoO_3 loading of 10wt%

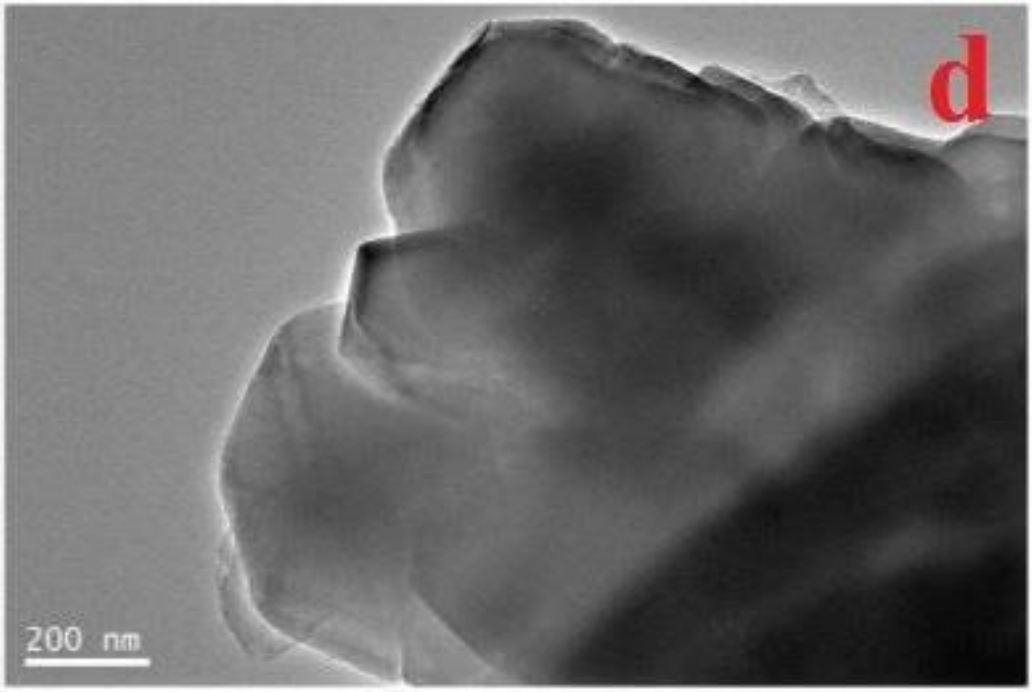

Fig. 3.8d TEM image of a post-run (5h MTH reaction, 400 ^{o}C, 1atm, WHSV= 2h^{-1}) pure H-ZSM-5 sample without MoO_3 clusters diapered on the crystal surface

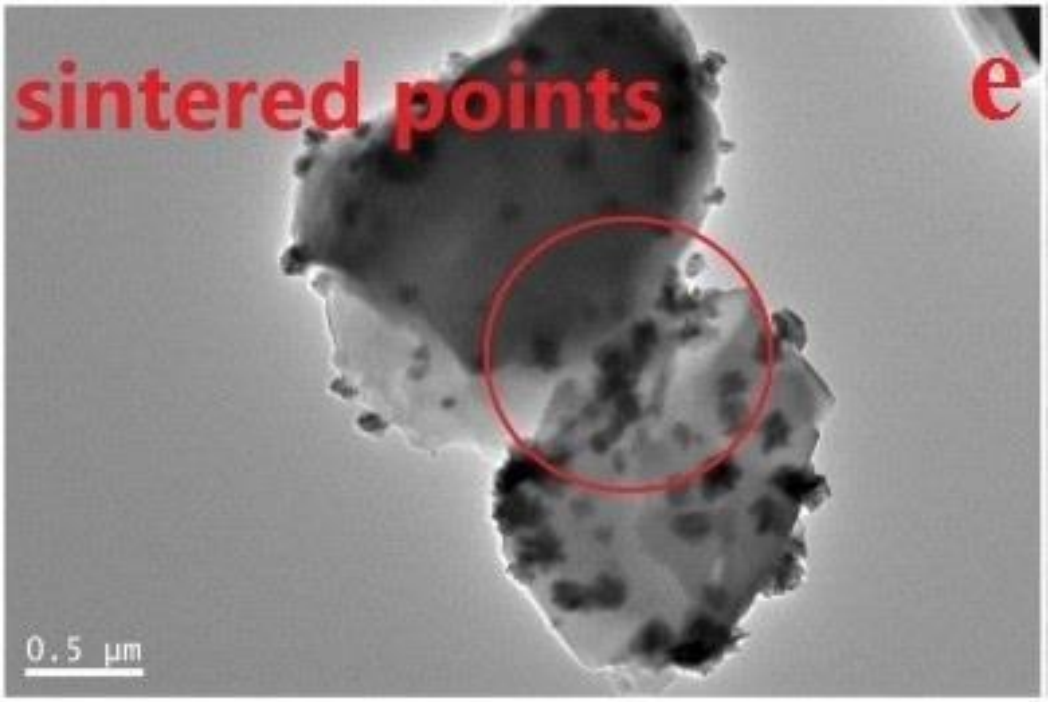

Fig. 3.8e TEM image of a post-run (5h MTH reaction, 400 ºC, 1atm, WHSV= $2h^{-1}$) MoO_3/H-ZSM-5 sample with a MoO_3 loading of 7.5wt%, showing the sintered points between two zeolite crystals

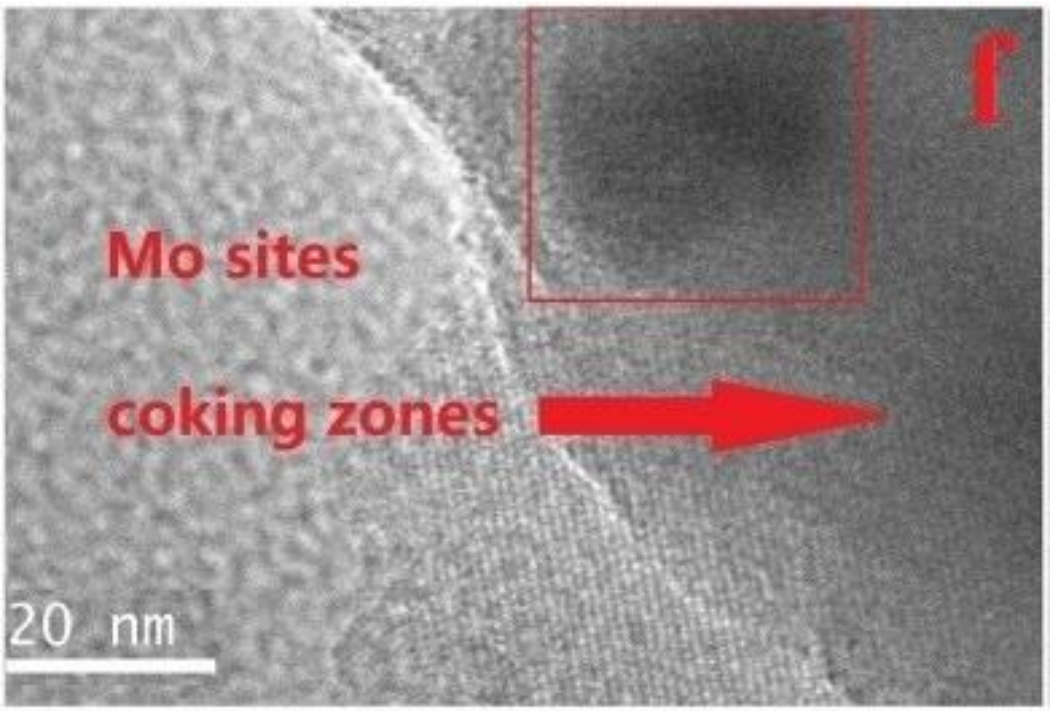

Fig. 3.8f TEM image of a post-run (5h MTH reaction, 400 ºC, 1atm, WHSV= $2h^{-1}$) MoO_3/H-ZSM-5 sample with a MoO_3 loading of 7.5wt%, showing the amplified coking areas near the Mo species

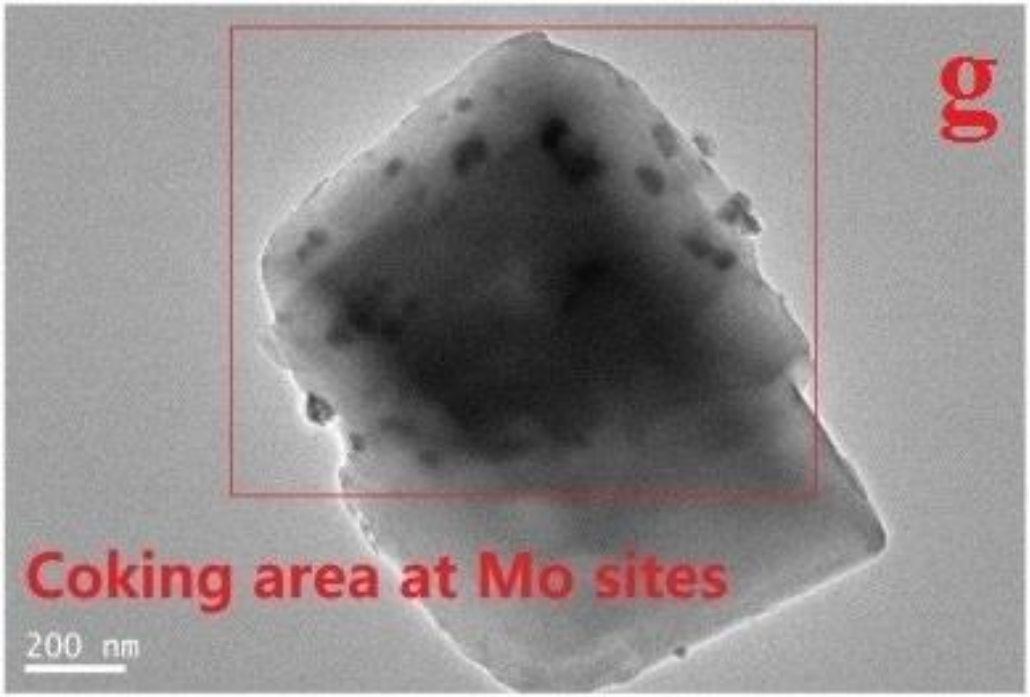

Fig. 3.8g TEM image of a post-run (5h MTH reaction, 400 ºC, 1atm, WHSV= $2h^{-1}$) MoO_3/H-ZSM-5 sample with a MoO_3 loading of 7.5wt%, showing the coking areas concentrating at the surface Mo sites in an overall vison

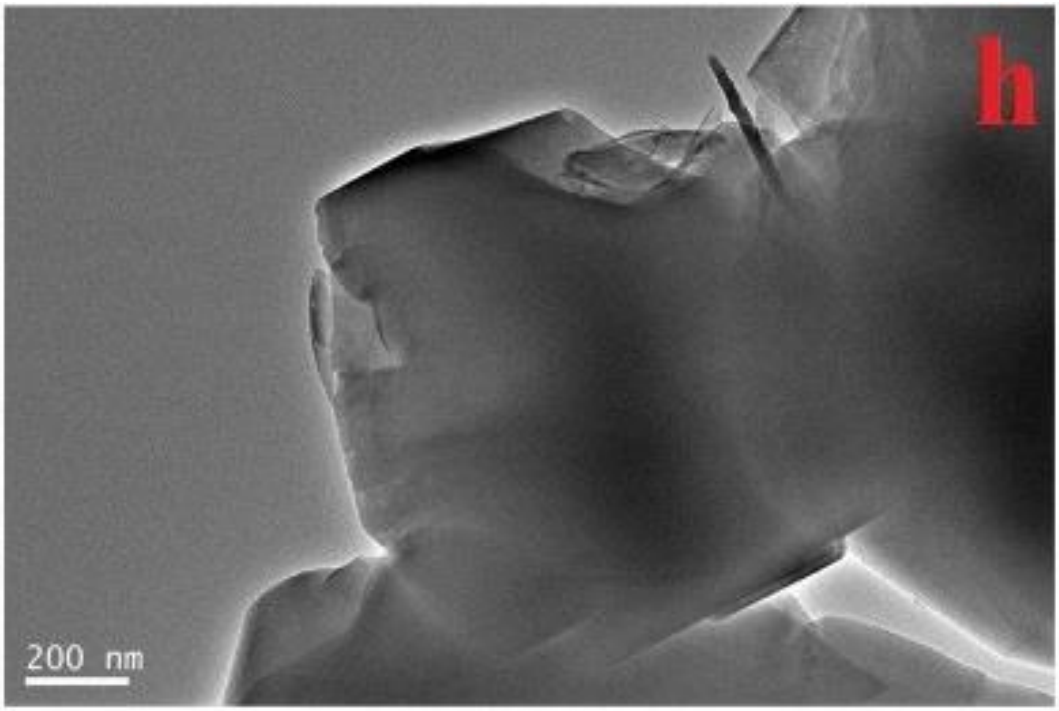

Fig. 3.8h TEM image of a post-run (5h MTH reaction, 400 ºC, 1atm, WHSV= $2h^{-1}$) pure H-ZSM-5 sample without surface-dispersed MoO_3 clusters, showing the uniformly-spread coke species over the entire zeolite crystal surface

3.3.7 Brunauer–Emmett–Teller (BET) measurements

The BET results of fresh and post-run (coked) samples are shown in Table 3.1. Measured surface areas of H-ZSM-5, 5wt% MoO_3/H-ZSM-5, 7.5wt% MoO_3/H-ZSM-5 and 10wt% MoO_3/H-ZSM-5 are 323.6, 309.5, 302.9 and 253.0 m^2/g respectively, corresponding pore volumes are 0.182, 0.177, 0.174 and 0.149 cm^3/g respectively, suggesting that the loaded MoO_3 did not significantly affect the zeolite surface area and also the pore volume, up to the 7.5wt% loading level.

Table 3.1 BET analysis on fresh and post catalytic run H-ZSM-5 samples

Sample	Surface area m^2/g	Pore volume cm^3/g
H-ZSM-5	323.6	0.182
5wt% MoO_3/H-ZSM-5	309.5	0.177
7.5wt% MoO_3/H-ZSM-5	302.9	0.174
7.5wt% MoO_3/H-ZSM-5-500 ^oC	295.1	0.168
10 % MoO_3/H-ZSM-5	253	0.149
Post-run H-ZSM-5	17.6	0.018
Post-run 5wt% MoO_3/H-ZSM-5	9	0.014
Post-run 7.5wt% MoO_3/H-ZSM-5	5.3	0.012
Post-run 7.5wt% MoO_3/H-ZSM-5-500 ^{o}	7.5	0.014
Post-run 10 % MoO_3/H-ZSM-5	2.4	0.008

From calibration studies, the standard deviation of the measured parameter is set as unity in the last decimal. (e.g. 0.182 +/- 0.001 and 323.6+/- 0.1)

There is apparent loss on both zeolite surface area and pore volume when the loading level of MoO_3 rises up to 10wt%. As suggested by Borry et al., the Mo content required for a monolayer distribution of MoO_3 on H-ZSM-5 is about 4-5wt%. [159] The distribution of MoO_3 within this range does not significantly affect the

zeolite porous properties. In our experiments, when the MoO_3 content exceeds this level (e.g. 10wt% of MoO_3), it appears that the surface MoO_3 species have effectively blocked the zeolite pores to a greater extent, leading to the apparent reduction of zeolite surface area and the unavoidable partition of zeolite pore space.

The 500 ^oC prepared 7.5wt% MoO_3 H-ZSM-5 possesses slightly smaller surface areas and pore volume than the 400 ^oC prepared 7.5wt% MoO_3 H-ZSM-5, possibly because more zeolite channel spaces are occupied by the inwardly migrated MoO_3 species. Here the higher temperature promoted inward migration of MoO_3 seems to contribute limitedly to the zeolite porous changes, however, the Brønsted acidity of zeolite was indeed reduced (Fig. 3.6).

All samples have experienced severe loss on porous properties after the MTH reaction, such an apparent 'coking' effect is frequently seen in zeolite catalyzed reactions, and has been considered as the main reason for catalyst deactivation. Although the numbers are quite close, there is still an observed decrease on sample surface areas and pore volume when the MoO_3 loading level increases. We noticed that the Mo catalytic sites would have promoted the reaction coke formations, on the other hand, pore blocking by 'overloading' MoO_3 species may also contribute to the accumulation of coke species, which occurs on the zeolite surface and particularly at where those MoO_3 species migrate into the channels.

3.3.8 Catalytic performance

Yields of benzene, toluene and xylenes (BTX)

After 5h MTH reaction at the selected 400^{o}C temperature, the original H-ZSM-5 achieved nearly 100% methanol conversion with only trace amounts of methanol left in the liquid product. Among all the MoO_3 loaded samples (400^{o}C prepared), the 5 wt% MoO_3 loaded sample exhibited the highest methanol conversion (about 87%); catalysts of higher MoO_3 loading levels showed lower conversion of methanol (about 80% over the 7.5 wt% MoO_3 loaded sample, 67% over the 10 wt% MoO_3 loaded sample) due to a faster catalyst deactivation.

Aromatic products (e.g. the methylated-benzenes) are the major components in MTH liquid product, they are also the functional catalytic centres in a MTH reaction. Their formation includes a series of complicated chemical steps, mainly consisting of olefin expansion (methylation) and aromatization (cyclization and further dehydrogenation). [14] The transformation of methylbenzenes in a MTH process yields olefins (these olefins are subsequently converted to secondly formed aromatics) via a series of methylation/de-alkylation steps that also decide the ratio between different aromatic products, therefore is the core part of the MTH catalysis. Fig. 3.9 schematically illustrates the chemistries involved in the above process, and here the mostly accepted ‘side-chain-methylation’ theory is employed to explain the catalytic role of these methylbenzene hydrocarbon pools and the relevant reaction inner-transformations. [14]

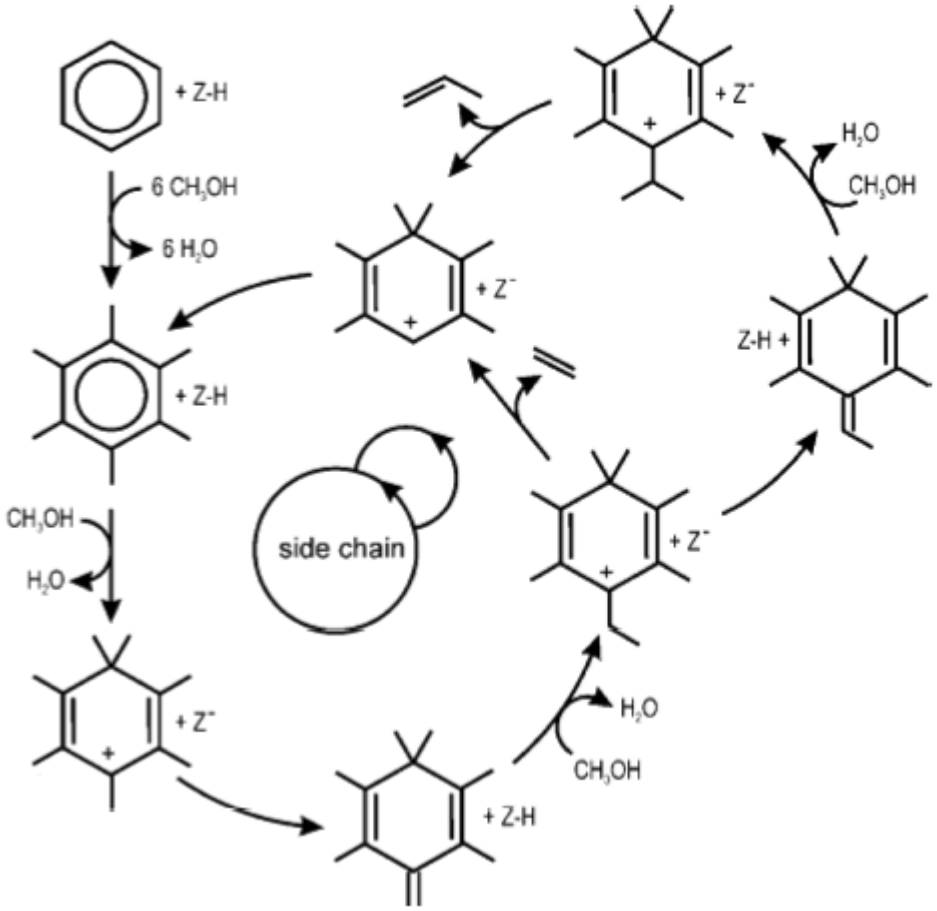

Fig. 3.9 Schematic representation of the ‘side-chain methylation’ mechanism for MTH process, showing the transformation between different methylbenzenes, and formation of olefin, adjusted from [14]

Acidic zeolite (Z-H) easily dissociates methanol with water formation, which also results in the active C^+H_3 (methenium ions) species. The C^+H_3 species are continuously added onto the benzene ring structure (benzene ring methylation), in which process different methylbenzenes are formed. On the other hand, there is also gem-methylation occurring on the benzene ring, which leads to the formation of benzennium cations (cyclohexadienyl cation that appears as a reactive intermediate in electrophilic aromatic substitution). The benzennium cation is not stable, thus can be instantaneously deprotonated (Z-H is reformed) to form an exocyclic double bond. This bond is the starting point for side-chain methylation of benzene ring, after which

elimination of ethylene and propylene regenerate the original hydrocarbon-pool species. Here the transformation between zeolite protons (H^+) and the carbon cations (methenium and benzennium ions) reduced the potential energy barriers for methanol conversion to olefins, and the transfer between different methylbenzenes. It should be noted that the ratio between different methylbenzenes (e.g. toluene/xylene) in MTH liquid product distribution is an indirect reflection of the above scheme.

Analysis on our liquid product was concentrated on selected aromatics, e.g. alkylated (poly-methyl) benzenes; non-aromatic hydrocarbons, e.g. cyclohexane, are not the interest of this research. The major observation is that MoO_3 loading on zeolites promoted a higher product selectivity (reflected by the improved product yields) to benzene, toluene and xylenes (Fig. 3.10), although it also resulted in an earlier catalyst deactivation (reduced methanol conversion). The highest BTX selectivity was achieved by the 7.5 wt% MoO_3/H-ZSM-5 sample (400 ^oC prepared) even though its catalytic activity was partially degraded by the end of the reaction time (this is reflected by the reduced gas yields at 300 min in time-on-stream, as shown in Fig. 3.11c). Interestingly, a higher loading level of MoO_3, increased from 7.5wt% to 10wt%, brought in a noticeable drop of all product yields, also including the BTX products. This is possibly due to the 'overloaded' Mo species (10wt% MoO_3) which possess a more obvious pore-blocking effect rather than accelerating the desired product formation.

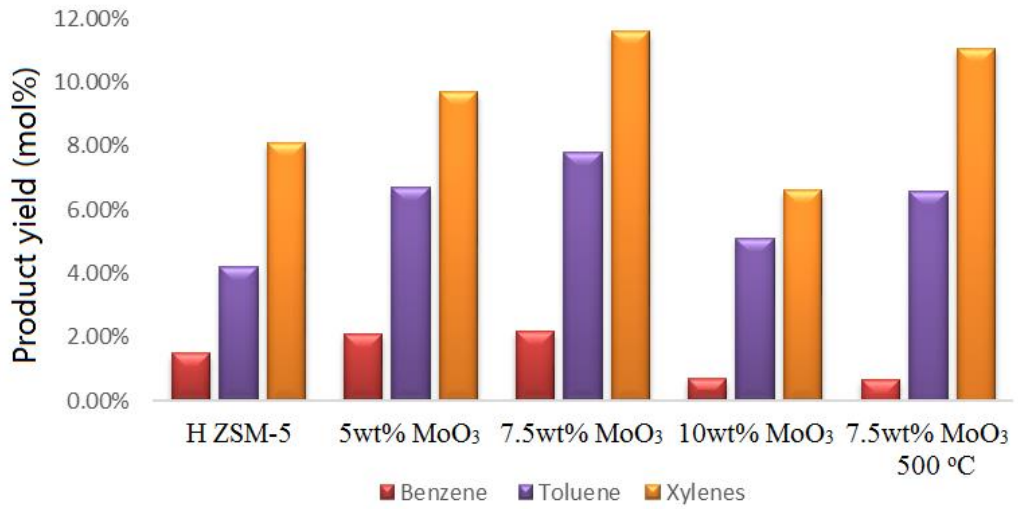

Fig. 3.10 Yields of benzene, toluene and xylenes after a 5h catalytic test**;** WHSV = $2h^{-1}$, catalyst bed temperature 400 °C, and atmosphere pressure conditions

The catalytic function of MoO_3, when employed in a hydrocarbon transformation process, normally depends on the promoted C-H bond activation (dissociation), which contributes to the molecular expansions as well as the hydrocarbon dehydrogenations (here the H atom becomes easier to be released from the hydrocarbon molecule and thus accelerates the dehydrogenation process), both of which would benefit to the improved aromatics yield. [156-158, 173] The obtained higher yield of aromatics, is we believe the evidence for the catalytic roles of those Mo species inside the zeolite channels (they have been reported to catalyze the aromatization of small hydrocarbons with the promoted C-H activation, but only at those Brønsted acid sites inside the zeolite channel). [159, 162] By contrast, it seems that the MoO_3 species on the zeolite surface, do not contribute significantly to the hydrocarbon transformations, and their influence therefore is more or less on the product transportations (a possible reason for the catalyst deactivation). Although the exact C-H bond activation mechanism and the corresponding chemical composition of catalytic Mo sites inside

the zeolite channel need further explanations (this will be discussed in the below), it is clearly seen that the distribution of Mo species in H-ZSM-5 structure, whether inside channels or on zeolite surface, without question, is the most decisive condition for the observed MTH performance over MoO_3/H-ZSM-5 catalysts. On the other hand, too high a MoO_3 loading level (e.g. 10wt% MoO_3) also eliminates the zeolite Brønsted acid sites (Fig. 3.6) that are another essential condition for the catalytic hydrocarbon conversions. Therefore, only a balance between the loaded MoO_3 amount, and the preserved number of Brønsted acid sites could guarantee a satisfactory MTH performance; moreover, such a balance, as we have observed, is highly dependent upon the MoO_3 loading levels, as well as the catalyst preparation condition. The 500 ^oC prepared 7.5wt% MoO_3/H-ZSM-5 sample exhibited lower yields of aromatics than the 400 ^oC prepared 7.5wt% MoO_3/H-ZSM-5 sample (see Fig. 3.10), most possibly due to a much poorer methanol conversion rate (approximately 69%), it seems that more Brønsted acid sites were lost due to the promoted MoO_3 migration into the H-ZSM-5 channels, as a result of the higher calcination temperature. However, the portions of alkylated benzenes (e.g. toluene and xylenes) were increased as compared to benzene showing the promoted C-H bond activation (this may help the alkylation steps).

Gaseous olefin time-on-stream (TOS) yield

The major gaseous hydrocarbon production in time-on-stream for each sample is shown in Fig. 3.11 a-e.

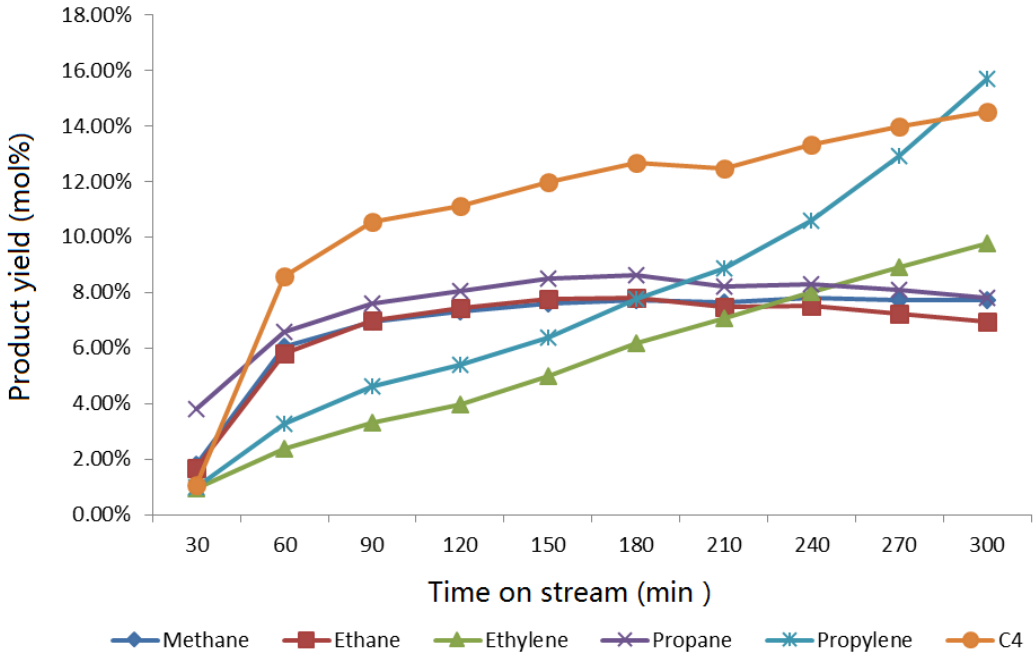

Fig. 3.11a Gas yields over the parent H-ZSM-5 (400 ^{o}C prepared) in time-on-stream MTH reaction at a temperature of 400 ^{o}C, atmosphere pressure

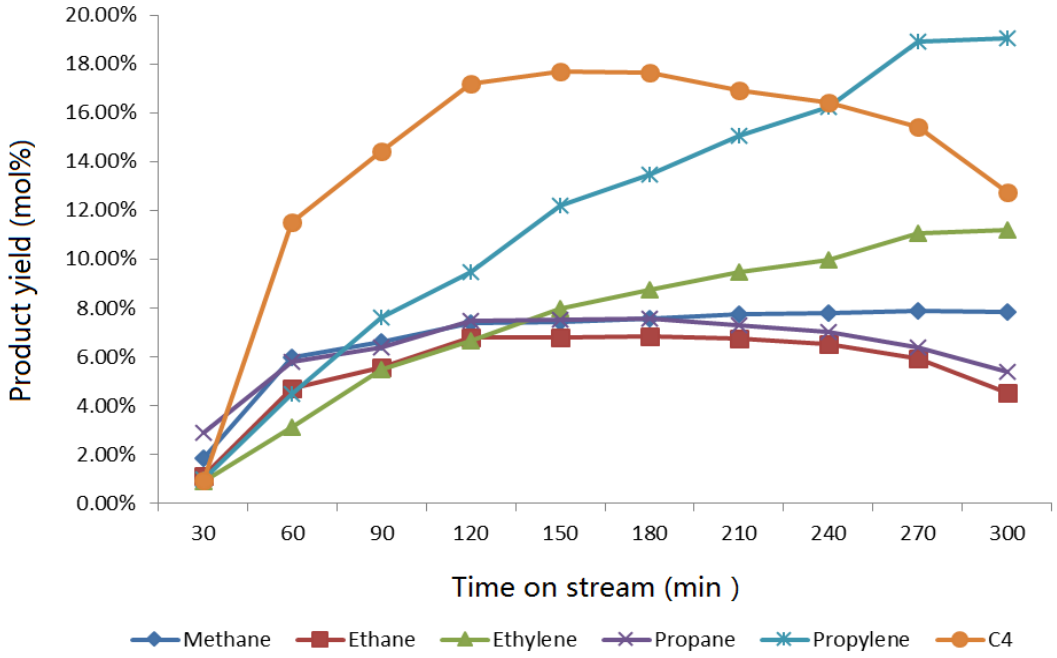

Fig. 3.11b Gas yields over 5wt% MoO_3/H-ZSM-5 (400 ^{o}C prepared) in time-on-stream MTH reaction at a temperature of 400 ^{o}C, atmosphere pressure

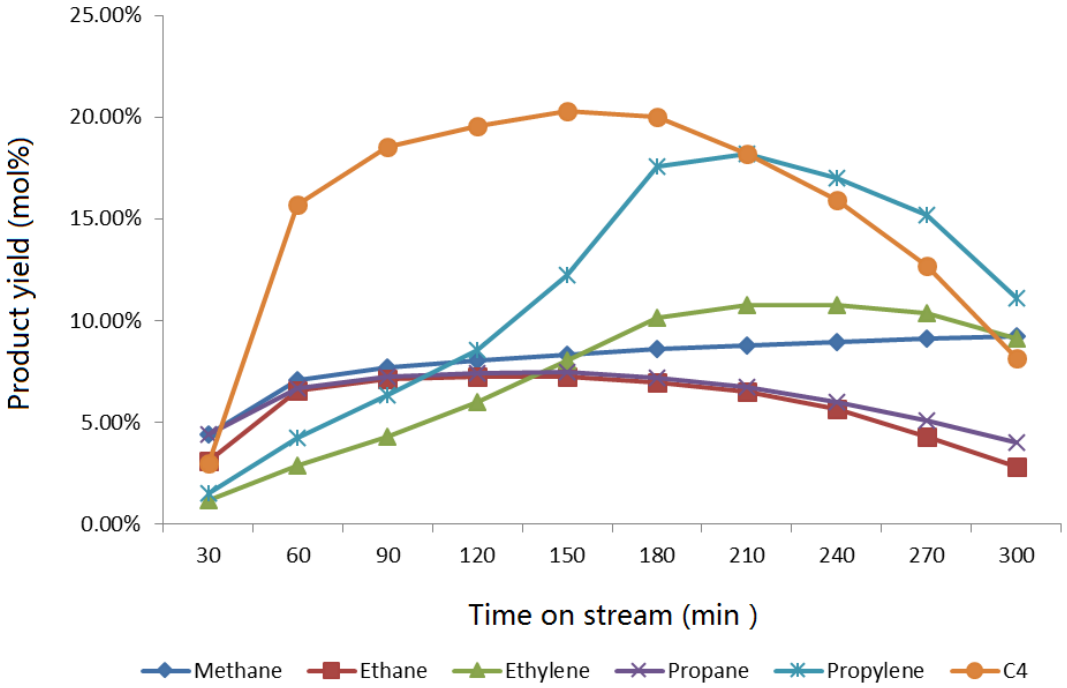

Fig. 3.11c Gas yields over 7.5wt% MoO_3/H-ZSM-5 (400 ^oC prepared) in MTH reaction at a temperature of 400 ^oC, atmosphere pressure

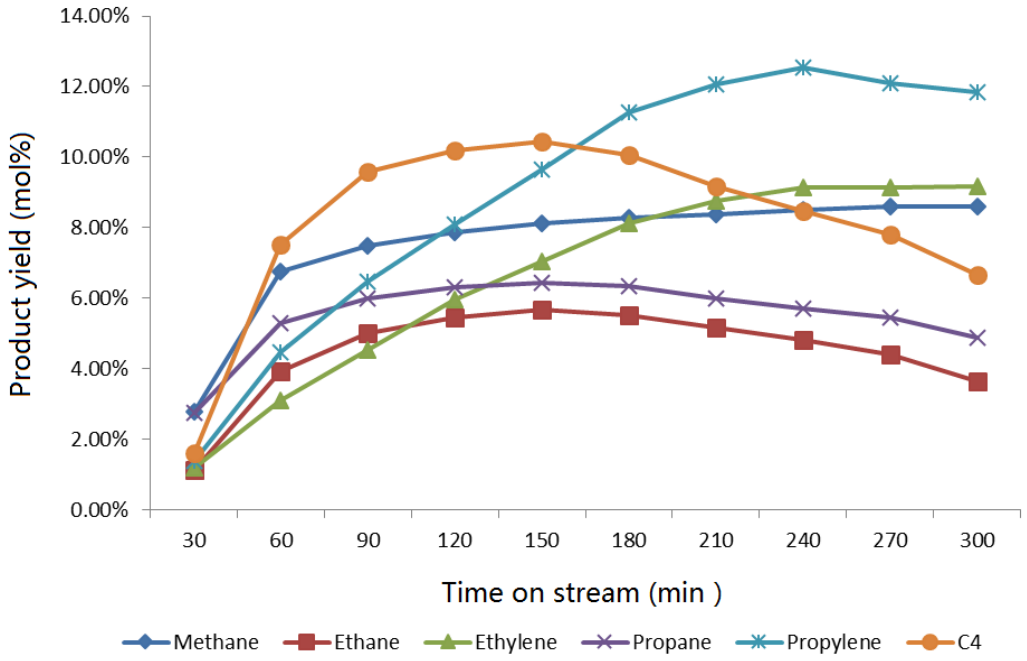

Fig. 3.11d Gas yields over 10wt% MoO_3/H-ZSM-5 (400 ^oC prepared) in time-on-stream MTH reaction at a temperature of 400 ^oC, atmosphere pressure

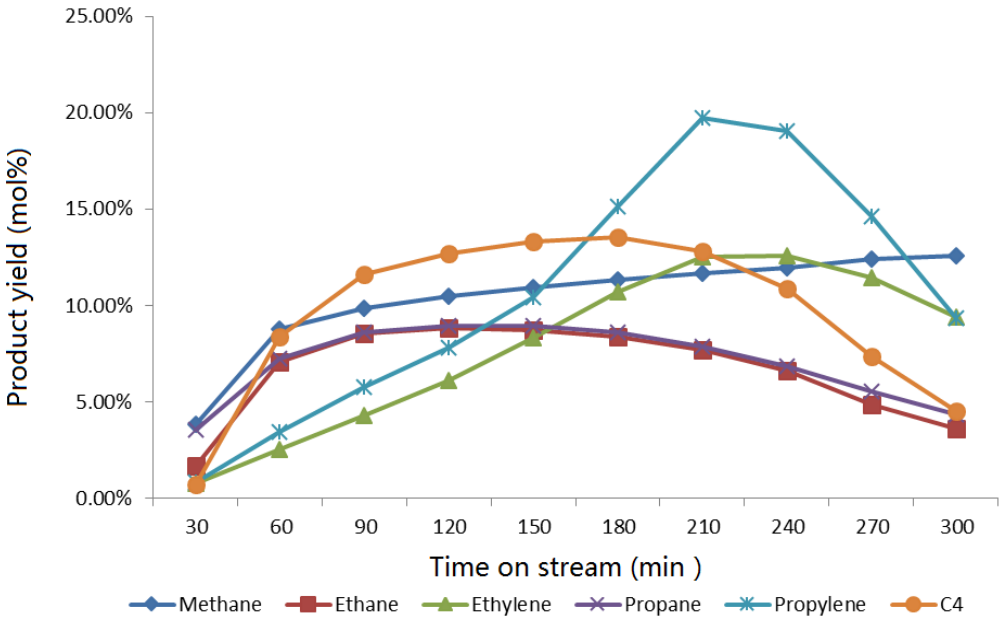

Fig. 3.11e Gas yields over 7.5wt% MoO_3/H-ZSM-5 (500 ^oC prepared) in time-on-stream MTH reaction at a temperature of 400 ^oC, atmosphere pressure

It should be noted that data of each sampling point only represents the instantaneous yield (mol%) of a gas product (see formula in page 102), achieved by comparing the methanol consumption of the gas product (mol/h) with the instantaneous methanol injecting rate which is approximately 0.0625 mol/h based on a methanol WHSV of $2h^{-1}$ and a catalyst loading of 1g.

In order to facilitate the following explanations on the observed time-on-stream gas yields. Here we further compared the gas yields (C_4 mixtures are not listed) achieved by different catalysts at the selected time point of 150 min (table 3.2). This time point has been noted to divide the whole reaction scenario into two equal time periods, and at which there have been observed distinguished gas yields among different samples.

Table 3.2 Gas yields over different catalysts at the time point of 150min

Sample	Methane	Ethane	Ethylene	Propane	Propylene
H-ZSM-5 (400 °C prepared)	7.59%	7.76%	4.98%	8.51%	**6.39%**
5wt% MoO_3/H-ZSM-5 (400 °C prepared)	7.43%	6.79%	7.99%	7.52%	12.18%
7.5wt% MoO_3/H-ZSM-5 (400 °C prepared)	8.34%	7.23%	8.01%	7.45%	**12.23%**
10wt% MoO_3/H-ZSM-5 (400 °C prepared)	8.13%	5.66%	7.05%	6.45%	9.64%
7.5wt% MoO_3/H-ZSM-5 (500 °C prepared)	10.91%	8.73%	8.34%	8.97%	10.42%

From calibration studies, the standard deviation of the measured data is set as unity in the last decimal. (e.g. 7.59% +/- 0.01%)

In the group of 400 °C prepared catalyst. The parent H-ZSM-5 exhibited a slow but gradually increasing gas olefin yield through the whole reaction time (the separation of butanes and butylenes was limited by our instrument, herein we report the total C_4 yield; other potential gas components, e.g. the C_5 species were not analyzed due to the restricted detecting time, which was suggested by the GC supplier for an efficient detection within the 30mins GC running time). By contrast, the samples with 5wt% and 7.5wt% MoO_3 achieved apparently higher propylene and C_4 hydrocarbon yields (the enhanced C_4 olefin yield was supposed to contribute to the total C_4 production) in

the first 150 min reaction period, especially for propylene (for example, about 6.39 mol% over H-ZSM-5 vs. about 12.23 mol% over 7.5wt% MoO_3/H-ZSM-5 at the time of 150 min). Both 7.5wt% MoO_3/H-ZSM-5 and 10wt% MoO_3/H-ZSM-5 samples experienced a more apparent peak period of gas production at or near 210 min, and subsequently became less active. The performance of these two samples implies an early deactivation of the catalyst, which could be attributed to a complexity of various reasons, but most possibly pointing to the accelerated coke formation. A comparison between these two samples also points out that overloading of MoO_3 (e.g. 10wt %) produces further hindrance to the MTH performance, as reflected by the more severely inhibited gas yields (Fig. 3.11d). It should be noted that before approaching the partially deactivated status at the end of the reaction time, the 7.5wt% MoO_3/H-ZSM-5 sample showed noticeably higher propylene and total C_4 yields in time-on-stream than all other samples tested, and when combined with its highest BTX yield, we noted a best 5h MTH performance for this sample. Here the ethylene time-on-stream yield was also improved by MoO_3 to some extent. Both the 5-7.5wt% MoO_3/H-ZSM-5 samples reached an ethylene instantaneous yield of about 10 mol% at the end of the 5h MTH reaction.

Another parallel test on the 7.5wt% MoO_3/H-ZSM-5 sample prepared via 500 ^oC calcination was demonstrated in Fig. 3.11e, the reaction conditions were the same as other samples (i.e. 400 ^oC). More obvious catalyst deactivation was observed starting at around 210min, before which an increase on the olefin yields especially for propylene was also monitored during the time period of 30-180 min.

3.3.9 Thermogravimetric analysis (TGA) on coked sample

TGA experiments were carried out in air (100ml/min), in the temperature range of 20-1100 ºC to quantify the coke depositions on the spent catalysts (Fig. 3.12).

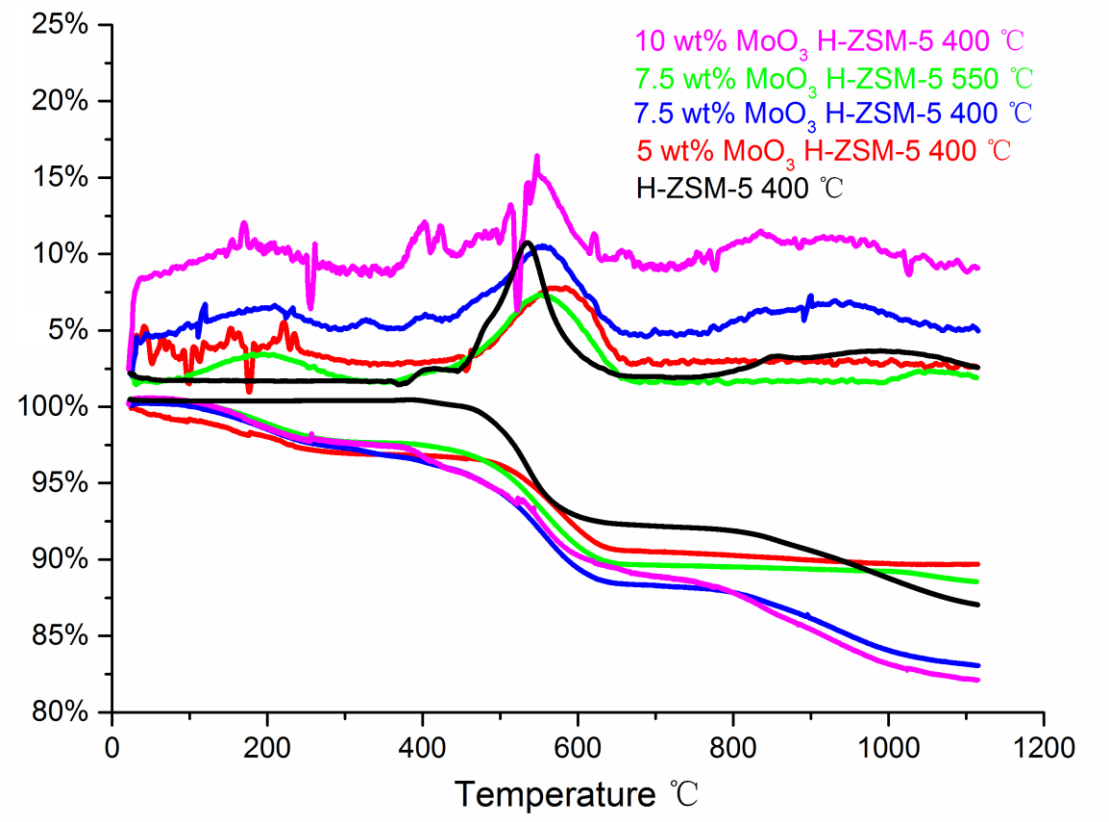

Fig. 3.12 TG-DTG plot of the spent catalysts, in the temperature range of 20-1120 ºC, included DTG (the top) and TG (the bottom) profiles

As illustrated in Fig. 3.12, the weight loss stage of 400-600ºC in the TGA profile mainly represents the onset (at which temperature range those carbons start to deposit) of 'hard coke' formation on the spent catalyst, which has been considered to be the major reason for catalyst deactivation. [180] Accordingly, the derivative thermogravimetry (DTG) curves also show a significant peak in this temperature range. The results shows that the 10wt% MoO_3 H-ZSM-5 sample contains higher

amount of coke contents than other catalyst samples (reflected by the total weight loss of about 17.5wt % mostly concentrated at 400-600^{o}C), and the 7.5wt% MoO_3 H-ZSM-5 sample (400^{o}C prepared) shows slightly less coke deposits. Interestingly, the 7.5 wt% MoO_3 H-ZSM-5 prepared at 500^{o}C has a somewhat smaller amount of coke formation. A possible explanation would be the higher temperature employed in catalyst calcination resulted in further loss of the zeolite Brønsted acid sites, on which the coke formation originally occurs during the MTH reaction. This is also supported by our FT-IR results of the as-prepared catalysts, which shows less amount of Brønsted acid sites on the 500^{o}C prepared 7.5wt% MoO_3/H-ZSM-5. The enhanced coke formation on 10wt% MoO_3/H-ZSM-5 is more complex. Although more Brønsted acid sites were lost due to the high MoO_3 loading level, which slows down the coke formation from the outset of the reaction, the corresponding blocking effects on the diffusion of large molecule products (e.g. aromatics) by the overloaded surface Mo species appears to play a more important role and make the coke formation accomplished in a shorter time by greatly accelerated product accumulation. In this case, the smaller products (e.g. gas olefins) are more easily trapped within the zeolite channels and finally converted into coke precursors (large ring structure hydrocarbons, such as toluene), then the coke species (poly-aromatics). [9, 14, 180]

3.3.10 Further explanations on observed catalytic performance

Recent investigations [9, 34, 151, 181] on C_2/C_3 olefin selectivity of the MTH process using H-ZSM-5 proposed a dual-pathway scheme for the olefin generation, centered on 1) A so-called "classic route" in which ethylene and propylene are eliminated from the hydrocarbon pool molecules by de-alkylation, and 2) Formation of C_{3+} olefins also via intra conversion (e.g. methylation & cracking) of the previously formed olefin products. As is pointed out by Svelle et.al, the second route played an important role for the yield of propylene and other higher olefins. [151]

The above findings can help to explain the promoted product yields achieved by the MoO_3 loaded samples (Fig. 3.10 & 3.11). The earlier enhanced propylene and C_4 hydrocarbon yield (here we make the assumption that the enhanced butylene yield might have contributed to the total C_4) can be attributed to those MoO_3 species that have been effectively transported into the zeolite channels. There, the inner-channel Mo species initiate the activation of C-H bonds for chain growth methylation as well as the cracking of larger molecules (essential steps involved in the second route of the MTH 'dual-pathway' mechanism), [162, 173, 182] thus, greatly promoted the propylene and butylene yields. The activation of C-H bond and resulting hydrocarbon transformations by Mo based catalysts have been reported previously. [174-176, 183] A possible explanation is the reduction of the MoO_3 precursor by both H_2 and alkanes, resulting in molybdenum carbide formation which promotes the dissociation of the

C-H connection. One study on CH_4 dehydro-aromatization with co-fed H_2 and methanol (600 ^oC for catalyst calcination, and up to 500 ^oC for reaction), reported the formation of molybdenum carbide as well as its attendant well recognized catalytic behavior in promoting the formation of aromatics and methylation on benzene-ring structure. [184] However, it was noted that a higher temperature, some 800 ^oC or above, is required for efficient carburization of MoO_x into the catalytic carbide species. [178] Direct conversion of MoO_3 into molybdenum carbides at 400 ^oC (673K) was once demonstrated by other researchers, [185] but a very high pressure (some 379 bar) was required for carbide formation.

The highly-surface-dispersed and deeply-channel-deposited nature of those Mo species makes it very difficult to detect any short-time-period-existing 'transition phase' during the MTH reaction, which might be the actual catalytic compounds that promoted the observed product yields. Of course, our results are for completed catalytic reactions and there is a clear need for a future in-situ investigation. An earlier report has highlighted molybdenum oxycarbide (MoOCx) or oxide carbide as a 'transition state' formed from the molybdenum oxide by partial reduction with methane and ethylene in a temperature range close to our experiments. [186] During methanol conversion, CH_4 and H_2, as well as other low-carbon-number alkanes, are continuously generated as typical products (they are also potential reductants) simultaneously with olefins; thus, we propose that molybdenum oxycarbide as a transition-state resultant of the MoO_3/MoO_x precursors is formed inside the zeolite channels as a result of the partial reduction of molybdenum oxide with those

already-formed alkanes, olefins and H_2. This catalytic material has previously been demonstrated to polarize the C-H bond leading to further bond dissociation. [159] In a comprehensive study of Fisher-Tropsch catalytic processes, Adesina and co-workers reported a two-stage transformation of Mo oxide to MoC_{1-x} carbide via an oxycarbide phase formed in the temperature range of 380-480 ^oC from a MoO_3 precursor (by reduction with alkanes and hydrogen), and their study well supported our assumptions on the catalytic Molybdenum oxycarbide. [187]

The potential formation of molybdenum oxycarbide, or other forms of Mo based catalytic sites, is a characteristic catalytic property of those MoO_3 species transported into the zeolite channels, as the inside-channel zeolite Brønsted acid sites are required (this also leads to the loss of Brønsted acid sites). [151, 158, 159, 162, 177, 179, 188] While these inside-channel Mo species promote an early-time accelerated catalytic reaction in the transition-state form of molybdenum oxycarbide, the MoO_3 clusters/oligomers located near/at the zeolite channel openings also reduce the access to the inner channel space. In this case, reactant methanol can still move into the zeolite channels; but products of larger molecules, such as aromatics, will have a more difficult diffusion due to this 'physical' blocking process. Furthermore, any aromatic ring structures with an 'electron rich' property may be attractive to the Mo^{6+} cations; therefore, the aromatic products could also be chemically trapped by the MoO_3 species (or other kind of Mo^{6+} structures involved in the reaction) at the zeolite channel openings. It is particularly noteworthy that the blocking of zeolite channels by both reaction product accumulation and anchored molybdenum oxide, and other

species has a considerable influence on the liquid product selectivity, e.g. larger products such as tri-methyl benzene with more alkyl groups are more likely to be trapped inside the zeolite channels, leading to our observed higher selectivity to benzene, toluene and xylenes (Fig. 3.10).

One ultimate result of the above 'product restriction' governed by the pore-blocking MoO_3 species, is that any resulting product transportation out of the inner space will become increasingly more difficult in time-on-stream. More olefins trapped inside the zeolite channels would go through the oligomerization and dehydrogenation steps (aromatization), finally converting into aromatics. The previously enhanced olefin yield (Fig. 3.11 c-d) would naturally fall with attendant higher selectivity to aromatics, further accelerating the accumulation of aromatic products possibly at the zeolite channel openings. As mentioned above, these trapped aromatics finally become the precursors of coke species. This is in agreement with the hypothesis of Mores' et al that coke is formed at specific positions 'close to' the zeolite surface. [180]

The unique catalytic performance (observed highest selectivity to BTX, and early enhanced yield of valuable propylene and C_4 products) of the 400 ^oC prepared 7.5wt% MoO_3/H-ZSM-5 is mainly ascribed to a proper balance between the number of inside-channel Mo catalytic sites and a relatively high (maintained) intrinsic zeolite Brønsted acidity as observed in our series of characterizations. It is clear that the higher temperature (500 ^oC) catalyst calcination induced a faster inner migration of the Mo species, leading to more obvious loss of zeolite Brønsted acid sites, which

may be more difficult to achieve the Mo / Brønsted acidity balance. We note that a moderated, lower calcination temperature (400 °C) employed in catalyst preparation gives more freedom to approach such a balanced status, thus, leading to the observed enhanced catalytic results.

3.3.11 A short discussion into other catalysts and their performances

Based on the fact that an aromatic hydrocarbon pool dominates in the MTH process, there should be enough secondly-generated aromatics in the system, and therefore a high aromatics yield. On the other hand, to form those aromatics, the dehydrogenation of alkenes and other hydrocarbons (the aromatic precursors) donates H_2 to the reaction system, and therefore promotes the yield of gas alkanes as there is a simple hydrogen transformation between the aromatics and the alkanes, in which process the olefins (intermediates/primary products) are consumed either by dehydrogenation (an essential step in aromatization) or hydrogenation. [14] The above discussion indicates that a general MTH reaction mainly yields aromatics and alkane, with low olefin yields, unless the zeolite structure has a selectivity to those olefin products (e.g. SAPO-34 that only allows gas molecules to yield from the cavity). This has been observed in many zeolite promoted MTH process taken place in both fixed-bed reactor and fluidized-bed reactors, especially for ZSM-5 zeolite. [16, 189]

By contrast, our project aimed to selectively enhance the olefin methylation process (a parallel way to the aromatic methylation), which happened to promote the olefin

hydrocarbon pool catalysis in the early MTH reaction period (i.e. before 150 min in a total 300 min MTH reaction). Although this advantage became weaker due to the catalyst deactivation in the later reaction stage, the enhanced olefin expansion (methylation), indeed resulted in an enhanced gas olefin yields. It is supposed that the abundance of expanded-olefin species in the system gave more chances for those small gas olefins to be formed (e.g. reformed by larger olefin cracking via β-scission) and transported out (observed in the gas yields). The competition between aromatics/olefins both performing as MTH hydrocarbon pool catalytic centre is a unique property of H-ZSM-5. [24] The current stage work is limited by the quantification of a comprehensive product family, and a hydrogen yield in time-on-stream, therefore this has become a major target for our future work. We believe that the catalysis observed in time-on-stream will be finally converted into the coke formations, and reflected by the reduced gas product yields in the later reaction period.

Previous works on metal modified H-ZSM-5 have employed several commonly used metal promoters, in most cases they are introduced by impregnation of zeolite with their nitrate forms. [15] It has been noted that incorporation of La and Ag led to an apparent improvement in light alkene selectivity. [190] This was attributed to enhanced shape selectivity of the silicate resulting from reduction of the apparent pore-size of the zeolite channels, therefore, in a more ‘physical/mechanical way’. By contrast, our MoO_3/H-ZSM-5 focused more on the chemistry aspect, by facilitating the olefin based hydrocarbon pool catalysis. Again, this could be an extension of the

research work on C_2/C_3 selectivity of H-ZSM-5 promoted MTH reaction (this work firstly pointed out that olefin hydrocarbon pools compete with the aromatics). [24] One common observation between our research and the previous researches is that the active time-on-stream was slightly decreased to coke deposition. We believe that the enhanced olefin yields are only 'transparent', and could not be a reaction terminal, which is supported by the thermodynamics.

3.4 Conclusion

A series of MoO_3/H-ZSM-5 (Si/Al=25) catalysts were prepared via calcination at a lower-than-usual temperature (400 ^oC as compared to 500 ^oC or higher that is routinely used for the calcination of metal oxide loading zeolite catalysts) and subsequently examined in the MTH reaction at that same temperature (400 ^oC). For comparison, a sample of selected MoO_3 loading level (7.5 wt%) prepared at the more conventional, higher temperature of 500 ^oC was also tested at 400 ^oC (other experimental conditions remained the same).

Owing to the lower temperature (400 ^oC) calcination, molybdenum oxide (MoO_3) was preferentially dispersed on the zeolite surface, while only the higher loading level of MoO_3 (7.5 wt% or higher) led to observable migration of the Mo species into the H-ZSM-5 channels, with concomitant partial loss of the zeolite Brønsted acidity. The 400 ^oC prepared samples, when employed in the MTH reaction at 400 ^oC, showed most interesting catalytic performance. It was noticed that the early-period gas yield, especially for propylene and C_4 products, was accelerated, which was then gradually

converted into the enhanced liquid aromatic formation.

The 7.5 wt% MoO_3/H-ZSM-5 sample prepared at 400^oC allowed us to achieve a balance between the zeolite surface dispersion of Mo species and their migration into the zeolite channels. Thus, while the extra catalytic properties were effectively introduced by the Mo species, the necessary Brønsted acidity of H-ZSM-5 was properly preserved. This sample therefore exhibited the highest yields of benzene, toluene and xylenes (BTX), with the early-time gas product yield also enhanced to somewhat extent, which is noticed to be the best catalytic performance among all the tested samples. However, MoO_3 loading level higher than 7.5wt% may lead to an earlier catalyst deactivation by the accelerated coke accumulation at, or near, the zeolite channel openings.

This research highlights the importance of calcination temperature for careful adjusting the Mo promoter distribution in the employed H-ZSM-5 system. The applied lower temperature gives us more freedom to tailor the MoO_3 migration by changing the MoO_3 loading levels, so as the catalytic performance can be accordingly improved.

Chapter 4 Scale-up of Methanol-to –hydrocarbon (MTH) reaction over Al-incorporated nano H-ZSM-5 catalyst

4.1 Project objectives

Recent MTH studies have concentrated on the application of nano zeolite catalysts, which have a particle size of several hundred nano meters or smaller. [189, 191] For instance, nano H-ZSM-5 exhibits larger surface area, easier access to incoming reactants, shorter diffusion distance and better coke tolerance. [189, 191, 192] However, industrial zeolite catalysts are routinely manufactured into larger solid bodies (from millimetres to centimetres in size), and of different shapes (e.g. beads, pellets, tablets and columnar extrudates), which are composed of active phases (e.g. zeolites), supports or binders to provide mechanical strength as well as other promoters and additives. [10] The prepared catalyst then possesses a more complex porous system, markedly different from the parent zeolite. [32]

It seems that regular laboratory-scale tests on those technical form zeolite catalysts (shaped, with binder incorporated) may not be readily transferrable to real industrial applications. The limited catalyst dosage (typically less than 1g) of course depreciates the value of such experimental observations, particularly, sometimes those already-shaped catalysts have to be ground back and tested in

powder phase. [27, 31, 193] To overcome the above difficulties, ‘Pilot test’ and larger scale factory experiments enable the loading of shaped catalysts in a huge volume but greatly increase the cost, and therefore are not routinely employed by researchers in academic environments.

By successful scale-up of laboratory test with a customized instrument that can allow catalyst loadings of many times the normal lab dosage (still perhaps less than the demand for real production and a ‘Pilot test’), and in more critical, close-to-factory reaction conditions (e.g. higher pressures), we managed to test a group of shaped nano H-ZSM-5 catalysts (made into industrial rod shape with the help of Al binders) with the obtained results better reflecting their potential industrial outputs. Most of the previous scaled up and ‘piloted’ MTH tests employed conventional micro size zeolites. [11, 31, 189] In contrast, our study focuses on the utilization of nano H-ZSM-5 zeolite and the potential influence of the binding processes on their catalytic properties. We are particularly interested in the early-time catalytic behaviour (this occurs in the first several hours) as it significantly influences the following product yields as well as the resulting coke formation over the operating catalyst. Therefore, the 5h reaction time length employed by our experiments is much shorter than the time period of normal industrial run-cycle which usually takes up to thousands/hundreds of hours/days. Besides, with our precisely designed experimental conditions and particularly a much slower methanol feeding rate, the early catalytic performance of employed samples are better illustrated (here the gas yields over

most catalysts reached a stable level just by the end of the 5h test).[15, 189, 194, 195]

4.2 Experimental conditions

4.2.1 Catalyst preparation

Powder nano H-ZSM-5 zeolites (Si/Al = 20, 60 and 120, pre-calcined to remove the ammonium, supplied by Qingdao Lianxin Chemical Co. Ltd, China) were mixed with peptized boehmite (AlOOH) to form the first-step paste (63.6 wt% nano ZSM-5, mixed with 36.4wt% boehmite in distilled water, 100g total solid mixture / 25ml water). Before the extruding process, sesbania powder (herbal plant seeds, the major component is galactomannan, removed by calcination) was added as shaping promoter (sesbania power weight / clean zeolite weight = 1:12). A mini screw extruder (designed and manufactured by Qingdao Lianxin Chemical) was used for shaping (the shaped catalyst extrudates possess a rod shape with a diameter of 2.0 mm and are cut into 0.3-0.5 cm in length). The fresh extrudates were then dried in air for 24h before calcination in a thermal oven for 5h (550 ^{o}C). The obtained Al-incorporated catalyst possesses 70wt% of zeolite and 30wt% of γ-Al_2O_3 (expected resultant) after calcination, in case of a 25wt% weight loss due to the transformation of boehmite into γ-Al_2O_3. The applied zeolite/Al_2O_3 ratio is to reserve the zeolite properties in a maximum with the most satisfied binding effects. Our preparation steps are similar with other researches, only a pre-calcination step before the all the

preparation steps is employed to activate the NH_4-ZSM-5 into H-ZSM-5 for more straightforward interactions between the zeolite acid sites and the introduced Al species.[27] Catalysts were tested in the form of extrudates, but all the extrudates were ground and sieved into particles of 0.074 mm and smaller for characterizations. The instruments, original zeolite powders and prepared extrudates are shown in the Fig.4.1a &b.

Fig. 4.1a mini screw extruder employed for catalyst shaping

Fig. 4.1b 1g nano H-ZSM-5 (Si/Al=60) powders (left) and 5g extrudates (right)

4.2.2 Characterization methods

The scanning electron microscopy (SEM) images were obtained with a JEOL scanning microscope 840F (JSM840F) instrument. Before analysis, sample powders were deposited onto the dust free scanning platform and trapped by carbon-based cements.

Transmission electron microscopy (TEM) measurements employed a JEM-2100UHR microscope (200kV) instrument. Samples were dispersed in ethanol and baked out in vacuum after transferring onto the carbon coated copper grids.

Sample surface area was measured in Brunner-Emmett-Teller (BET) analysis with a JW-BK132f surface area analyser (Beijing JWGB, China). The Al sources (boehmite and individually prepared γ-Al_2O_3) were also measured as reference. The total surface area was calculated from adsorption data at p/p_0 = 0.003-0.05.

^{27}Al, ^{29}Si and ^{13}C NMR experiments carried out with a Varian VNMRS spectrometer at ambient temperature with a resonance frequency of 104.198, 79.438 and 100.562 MHz, respectively. Cross Polarization (CP) for ^{13}C NMR and Direct Exitation (DE) for ^{27}Al and ^{29}Si were employed in the experiment. The ^{27}Al NMR were performed on a 4mm probe, with an acquisition time of 20.0 ms, a recycle time of 5.0 second, and a sample spinning rate of 12.118 KHz. The ^{29}Si NMR spectra were recorded with a 6mm probe at sample spinning rate of 6 KHz, in an acquisition time of 20.0ms, with recycle delay of 5.0 second. The ^{13}C CP NMR used a 6mm probe,

with data acquisition in 30.0ms, recycle delay of 2.0 second and sample spinning rate at 6 KHz. The conditions are based on some previous works. [196]

XRD data was obtained with a PANalytical X'Pert PRO diffractometer using Cu Kα1 radiation, and the scan diffraction angle varied from 5^o to 70^o (2θ) with a scan rate of 0.8^o / min.

The NH_3-TPD analysis was performed using a TP–5078 Auto TPD system (Xianquan Co. Ltd, China). Samples (500mg) were carefully pre-heated in N_2 at 400 ^{o}C for 2h to remove the moisture. The NH_3 adsorption (NH_3:N_2=1:3) performed at 120 ^{o}C for 30 min, and the system was then cooled down to room temperature for 1h stabilization in pure N_2. NH_3-adsorbed samples were heated with a temperature ramping rate of 8 ^{o}C / min from room temperature to 600 ^{o}C, the desorbed NH_3 was recorded with a Thermal Conductivity Detector (TCD).

FT-IR data were collected using a Perkin-Elmer Spectrum RX1 FT-IR spectrometer. Ground sample powders were diluted with KBr (1:997 in weight), then shaped into tablet for IR measurement.

Raman spectra were recorded on a Perkin-Elmer Raman Station 400F Raman Spectrometer. The sample powders were supported on a piece of microscopy glass during the scanning.

A SDT Q600 (TA instruments) thermogravimetric analyser was used to measure the coke content over the used catalysts. The coke amount is determined by the sample weight loss during temperature programmed calcination in air from 20 to 1120 ^{o}C (temperature ramping rate 10 ^{o}C /min).

50mg of post reaction (coked) sample was used each time.

The catalyst tests employed a fixed bed reactor system which is illustrated schematically in Fig. 4.2. Particularly, the reactor is customized to enlarge the loading volume for the catalysis to scale up, and other components of such a system are also used to support the greatly increased total reaction duty. The available catalyst bed height is designed to be 5 times of the reactor inner diameter to avoid flow turbulence.

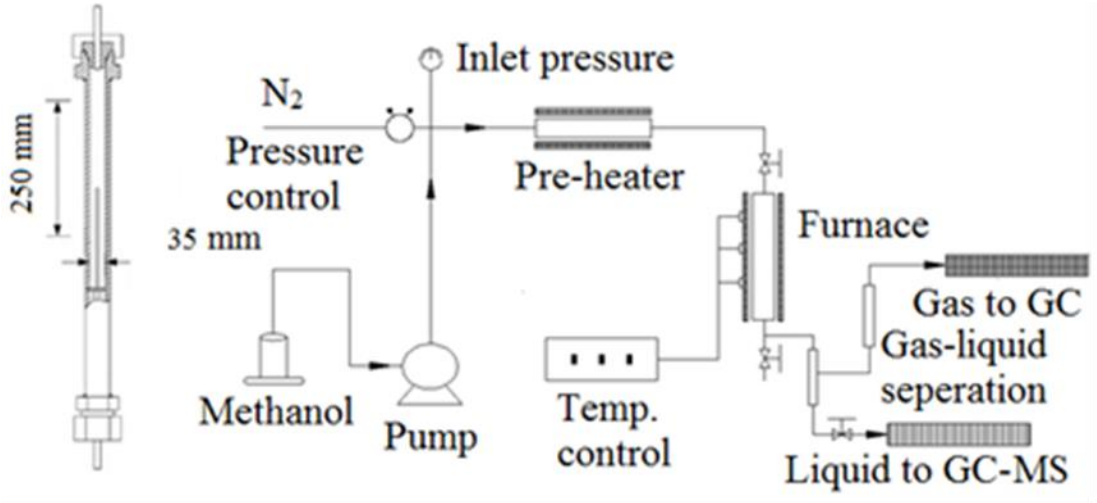

Fig. 4.2 Schematic of the customized reactor (inner diameter = 23.74 mm, designed available catalyst bed height / inner diameter = 5:1, calculated available catalyst bed height = 118.7mm) and the catalyst testing system

20 grams (bulky density: 0.4779g / ml for extrudates, 0.1550g / ml for zeolite powders) of each sample were loaded in the middle of the tubular reactor, supported by carborundum (Fisher, 24 grit). Methanol (Sigma, reagent standard) was injected by a HPLC pump, and preheated in the preheater at 150 ^{o}C to fully vaporize into gas phase. A reduced methanol Weight Hourly Space Velocity (WHSV) of 1.5 h^{-1} was applied in the reaction. N_2 was used as carrier gas to bring the vaporized methanol into reactor (300 ml/min, higher speed is not recommended and may result in inner

tubular jam). The catalyst bed temperature was set at 450 ºC under 6 bar inner pressure. The gas and liquid products were well separated at the end of the system (water cooling used). Gas products were analysed with Shimadzu GC-2010SE GC system (RESTEK MXT-1HT column). The data were obtained from thermal conductivity detector (TCD) for non-hydrocarbons and flame ionized detector (FID) for hydrocarbons every 30 mins after the methanol injection started. Liquid products were collected at 1 hour after the reaction and separated into water and oil phases via still standing treatment (30 mins). Each phase was analysed with Shimadzu GCMS-QP2010 Ultra High-end GC-MS system (SHIM-5MS column). Catalytic performance of each sample is measured by the calculations below based on previous literatures and adjusted to the current study. [197, 198]

$$\text{Methanol conversion (mol\%)} = \frac{[\text{methanol injected}] - [\text{methanol unreacted}]}{\text{methanol injected}}$$

$$\text{Gas product yield in TOS (mol\%)} = \frac{[\text{production of a gas product in TOS}] \times [\text{number of carbon in the gas product molecule}]}{\text{methanol injection in TOS}}$$

$$\text{Liquid product yield (mol\%)} = \frac{[\text{amount of a liquid product}] \times [\text{number of carbon in the liquid product molecule}]}{\text{methanol injected}}$$

4.3 Results and discussion

4.3.1 Catalytic performances and explanations

All samples were tested for 5 hours in the above mentioned conditions. Aluminum incorporated samples are denoted with ‘Al’, but still marked with the Si/Al ratios of their parent zeolites (accurate measurements on the new Si/Al ratio of the Al-incorporated zeolite framework possess certain difficulty due to the restrictions in

the current technology, so the Al-incorporated samples are also named after their parent zeolites, this also helps to identify their parents). For example, Al-H-ZSM-5 20 means an Al-incorporated sample made from nano H-ZSM-5 zeolite with an original Si/Al ratio of 20; the corresponding parent zeolite is denoted as H-ZSM-5 20.

In gas analysis, we mainly focus on the product selectivity to ethylene and propylene, whereas only a total C_4 yield is reported. Further separation of C_4 products is restricted as it requires a much longer GC running time. The C_1-C_4 gas product yields in time-on-stream achieved by different samples are listed in Fig. 4.3 a-c (parent nano H-ZSM-5 zeolites of different Si/Al ratios), and Fig. 4.4 a-c (the corresponding Al-incorporated samples), respectively.

All samples tested have shown gradually increased gas outputs, which is as a result of the carefully reduced reactant feeding rate (here a WHSV of $1.5h^{-1}$ means every one hour, there is only 1.5g of methanol passed to 1g of loaded catalyst, which will effectively slow the accumulation of catalytic hydrocarbons). For methanol conversion, zeolite is not the only catalyst, and it takes time for the number of those organic catalytic centres (hydrocarbon pools that are also products of the MTH reaction) to reach a level that meets the highest product yields in the reaction, and therefore a reaction induction period dose exist. The restricted methanol feeding rate has extended the time for such induction as reflected by the gradually increased gas yields, on the other hand, scaling up of catalyst loading also needs more time for this period, which is due to a complexity of issues, such as the time dependent distribution of hydrocarbons in the catalyst bed. [9, 15, 33]

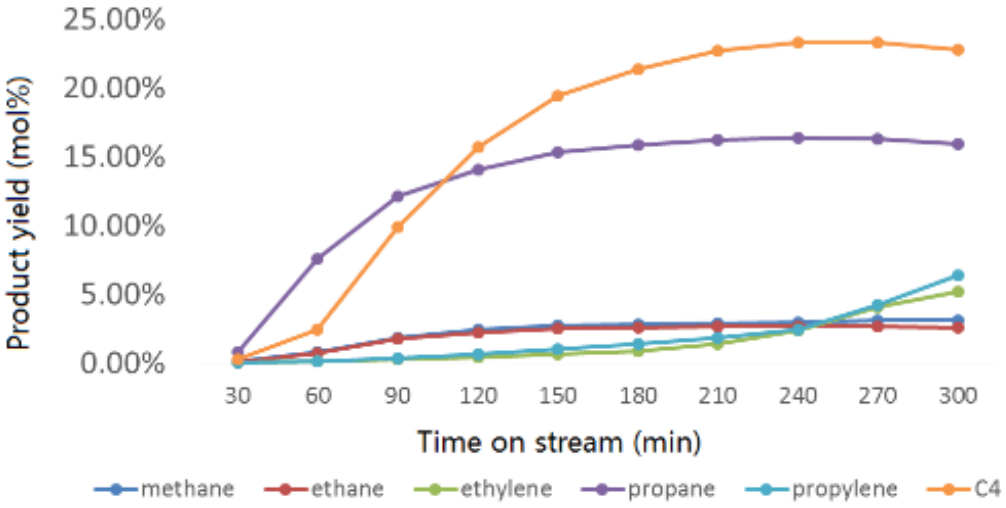

Fig. 4.3a 5h C_1-C_4 product yields in time-on-stream, H-ZSM-5 20

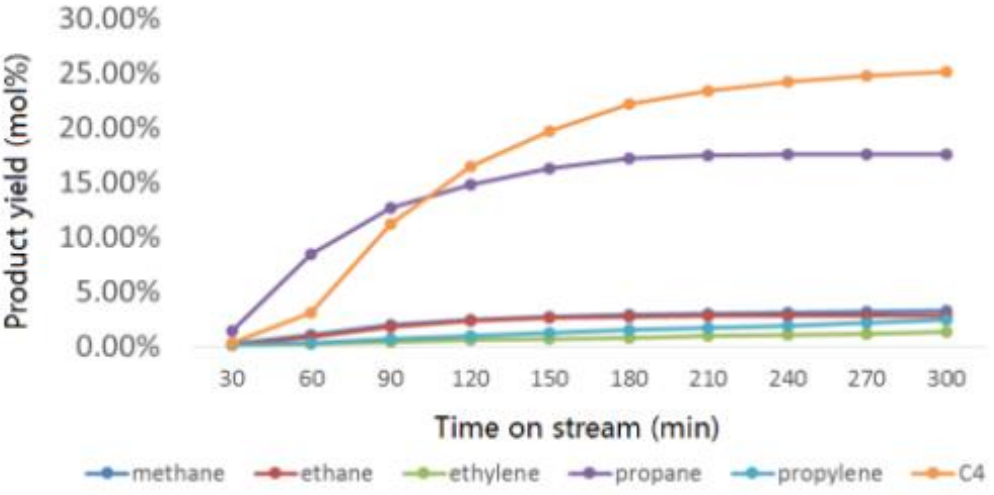

Fig. 4.3b 5h C_1-C_4 product yields in time-on-stream, H-ZSM-5 60

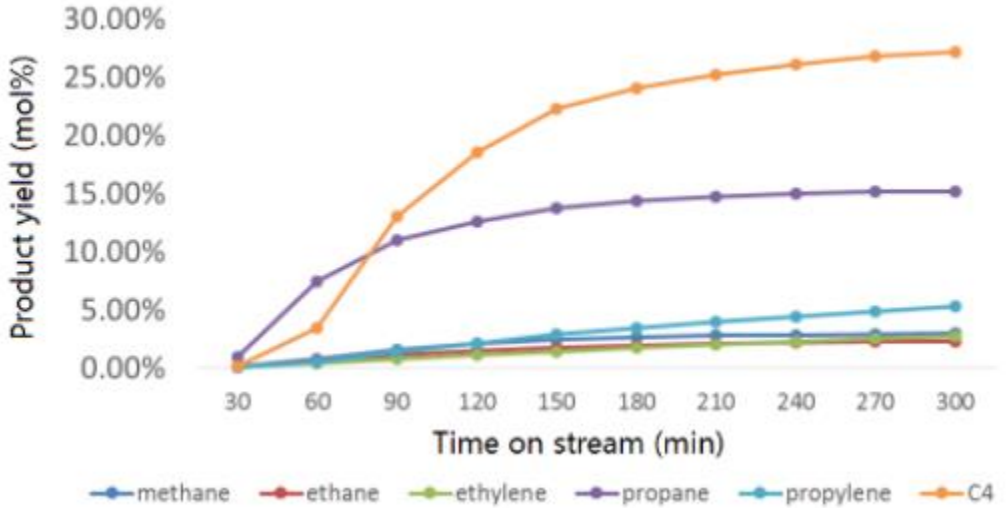

Fig. 4.3c 5h C_1-C_4 product yields in time-on-stream, H-ZSM-5 120

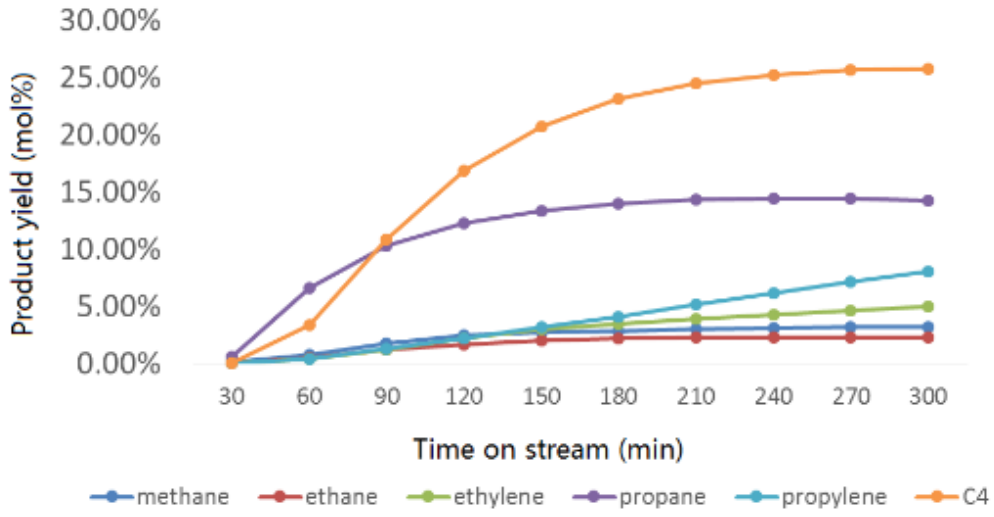

Fig. 4.4a 5h C_1-C_4 product yields in time-on-stream, Al-H-ZSM-5 20

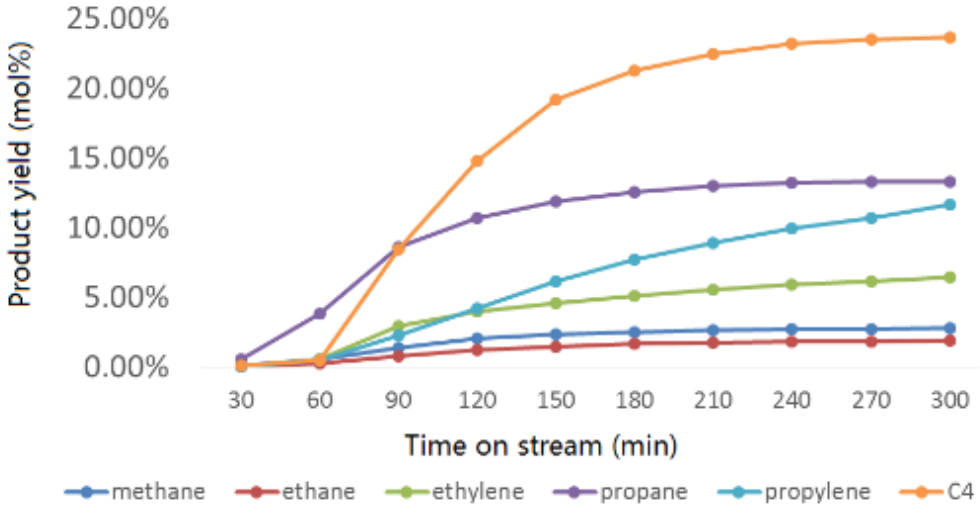

Fig. 4.4b 5h C_1-C_4 product yields in time-on-stream, Al-H-ZSM-5 60

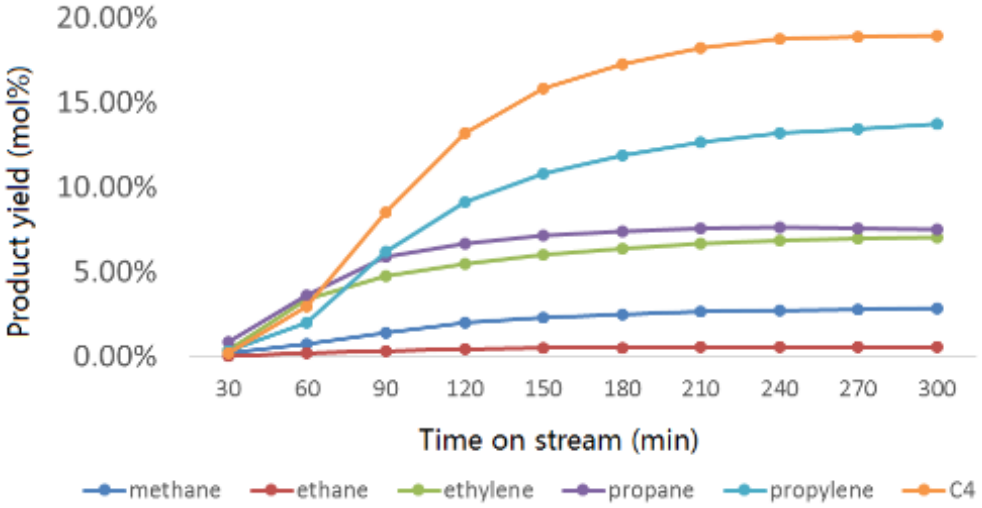

Fig. 4.4c 5h C_1-C_4 product yields in time-on-stream, Al-H-ZSM-5 120

Not surprisingly, the two catalyst groups showed distinguishable gas productions. While propane and C_4 mixtures dominated in the gas yields, which was observed on all tested samples in time-on-stream, apparently enhanced yields of ethylene and propylene were exclusively achieved by Al-incorporated samples. It should be noted that all the catalysis observed were based on a reduced reaction rate (WHSV = 1.5 h^{-1}), thus we believe that the recorded data do indeed represent the intrinsic properties of sample with very limited influence from slowly depositing cokes. Importantly, these results indicate that the catalytically–active sites involved in the reactions have been modified as a result of the Al incorporation, leading to the divergent gas product selectivity.

Here the propylene yield showed a more significant difference between the two sample groups. There was always a less than 5 mol% propylene yield in time-on-stream over all the parent zeolites, whereas over Al-H-ZSM-5 120, a ~13.5 mol% yield of propylene was achieved by the end of the 5h reaction. Similar situation was also observed on the ethylene yields, where the highest ethylene yield was again achieved by the Al-H-ZSM-5 120 sample with a figure of ~6.9 in mol% at the end of the 5h reaction. The yield of methane was relatively stable in time-on-stream, keeping at a level below 5 mol% over both catalyst groups. The C_4 mixture was not successfully separated in a total 30 mins GC running time, and no apparent difference was shown between the tested samples, however, we still propose a potentially existed transformation from butane to butylene within the C_4 mixture over the Al-incorporated samples, which is based on the observations from C_2 and C_3

hydrocarbons.

We further extracted the olefin yields from the above data. Fig. 4.5a & 4.5b compare the propylene and ethylene yields achieved by different samples, highlighting the stark difference caused by the Al incorporation.

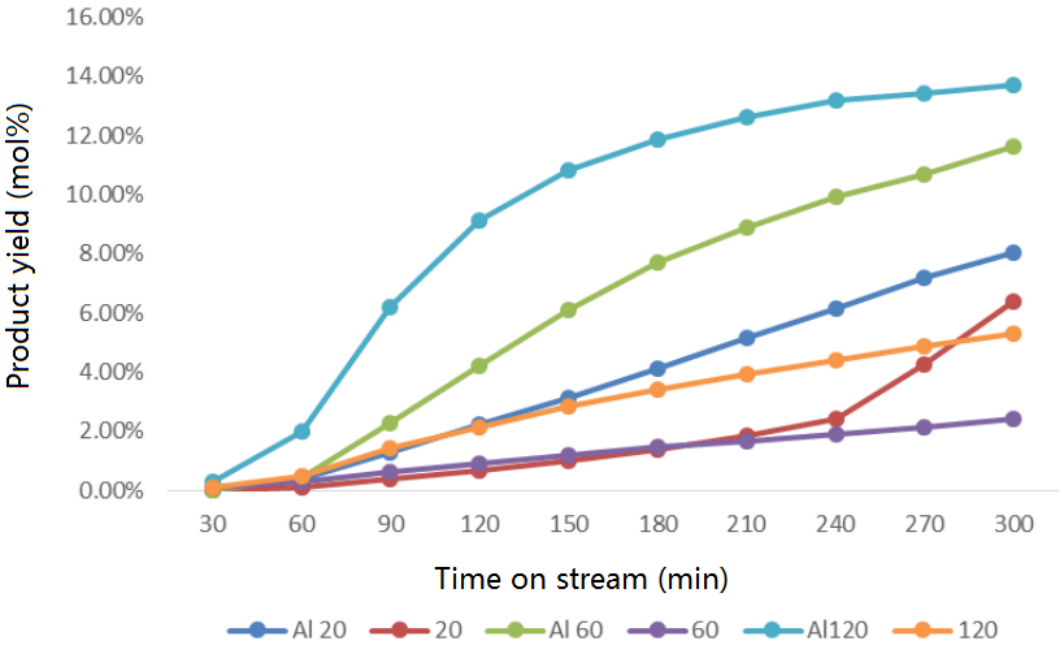

Fig. 4.5a 5h TOS propylene yields of different samples

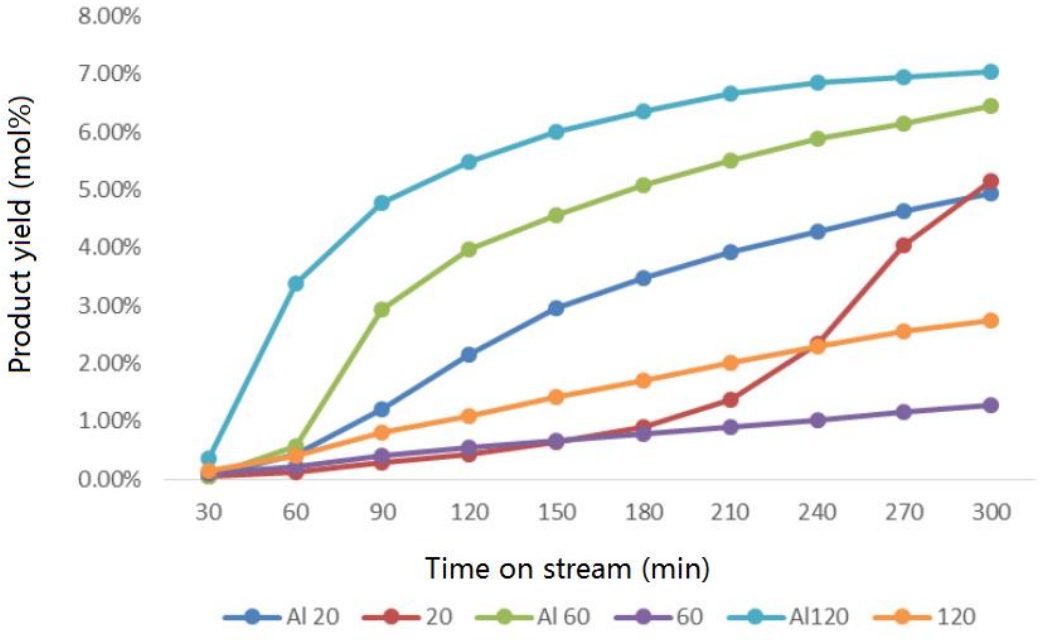

Fig. 4.5b 5h TOS ethylene yields of different samples

It is clearly shown both propylene and ethylene yields were apparently higher for the three Al-incorporated samples through the whole 5h reaction period. Here **t**he difference between samples in the same group is also highlighted, pointing out the significance of the parent zeolite Si/Al ratio in deciding the olefin yields for samples in the same group. Even in the Al-incorporated sample group, the observed gas product distribution still appears to be determined by the Si/Al ratio of the parent zeolite, although by Al_2O_3 incorporation, there will obviously be a new Si/Al ratio of zeolite framework in the Al-incorporated sample. As has been mentioned above, the Al-H-ZSM-5 120 sample exhibited the highest C_2-C_3 olefin yields, especially for propylene (for this sample, propylene yield was apparently higher than propane, in strong contrast to all other samples). Smaller parent zeolite Si/Al ratio leads to the fall of C_2-C_3 olefin yields, which happens in both sample groups; it is noted that the Al-H-ZSM-5 20 sample exhibited somewhat adjacent gas product yields as those parent zeolites.

Liquid products are mainly composed of aromatics, and the yields of benzene, toluene, xylenes and Tri-methylbenzene (major C_6-C_9 products in the reaction) are listed in Fig. 4.6. The Al-incorporated group exhibits apparently reduced aromatics yields. It has been observed that a medium Si/Al ratio (60) of parent zeolite is more favourable for the aromatics yield, in both sample groups. Among all the tested samples, the H-ZSM-5 60 sample obtained the highest total BTX yield after 5h reaction. Reaction over H-ZSM-5 120 produced more tri-methyl benzenes, thus, obtained the secondary high yield of the total C_6-C_9 aromatics. Al-H-ZSM-5 60

showed higher BTX yield and C_6-C_9 yield than the other two Al-incorporated samples, based on its higher xylenes yield.

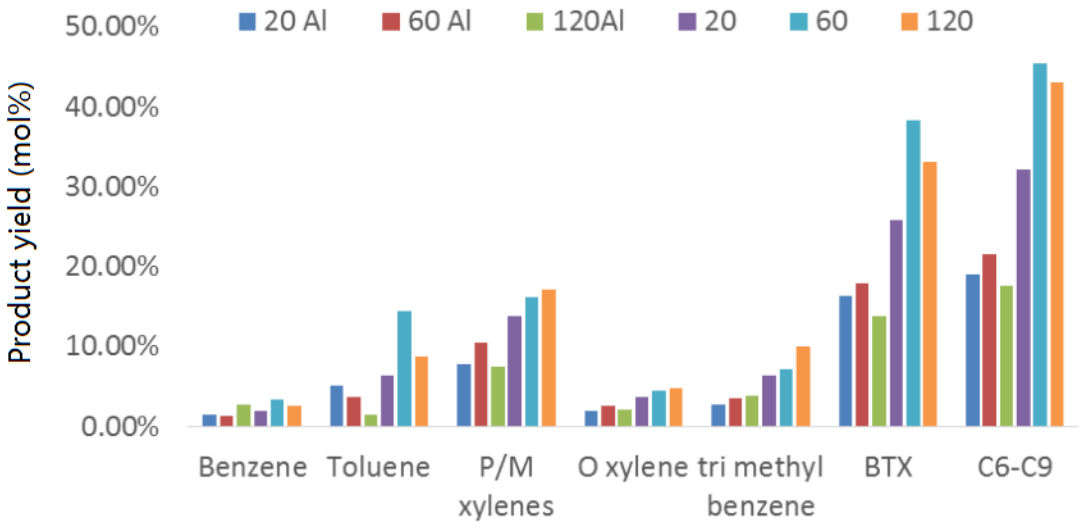

Fig. 4.6 The main aromatic product distribution (yield in mol %) of different samples (5h MTH reaction, 450 ^{o}C, 6bar, WHSV= 1.5h^{-1})

**Note that each color represents the product yields achieved by one catalyst sample, and an ideal 100 mol% accumulation is not shown, due to the limitation in all-product quantification, and the conversion of methanol into coke species (carbon deposits trapped on/inside zeolite structure, see TGA results in Fig. 4.26)*

C_6-C_9 are made up of compounds that are non-aromatics but have carbon number of 6-9.

The above observations have shown some consistency between the parent H-ZSM-5 group and the Al-H-ZSM-5 group. As has been mentioned, in each group the product distribution over a particular sample, e.g. the selectivity to olefins, is still mainly decided by the Si/Al ratio of parent zeolite. This seems to also determine the actual number of zeolite Brønsted acid sites in each sample, no matter whether there is incorporated Al binder phase, or not. Here the possible neutralization of Brønsted acid sites by the binder Al (AlOOH) was reported previously, [11, 199, 200] but just showed limited influence, and there is also a later complementary process of the

zeolite framework Al sites from the binder Al, which forms more potential Brønsted acid sites (this will be discussed in the following contents); therefore, the zeolite Brønsted acidity could be well preserved in the presence of Al binders. In most cases, the preserved Brønsted acid sites in the Al-H-ZSM5 sample are mainly from the parent zeolites, thus their amount is also determined by the parent zeolite Si/Al ratio. This is supported by the NH_3-TPD results in Fig. 4.7.

Many studies have reported that catalysts with a higher acid strength and higher acid site density (the number of Brønsted acid sites) lead to a faster MTH reaction rate. [9] Here, the larger the amount of acid sites, the faster the chemical steps involved in the MTH process and the aromatic (main coke precursors) formation would be, and hence the faster the coking rate. This is due to the reaction thermodynamics of hydrocarbon transformation when occurs in a space limited system, where the exothermic, acid (proton, H^+) promoted polymerization reactions dominate to reduce the volume of products. On the other hand, the higher the density of acid sites, and therefore the closer these sites are to each other — the larger the number of successive chemical steps undergone by reactant molecules along the diffusion path within the zeolite crystallites. This also leads to the more favorable conditions for the condensation reactions, based on which the aromatic products (a more condensed, higher density product than the gas olefins) are more favored by the reaction system. [12] The above discussions can certainly explain the observed higher yields of aromatics by the parent nano H-ZSM-5 group (without Al binder phase, there are more Brønsted acid sites in the parent nano H-ZSM-5 zeolites).

In both sample groups, a medium level of Brønsted acid sites (governed by a parent zeolite Si/Al of 60) leads to the highest yield of aromatics, this is because more Brønsted acid sites may further accelerate the transformation of MTH aromatic products (for ZSM-5 porous system they are mainly methylbenzenes) to some more condensed coke precursors (e.g. the polyaromatics), which happens to reduce the aromatic yield.

Although reducing the aromatics yield, the Al-incorporated samples possess a much higher yield of the gaseous olefins, in stark contrast to their parent zeolites. Here any explanation cannot simply centre on the acidic site amount, and we pay more attention to a potential intra-transformation between the olefin, alkane and aromatic products. Here olefins stand midway, and thus can be converted into either alkanes by hydrogenation, or aromatics by dehydrogenation. This is based on the widely accepted 'hydrocarbon-pool' mechanism, [201] and a later developed 'dual cycle' reaction scheme. [34, 151] Supposing a reaction balance does exist as a result of the above transformation, only promoted H_2 transfer can break out the previous balancing status. The H_2 transfer process, normally leading to 'capture' or 'loss' of H_2 on the olefin molecules, selectively converts olefins into alkanes, or aromatics. [11, 15, 30, 33]

It has been reported that one important synergistic effect of the introduced Al phases (AlOOH or resulted γ - Al_2O_3) is the promoted hydrogen abstraction during the hydrocarbon conversions. [30] This feature relies on an additional Lewis acidity introduced by the added Al^{3+} cations, and has possibly delayed the reaction inner

hydrogen transfers. Here the delay of H_2 transfer between different product types, no matter it works on hydrogenation or dehydrogenation, would help to preserve the earlier generated olefins, providing more chances for them to be transported out from the system. On the other hand, neutralization of zeolite Brønsted acid sites by the introduced Al binder phase (e.g. AlOOH) also effectively hindered the reaction inner aromatization process, as proton is recognised as essential for such catalytic chemistry. [11, 27, 30, 31] This further contributed to the higher yield of olefins over the Al-incorporated samples, and also reduced coke formation to somewhat extent. Our characterizations (NMR, FT-IR, and Raman) have shown more olefinic coke species are deposited on the Al-incorporated samples, whereas the coke species on the post-run H-ZSM-5 zeolites are mainly aromatics.

We also tested a pure Al_2O_3 sample (made from precursor boehmite via the same preparing procedure) under the same MTH conditions, only a negligible amount (the exact repeatability is not stable) of CH_4 or a mixture of small gas hydrocarbons can be observed during the 5h reaction time (in the case that there are continuous reactions, this part of gas yield may be caused by the last run-cycle that employed zeolites), with most methanol unconverted in the collected liquid. This further confirms that the observed special catalytic performance is a synergetic effect between the Al_2O_3 binder and zeolite, where the zeolite Brønsted acid sites are crucial for methanol conversion.

4.3.2 NH_3-TPD

Fig. 4.7 shows the plots of Temperature-Programmed-Desorption of Ammonia (NH_3-TPD) obtained from Al-incorporated samples and the parent nano H-ZSM-5 zeolites.

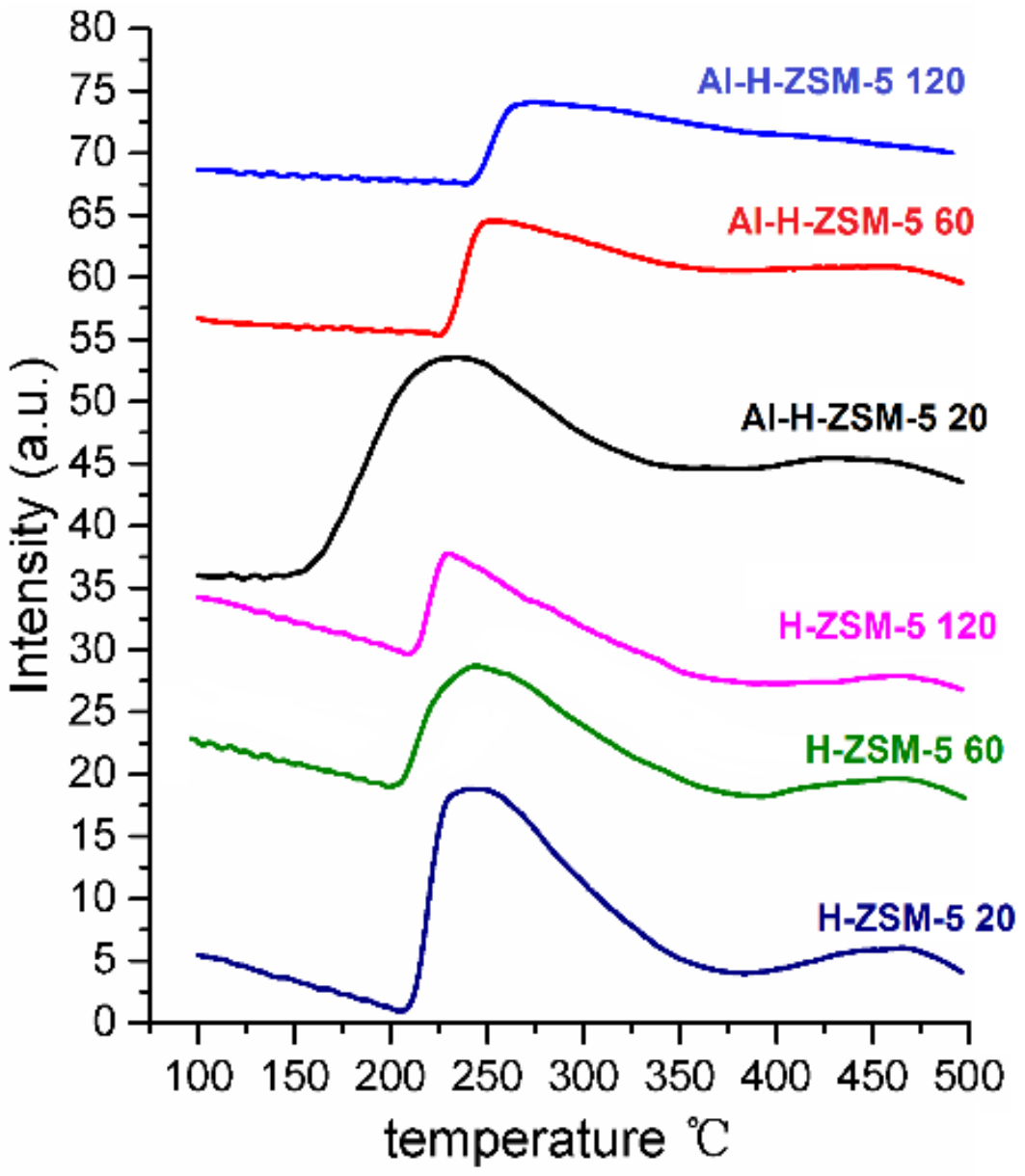

Fig. 4.7 NH_3-TPD plots of Al-incorporated samples and parent H-ZSM-5 zeolites (all before reaction)

In zeolite catalysis, the solid acidity distribution, i.e. different acid sites and their abundance, possesses the most important impacts on many reactions. Zeolites are 'non-soluble' materials which may not be suitable for measuring their acidity in aqueous conditions (in most cases a direct H_{BH+}, the Hammett acidity cannot be directly obtained). Normally, probe molecules (that are bases which can be adsorbed/desorbed on the zeolite acid sites) are employed as indicators to demonstrate a 'map' of the zeolite acidity distribution. An ideal (defect-free) zeolite in the acid form should not have Lewis acid sites, but these can be introduced by ion-exchange or by steaming to create defect sites associated with extra-framework aluminum. Some zeolite catalysts contain polyvalent cations and various defect sites, and they clearly have Lewis sites, although these are not nearly as strong as those on metal halide powders. Fortunately the consensus was that zeolite HZSM-5, with little or no Lewis acidity, was one of the strongest zeolite solid acid catalysts, and we were able to focus on the Brønsted acidity. [202] It should be noted that in the present research we have the extra Al binder phases, which possess rich Al^{3+} centres that would rise a certain level of the sample Lewis acidity. Therefore, the employed acidity measurement should also reflect the corresponding changes due to those Al^{3+} Lewis centres. Here we employed NH_3 molecule as the probe, and they can be adsorbed by the zeolite acid sites, but desorbed at different temperature ranges owing to the differential acid strength of the acid sites. Normally a clear separation along the temperature axis in a NH_3-TPD plot can be directly read.

In the NH_3-TPD results of acidic-zeolite based catalyst, special attention is usually paid to two desorption peaks located at temperatures of ~220 ^oC and ~450 ^oC. The desorption peak at lower temperature is related to those weak acid sites, e.g. Si-OH group, or extra framework Al-OH group, which only imbue limited catalytic function in zeolite catalysis. By contrast, the higher temperature desorption peak corresponds to those strong acidic sites mainly in the zeolite structure, such as the framework Brønsted acid sites. [9, 171, 203] We observe a shift of the lower temperature desorption peak from 220 ^oC to 270 ^oC on Al-incorporated samples, especially for the Al-H-ZSM-5 60 and Al-H-ZSM-5 120 samples. Furthermore, their higher temperature desorption peaks were also notably reduced in height. Such changes in acidic properties inferred from these data clearly point to an effective incorporation of the Al binders. Here the shift of lower temperature desorption peak arises from the additional Lewis acid sites imported by AlOOH, the Al^{3+} cations possess some medium acid strength (the ability to trap a NH_3 moleclue), and therefore release NH_3 molecules at temperatures around 270 ^oC. Erosion of the 450 ^oC desorption peak is attributed to the partial neutralization of the Brønsted acid sites by the introduced Al species, possibly occurring during the catalyst preparation, and as a result of the series of Al transfers between the binder phase and zeolite. Similar phenomenon was firstly reported in previous studies on methanol-butene cracking and paraffin transformations, which was also noted to support an improved coke tolerance. [30]

4.3.3 SEM, TEM and corresponding BET analysis

The SEM images are employed to display the evolution of parent H-ZSM-5 zeolites, recorded at different stages: in original status (Fig. 4.8a, 4.9a, 4.10a), extruded and calcined (Fig. 4.8b, 4.9b, 4.10b), and after MTH reaction (Fig. 4.8c, 4.9c, 4.10c). The MTH reaction conditions are: 5h MTH reaction, 450 ^{o}C, 6bar, WHSV= 1.5h^{-1}.

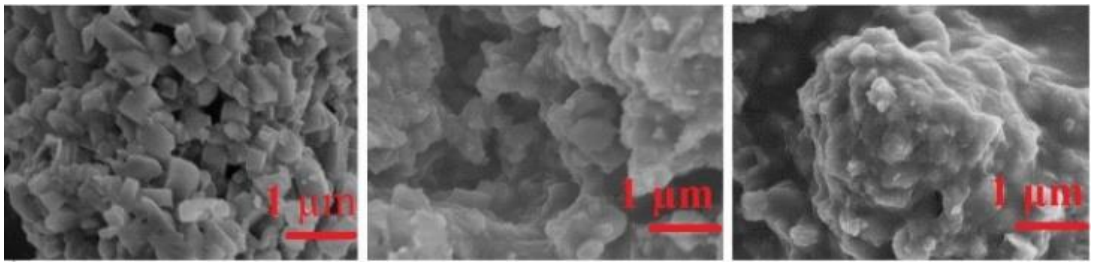

Fig. 4.8a nano H-ZSM-5 (Si/Al=20), 4.8b Al-H-ZSM-5 20, and 4.8c post-reaction Al-H-ZSM-5 20, shown in an order from left to right

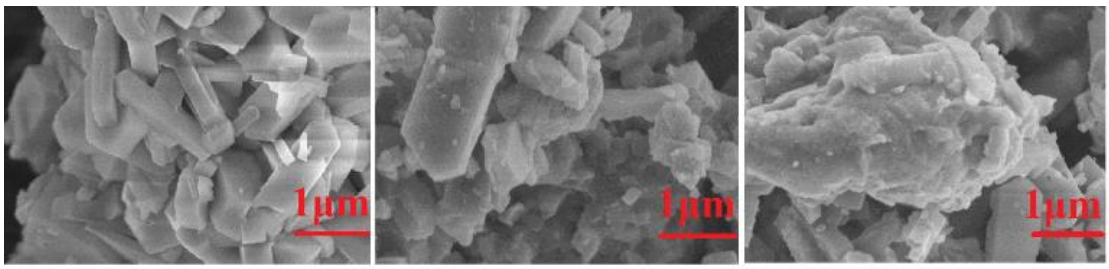

Fig. 4.9a nano H-ZSM-5 (Si/Al=60), 4.9b Al-H-ZSM-5 60, and 4.9c post-reaction Al-H-ZSM-5 60, shown in an order from left to right

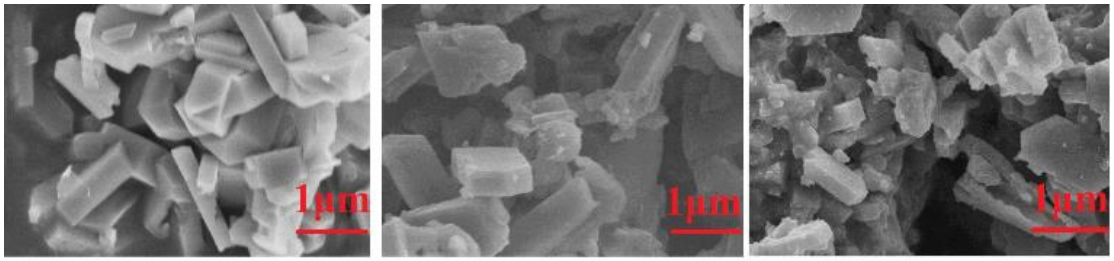

Fig. 4.10a nano H-ZSM-5 (Si/Al=120), 4.10b Al-H-ZSM-5 120, and 4.10c post-reaction Al-H-ZSM-5 120, shown in an order from left to right

These data clearly show that the binder compounds have effectively changed the morphology of the parent nano H-ZSM-5 zeolites, at the selected Al incorporating level (γ-Al_2O_3 takes 30wt% in the shaped catalyst). The parent zeolites are nano particles in cubic (Fig. 4.8a) or rod (Fig. 4.9a and Fig. 4.10a) shapes, with sharp edges, and more clearly isolated in the SEM pictures (more intercrystalline spaces can be seen between the crystal particles). It is obvious that all the extruded samples are most effectively 'bound' by the Al binders (Fig. 4.8b, 4.9b and 4.10b), and this binding effect becomes more apparent on samples with a smaller parent zeolite Si/Al ratio. While Al-H-ZSM-5 60 and Al-H-ZSM-5 120 still possess large portion of nano crystal particles with clear and sharp edges (Fig. 4.9b and 4.10b), the particles of Al-H-ZSM-5 20 are obviously agglutinated, in a thicker look (Fig. 4.8b), with more intercrystalline spaces occupied by the binder compounds. Strikingly, this sample even became more severely agglutinated after the MTH reaction, and shown in a gel look in the SEM picture (Fig. 4.8c). Although more intercrystalline spaces have been lost after the MTH reaction, there is still certain amount of the edge-clear, visually shown isolated nano particles left in the Al-H-ZSM-5 60 and Al-H-ZSM-5 120 samples (Fig. 4.9c and 4.10c).

The above SEM images clearly reveal an unavoidable loss of surface area of the parent nano zeolites by the Al incorporation and the subsequent MTH reaction. This is in accord with our BET analysis results (Table. 4.1). All the Al-H-ZSM-5 samples lose about 10% surface area as compared with their parent nano zeolites. The spent catalysts' surface areas further decreased with coke formation, and the loss varied due

to different parent zeolite Si/Al ratios. Interestingly, there is only small difference between different unreacted Al-H-ZSM-5 samples (visually judged from the SEM picture, the Al-H-ZSM-5 sample would have lost more surface areas). Besides, comparison between extruded samples and their ground powders shows only negligible difference caused by 'shaping'. It appears that the loss of surface area is therefore mainly caused by the incorporation of binder phase. The surface areas of the employed binder precursor (Pseudo-boehmite, uncalcined) and the supposed binder phase (γ- Al_2O_3) were also measured; their much smaller surface areas provide further support for the above explanation.

Table. 4.1 BET surface area of the prepared samples

Pseudo-boehmite uncalcined 205.3 m^2/g, resultant after calcination 238.0 m^2/g

Sample name	Surface area m^2/g
nano H-ZSM-5 20 powder	399.9
nano H-ZSM-5 20 powder (post run)	202.9
Al H-ZSM-5 20 extrudate	364.6
Al H-ZSM-5 20 poweder (ground)	361.9
Al H-ZSM-5 20 extrudate (post run)	248.1
nano H-ZSM-5 60 powder	402.1
nano H-ZSM-5 60 powder (post run)	217.7
Al H-ZSM-5 60 extrudate	366.4
Al H-ZSM-5 60 poweder (ground)	360.8
Al H-ZSM-5 60 extrudate (post run)	284.4
nano H-ZSM-5 120 powder	403.3
nano H-ZSM-5 120 powder (post run)	234.4
Al H-ZSM-5 120 extrudate	356.8
Al H-ZSM-5 120 poweder (ground)	403.3
Al H-ZSM-5 120 extrudate (post run)	292.5

From calibration studies, the standard deviation of the measured parameter is set as unity in the last decimal. (e.g. 399.9 +/- 0.1)

The TEM images further confirmed the binding effect by the incorporated Al species. As shown in Fig. 4.11 (a-c), the Al binder phases, more transparent in the TEM image, homogenously spread over the surface of zeolite crystal particle, binding different particles, also partially filling the intercrystalline space. In the magnified vision (Fig. 4.12 a-c), the Al binder phases binding to the zeolite crystal edges are more clearly shown.

The post-run Al-H-ZSM-5 20 (Fig. 4.13a) exhibits more coking areas (black shadows in the picture) than the other two samples, which has been observed in multiple scans. It should also be noted that the observed coking zones are mostly located at (or near) the zeolite crystal edges (more obviously shown on the coked Al-H-ZSM-5 60 and coked Al-H-ZSM-5 120 samples, in Fig. 4.13b and Fig. 4.13c). Particularly, those areas are where the Al binder phases exist. It seems that the coke species show some preference to be deposited near the Al binders.

For a better understanding, we selectively choose another two TEM images in a '100nm' vision to show the difference between Al-H-ZSM-5 20 samples before and after MTH reaction (Fig. 4.14). It is very clearly illustrated in the pictures, due to the increased density as a result of the coke deposition, the coking areas on post-run (coked) sample are much darker, whereas the fresh, unreacted sample reveal good transparency in the TEM picture.

**Samples shown in the Fig. 4.11-4.13 are coked in the conditions of: 5h MTH reaction, 450 ^{o}C, 6bar, WHSV= 1.5h^{-1}.*

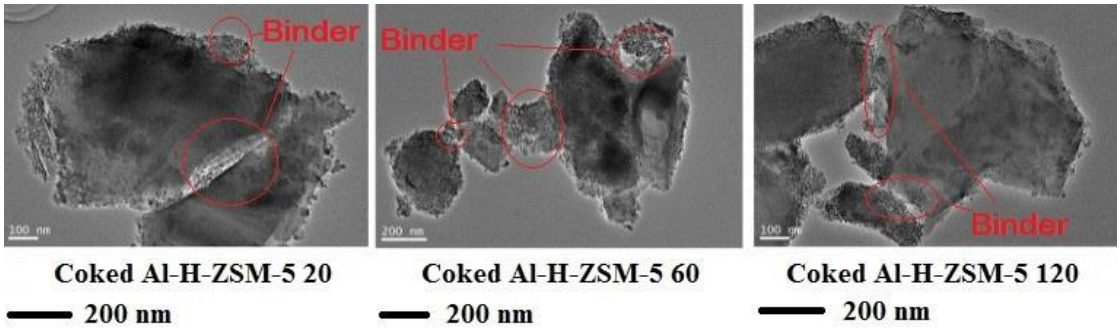

Fig. 4.11 (a-c, coked, Al-incorporated samples) TEM pictures show the Al binder phases (more transparently shown) binding the coked zeolite crystal particles (the coking areas are shown in black color).

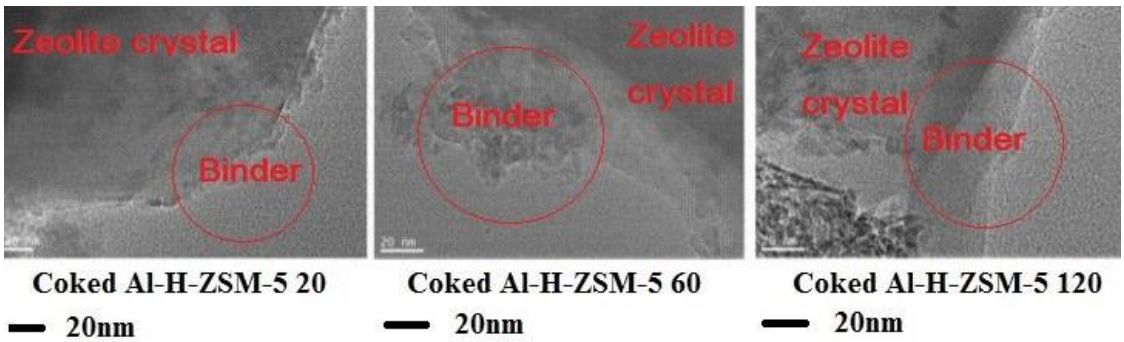

Fig. 4.12 (a-c, coked, Al-incorporated samples) The zeolite crystal edges are shown in a darker color, while the brighter, more transparent areas are the Al binder phases.

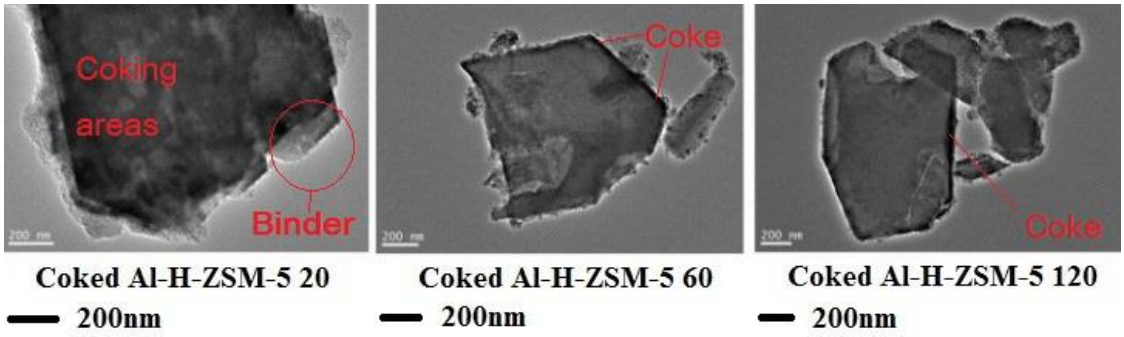

Fig. 4.13 (a-c, coked, Al-incorporated samples) TEM pictures show the coking zones (black shadows) covering the zeolite crystal surfaces, and preferably located at the crystal edges, and these locations are where the Al binder phases exist.

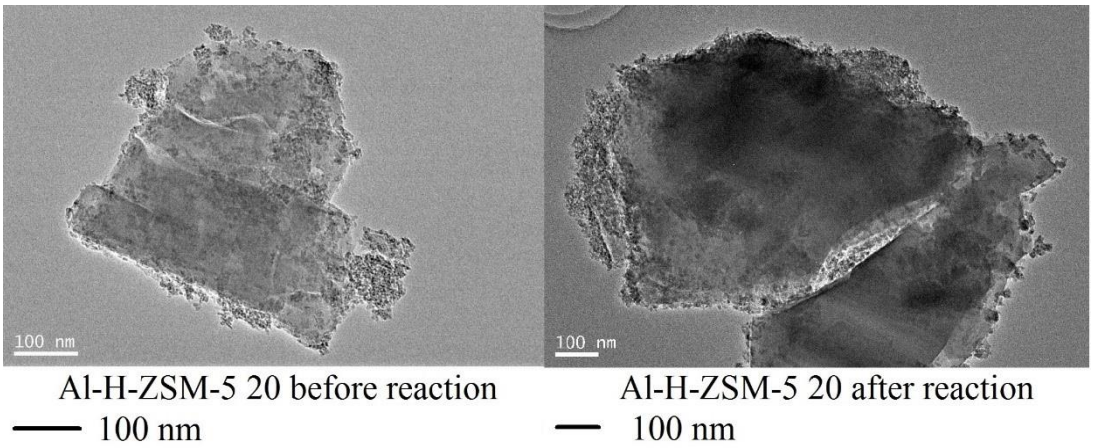

Fig. 4.14 Al-H-ZSM-5 before reaction in comparison with Al-H-ZSM-5 after reaction, the coking zones are shown in dark black color in the right picture. The sample shown on the right hand side is coked in the conditions of: 5h MTH reaction, 450 ^{o}C, 6bar, WHSV= 1.5h^{-1}.

4.3.4 XRD

In our XRD results (Fig. 4.15), the crystallites from Al-incorporated samples before and after MTH reaction are compared, and they all rest on a complexity of multiple crystal phases (there could be extra crystal phases induced by the Al incorporation), which is different from the parent zeolites (there is only zeolite crystal structure). Here the patterns of parent nano H-ZSM-5 60 and γ-Al_2O_3 are also presented for assessment of the potential changes on zeolite framework and identification of the potentially introduced new crystal phases.

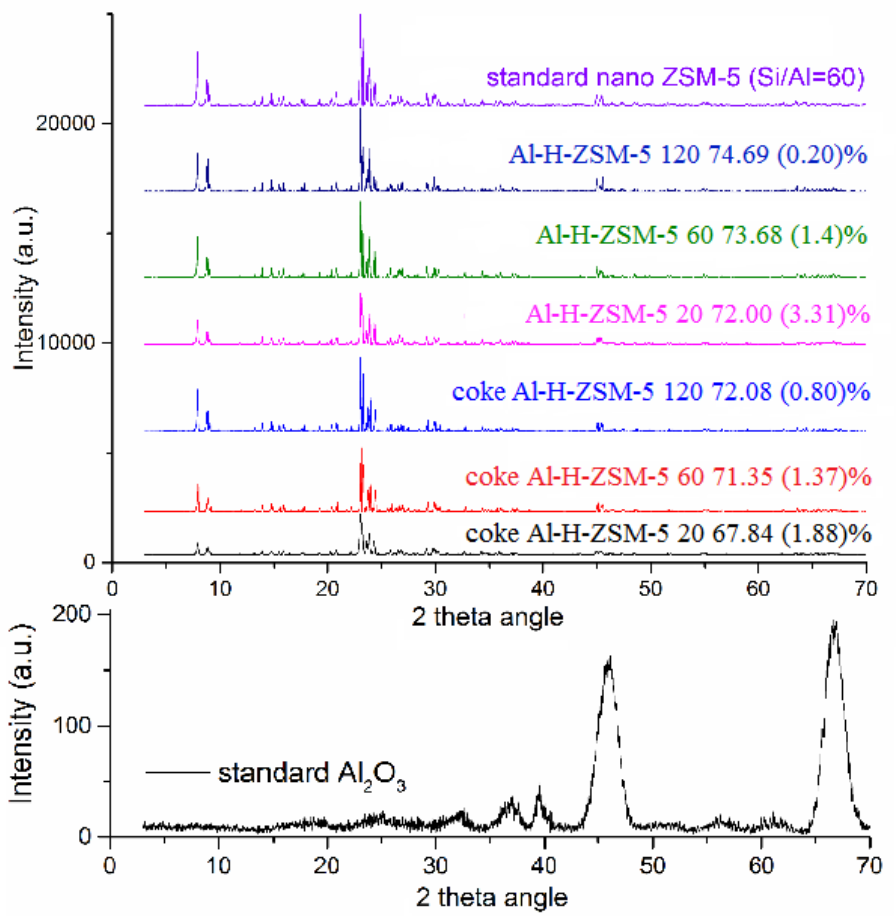

Fig. 4.15 X-ray diffraction of Al incorporated samples (fresh & coked), standard nano H-ZSM-5 (Si/Al=60) and γ-Al_2O_3 (Note the diffraction pattern of Al_2O_3 is amplified, for a straightforward comparison). Crystallinity calculation is correct to two decimal places, with possible error shown in the bracket.

For data treatments and relevant calculations, we use MDI-Jade (version 6.5) to measure the crystallinity of selected samples, based on the signals obtained from the 3 peaks most obviously shown in the XRD patterns (diffraction angles in 2θ: 23.06，23.26，and 24.31). [204]. All Al-incorporated samples possess somewhat good crystallinity (~70%), which does not vary significantly among different samples. There are also limited changes between the unreacted and coked samples, showing the zeolite crystal structures were well maintained during the MTH reaction, possibly protected by the incorporated Al phases. The Al-H-ZSM-5 20 sample showed the greatest loss in crystallinity after the MTH reaction, in somewhat agreement with the SEM results (Fig. 4.8c). This is possibly due to its highest coke deposition among all the Al-incorporated samples. Another possible explanation could be the reaction inner transformation of Al species between the zeolite framework and the binder phases (This may have proceeded most intensively on this sample as the parent H-ZSM-5 20 has the largest number of framework Al sites). This phenomenon assimilates the zeolite framework Al sites and the binder Al sites that are in similar structures, which may complement the zeolite Al sites during the MTH reaction, or, in some cases has resulted in the partial loss of zeolite framework (a negative effect), although there is still a relevant academic controversy. [11, 199, 200]

Interestingly, no peaks representing the crystal phase γ-Al_2O_3 are seen in the above results. However, in the amplified XRD patterns (Fig. 4.16), the diffraction peak at 2 theta = 67.3, characteristic of the crystal γ - Al_2O_3 is observable, although the obtained signal possesses a very poor intensity (the standard H-ZSM-5 also

exhibits weak diffraction peaks at this position, giving some difficulty in specification). [205] In this case, coked Al-H-ZSM-5 samples show much stronger signals than the unreacted samples, while the related peak is more apparently shown for the Al-H-ZSM-5 20 sample as compared with other two unreacted samples. Based on the combined XRD and SEM results, we propose that a well-developed dispersion of γ - Al_2O_3 as binder phase in the catalyst system has been achieved. The Al_2O_3 crystal phase did emerge after extrusion in a very small amount (more are dispersed in amorphous status), which, interestingly, became even more apparent after the MTH reaction.

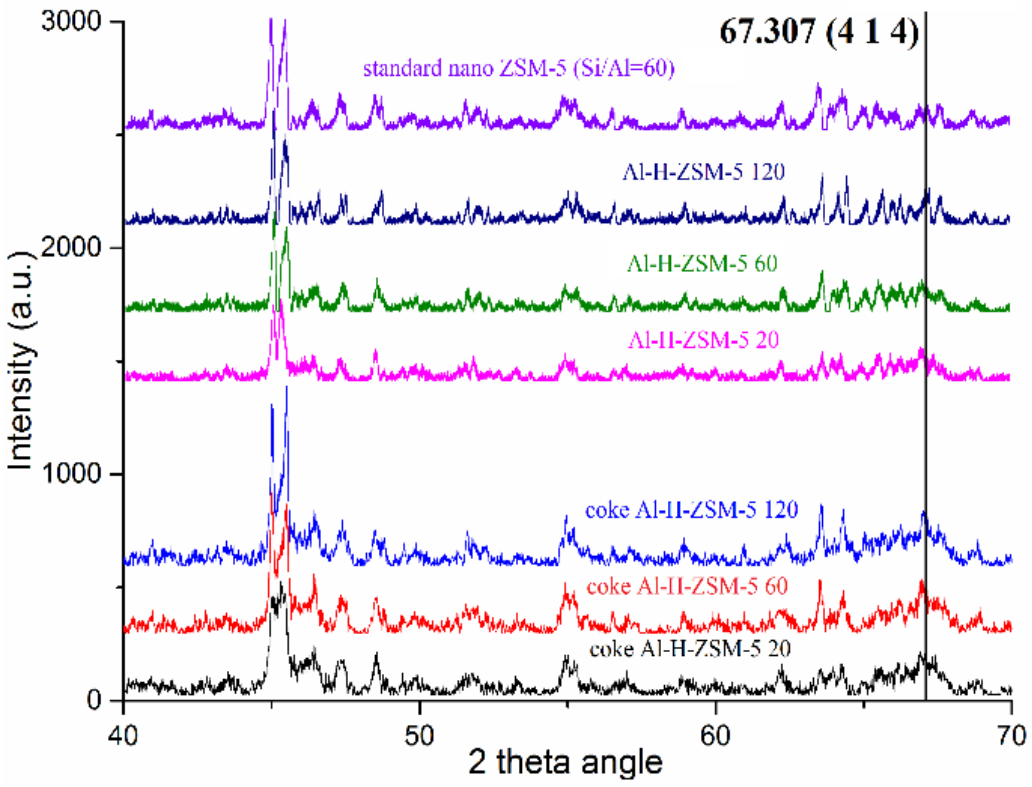

Fig. 4.16 Amplified XRD patterns focusing an angle range of 40-70 (2 theta)

4.3.5 ^{27}Al and ^{29}Si NMR

^{27}Al NMR spectra

^{27}Al NMR spectra of parent nano H-ZSM-5 zeolites (before reaction and coked) and Al-H-ZSM-5 samples (before reaction and coked) are illustrated in Fig. 4.17.

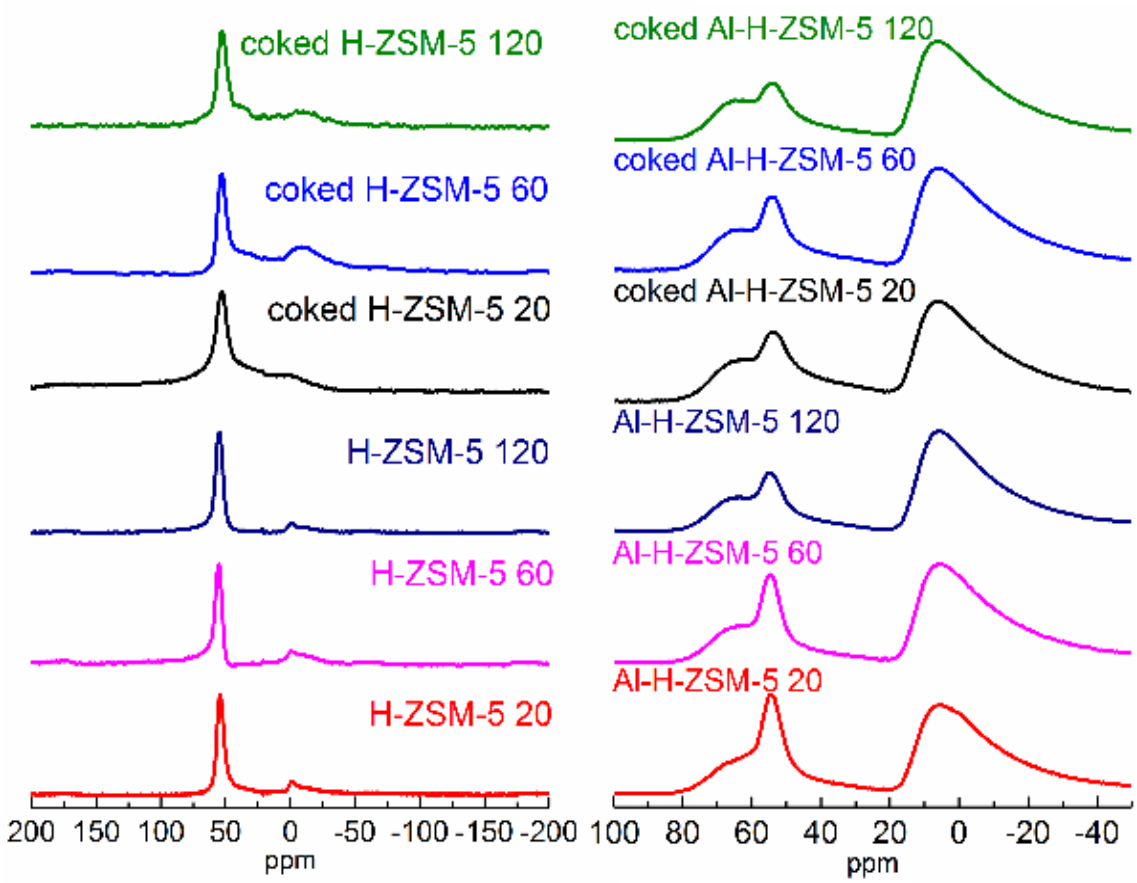

Fig. 4.17a (left) ^{27}Al NMR spectra of parent nano H-ZSM-5 zeolites (before reaction and coked); and b (right) ^{27}Al NMR spectra of Al-H-ZSM-5 samples (before reaction and coked)

All parent nano H-ZSM-5 zeolites have shown the peaks representing the tetrahedrally coordinated zeolite framework aluminium (55 ppm) and the peaks representing the octahedrally coordinated extra-framework aluminium (0ppm). [196] The 55 ppm peak intensity is obviously stronger than the one at 0ppm.

Coking of parent zeolites produces a small diminution of the signals at 55ppm, while broadening the peaks at 0 ppm. The broadening effect is more obviously shown on the coked H-ZSM-5 20 zeolite, as the 0ppm peak is somewhat flattened in the spectra. The 55ppm peaks are reduced in height in the spectra of Al-H-ZSM-5 samples but have broadened, with a newly observed shoulder at 70 ppm assigned to the tetrahedrally coordinated extra-framework Al sites normally seen in $\gamma - Al_2O_3$. [205] The formation of $\gamma - Al_2O_3$ in Al-incorporated samples is better supported by a newly emerged, much stronger peak centred at 12ppm, which is assigned to the chemical shift of framework Al sites in $\gamma - Al_2O_3$ (Al atoms octahedrally coordinated by oxygen in $\gamma - Al_2O_3$). As a result, the peak at 0 ppm related to the zeolite extra-framework Al is overlapped by this newly formed huge peak.

By comparing the signal intensities (e.g. peak height) of peaks at 55 ppm and 12 ppm, the concentration of zeolite framework Al in those Al-incorporated samples can be roughly estimated. It seems that the difference is mainly determined by the parent zeolite Si/Al ratio. The height of peak at 55ppm gradually decreases as the Al-incorporated sample's parent zeolite Si/Al ratio goes up from 20 to 120, in both unreacted and coked groups.

The observed results reveal a well combination of the newly introduced Al phases with the parent zeolite Al sites. The newly formed $\gamma - Al_2O_3$ phase very effectively binds the zeolite nano particles, fully filling the interconnecting intercrystalline spaces, more homogenously spreads over the zeolite particle surface, rather than coagulating,

in crystals (the XRD response of $\gamma - Al_2O_3$ is so poor in strong contrast to the corresponding ^{27}Al NMR signals).

Although those zeolite Al sites have been 'diluted' in the above case, a possible complement from the introduced Al binder phases might have occurred. Also as has been mentioned in the above XRD results discussions, there have been some work suggesting an Al migration/transfer that occurs in the catalyst preparation and later catalytic process by which the binder framework Al (12ppm, octahedrally coordinated) could be transferred into the zeolite framework Al (55ppm, tetrahedrally coordinated), possibly through a transition state of binder extra-framework Al (70ppm, tetrahedrally coordinated), and the presence of Al binder was observed to lead to significant enhancement of catalytic activity and reaction stability in many acid zeolite catalysed reactions. [11, 27, 199, 200]

As has been pointed out earlier, 55ppm peaks are not increased in intensity in the spectra of Al-H-ZSM-5 samples, but exhibit a degree of peak broadening. Here the transfer of Al between binder framework and zeolite framework is not a simple, direct complement of the zeolite framework Al sites (55ppm). The broadening at 55ppm implies that more tetrahedrally coordinated Al sites are formed in the zeolite structure. They could exist either in the zeolite framework (55ppm), or outside (reflected by the broadening of 55ppm peak). Here the binder Al sites corresponding to the 77ppm peak, which also possess a tetrahedrally coordinated structure could be the best transition state before these newly formed, tetrahedrally coordinated zeolite Al sites. Although the consumption of binder framework Al sites (12ppm) is not clearly shown

(this is due to the huge peak at this position), the emergence of 70ppm peak, and the accompanied broadening on 55ppm peak do suggest a potential transformation, firstly from the binder framework Al (12ppm) to the binder extra-framework Al (70ppm), then to the tetrahedrally coordinated zeolite extra-framework Al (reflected by the broadening of 55ppm peak), and finally to the zeolite framework Al (55ppm). The two types of Al atoms (55ppm and 70ppm) are all tetrahedrally coordinated with oxygens, and the overlapping of their peaks in the NMR spectra reveals an easy transformation.

The spectra of 3 coked Al-incorporated samples are quite similar, it seems that the distribution of different Al sites in these samples have been somewhat stabilized. Here a 'pool of tetrahedrally coordinated Al' may exist as a result of the Al incorporation. Coking reduces the signal intensity at 55ppm as the coke species cover the zeolite Brønsted acid sites (these are zeolite framework Al sites) and lead to their chemical environment changes. On the other hand, the zeolite framework Al could be complemented from the potentially existed 'tetrahedrally coordinated Al pool'. Such a pool may balance the Al distributions between binder phases and zeolite, which happens in many cases such as the catalyst preparation, or varies of reactions. Besides, we propose the Al species in such a pool could be mostly located at the zeolite boundaries, as shown in the EM pictures, binding the zeolite crystal particles. The above hypothesis goes some way in explaining the ^{27}Al NMR spectra, and is also supported by similar studies in the literatures. [11, 199, 200]

^{29}Si NMR spectra

All the samples involved in this research give intense signals in the ^{29}Si NMR spectra (Fig. 4.18a and 4.18b).

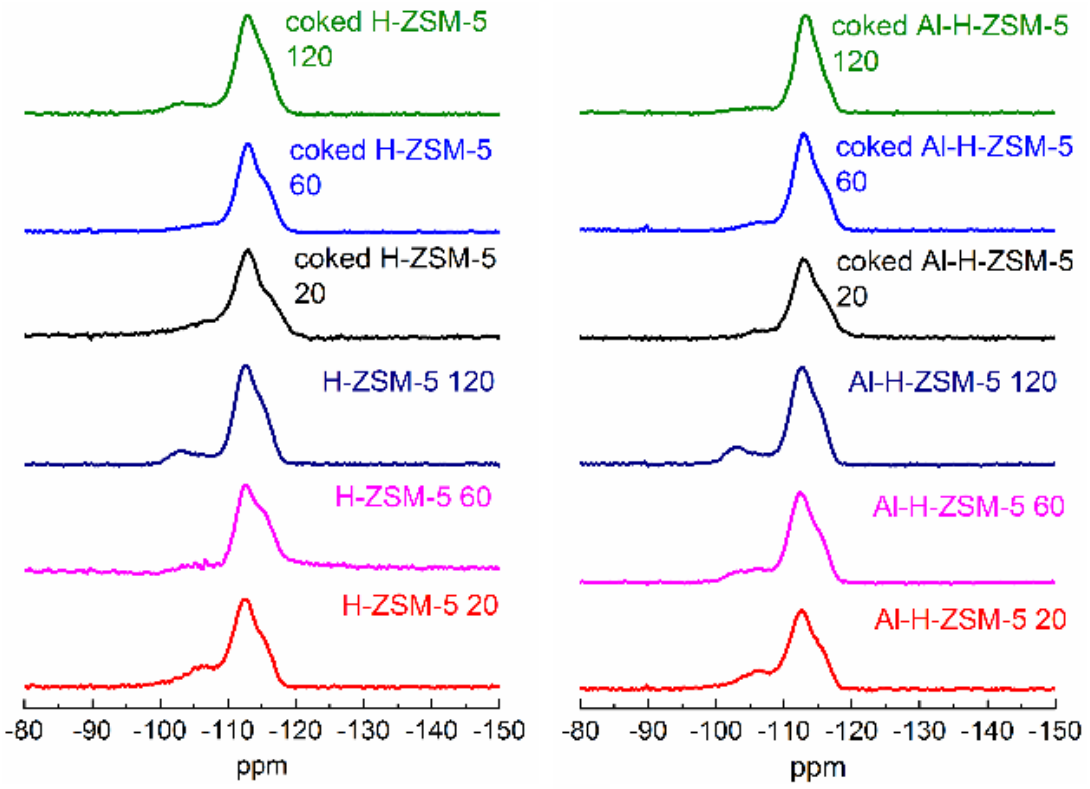

Fig. 4.18a (left) ^{29}Si NMR spectra of parent H-ZSM-5 zeolites (unreacted and coked); and b (right) ^{29}Si NMR spectra of Al-H-ZSM-5 samples (unreacted and coked)

The ^{29}Si NMR spectra are quite similar among different samples. However, the lower intensity, high frequency part of the bandshape (-110 to -100ppm) does vary noticeably. From detailed deconvolutions, either 3 or 4 lines in an unconstrained fit have been attempted. While each simulation appears to represent the overall bandshape, the results are quite variable. Typical deconvoluted spectra of each sample are shown in the Fig. 4.19-4.21.

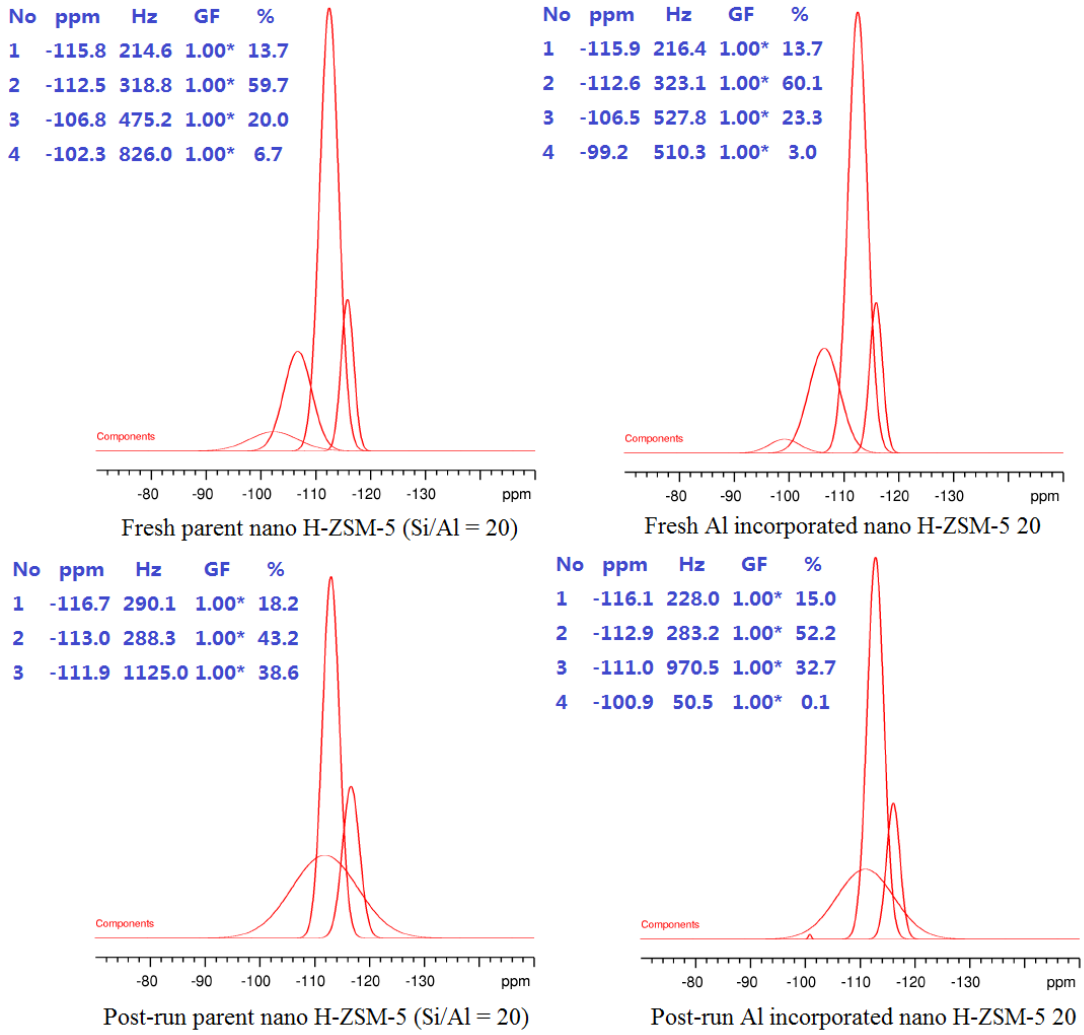

Fig. 4.19 de-convoluted ^{29}Si NMR spectra of samples based on nano H-ZSM-5 (Si/Al=20)

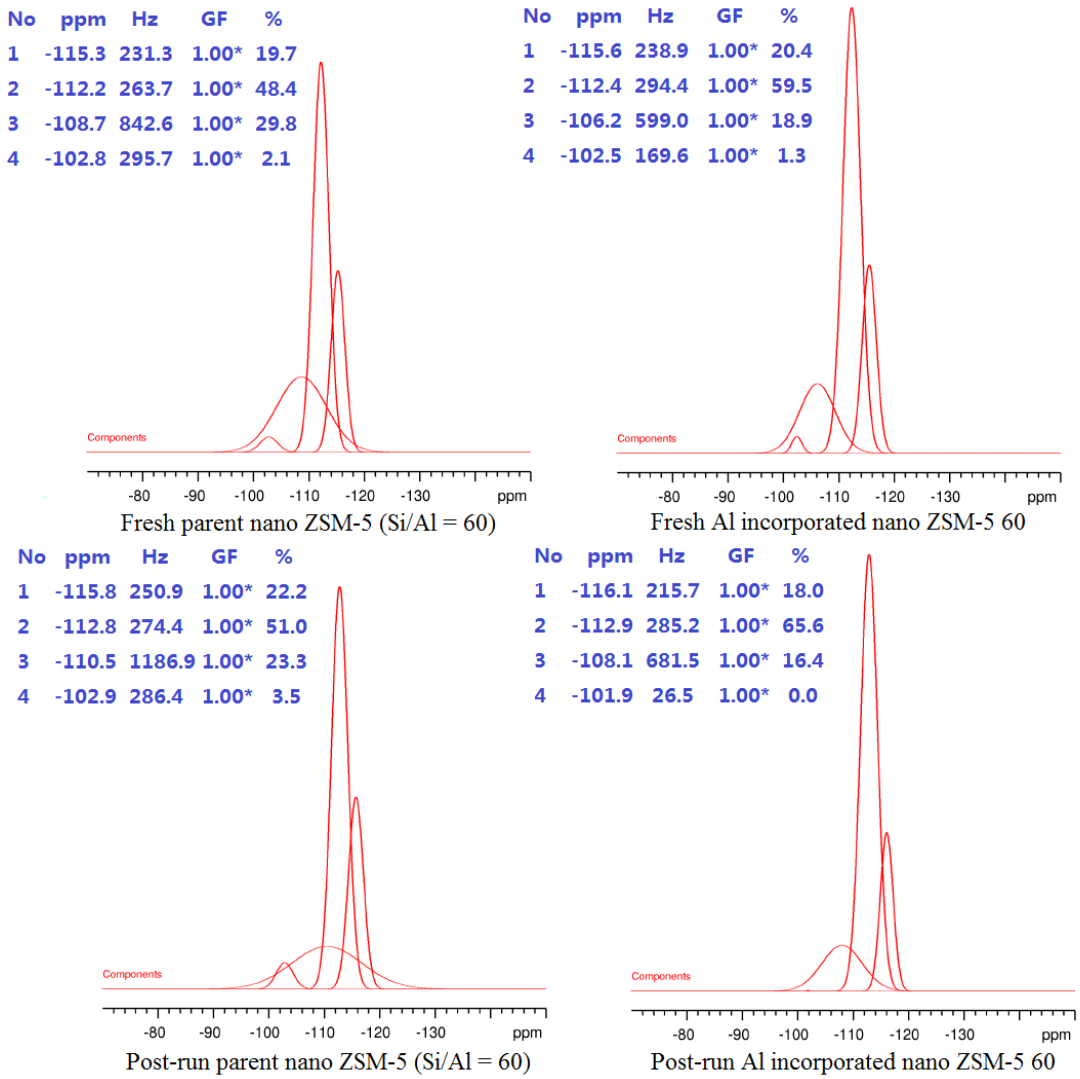

Fig. 4.20 de-convoluted ^{29}Si NMR spectra of samples based on nano H-ZSM-5 (Si/Al=60)

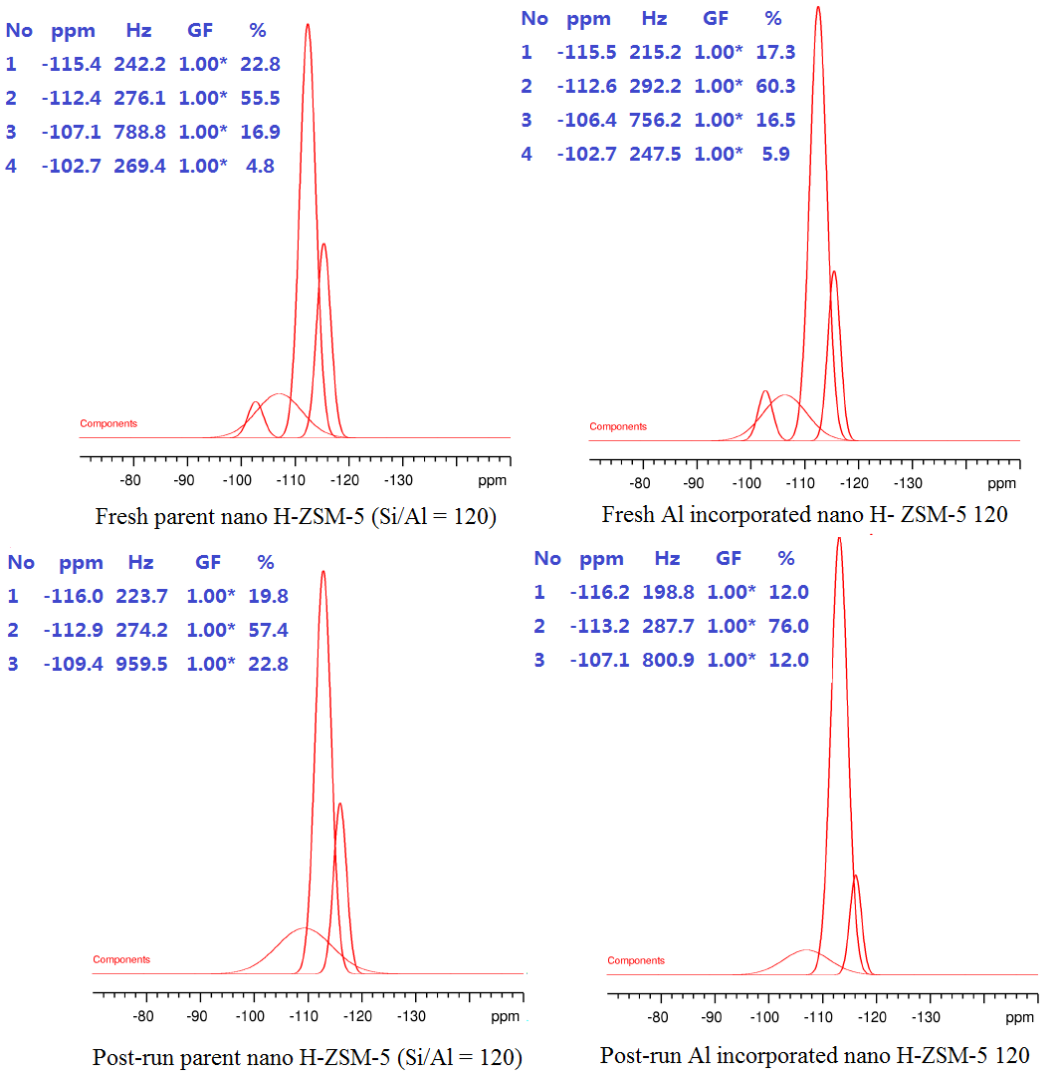

Fig. 4.21 de-convoluted ^{29}Si NMR spectra of samples based on nano H-ZSM-5 (Si/Al=120)

All unreacted samples possess a deconvoluted peak at round -106ppm, which corresponds to the Brønsted acid sites (Si-Al-OH, 3Si:1Al) in the zeolite framework (they are also the zeolite framework Al sites). [206] This peak disappeared after the MTH reaction as observed on most post-run samples; instead, a peak at around -111ppm emerged. Here we attribute the newly presented -111ppm peak to those Brønsted acid sites that are covered by the reaction formed coke species. The signal intensity of this peak ('%' in the total peak area integration, as shown in Table. 4.2) reflects the coke deposition on a particular sample, and is noted to increase with a smaller parent zeolite Si/Al ratio, in both H-ZSM-5 (post-run) and Al-H-ZSM-5 (post-run) groups. Here a smaller zeolite Si/Al ratio indicates more Brønsted acid sites in the parent H-ZSM-5 zeolite, so as its corresponding Al-incorporated sample (this is also confirmed by our NH_3-TPD results, as shown in Fig. 4.7). It has been noted that zeolite catalysts with more Brønsted acid sites form more coke species in most reactions, and this can well explain the above observations. [9, 15]

Table 4.2 signal intensity of chemical shifts at around -106 ppm, and -111ppm

Samples	at around -106 ppm	at around -111 ppm
H-ZSM-5 20	29.8% (-108.7 ppm)	no signal
H-ZSM-5 60	20.0% (-106.8 ppm)	no signal
H-ZSM-5 120	16.9% (-107.1 ppm)	no signal
Al-H-ZSM-5 20	23.3% (-106.5 ppm)	no signal
Al-H-ZSM-5 60	18.9% (-106.2 ppm)	no signal
Al-H-ZSM-5 120	16.5% (-106.4 ppm)	no signal
H-ZSM-5 20 post-run	no signal	38.6% (-111.9 ppm)
H-ZSM-5 60 post-run	no signal	23.3% (-110.5 ppm)
H-ZSM-5 120 post-run	no signal	22.8% (-109.4 ppm)
Al-H-ZSM-5 20 post-run	no signal	32.7% (-111.9 ppm)
Al-H-ZSM-5 60 post-run	16.4% (-108.1 ppm)	no signal
Al-H-ZSM-5 120 post-run	12.0% (-107.1 ppm)	no signal

Interestingly, no peak around -111ppm is observed in the spectra of Al-H-ZSM-5 60 (post-run) and Al-H-ZSM-5 120 (post-run). Instead, there have been observed slight shifts of the -106ppm peak to -108ppm, and -107ppm, respectively, which shows there are only limited changes of the chemical environment of the zeolite framework Al after the MTH reactions. The most likely explanation could be the zeolite framework Brønsted acid sites were well protected by the incorporated Al binders from being 'consumed' by the reaction formed coke species. Such 'protection', may arise from a complement of the zeolite framework Al from the above mentioned pool of tetrahedrally coordinated Al, or, there have been some reports on the selective dispersion of coke species on the incorporated Al binders, which also effectively avoids the coke accumulation on zeolite framework. [10-12, 15, 27, 199, 200]

It should be noted that the deconvolution of ^{29}Si spectra is a supplementary to the explanations on observed catalysis and zeolite structure changes. The exact deconvolution results may vary among different calculations where errors are allowed in a restricted range. The data presented are obtained by colleagues from National NMR laboratory at Durham University (funded by EPSRC).

4.3.6 Studies on catalyst deactivation and coke formation

The coke species generated in the reaction were studied by the Cross-Polarization (CP) ^{13}C NMR (Fig. 4.22), FT-IR (Fig. 4.23, and 4.24 a-b), and Laser-Raman (Fig. 4.25) techniques, targeting on the identification of different coke deposits formed on the catalyst surface; the total coke amount was evaluated with TGA analysis.

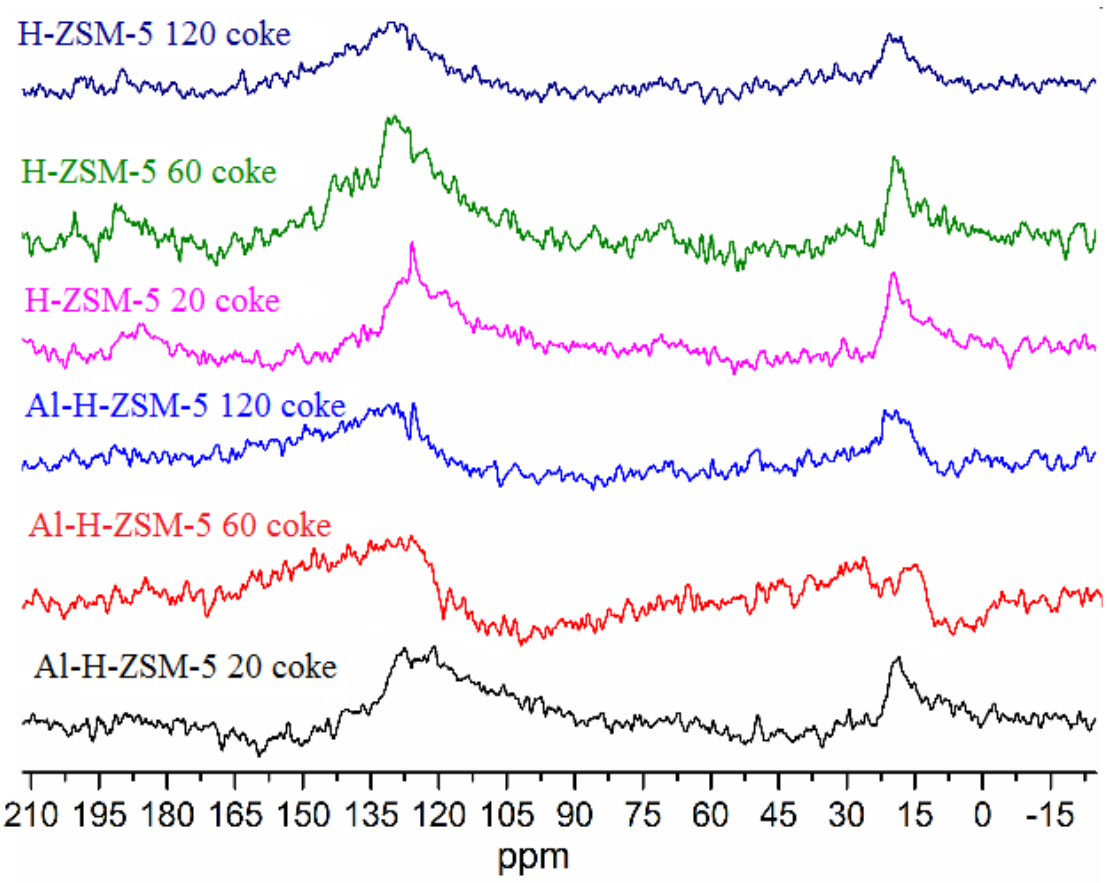

Fig. 4.22 CP ^{13}C NMR spectra of coked samples after MTH reaction

Regarding ^{13}C NMR, the only limitation, i.e. the low natural abundance of the ^{13}C isotope (only 1.1%), can be avoided by the use of ^{13}C enriched reactants and/or by the CP technique. [12] There is relatively small amount of carbon in the post–run samples

but the ^{13}C NMR signal can be boosted by the CP technique. The most obvious signal appears to be from the methylated aromatic species (a broad region mainly characteristic of benzene, toluene, and xylenes, highlighted at around 129 ppm), and with stronger intensity for those post-run pure zeolites (there is a very sharp peak at 129 ppm in the spectra of coked H-ZSM-5 20). [207] In each case, the aromatic residues also exhibit weak spinning sidebands at 70 and 190 ppm, and again, more clearly observed for those coked pure zeolite samples. On the other hand, organic residues on the coked samples also show a broad aliphatic/olefinic product distribution with chemical shifts between 10-40 ppm, where signals appear to be mainly from the CH_2/CH_3 groups. [208] In this case, it is noted the post-run parent nano zeolites and coked Al-H-ZSM-5 20 mainly possess C_3 based (propane and propylene) carbonaceous deposits with resonance bands between 15-17 ppm. [207] In comparison, aliphatic/olefinic coke species on other Al-H-ZSM-5 samples (60 and 120) show more favourite to the C_4 based compounds. Spectra of these two samples exhibit a broadening tail of the peak at 17 ppm, extended to 40 ppm. The observed NMR bands suggest a possible accumulation of n-butane (13.4 and 25.9 ppm) and/or isobutene (24.3 and 25.9 ppm) species on the catalyst external surface. [209] It should also be noted that there are also resonances observed at higher chemical shifts characteristic of heavier linear/branched olefins (shown by the bands at 150-170 ppm) in the spectra of the above two samples (Al-ZSM-5 60, and 120). [207] The above ^{13}C NMR results have indicated different coke/precursors distributions on pure zeolites and their Al-incorporated derivate. The pure zeolites focus more on the yield of

aromatics, with essential accumulation of light olefins, while the Al-incorporated samples show more preference on the deposition of olefins and light aliphatic products. The Si/Al ratio of the parent zeolites also leads to some difference for samples in the same group.

FT-IR was also employed for coke analysis in the present research. A general scan of all coked samples is presented in the Fig. 4.23, showing well maintained zeolite structure of those Al-incorporated samples even after the reaction.

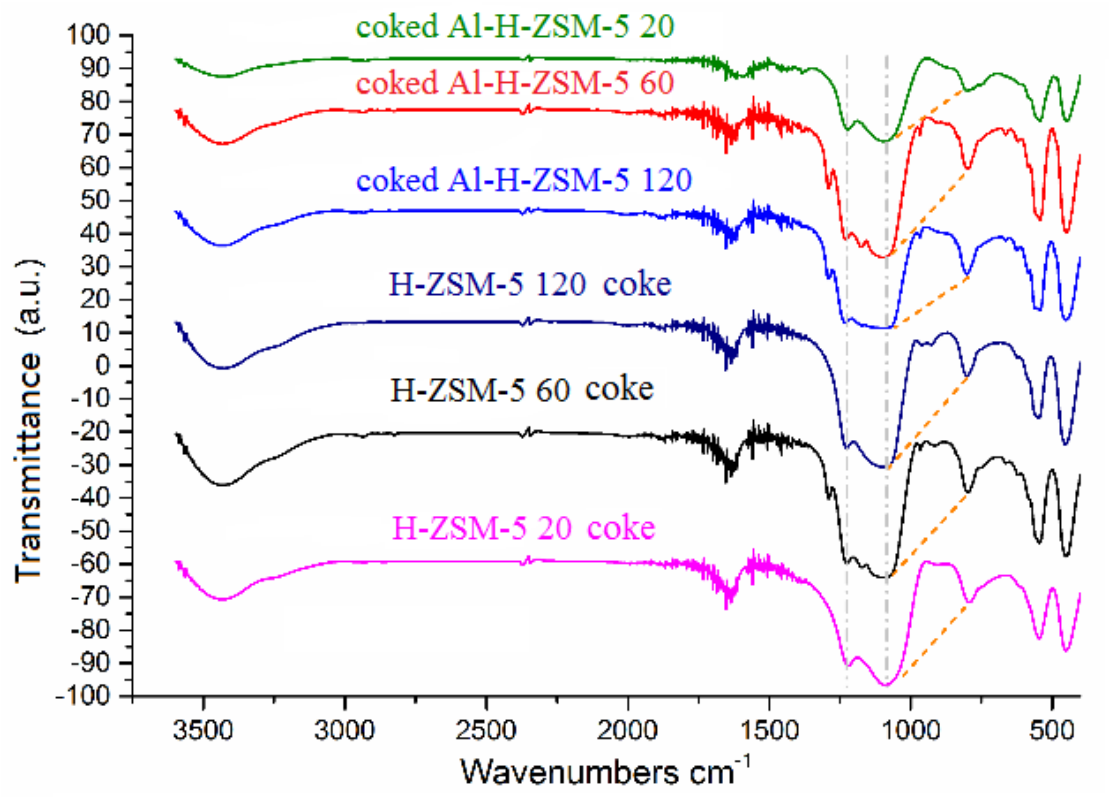

Fig. 4.23 FT-IR spectra (3500-400 cm^{-1}) of all coked samples

Further study was carried out for a further specification of coke species and their precursors deposited (Fig. 4.24a, 3500-2000 cm^{-1}; and Fig. 4.24b, 2500-1200 cm^{-1}).

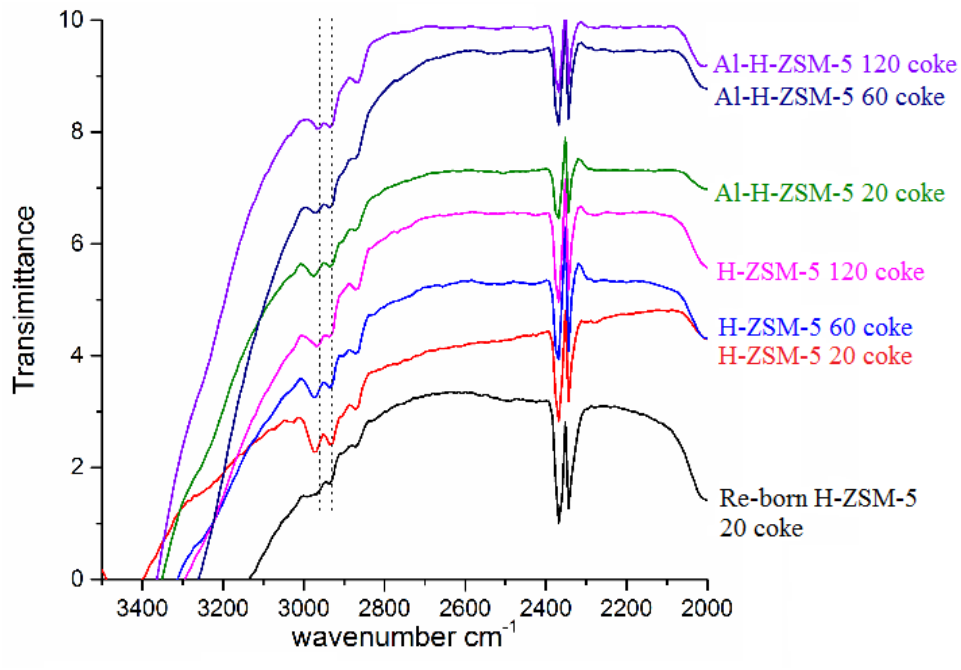

Fig. 4.24a FT-IR spectra of all coked samples (3500-2000 cm^{-1})

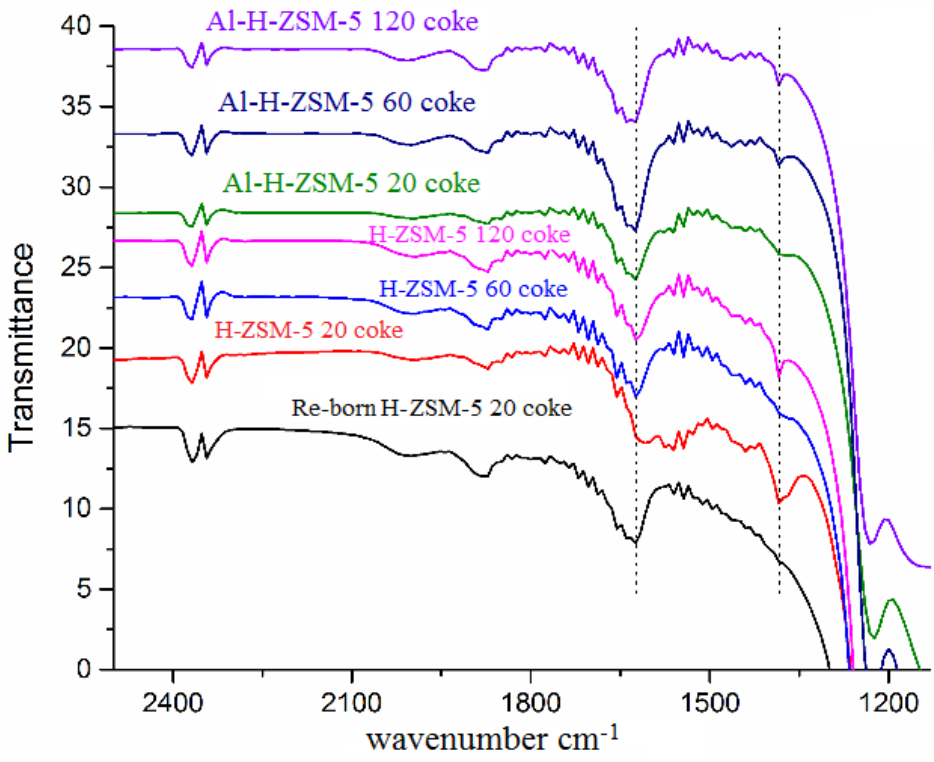

Fig. 4.24b FT-IR spectra of all coked samples (2500-1200 cm^{-1})

In the Fig. 4.24a, the bands at about 2900 cm^{-1} and 2825 cm^{-1} are ascribed to the stretch mode of methyl groups on the aromatic ring structure, and their occurrence was in accordance with the methylated benzenes (toluene, xylenes) adsorbed on

zeolites in previous researches (calcination in air also leads to their disappearance, as observed on the reborn sample). [210-212] The accumulation of these surficial aromatics is one of the most important reasons for the catalyst deactivation as they are the major component/precursor of the coke species. [9] Our findings reveal a Si/Al ratio dependent (as shown in Fig. 4.24a, aromatics deposition increases with smaller parent zeolite Si/Al ratio) aromatics accumulation during the MTH process, for both the parent zeolites and the Al-incorporated samples. Also in accordance with the above ^{13}C NMR results (Fig. 4.22), the coked parent zeolites generally possess stronger aromatics signals than the coked Al-incorporated samples. The bands of 1300-1700 cm^{-1} in the FT-IR spectra can be associated with the C-C stretching modes of unsaturated (olefinic, polyenyl, aromatic, polyaromatic) function groups and the CH bending mode of paraffinic groups. [12, 213] In the Fig. 4.24b, only the spectra of coked nano H-ZSM-5 20 shows apparently enhanced signals in these bands, in a strong comparison with other coked samples and especially its reborn sample (the coking species are removed by calcination in air at 550 ℃).

The above FT-IR data suggest more apparent coke formation occurred on the parent nano zeolites, in the observed MTH reaction, and also decreased with their zeolite framework Si/Al ratio; this is also supported by the previous studies. [9, 12, 15, 214] It should be noted that a larger than usual catalyst loading, and reduced methanol feeding rate were applied in this research; and even under such mild reaction conditions, the incorporation of Al binders were also observed to effectively reduce the chance of coke formation. Not surprisingly, this gifted coke tolerance is supposed

to work since the beginning of the reaction, and will affect the subsequent MTH process.

Of course, our results are for completed catalytic reactions and there is a clear need for a further investigation into the zeolite framework changes and especially the corresponding influences on zeolite hydroxyl groups (-OH), which are as a result of the coke formation. However, limitations such as a lack of the in-situ instrument have restricted such explorations and we will put this work into a short time future work. In fact, the above comprehensive NH_3-TPD (zeolite acidity) and solid state NMR (framework change) studies have somehow well complemented the related gaps.

Coke nature in our experiments was also illustrated by the Laser-Raman spectroscopy as shown in Fig. 4.25.

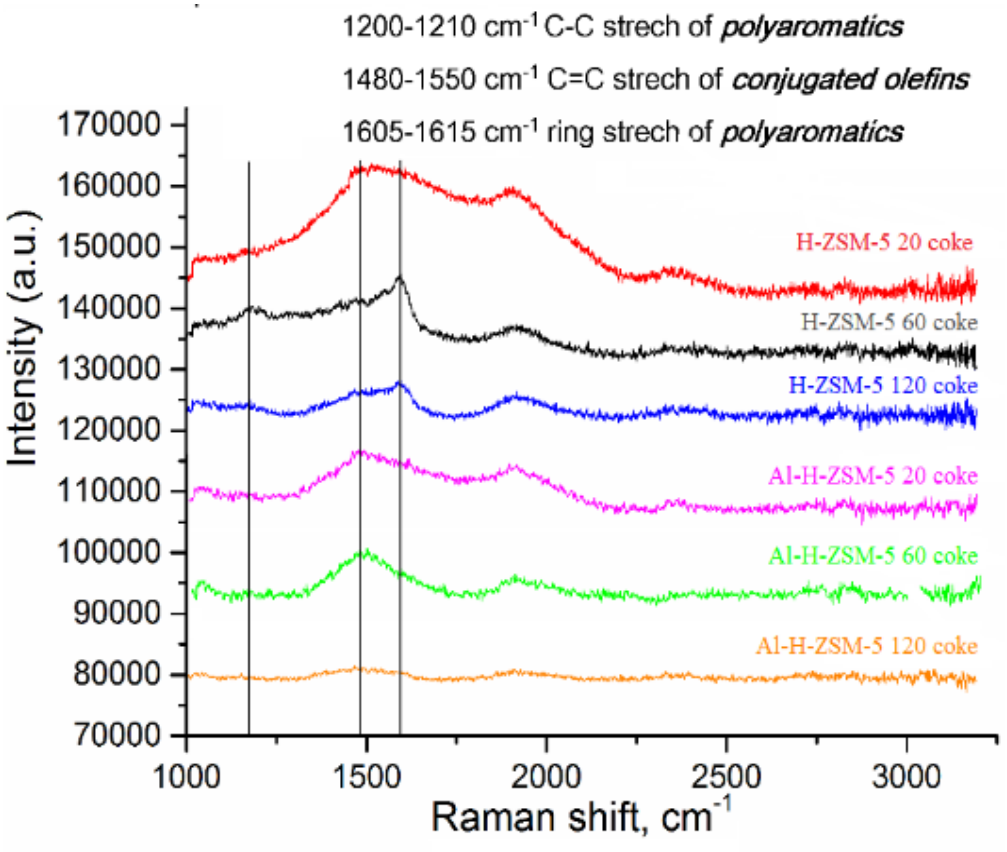

Fig. 4.25 Laser Raman spectra of coked samples

The Raman bands at 1400-1650 cm^{-1} are attributed to the typical carbonaceous depositions formed on the zeolite surface (the exact band positions may vary in different researches), [215] The 1605-1615 cm^{-1} band (Graphite band or 'G-band') associated to the ring stretches of aromatic molecules is clearly observed on those coked parent zeolites. [216, 217] This signal highlighted at 1605 cm^{-1} raised a sharp peak in the spectra of the coked H-ZSM-5 60 and H-ZSM-5 120 samples, although for the coked H-ZSM-5 20 sample, the expected peak at the same position is definitely covered (shown in a more flat shape, but ^{13}C NMR spectra of this sample shows a sharp aromatic peak) by the greatly enhanced overlapping signals (this also demonstrates a much severer coke formation on this sample). On the other hand, the spectra of the coked parent zeolites also show slightly enhanced signals at the bands of 1200-1210 cm^{-1}, which is associated to the C-C stretch of the poly aromatics pointed by previous studies. [216] The above spectral evidences reveal a fact that there were more aromatic based coke species deposited on those coked parent zeolites, further supporting the FT-IR (Fig.4.24a and 4.24b) and ^{13}C NMR (Fig. 4.22) data. In comparison, for the coked Al-incorporated catalysts we observed apparently enhanced signals at bands of 1480-1550 cm^{-1}, as shown by the rising peak centred at about 1480 cm^{-1} in the Raman spectra. This peak (more obvious for the Al H-ZSM-5 20 and Al H-ZSM-5 60 samples) has been assigned to the C=C stretching vibration of the conjugated olefins (or polyenes), with extended tail shifting towards to the bigger wavenumber bands (1545-1550 cm^{-1}) also considered as the evidence for the deposited olefinic compounds. [12, 216] The observed Raman spectra, again, further

confirm the difference in selectivity to various coke species between the pure zeolites and Al-incorporated samples, showing the preference to aromatic based coke species of the parent zeolites and the favouritism of olefinic (non-aromatic) coke species by the Al-incorporated samples.

The TGA results (Fig. 4.26) show the total amount of coke formation over individual samples, which is also determined by the parent zeolite Si/Al ratio in both sample groups. Here the coke resistance by the incorporated Al species is also reflected by the much lower coke deposition levels in the Al-H-ZSM-5 samples.

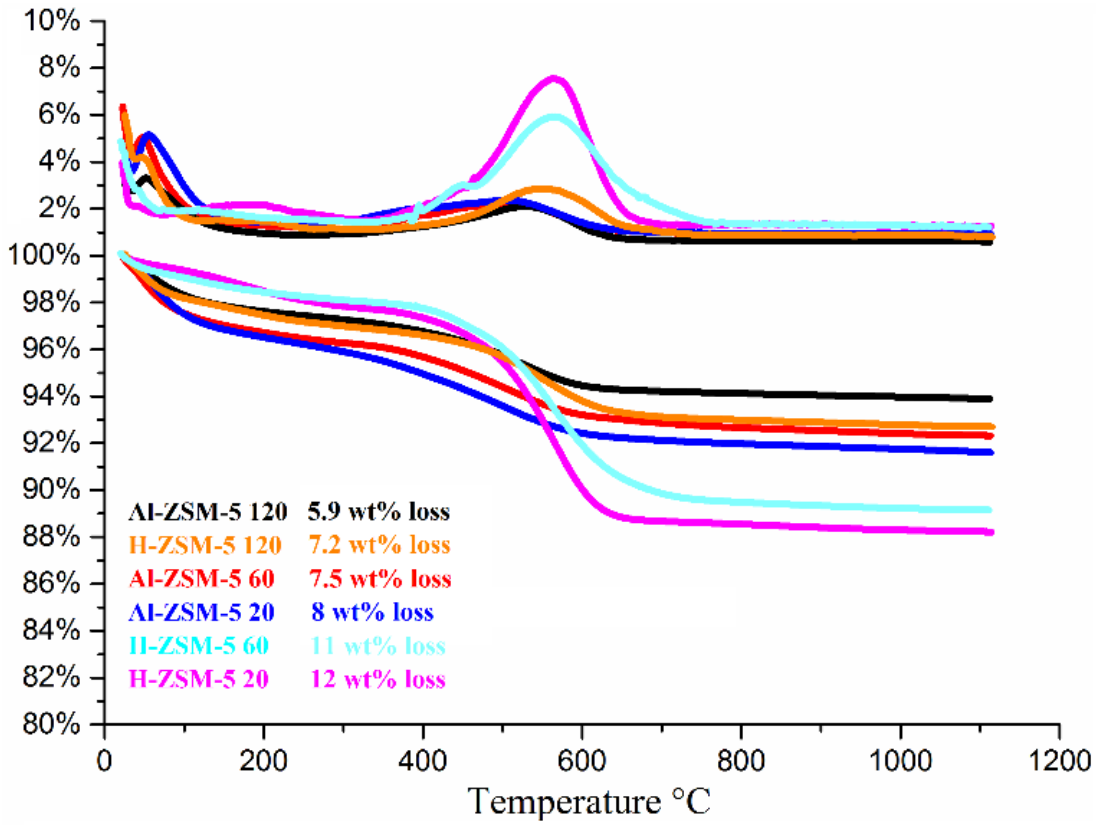

Fig. 4.26 Thermogravimetric analysis (TGA) plot of the post-reaction samples (bottom), and corresponding derivative thermogravimetry (DTG) curves (top)

In the above TGA results, the most obvious changes starting at about 625 ℃ in the curves (also clearly shown by the derivative thermogravimetry 'DTG' peaks at the same position) are mainly due to the coke species formed at higher temperatures (450 ℃ and higher), with large portion of aromatics. [12] Again, they are more apparently observed on those parent H-ZSM-5 zeolites.

Further investigation into the changes of catalyst porous and surface properties carried out with the BET analysis, and the results are shown in the above Table. 4.1. The original H-ZSM-5 nano zeolites lost more surface areas than the Al incorporated samples; again, the extent to which surface areas were lost for a special sample is also determined by the Si/Al ratio of the parent zeolite, this happens in both groups.

4.4 Conclusion

Based on the above observations, we believe that the major catalytic activities of shaped Al-incorporated nano H-ZSM-5 catalysts, for efficient methanol conversion processes, are mainly dependent upon the amount of Brønsted acid sites in the zeolite framework, which is determined by the Si/Al ratio of the parent zeolite. However, the incorporated Al binders have unique impacts on the time-on-stream gas olefin yields. The obtained catalytic properties rely on a delayed H_2 transfer process, which is possibly due to the incorporated Al cations. The key findings herein, are that this co-catalysis by the zeolite and binder phases would considerably adjust the early time MTH performance leading to a higher yield of the gas olefins which would definitely affect the subsequent long term reaction behaviours. The protecting effects on the Brønsted acid sites by the incorporated Al binders are attributed to a potentially existing pool of tetrahedrally coordinated Al. The Al binder phases also help to prevent coke accumulation on catalytic sites by efficient dispersion of coke species, also observed in the TEM pictures. Coke formation over different sample groups is various, but we have shown a favourite of aromatics on the parent H-ZSM-5 zeolites, and a preference to olefinic species on the Al-incorporated samples.

Our experimental design based on an amplified fixed-bed reactor is a step towards a larger-scale catalyst test more relevant for any subsequent industrial implementation of nano zeolites. With the detailed study on coke distributions, we also completed some relatively unexplored areas in the MTH research.

Chapter 5 Measuring coke formation on acid zeolite catalysts by microwaves

5.1 Summary

Progressive and unavoidable coke formation leading to the deactivation of solid acid catalyst (e.g. zeolite) is a ubiquitous problem in the modern petrochemical and energy-transformation industries. To date, various electromagnetic-based techniques have been applied in coke analysis and these include Infrared, Ultraviolet-Visible, Laser-Raman, and NMR spectroscopies, etc. However powerful these techniques are in characterizing the nature of coke formation, none possesses the attributes of a complete-sample volumetric interrogation while also exhibiting high sensitivity to any deeply dehydrogenated coke species. Here we report a novel approach based on microwave absorption measurement (microwave cavity perturbation analysis) and its application to effectively interrogate both the amount and the chemical composition of catalytic coke deposition in acidic zeolites. The employed straightforward cavity (axially polarized electric field antinode in a TM_{010} mode) can rapidly and non–intrusively (contact-less) measure the coked zeolites (achieved by methanol conversion) with full-sample-body penetration (volumetrically). Data are presented across a wide range of coking levels based on different coke compositions, and the signal sensitivity is characteristic of particular coke species with obviously enhanced response to those deeper dehydrogenated coke compounds (e.g. poly-aromatics). We

believe that this new method shows great potential as an efficient tool for rapid and comprehensive determination of catalyst coking.

5.2 Short introduction

Acidic zeolite catalysts, such as zeolite H-Y, H-ZSM-5 and H-SAPO-34 are widely employed across the modern petrochemical and fine-chemical industries, for their excellent catalytic performances in hydrocarbon conversions and related chemistries. [218, 219] However, progressive product/intermediate accumulation in/on these porous catalysts followed by inevitable dehydrogenation into coke deposits always leads to catalyst deactivation, necessitating catalyst replacement to maintain the reaction activity and minimise production interruptions. [9, 193, 220, 221]

For zeolite catalysed hydrocarbon conversions, conjugated olefins, poly-aromatics, and other pre-graphite (deeply de-hydrogenated, sp^2 carbon rich) species are the major components in coke deposition and therefore allow the detection of their existence via electromagnetic (*EM*) spectroscopy on the targeted chemical structures, e.g. C=C bond in an olefin molecule. [9, 12, 14, 16, 221, 222] By far, Fourier-Transform Infrared (FT-IR) Spectroscopy, [223] better applied for in-situ studies, [224] plus Laser-Raman (optimized by Vis to UV) [41, 42] have been employed to draw a complementary picture of the various coke compounds. However, problems caused by complex sample preparation (e.g. when IR sample needs to be mixed with KBr), atmospheric contamination of samples (e.g. moisture in air) and rigid temperature

requirements greatly limit the application of these measurements. [12, 222] More importantly, one common feature of the above spectroscopies, as well as UV-Vis, is a 'beam to sample' working mode when applied in coke analysis, according to which the electromagnetic wave propagates to a single point on the sample surface then transmission or reflectance data are recorded. Disadvantages include a localized, single point interrogation and the lacking of information from inner pore coke species due to the limitation of energy penetration (here incident radiations need to pass through the material layers to reach the inner part of sample, in which process energy is gradually absorbed, and a thin film of sample is normally required). [9, 12, 41, 42, 222, 223] On the contrary, Nuclear Magnetic Resonance (NMR) spectroscopy works in a 'sample-inside-electromagnetic-field' mode, where the sample is instead bathed in the electromagnetic (i.e. magnetic) field for measurement with the entire sample body volumetrically interrogated (not focused on a single point on the sample surface). Normally, complete energy penetration to each part of the sample is allowed, where sample thickness is no longer the major technical issue, thus, is better for analysis of cokes located deeply inside the zeolite pores/channels. However, problems of ^{13}C NMR in coke analysis arise by the high cost and low efficiency of ^{13}C isotope exchange; and in the case of Cross Polarization (CP) without ^{13}C exchange, the signal of deeply dehydrogenated coke species is extremely poor due to the dissipation of hydrogen in substance. [225, 226]

5.3 Microwave cavity configuration

Similar to NMR, in this work, a sample is inserted into a quasi-static electric field generated inside a microwave resonant cavity for measurement. Here the change of inner cavity *E*-field is attributed to the entire sample body, of which each part is affected by the electric field antinode, thus will be measured owing to its corresponding dielectric properties. [68, 69, 227] The most important feature of such a whole-body, volumetric interrogation presents two advantages when applied for coke analysis: 1) the measured data reflects the integrated total coke accumulation of a sample, rather than being obtained from a beam-focused point on the sample surface. 2) the response derives from the fact that the functions (e.g. polarization) of employed *E*-field work through all parts of the sample body, and this full-penetration effect well measures coke contents hiding deeply in the zeolite structure. [68] More importantly, the technique is better suited to deeper dehydrogenated coke species with excellent signal response, thus it complements the gap in capabilities of CP ^{13}C NMR.

The employed microwave cavity uses a TM_{010} mode working around 2.45GHz. [68, 69] Schematic of representative resonant traces showing $|S_{21}|^2$ (transmitted microwave power) as a function of frequency is shown in Fig. 5.1. [68] It can be seen that the introduction of sample into the *E*-field antinode of TM_{010} mode causes a negative shift in the resonant frequency (*f*), and an increase in the bandwidth (*BW*). From the change in resonant frequency (Δf) and the change in bandwidth (ΔBW) we can infer the dielectric properties (complex permittivity) of sample (All frequency and bandwidth

measurements are adjusted to account for the presence of the quartz sample tube). Here, the complex permittivity (ε^*) is defined as $\varepsilon^* = \varepsilon' - j\varepsilon''$, where the real part ($\varepsilon'$) describes the polarization of the material in response to electromagnetic fields and the imaginary part (ε'') describes the electromagnetic energy absorption (dielectric loss) in the sample. [49, 66]

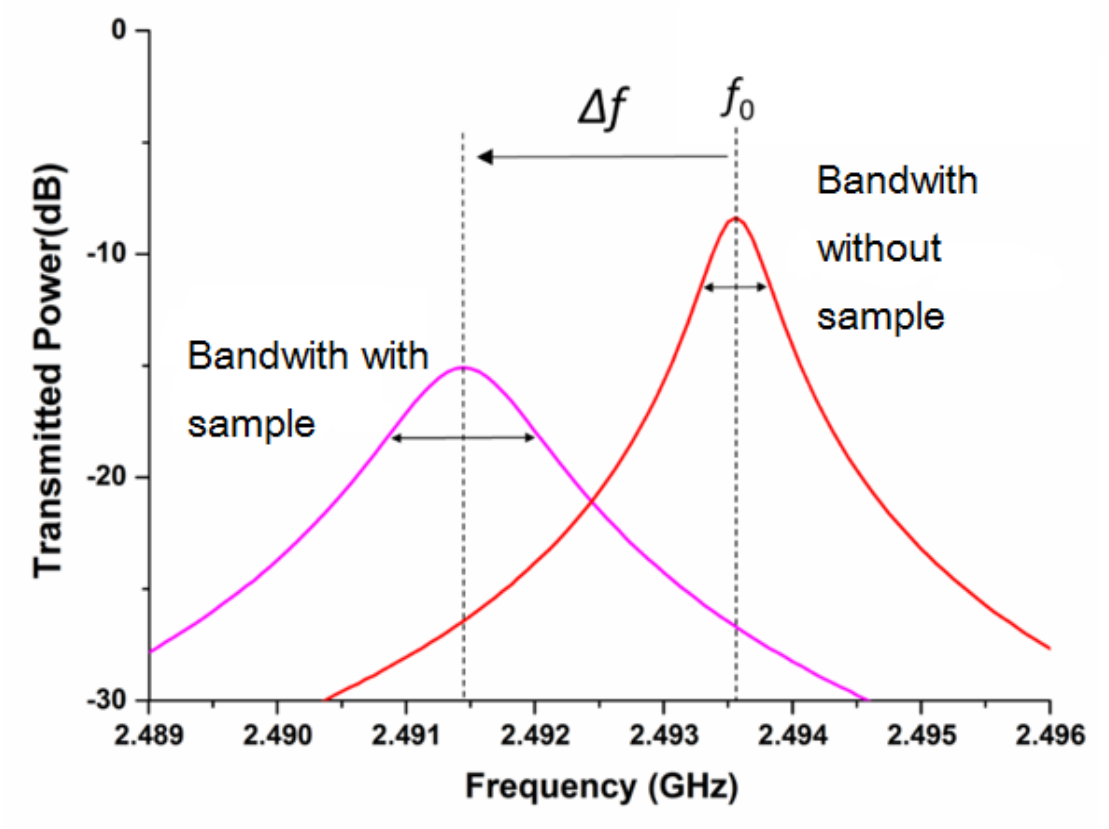

Fig. 5.1 Schematic of example resonant traces showing the induced changes of a MW resonant cavity, consisting of a shift in frequency and change of bandwidth.

In this work, we focus on the imaginary permittivity, ε'', of the coked catalyst samples, obtained and adjusted from [227]

$$2\varepsilon'' A V_s = \frac{\Delta BW}{f_0}.$$

Here f_0 is the unperturbed frequency. A is a constant determined by the size and

geometry of the cavity. For the employed system, the A value is approximately 7.34×10^{-3}, as detected using a PTFE sample of known complex permittivity. [228] V_s is the effective volume of the sample in the cavity (i.e. ~0.126cm^3). [68] Importantly, here we recorded the induced shift of the applied E-field characteristic of the whole sample body inserted into the cavity. Thus, the analysis is not limited to a single point of the sample as is commonly the case in, for example, Laser-Raman. This is a non-destructive, non-invasive and contact-less measurement, plus data acquisition takes only milliseconds and shows excellent repeatability among multiple tests. Besides, previous researches have shown that these measurement can be taken at higher temperatures, which could lead to future in-situ applications and real-time monitoring of catalyst deactivation. [229]

Microwave measurements of samples were carried out in a cylindrical host cavity, as shown schematically in Fig. 5.2a. Sample was placed in a thin-walled high-purity quartz tube and introduced axially through a small insertion hole in the centre of the top and bottom plates of the cavity (Fig. 5.2b). The cavity is made from aluminum and we have obtained an unloaded quality factor of ~8000 at room temperature. The internal dimensions of the cavity are radius a = 4.6 cm and length d = 4.0 cm. Here we choose TM_{010} mode for the complex permittivity measurement of sample since it has a highly uniform electric field near the cavity axis, resulting in minimal depolarization of sample in this experimental configuration. [230, 231]

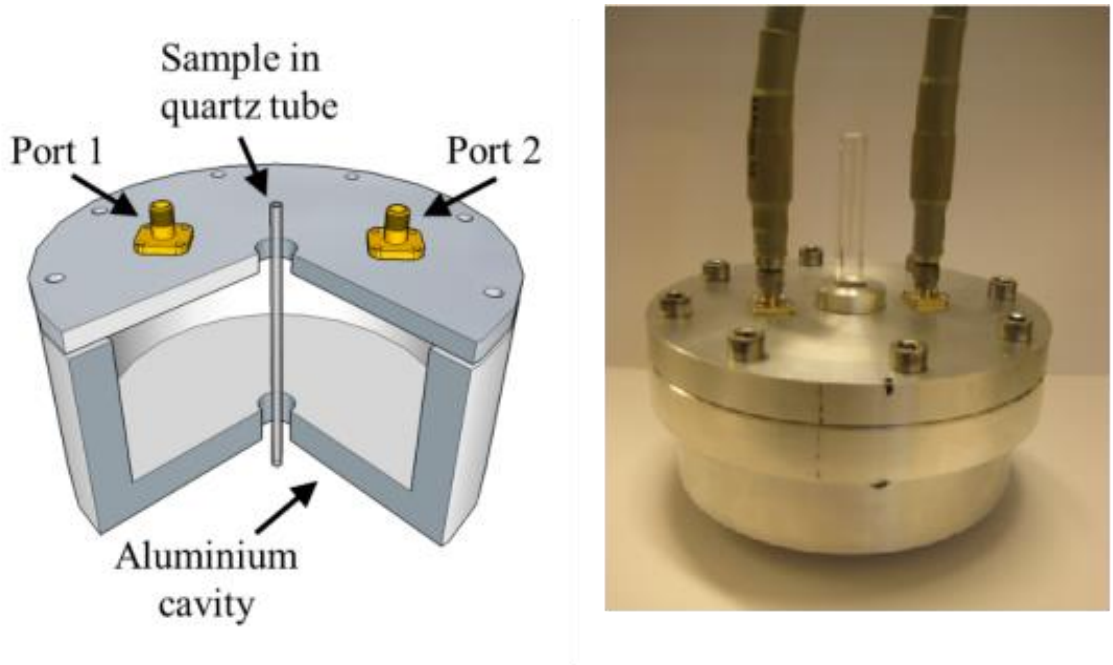

Fig. 5.2a (left)**,** quarter section of a perturbation cavity, cut to show the location of the sample tube (inner diameter 2mm), and Fig. 5.2b (right), exterior look of the cavity

The electric field in this mode is directed parallel to cavity axis, thus, parallel to the axis of the sample tube giving only minor modification of the local electric field in the presence of the quartz tube. The distribution of electric field magnitude is shown in Fig. 5.3(a-c). For tubes of inner radii $r \ll a$, we may assume the electric field sample impregnated inside to be uniform in the employed TM_{010} mode. [68] In our work, r/a =~0.022, so the *E*-field remains highly uniform when applied to the sample. The radius '*a*' is chosen so that the TM_{010} mode has a resonant frequency near 2.45 GHz (the exact working frequency may change in a small range in different tests and only causes a negligible difference). The cavity aspect ratio d/a is tuned to be small enough for the TM_{010} mode to be the dominant mode and clear of other, higher order modes in the cavity, but not too small to significantly compromise the high Q factor or the axial uniformity of the electric field.

All microwave measurements are performed using an Agilent E5071B network

analyser. Measurements of the transmitted microwave power $|S_{21}|^2$ are performed in the frequency domain, and non-linear, least-squares curve fitting to a Lorentzian response is used to determine resonant frequencies and loaded quality factors (denoted as Q_L). Cavity excitation is provided by a pair of square-flanged SMA jack connectors (supplied by Farnell Ltd.), at radial positions 3.0 cm from the axis. These open circuit terminations, with an extended centre conductor, providing capacitive coupling to the electric field of the TM_{010} mode. We remove the effects of cavity couplings by converting Q_L into the unloaded quality factor Q in each case. The sample tubes were filled to a depth of 5 cm with the powder samples (4.0 cm of which will be in the active region of the cavity). The active sample volume is therefore 0.126 cm^3.

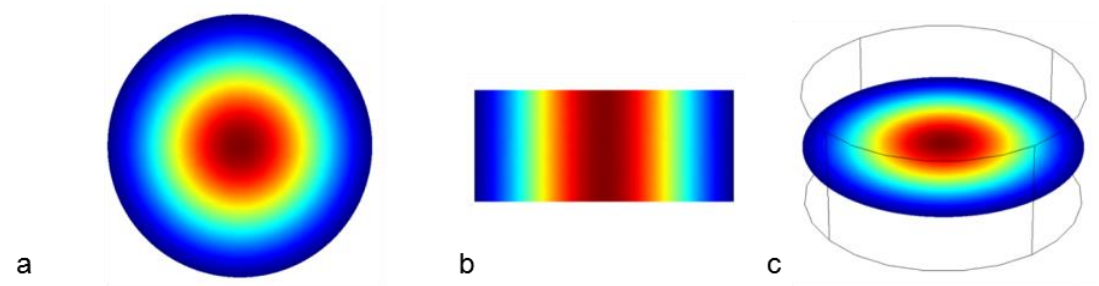

Fig. 5.3 a-c, (a) plan view, (b) side view, and (c) slant view of the electric filed distribution in the employed TM010 mode resonant cavity

5.4 Experimental conditions

The catalyst tests were carried out in a fixed-bed-reactor system (Fig. 5.4).

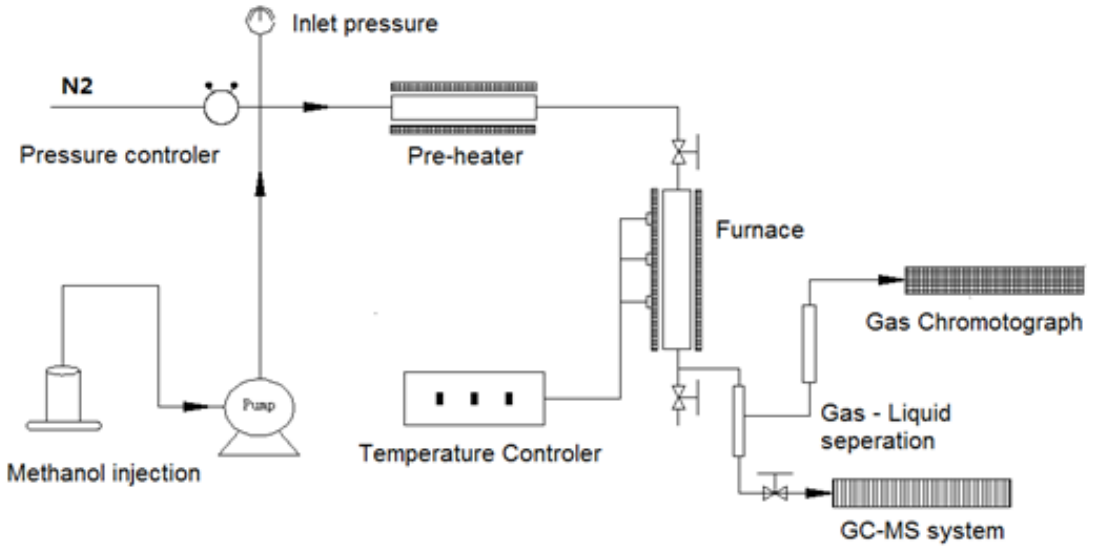

Fig. 5.4 Experimental system employed in the coking MTH reactions.

During each test, 1.0 gram of catalyst sample was loaded in the middle of the tubular reactor, supported by carborundum particles (Fisher, 24 grit). Methanol (Sigma, reagent standard) was injected by a HPLC pump, and preheated at 150 ^{o}C to fully vaporize into gas phase, then carried by the N_2 flow (5ml/min). An enhanced WHSV (Weight-Hourly-Space-Velocity) of 8 h^{-1} was applied (i.e. every one hour, 8 grams of methanol were delivered to 1 gram of catalyst for conversion) in the reaction. This heavy-than-usual methanol conversion duty was designed for a faster coke formation, and resulted in distinguished coke compositions over different samples, owing to the variety in zeo-type, reaction length, as well as sample position in the catalyst bed. The catalyst bed temperature was set at 450 ^{o}C under atmosphere pressure, for the maximum coke accumulation within the 5h reaction period.

The post-run samples were carefully unloaded from the tubular reactor, after cooled down to the room temperature. For the nano zeolites, the firstly pour-out 0.4g catalyst powders were collected precisely and marked as the coked catalyst-bed-top sample, whereas the later pour-out 0.5-0.6g catalyst powders were saved as the coked catalyst-bed-bottom sample. Grindings for 3 mins were employed before the characterizations on each sample for the best mixing effects and a fair result.

Physical mixtures of 'carbons' and zeolite were obtained by adding the solid samples (coked top ZEO 160/activated carbon/graphite) into fresh pure ZEO160 zeolite in pre-calculated amounts, respectively, then grinding for 3 mins until the color of mixture becomes uniform.

Raman spectra were recorded on a Perkin-Elmer Raman Station 400F Raman Spectrometer. The samples were supported on a piece of clean glass for scanning.

A SDT Q600 (TA instruments) thermogravimetric analyser was used to assess the coke content over the used catalysts. The coke amount is measured based on the weight loss of coked samples during temperature programmed calcination in air from 20 to 1120 ^{o}C (temp. ramp 10 ^{o}C /min). 50mg of spent sample was used each time.

^{13}C NMR experiments were carried out on a Varian VNMRS spectrometer at ambient temperature with a resonance frequency of 100.562 MHz. Cross Polarization (CP) technique was employed. The ^{13}C CP NMR used a 6mm probe, with data acquisition in 30.0ms, recycle delay of 2.0 second and sample spinning rate at 6 KHz.

Transmission electron microscopy (TEM) measurements were undertaken using JEM-3000F microscope (300kV). Samples were dispersed in ethanol and baked out in

vacuum after transferring onto the carbon coated copper grids.

5.5 Microwave absorption results and discussion

5.5.1 Cavity response effectively reflects the coke accumulation over catalysts

Before all analyses, precise loading of samples is required to avoid the influence caused by the difference in sample weight (0.15g sample is loaded in the tube in each analysis). We firstly tested a variety of zeolites (commonly used zeo-types) all coked by time-controlled methanol-to-hydrocarbon (MTH) reactions (the same sample was coked in two individual reactions for 2h and 5h, respectively), which led to distinguished coking statuses of the same zeolite. Further investigations were carried out into 3 different nano H-ZSM-5 zeolites (Si/Al ratios = 46, 60 and 160, ZEOLYST, USA) with various numbers of Brønsted acid sites, all coked in 5h MTH reactions. These zeolites with superior coke tolerance allow us to better separate their post run samples coked at different positions of the catalyst bed, all formed in the same reaction. The resultant coke depositions along catalyst bed from top to bottom are illustrated in Fig. 5.5, where the methanol flow direction is also demonstrated (this is also the direction of reactor inner gas flow driven by the carrier gas). We have selected nano H-ZSM-5 (Si/Al=160, marked as ‘ZEO 160’) samples for demonstration, which exhibit the most obvious visual color difference between

differently coked samples.

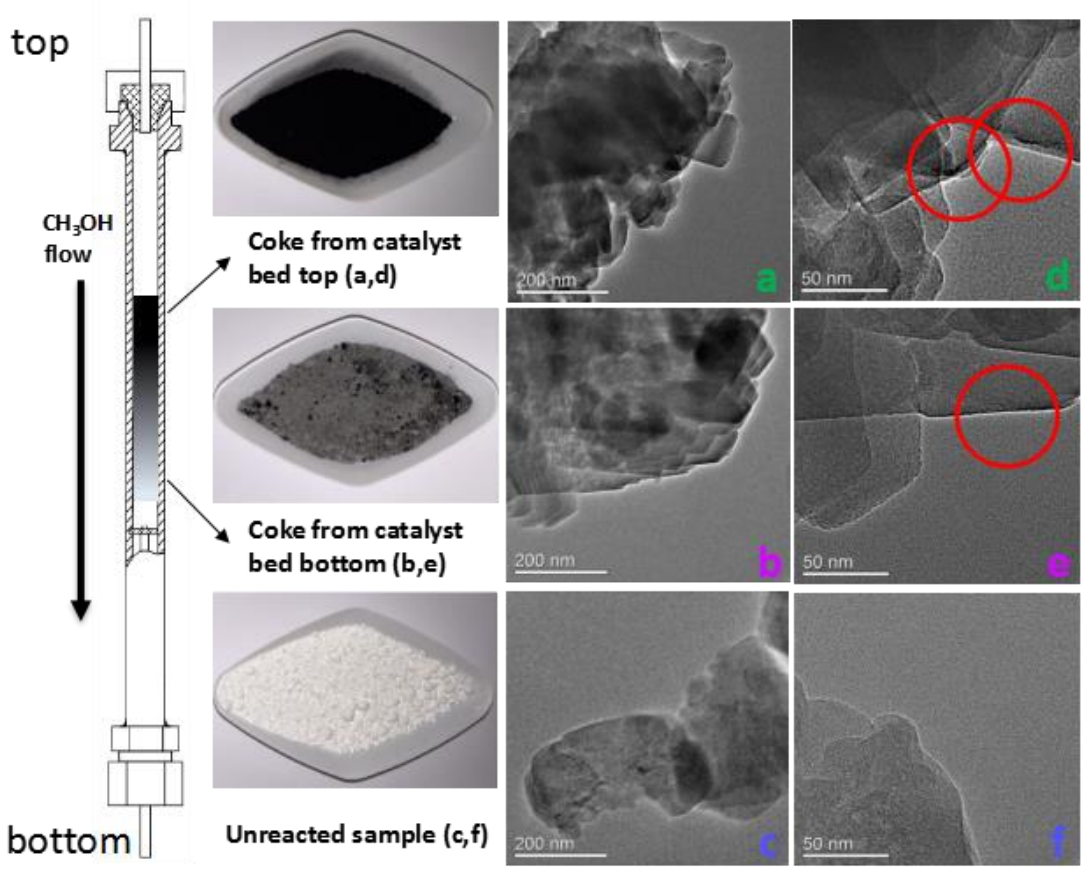

Figure. 5.5 a-c, 200nm vision Transmission Electron Microscopy (TEM) images of "coked top" (a), "coked bottom" (b) and un-reacted ZEO160 samples (c). d-f, 50nm vision TEM images of coked top (d), coked bottom (e) and un-reacted ZEO160 samples (f).

Corresponding bulky powders and a schematic representation of the coke depositions in color gradient along the methanol flow route inside fixed bed reactor are shown on the left.

The coked top sample, as shown visually in Fig. 5.5, is in darker black color (reflecting higher levels of coke deposition), whereas the coked bottom sample only exhibits light grey color (less coke deposits), all in stark contrast to the fresh-white unreacted zeolite. Also easily distinguished in the microscopy (TEM), the coked top sample possesses significantly larger black coke zones on the zeolite crystal surfaces (Fig. 5.5a), while those black coke areas are only randomly distributed on the coked

bottom sample (Fig. 5.5b), all observed in multiple scans. Darker areas are also observed on pure zeolite (Fig. 5.5c), probably due to the overlapping of crystals. However, only coked zeolites show some clear signs of superficial carbon deposition at the edges of crystals under vision of higher magnification (Fig. 5.5d & 5.5e), which is consistent with the results reported previously. [44] Again, the coked top sample (Fig. 5.5d) shows more intensively blacking edge regions in this case (this once more indicates more cokes are accumulated over this sample).

One notes that the increase in coking resulted in the coked top sample being easily distinguished from others in the obtained microwave plots, as shown by the greatly broadened and shifted resonant bands with greater associated insertion loss (light green) in Fig. 5.6.

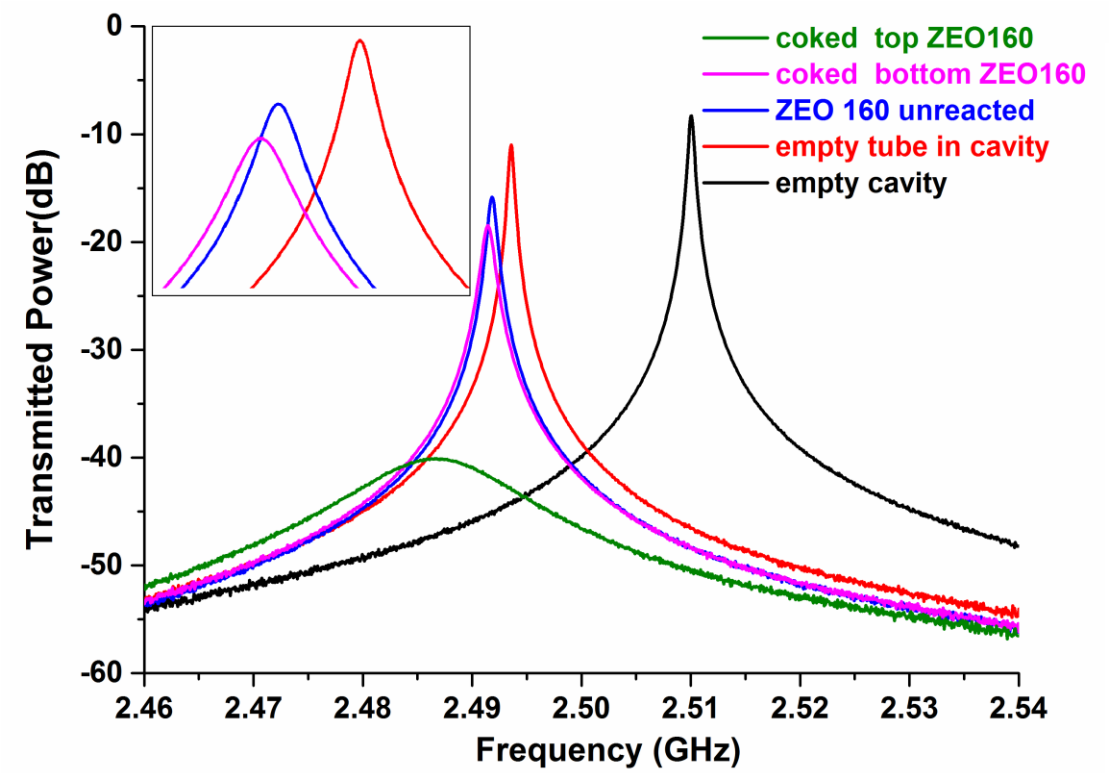

Fig. 5.6 MW plots induced by different samples (ZEO 160 group) and conditions

For calibration, the empty quartz tube also leads to a small shift of the resonant frequency (red), which is accounted for in measurements of ΔBW and Δf though dielectric losses associated with the sample tube are low, thus its ΔBW is nearly zero. The pure zeolite sample (blue) shows small Δf and poor ΔBW, and this is also the case (purple) for mildly-coked bottom sample (see the magnified inset in Fig.5.6). Note that the apparently poor resolution of the GHz scale in the above figure does not reflect the very high resolution of the measurement itself (~10^{-6} GHz).

5.5.2 Absorption efficiency characteristic of a particular coke composition

Exact dielectric loss values (ε") of coked samples were calculated from the recorded ΔBW and f_0, as shown in Fig. 5.7 a-b (the values of unreacted zeolites were also employed for comparison). Corresponding Raman (Fig. 5.8 a-b) and TGA data (Fig. 5.9 a-g) were used as references to evaluate the coke compositions and quantities. These data illustrate that microwaves can quickly and accurately response to the changes induced by the coke contents.

It should be noted that the pure zeolite body also possesses somewhat dielectric loss, and the obtained results in Fig. 5.7b indicate that this dielectric loss property may be even stronger than some cases where lightly-dehydrogenated coke species are deposited, as has been particularly observed on SASO-34 and MCM-22 zeolites (their coked samples do not show any clear sign of aromatics in the corresponding Laser-Raman results, by contrast, as shown in Fig. 5.8b the spectra evidences imply

that the major coke contents obtained by these two zeolites are most possibly some olefinic, or paraffinic species that are less dehydrogenated than aromatics). [12]

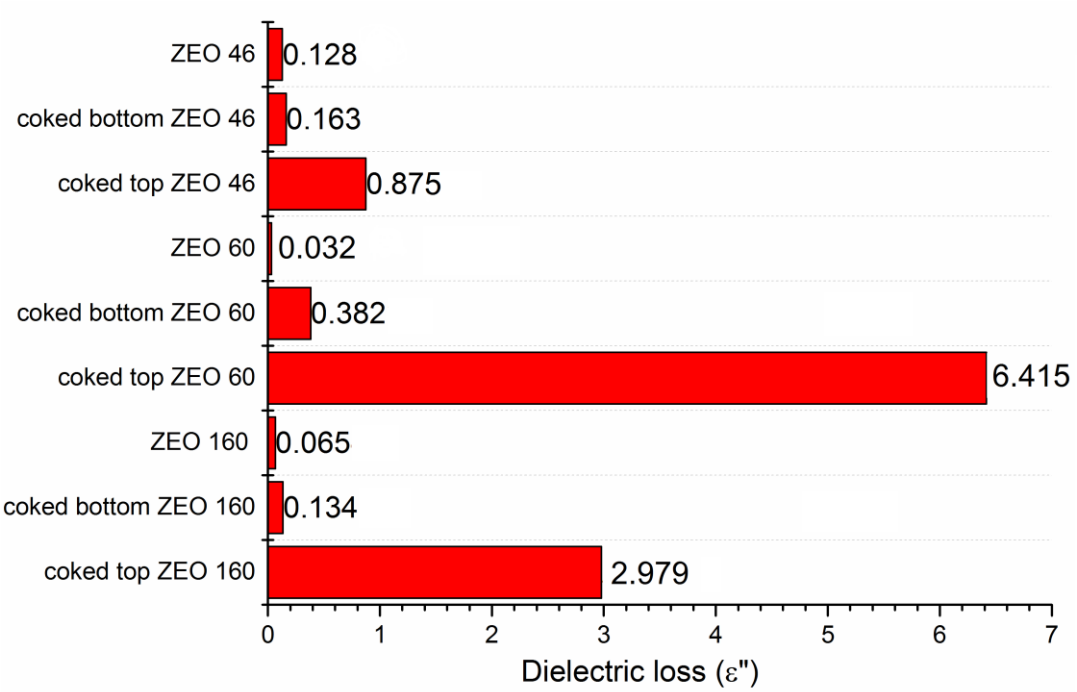

Fig. 5.7a Dielectric loss values (ε") of nano H-ZSM-5 zeolites, including the unreacted zeolite bodies, and corresponding coked top and bottom samples, the values were taken as an average of 5 times individual tests

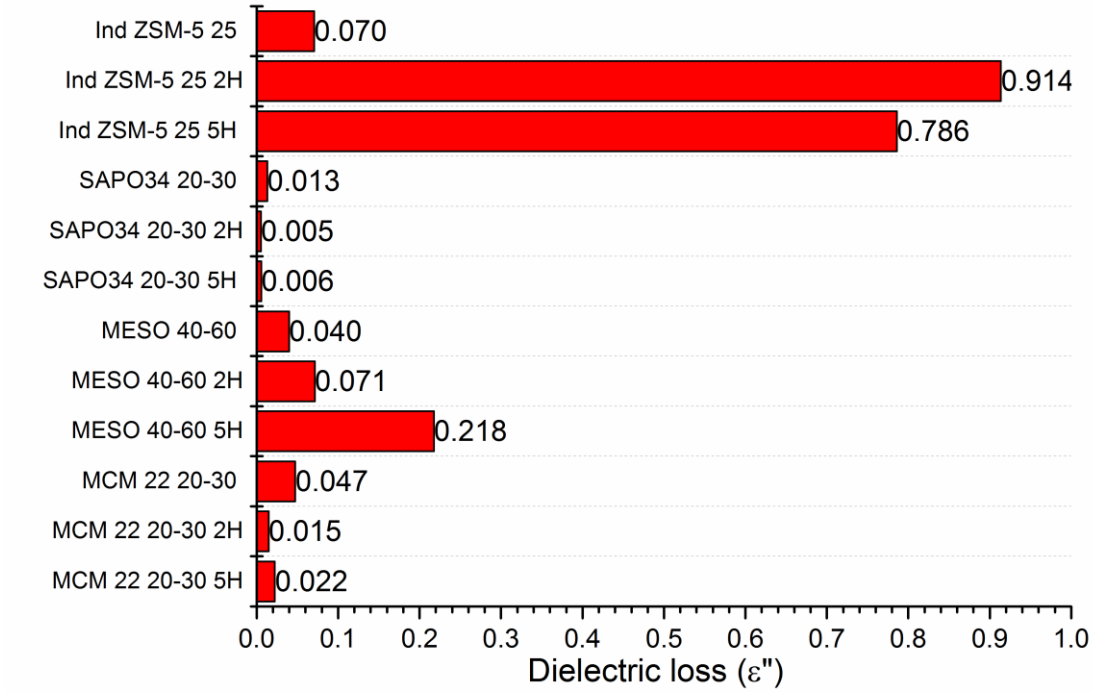

Fig. 5.7b Dielectric loss value (ε") of various zeolite types, including the clean zeolite bodies, and their 2h and 5h coked samples, the values were taken as an average of 5 times individual tests

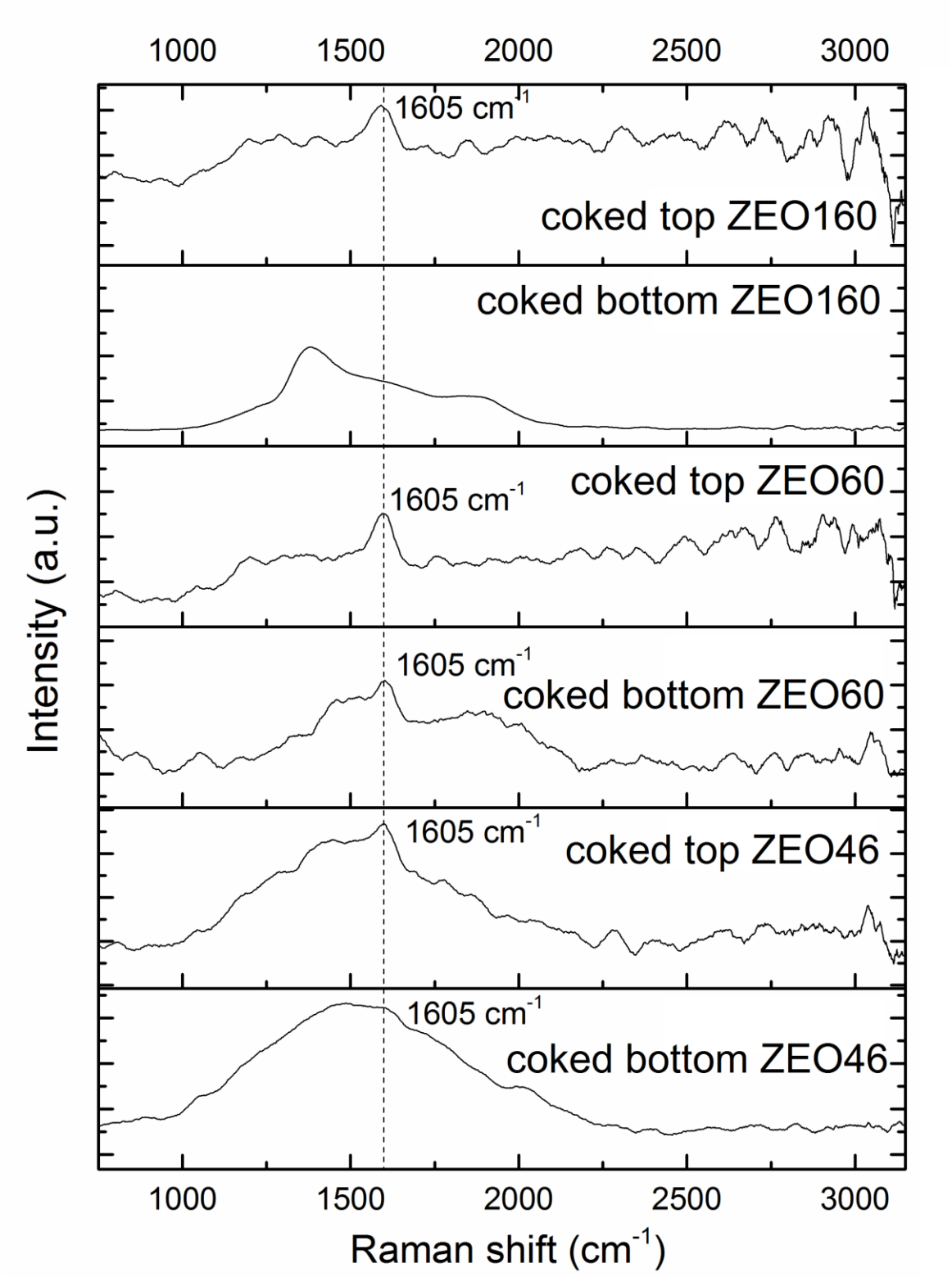

Fig.5.8a Raman spectra of coked nano H-ZSM-5 zeolites, samples from top and bottom positions of the same catalyst bed are illustrated, respectively

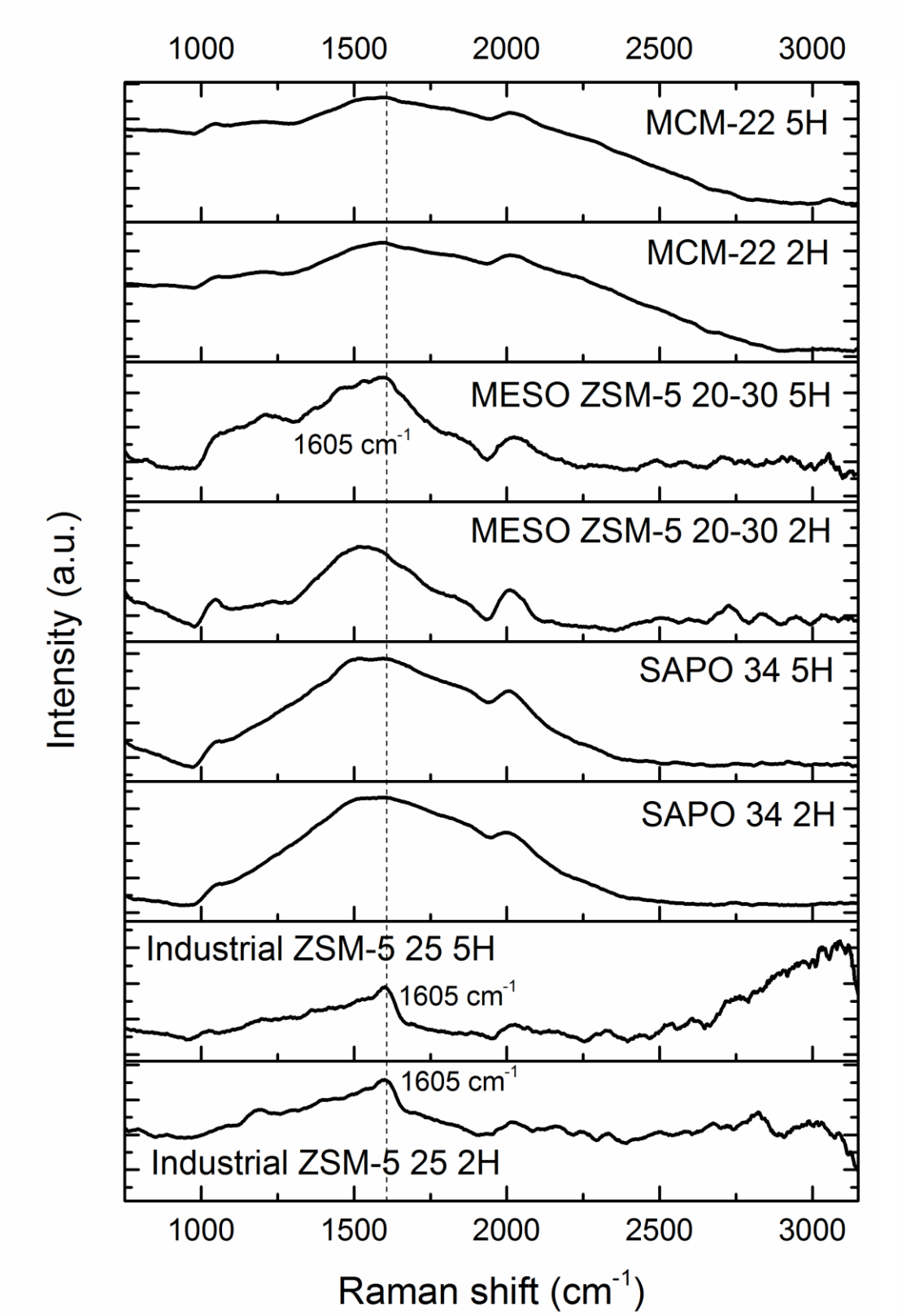

Fig.5.8b Raman spectra of coked different zeolite types, samples obtained from 2h/5h MTH reactions, respectively

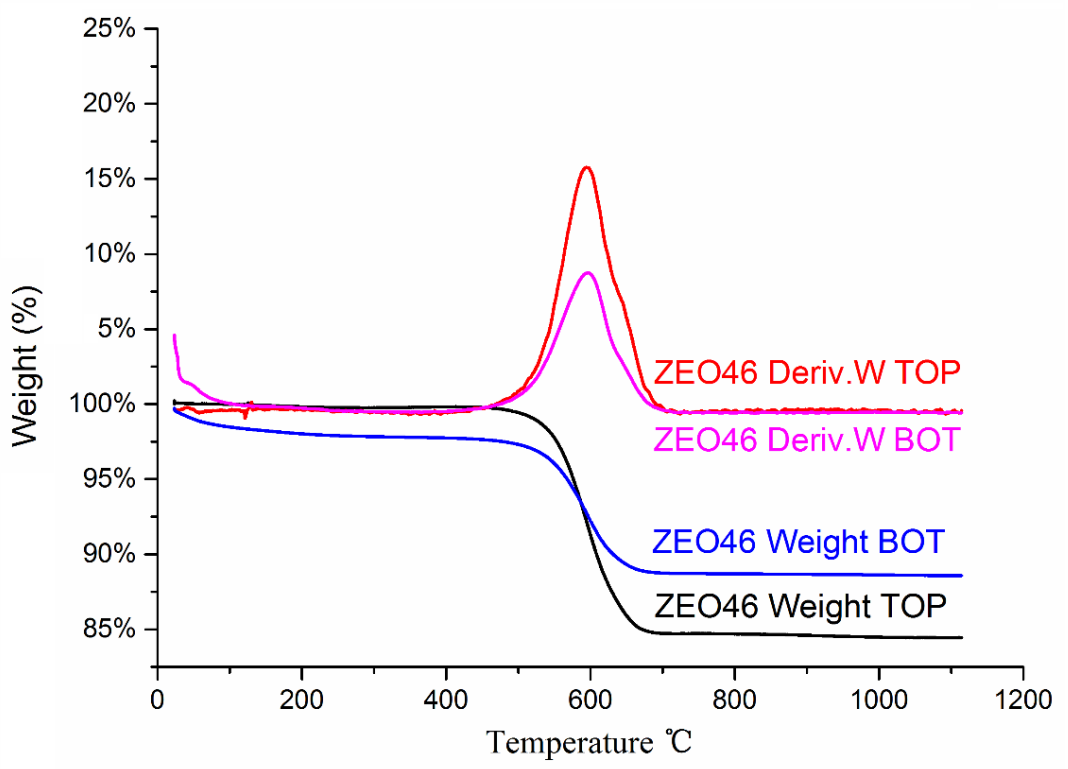

Fig.5.9a Thermogravimetric analysis (TGA) plots (bottom) of the coked nano H-ZSM-5 (Si/Al=46) samples, and corresponding derivative thermogravimetry (DTG) curves (top)

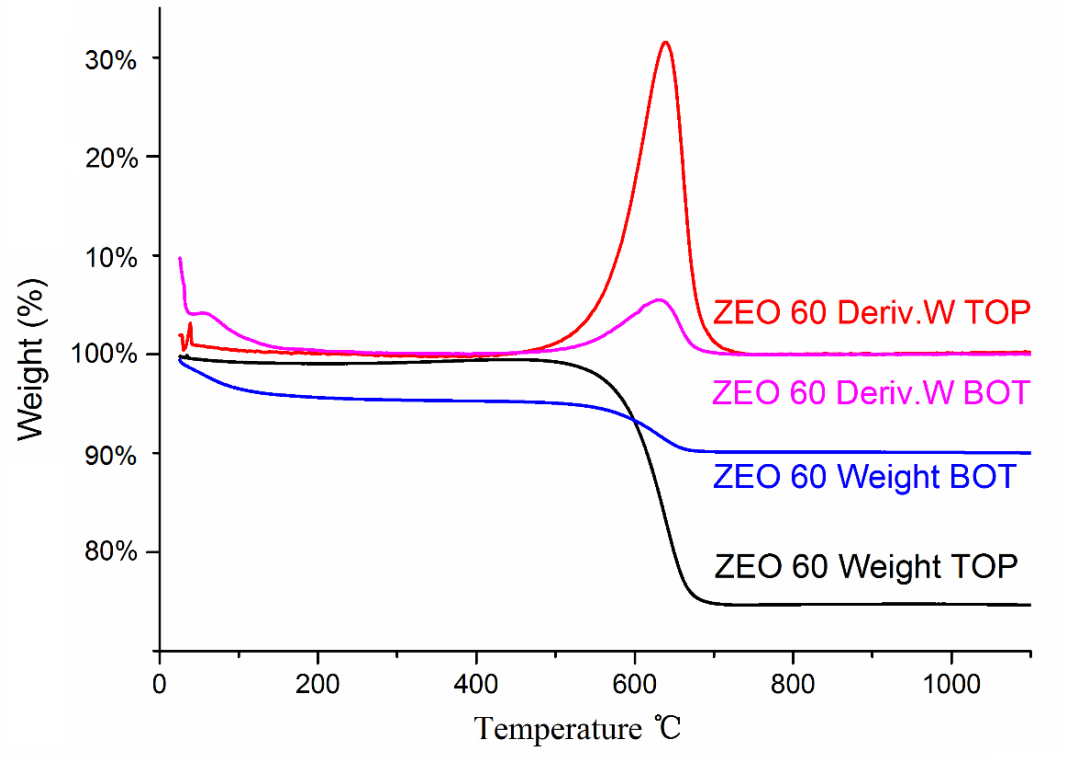

Fig.5.9b Thermogravimetric analysis (TGA) plots (bottom) of the coked nano H-ZSM-5 (Si/Al=60) samples, and corresponding derivative thermogravimetry (DTG) curves (top)

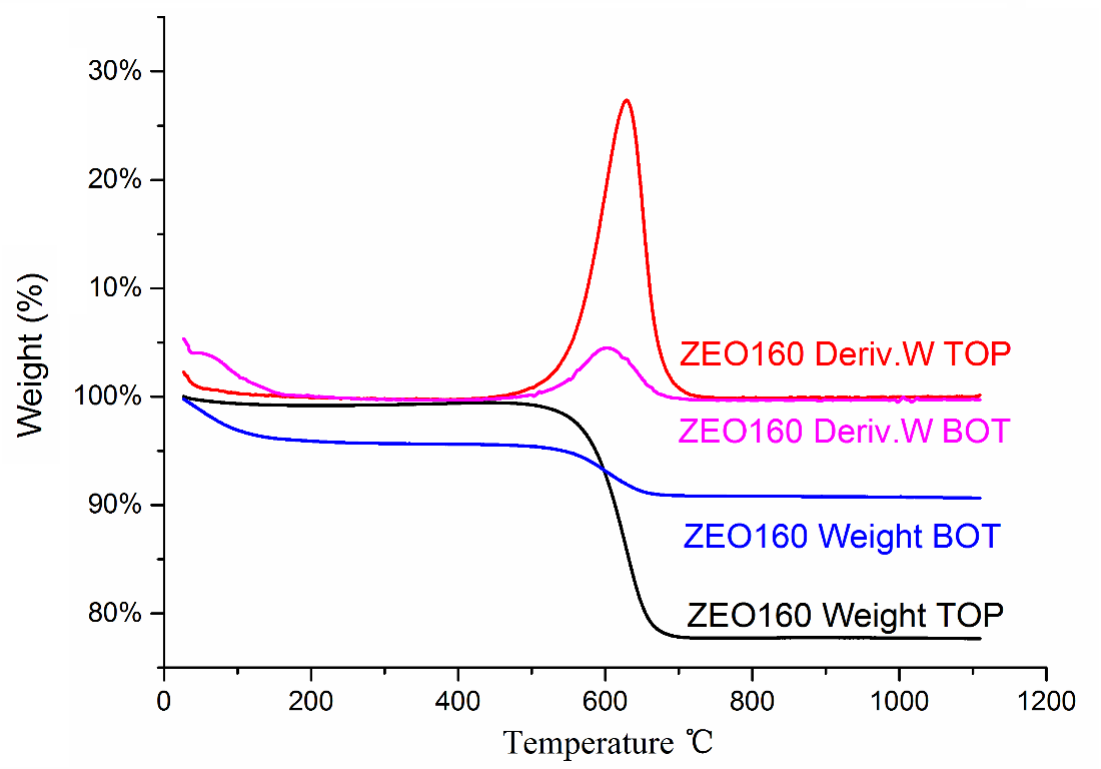

Fig.5.9c Thermogravimetric analysis (TGA) plots (bottom) of the coked nano H-ZSM-5 (Si/Al=160) samples, and corresponding derivative thermogravimetry (DTG) curves (top)

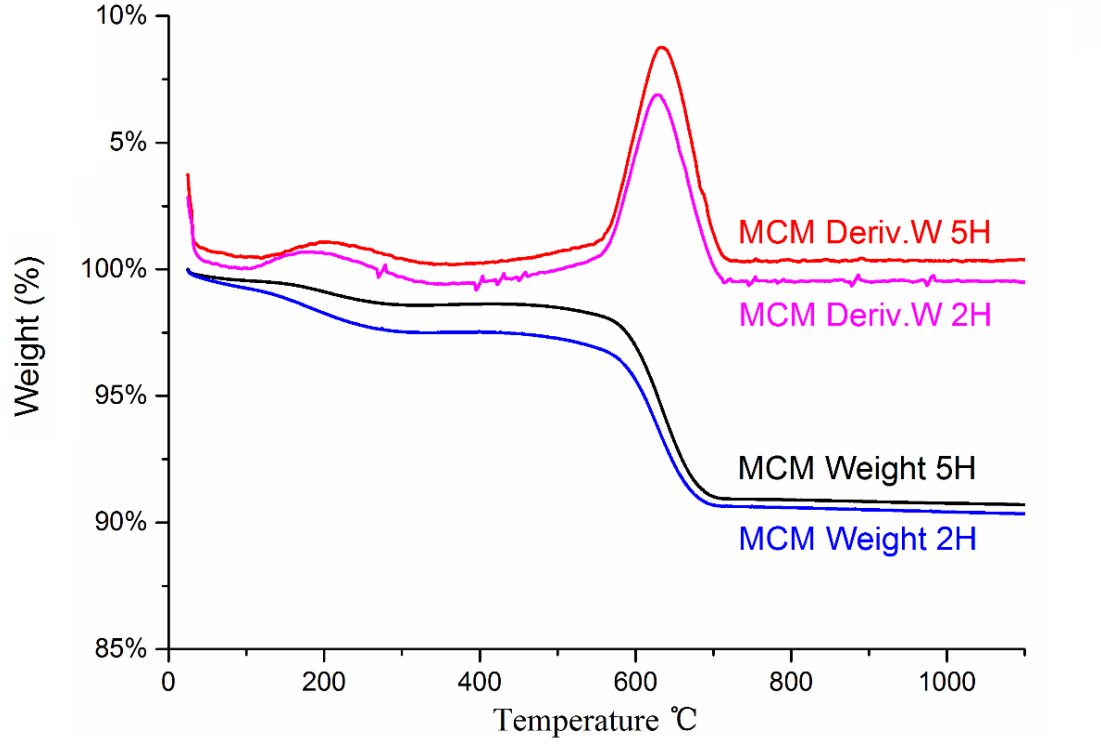

Fig.5.9d Thermogravimetric analysis (TGA) plots (bottom) of the coked MCM (Si/Al=20-30) samples, and corresponding derivative thermogravimetry (DTG) curves (top)

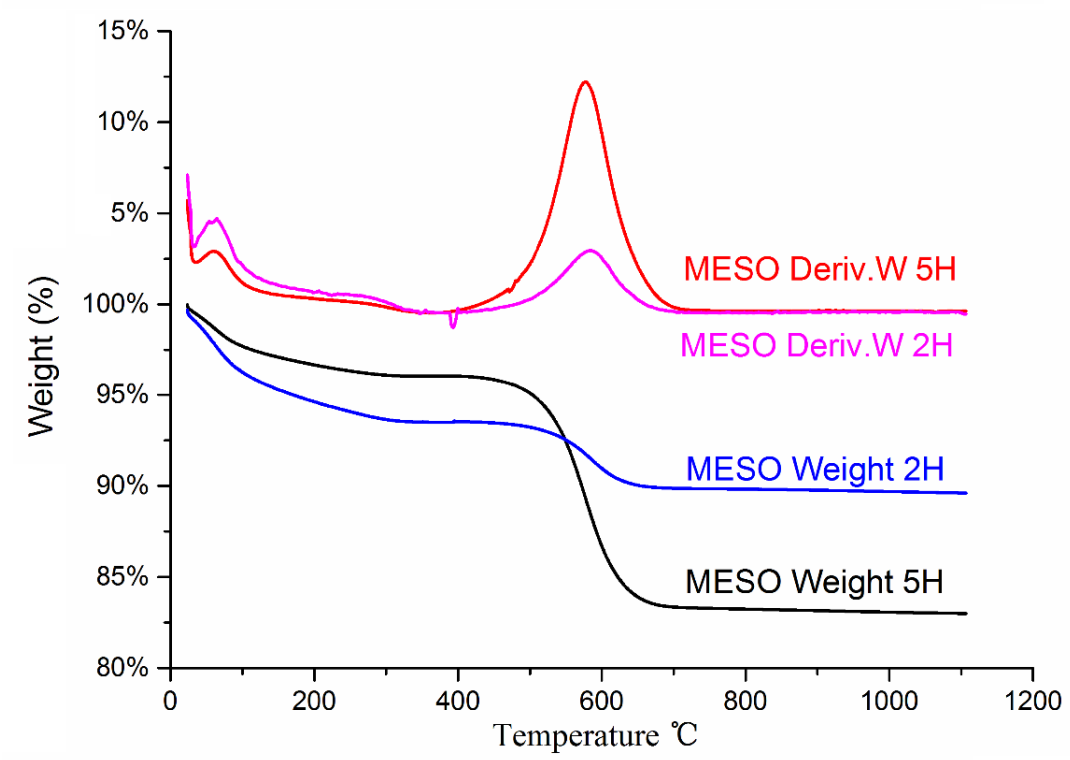

Fig.5.9e Thermogravimetric analysis (TGA) plots (bottom) of the coked mesoporous H-ZSM-5 (Si/Al=40-60) samples, and corresponding derivative thermogravimetry (DTG) curves (top)

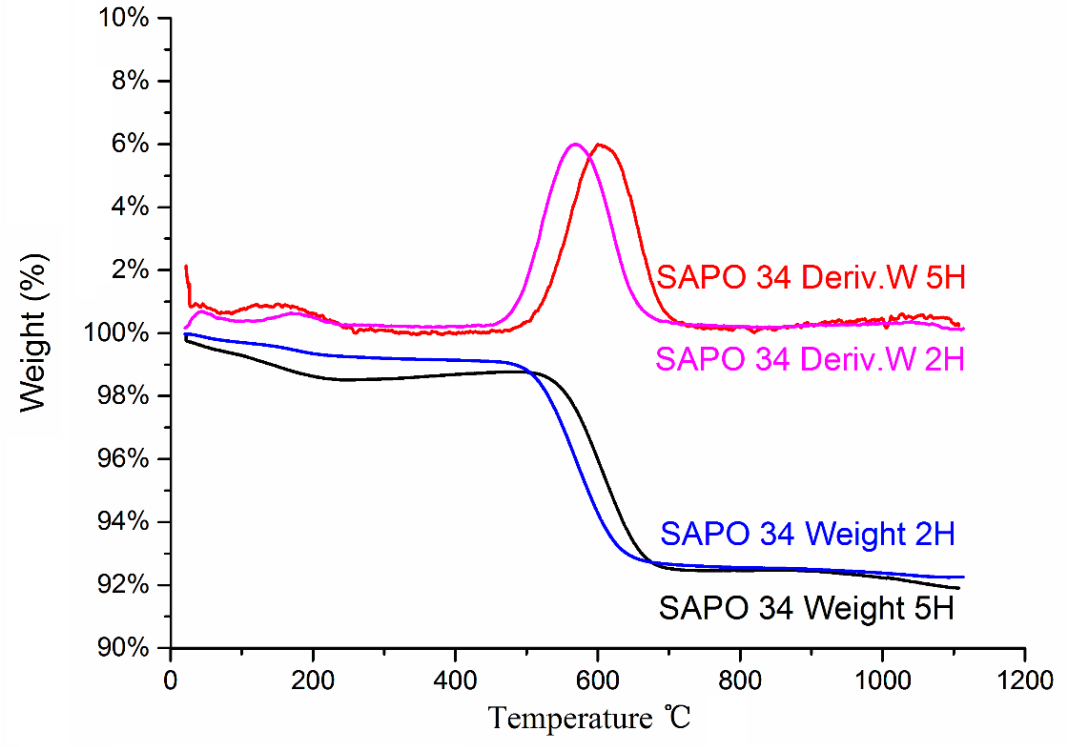

Fig.5.9f Thermogravimetric analysis (TGA) plots (bottom) of the coked SAPO-34 (Si/Al=20-30) samples, and corresponding derivative thermogravimetry (DTG) curves (top)

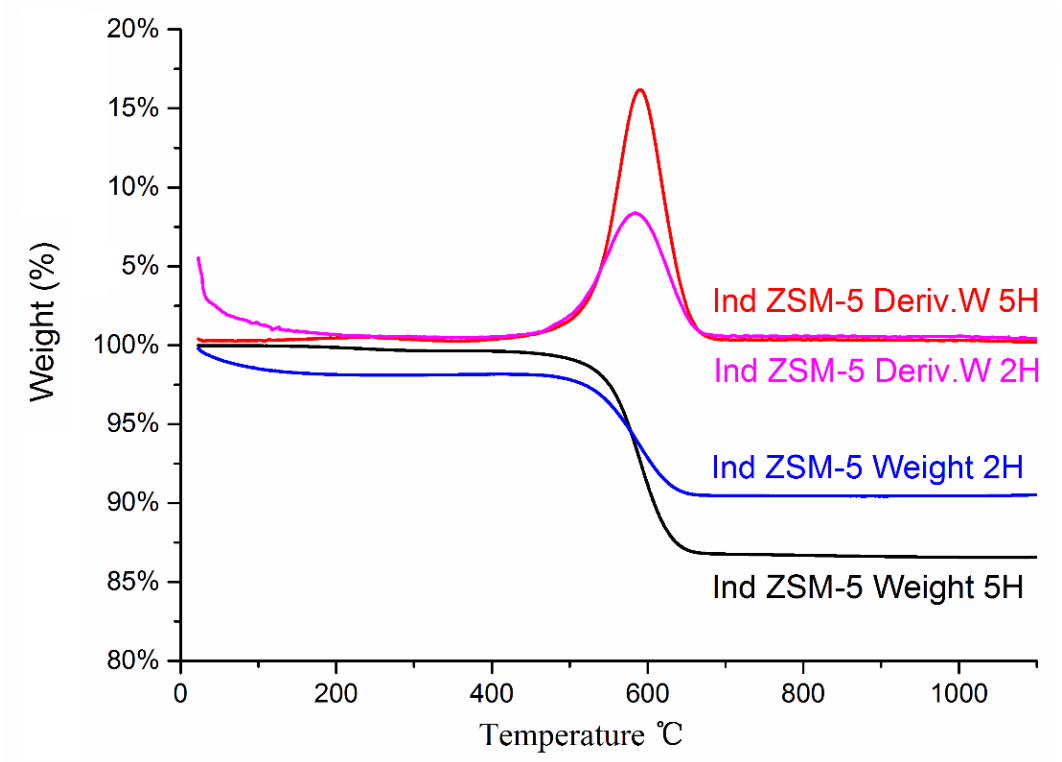

Fig.5.9g Thermogravimetric analysis (TGA) plots (bottom) of the coked industrial H-ZSM-5 (Si/Al=25) samples, and corresponding derivative thermogravimetry (DTG) curves (top)

The above TGA results clearly show that all post run catalysts have obtained somewhat coke deposits after the MTH reaction, at least 5wt% as reflected by the TGA curves. It seems that the much smaller difference in coke amounts may not be the major reason for the very distinguished dielectric loss values obtained by different samples. Here we believe the difference in ε" values is mainly attributed to the variety in sample coke compositions. SAPO-34 and MCM-22 zeolites do not have the uniformly developed 3-dimensional channels as what is for ZSM-5, as a result, they mainly yield olefin products and possess different coking behaviours in the MTH reaction. [9, 14, 16] The non-aromatic coke compositions achieved by these two zeolites possibly lead to the poor dielectric loss values of their coked samples. By contrast, all samples with clearly developed Raman peaks representing the aromatic

cokes (1605cm^{-1}) have shown significantly higher dielectric loss values. This correspondingship can be well supported by matching the data in Fig 5.7 and Fig. 5.8.

We are very interested in the contributions of different coke species to the dielectric loss values that can be measured by our technique. It should be noted that the dielectric loss value of a coked sample is not exclusively donated by the coke species as there are also other sample components such as the zeolite body. On the other hand, sample ε" is not a simple adding up of the ε" values of different components, in fact, it is an 'effective' value composed of complex contributions from each constituent material of the coked sample (for the cases of SAPO-34 and MCM-22, the sample ε" values are even reduced by the cokes). In order to build up a standard calibration profiles, for individual sample we have normalized the obtained ε" value by the weight of deposited cokes (weights of different samples in tube are quite close due to the precise loading and only cause very limited, negligible difference, so wt% from TGA is directly employed instead of the real coke weight in grams). The obtained data, ε"/wt% (Fig. 5.10a and 5.10b), shows the contribution of unit coke content to the complex dielectric loss value obtained by the coked sample, characteristic of the sample coke composition. The special format at the current stage, as we considered, makes the MW absorption data better combine with the TGA data (wt% of sample taken by the cokes is directly readable form the TGA curves); on the other hand, the presented data also reflect how coke concentration in sample affects the MW absorption at different coking levels, which possesses unique research significance for our extended studies (for instance, cokes of 1wt% result in different dielectric loss

values, between the cases that 10wt% and 20wt% cokes are deposited).

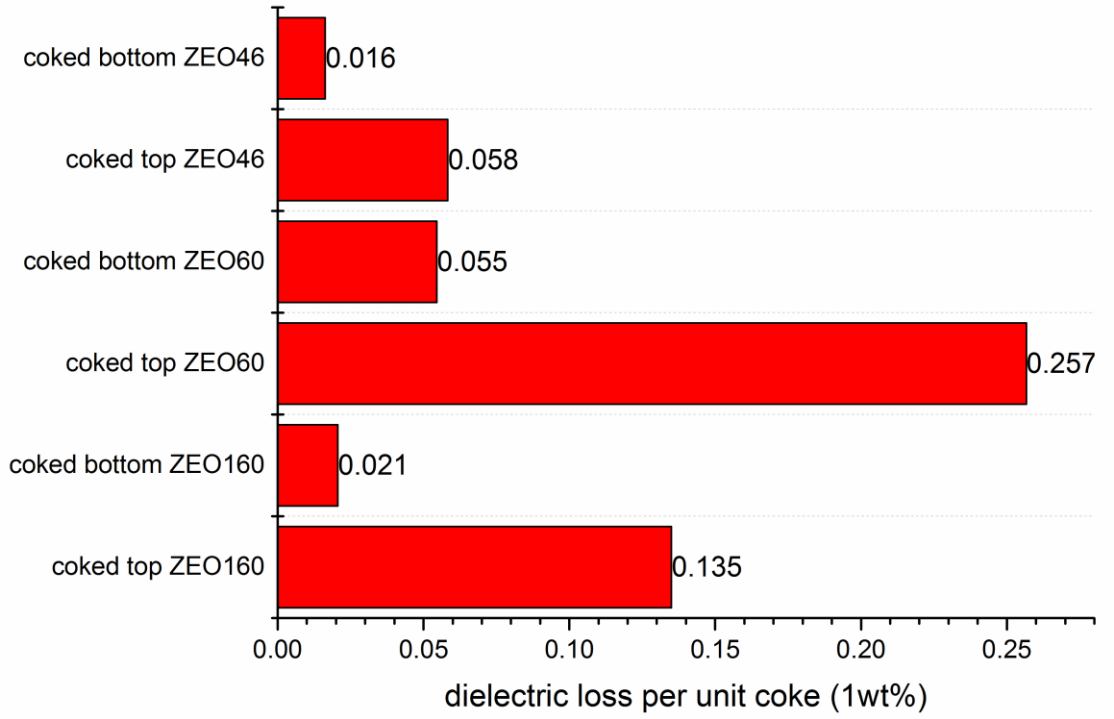

Fig. 5.10a Graph bar charts show normalized dielectric loss values (ε") by TGA weight loss (wt%) of each sample (coked nano H-ZSM-5 zeolites)

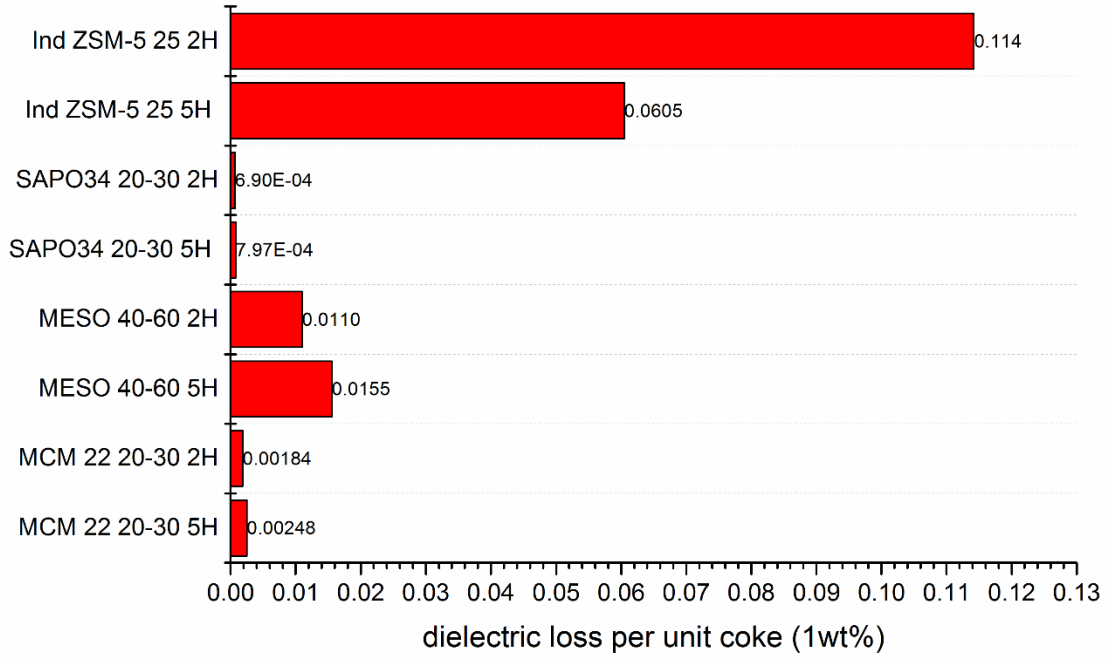

Fig. 5.10b Graph bar charts show normalized dielectric loss values (ε") by TGA weight loss (wt%) of each sample (multiple zeo-types)

Again, samples of ZEO 160 are chosen for discussion with all information (ε”/wt%, Raman and TGA) included in Fig. 5.11.

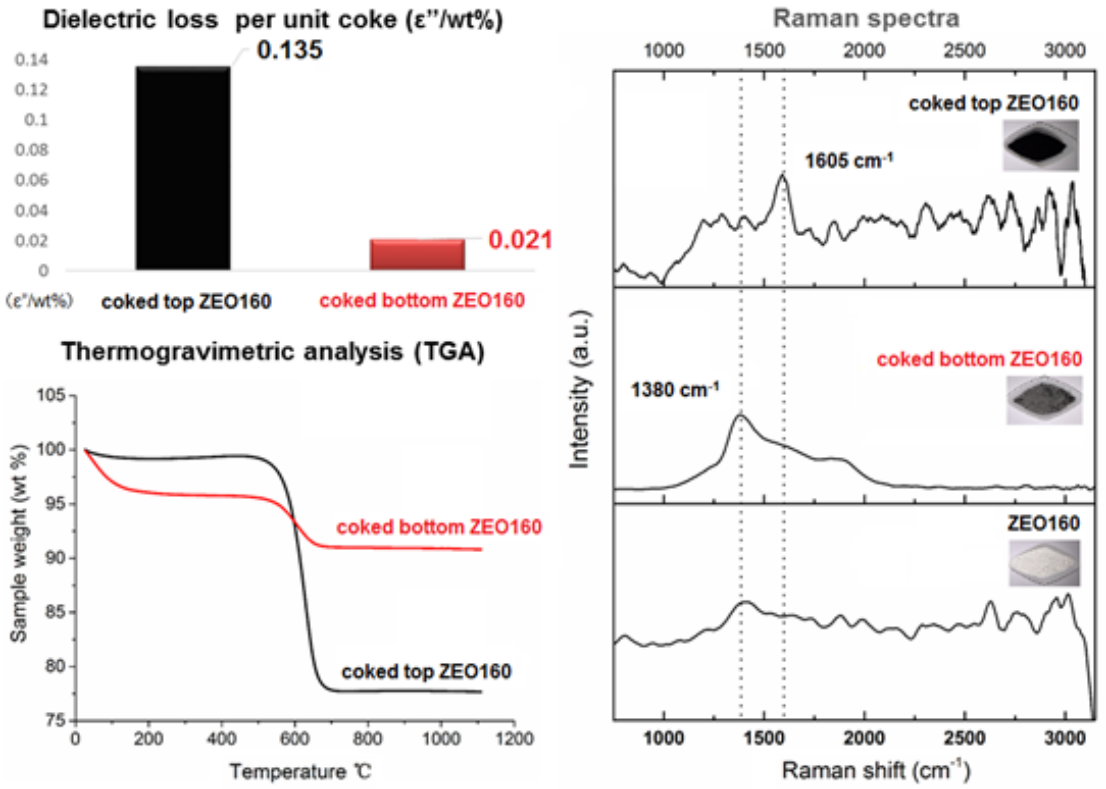

Fig. 5.11 Dielectric loss per unit weight coke (ε”/wt%) was calculated for coked top ZEO 160 and coked bottom ZEO 160 samples, respectively. TGA (physic & chemical approaches) indicates a total coke amount (wt% of post-run sample) without specification, whereas Raman (spectroscopy methods) helps in coke species identification but lacks of quantification information

Regarding to ZEO160, cokes in the upper (top) part of the catalyst bed are mainly composed of poly-aromatics (~1605 cm^{-1} band in Raman spectra) in a large amount, while the post-run bottom sample shows a much lower coke deposition, with mildly enhanced Raman signals at bands between 1300-1550 cm^{-1}, partially overlapped with the zeolite framework and most possibly assigned to some olefinic, or aliphatic deposits (less-dehydrogenated) as precursors to heavy coke species. [42, 232] As shown in Fig. 5.11, an apparently higher ε”/wt% value (0.135) is achieved by those

deposited poly-aromatic species which are predominant only in the coked top ZEO160 sample but hardly observable in the coked bottom ZEO160 sample. Similar results have been observed in other sample groups (Fig. 5.10a-b). Those samples all experienced the same MTH conditions, but vary in coke composition, due to different zeolite types, reaction time periods or loading positions in reactor. Our investigations reveal that poly-aromatics apparently lead to a higher dielectric loss value when present in large portion in these samples. Olefins, paraffins and other less-dehydrogenated species contribute to only limited dielectric loss values and when present in large proportions in coke contents can be readily separated from those aromatic cokes due to their much lower ε"/wt% values (e.g. 0.021 in Fig. 5.11) Therefore, by comparing the calculated 'ε"/wt%' value, different coke compositions can be separated.

Notably, the deeper dehydrogenated (graphitised) status of poly-aromatics could be a key character for their apparently higher dielectric loss values, where we would imagine a rich sp^2 carbon abundance exists. [12] This is borne out by the very poor or even invisible CP ^{13}C NMR responses on those samples (poly-aromatics rich) with higher ε"/wt% values, which reflects the high deficiency of hydrogen atoms (see appendix NMR Fig. ap.1-14, page 244). Removal of hydrogen forms more sp^2 carbons in the coke structure. [12] These sp^2 carbon centres in association possess highly mobile π electrons which are able to undergo Maxwell-Wagner polarization to a greater extent than the sp^3 carbons (this process generates current and causes energy loss in terms of heat), and lead to the enhanced dielectric loss efficiencies (reflected

by ‘ε”/wt%). [68]

It should be noted that the exact ε”/wt% values for most of the lightly-coked samples (e.g. the bottom or 2h reacted samples, where poly-aromatics are not predominant in total coke contents) should be lower than the currently presented data, as their TGA weight losses before 200 ^{o}C have not been taken into the calculation (this is because TGA weight loss due to moisture is also included in this temperature range), and there must have been a certain portion of coke weight accordingly missed due to the light organic deposits of lower volatile points (it seems that this is not the case for the heavily-coked samples with poly-aromatics dominating in coke). Therefore, we would imagine that the real difference in signal response or the microwave absorption efficiency (e.g. ε”/wt%) between the heavily-coked samples (poly-aromatics dominate) and lightly-coked samples (poly-aromatics are not predominant in cokes) would be much more obvious than the current stage results.

5.5.3 Short description of observed catalysis over tested samples

In this project, we mainly focused on the MW cavity response to different coke compositions, whereas the catalytic performances of tested samples are not fully reported. This is because the employed samples are all common zeolites which have been intensively studied in the previous literatures, [9, 12, 14, 220, 222]. On the other hand, time-on-stream monitoring of batch experiments are extremely time-consuming, which gives great pressures to other projects when there is a limited time of GC instrument occupation.

After careful consideration, we selectively presented the major aromatics yields obtained by the coked samples employed in our discussions. Here the MCM 22 and SAPO 34 zeolites mainly yield gas olefins, with very limited, negligible liquid oil production.

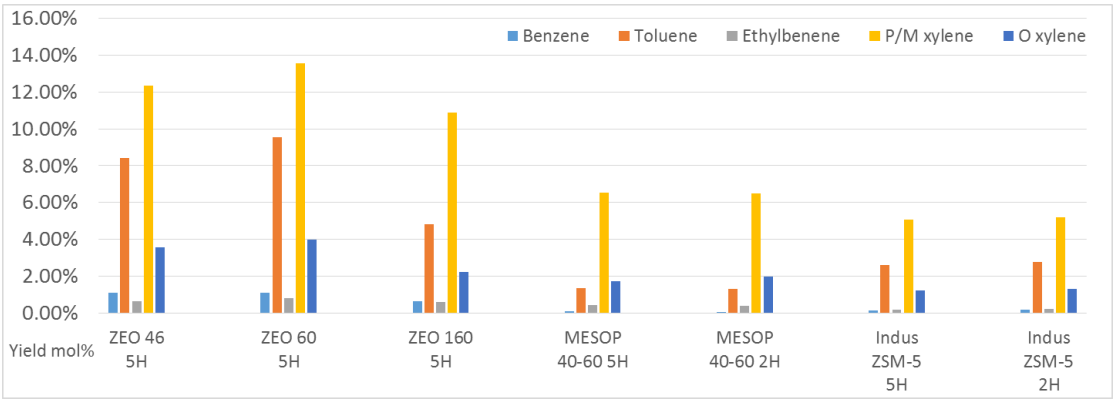

Fig. 5.12 Yields of major aromatic products achieved by different coked samples (SAPO 34 and MCM 22 are not included), achieved by MTH reactions at 450 ^{o}C, under atmosphere pressure, with a methanol WHSV = 8h^{-1}, reacted for 5h.

The 3 nano H-ZSM-5 zeolites have obtained much higher yield of aromatics as

compared with mesoporous H-ZSM-5 (micro particle size) and industrial H-ZSM-5 (regular micro-sized strong acidic sample, easier to get coked). Here the coke composition on different samples is mainly decided by the product transportability during MTH reactions, which is characteristic of different zeolite structures. For the nano zeolites, their smaller particle size, and gifted larger surface areas enables a faster product transportation, therefore, before the catalysts are coked by the deposited aromatics, more aromatics are transported out from the zeolite structure and present in product yields. Aromatics are also the major components in the cokes of mesoporous H-ZSM-5 and industrial H-ZSM-5, but these two samples apparently yield less aromatics due to the less effective product transport. [9, 14, 16]

There are other issues that have partially contributed to the coke formation on our tested zeolites, such as the employed MTH temperature, and a high reaction duty (methanol WHSV = $8h^{-1}$). However, we give a more important role to the zeolite cavity and particle size for controlling the MTH reaction product selectivity so as the corresponding coke compositions. [9] This is also the basis by which we managed to obtain the distinguished coke compositions.

5.5.4 Method verification: Physical mixtures of carbons/coked samples and pure zeolite

For verification of the above assumptions, we further measured 3 sample groups carefully prepared by mechanically mixing activated carbon (5wt%, 10wt% and 20wt% in the prepared mixtures), graphite (5wt%, 10wt% and 20wt% in the prepared mixtures), and particularly, coked top ZEO160 sample (coked top ZEO160 takes 5wt%, 10wt%, 20wt% and 50wt% in the prepared mixtures, corresponding to 1.1wt%, 2.2wt%, 4.4wt%, and 11wt% of the prepared mixtures are real coke contents, respectively, as TGA shows the undiluted coked top ZEO160 possesses ~22wt% coke contents) with fresh pure ZEO160 zeolite, respectively. In each case, both dielectric loss value ε" and MW plot are recorded to show the changes induced by different concentrations of coked sample / solid carbons in the prepared mixtures (Fig. 5.13-5.15).

Similar method was employed by Slocombe et.al, and it was noted the sample dielectric loss value correspondingly went up as the sp^2 hybridized content increased. [69] The solid carbons used in our research, of course, are much richer in sp^2 carbons than the nanodiamond particles employed by the reference study. Here high solid carbon concentrations (50wt% or higher) in the mixture resulted in 'over-saturated' signals, also reflected by 'zero peak' response in the MW plot. Therefore, the maximum solid carbon concentration in prepared mixtures was limited to 20wt%, and the 3 points picked at different concentrations were employed to draw a liner trend.

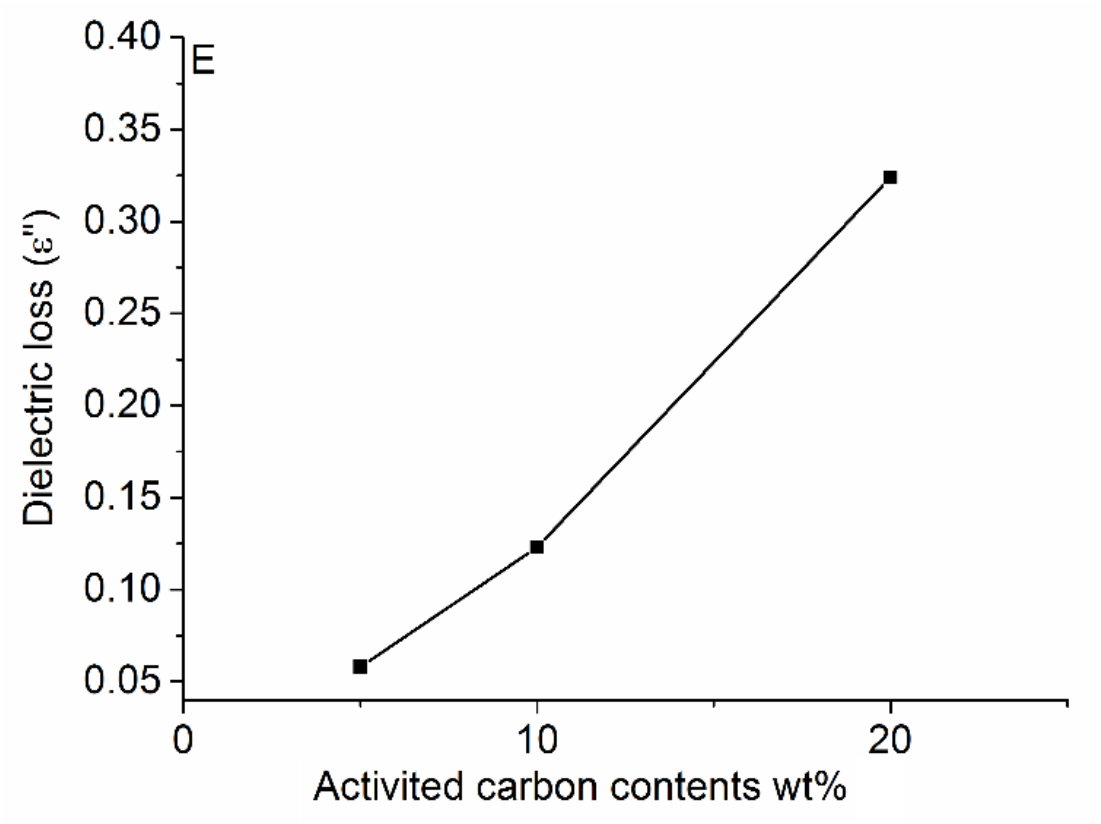

Fig. 5.13a Dielectric loss values as a function of activated carbon concentration

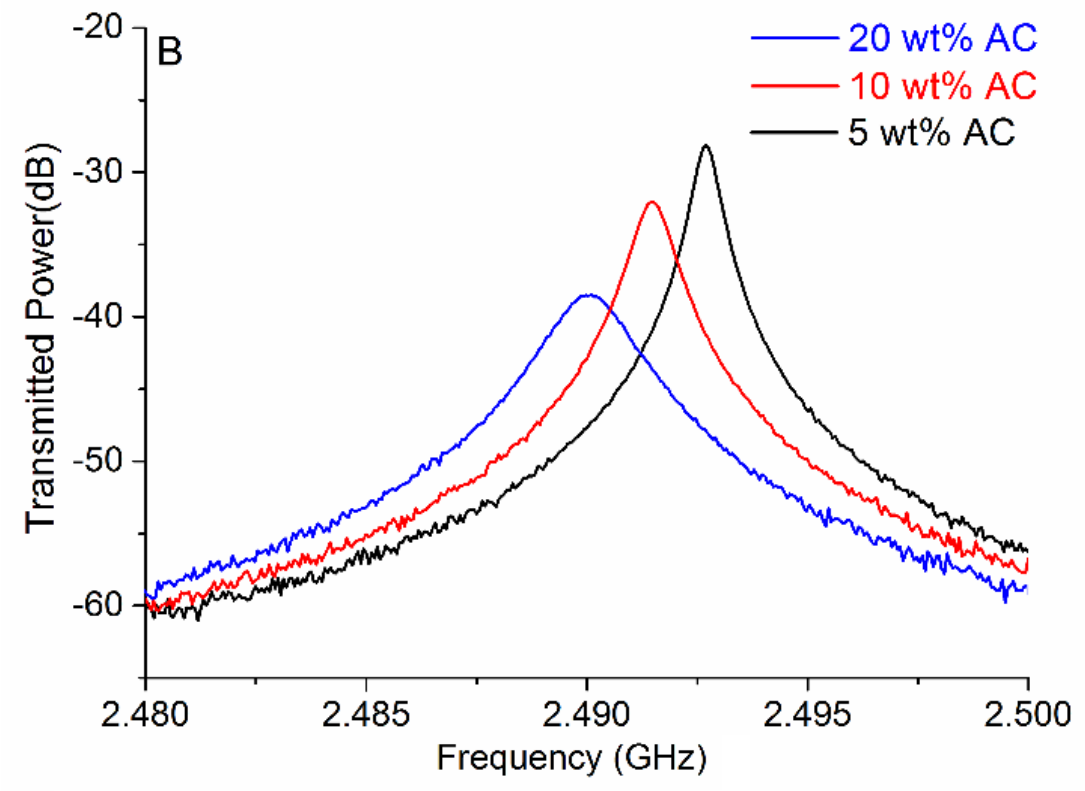

Fig. 5.13b MW plots corresponding to different activated carbon concentrations

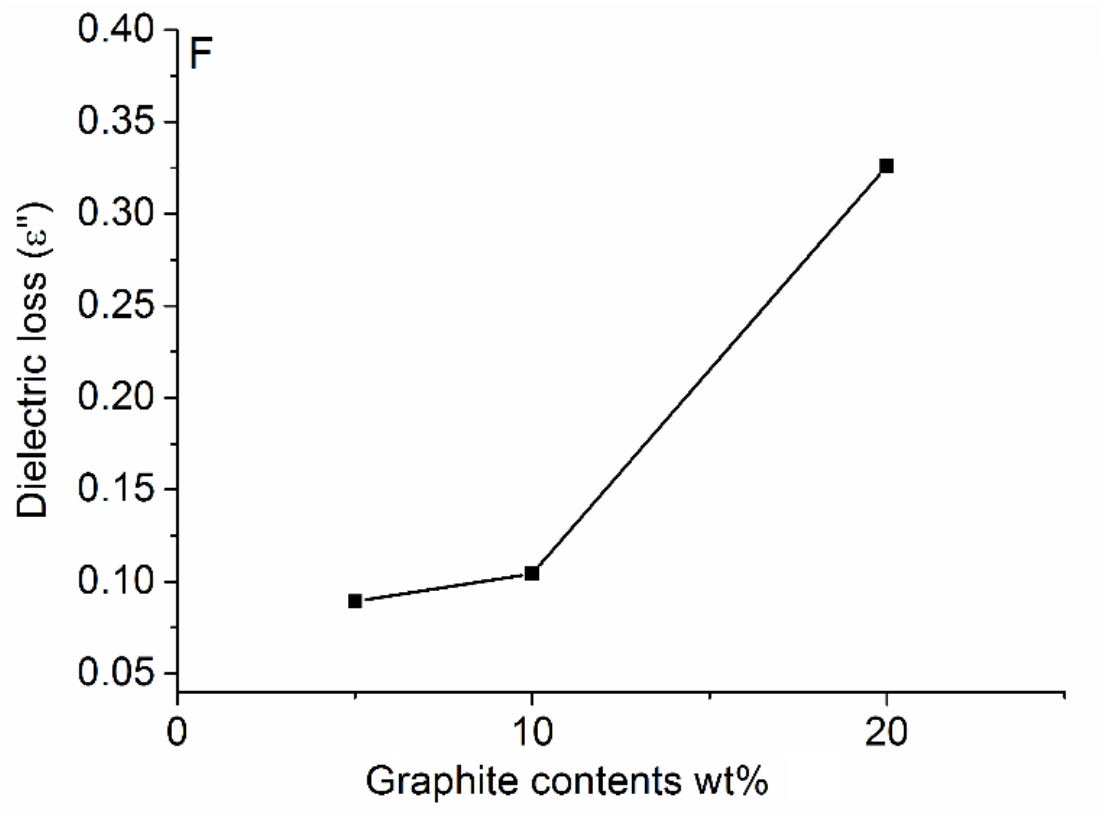

Fig. 5.14a Dielectric loss values as a function of graphite concentration

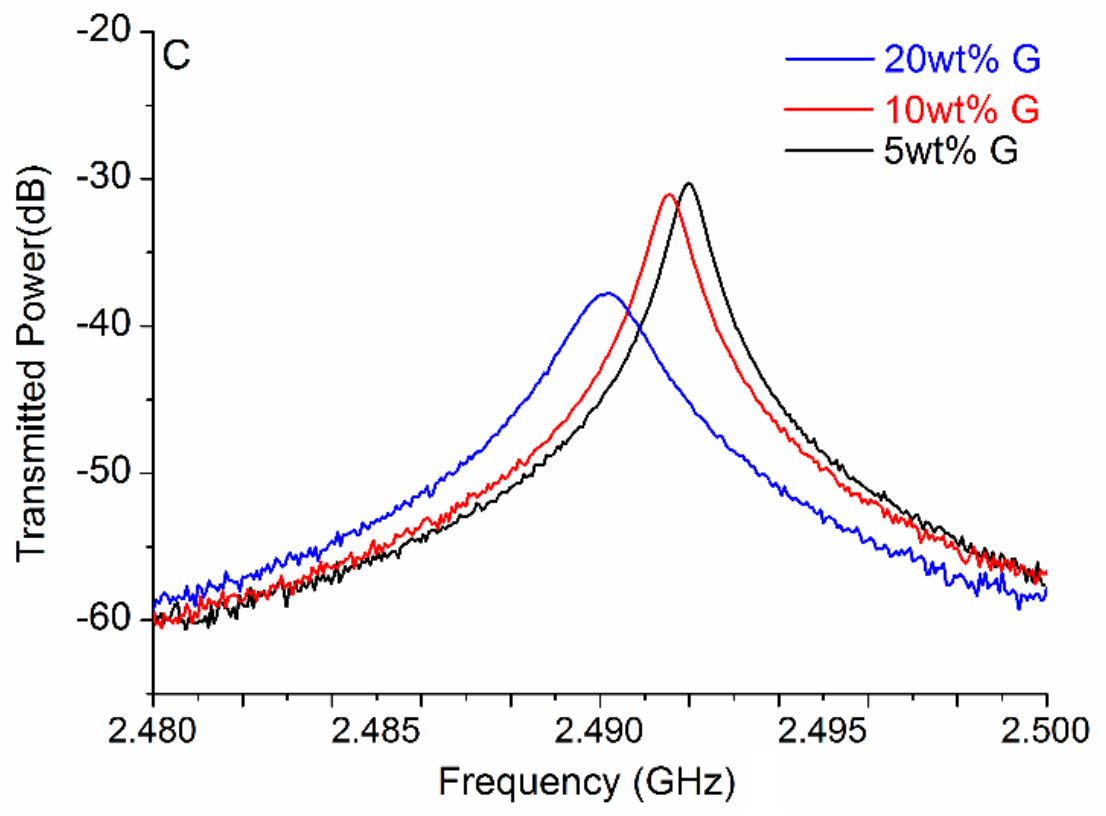

Fig. 5.14b MW plots corresponding to different graphite concentrations

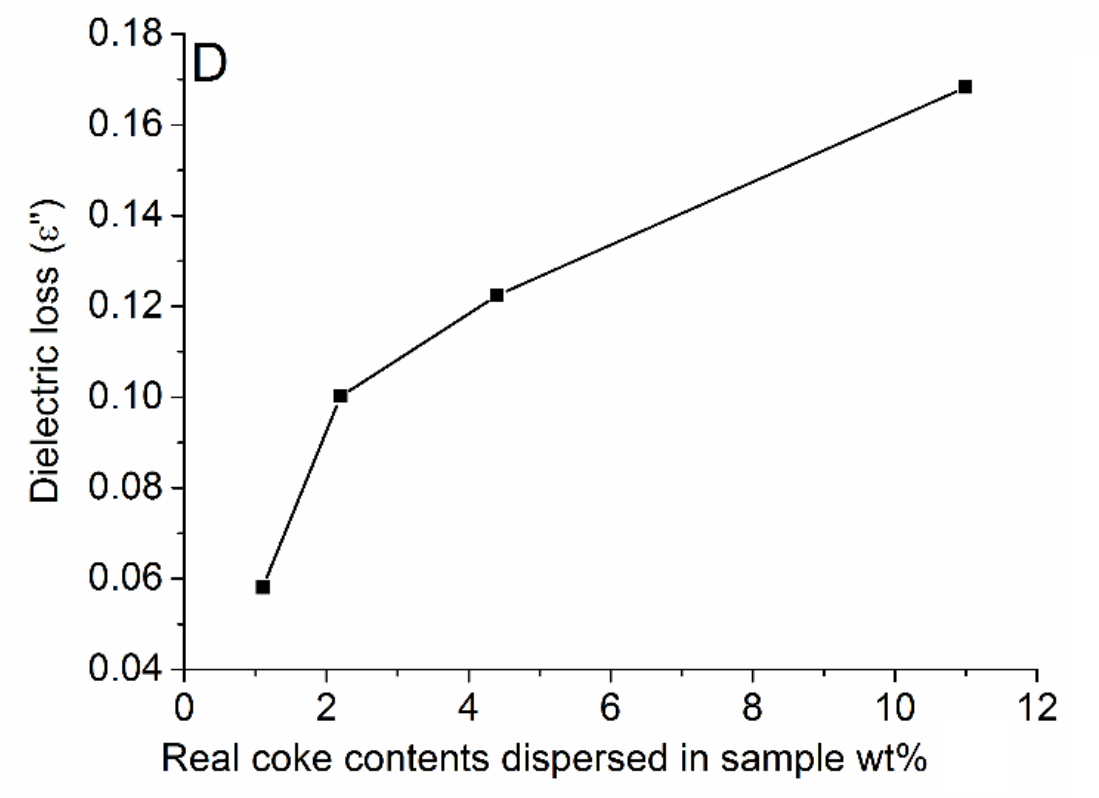

Fig. 5.15a Dielectric loss values as a function of the concentration of real coke contents in mixture (coked top ZEO160 + unreacted ZEO160)

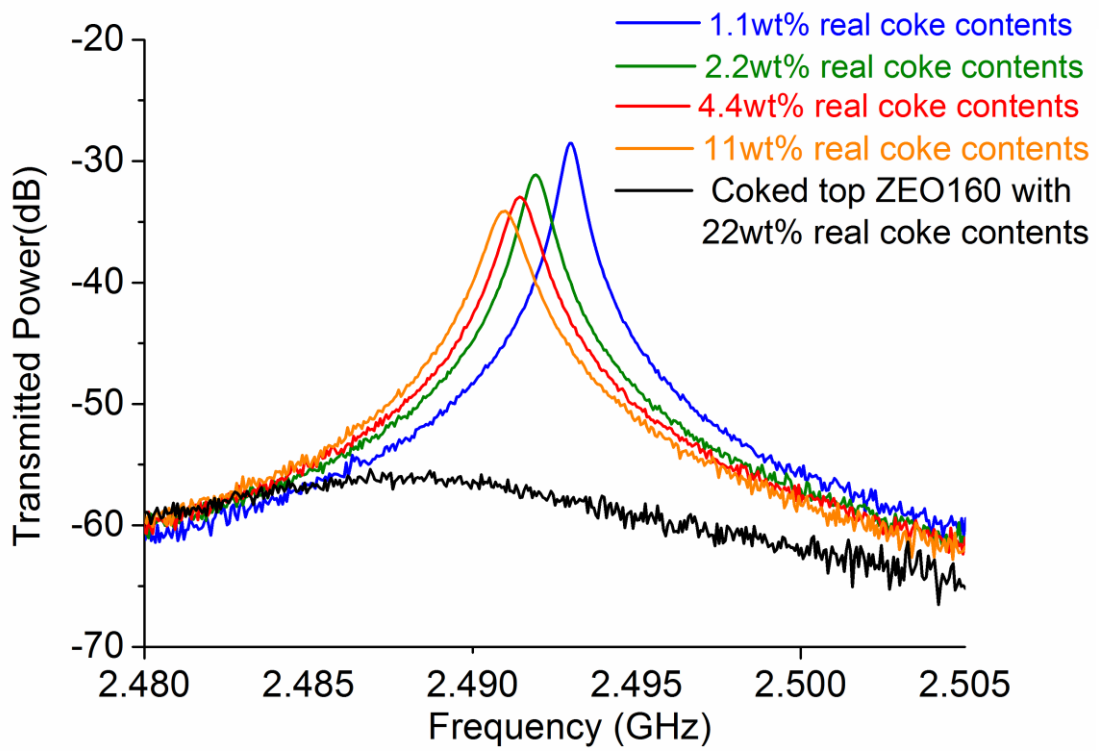

Fig. 5.15b MW plots corresponding to different real coke concentrations in mixture (coked top ZEO160 + unreacted ZEO160)

Since activated carbon and graphite are nearly pure carbons, in order to keep things consistent, the real coke contents (they can be treated as solid carbons) dispersed in the ‘coked top ZEO160 + unreacted ZEO160’ mixtures are employed (Fig. 5.15a and 5.15b).

Measured results confirm that solid carbon (activated carbon and graphite with rich sp^2 carbon abundance) dispersions in zeolite lead to dramatic increase of the sample dielectric loss value ε” as detected by our method. Besides, the ε” value also arises by increasing the coke contents (coked top ZEO160 sample) in the prepared mixtures. All the samples are well separated in the captured plots. We note that the undiluted coked top ZEO160 sample with 22wt% real coke contents exhibits a much higher ε” value (~2.979), not in a same magnitude, than all the mechanically mixed samples. Here the 22wt% coke contents are formed and dispersed naturally in the zeolite structure by reactions (a more uniform, effective, thinner-layer dispersion of carbon, less isolated by the zeolite structure), thus, possess a much higher microwave absorption efficiency. Mixing solid carbons with pure zeolite, and even diluting the same coked sample with pure zeolite cannot achieve the same effect, as the zeolite particles (with no coke deposits) further separate the coke species / solid carbons, which may restrict the dielectric loss efficiency of carbons in such case. [233] Herein, we propose that a more homogenously dispersed carbon deposition would further enhance the signal intensity of our technique, which happens to be the case that occurs in real coke formation over catalysts. Of course, this has also sparked our interests for a further study in the future.

5.6 Conclusion

We have demonstrated that different coking levels on acid zeolite catalysts can be readily distinguished by their dielectric loss properties, as reflected in their different ε" values achieved by our method. The contribution of unit coke contents to a complex dielectric loss value obtained by the coked sample, given by ε"/wt%, is entirely characteristic of the coke compositions formed under different experimental conditions. Particularly, we find that at the working frequencies near 2.45GHz, poly-aromatics dominate the microwave response, with outstanding ε"/wt% values, as compared to olefin/paraffin cokes. The observed results matched well with data obtained from previous coke characterization methods, e.g. Raman, TGA and ^{13}C NMR, but possess advantages in terms of volumetric measurement with full sample penetration, and higher sensitivity for deeply dehydrogenated cokes. The new microwave based approach targets on the nature of catalytic coke formation which is an evolution from sp^3 carbons to sp^2 carbons that forms graphite structures by progressive dehydrogenation under the reaction conditions. By far, the available electromagnetic waves that can be employed for catalyst analysis range from X-ray, to Ultraviolet, Visible, and Infrared, and here our findings embody the potential to extend the wavelength to the Microwaves.

Chapter 6 Conclusions & Outlook

In this short chapter, simple discussions are made for each projects, highlighting the important achievements with a simple forward look into their future applications.

6.1 Why these studies are important

For those poor-oil but coal-rich countries, coal chemistry based industry will still dominate in a long period, whereas problems such as increased CO_2 emission, higher cost in producing petrochemical products (e.g. aromatics, such as xylenes), and huge water usage are great challenges to be solved. Here methanol does play a most important role, as it has been given great hope to salt all the above problems when employed as a key intermediate product from coal. MTH process, with theoretically no CO_2 formation, generates high value petrochemical products, including aromatics and olefins (these two product types are the researching focus in our series of projects), and more importantly with water as the only non-organic liquid product (this part of water can be recycled). [15]

Further upgrading the current MTH technology requires improvements in the zeolite catalytic properties, via several approaches. The C-H bond activation governed by our Mo based promoters has shown enhanced early-time olefin production as well as a higher total aromatics yield in stark contrast to the original H-ZSM-5 zeolite. The Al-incorporation is an important exploration for the nano H-ZSM-5's larger scale

utilizations, and also gives a solution to face the harsher industrial reaction conditions (higher reaction pressures and etc.). The attempt to examine coke formation over a variety of zeo-types, with the microwave cavity perturbation technique, is for a more comprehensive analysis and prediction of catalyst deactivation. Particularly, we directly targets on the limitations in the traditional spectroscopy methods, such as limited penetrating depth for Raman and IR, as well as a very poor carbon signal response of those deeply-dehydrogenated compounds for ^{13}C NMR (Cross-Polarization without ^{13}C exchange).

The whole story of this thesis is made up of three components: 1) A method to enhance the zeolite catalytic properties with extra promoters; 2) An approach to scale up a good performance zeolite catalyst; as well as 3) A technique to monitor the potential catalyst deactivation by cokes. All of these are desired to contribute to a better MTH catalysis and rational zeolite catalyst design, and solve the increasing global energy and material crisis.

6.2 MoO_3/H-ZSM-5 prepared at a lower-than-usual temperature of 400 ºC

The most shining achievement in this project is no doubt that a lower-than-usual temperature of 400ºC, applied for both catalyst preparation (calcination) and MTH reaction, gave us more freedom to tailor the Mo active sites distribution in the H-ZSM-5 structure, balancing the number of zeolite channel Mo catalytic sites and the intrinsic zeolite Brønsted acidity.

Loading metal oxides, especially transition metal oxides as catalytic promoters, will effectively change the intrinsic zeolite acidity, thus, have more direct impacts on the resulted catalysis. [234-237] Here extra catalytic features, e.g. activation of a certain chemical structure in reactant/intermediate compounds, can also be introduced by which we can further adjust the reaction product selectivity. We attribute the catalytic function of those Mo active sites inside the H-ZSM-5 channel to the obtained C-H bond activation, which has helped to accelerate the olefin methylation and small hydrocarbon aromatization processes during the MTH reaction, thus, leading to the enhanced olefin yields and higher aromatics production. The MoO_3 species on the zeolite surface, as we supposed, has further reduced the actual size of zeolite channel openings, which resulted in the selectively higher BTX yield on those MoO_3/H-ZSM-5 samples.

Due to the technical limitations, a further specification of the catalytic Mo active sites formed inside the zeolite channels cannot be realized at the current stage, and we have proposed a Mo-oxy carbide structure based on the previous studies, which has the highest potential to be formed in our employed MTH conditions and also promotes the C-H dissociation by polarizations.

More efforts would be made on the investigations to draw the exact chemical structure of those Mo active sites that have catalyzed the 400^{o}C MTH reaction, better with in-situ instruments. Or, a possible way is to bring in theoretical calculations such as a Density Functional Theory (DFT) calculation, to further confirm the potentially-existed catalytic compounds. We will also try to adjust the coke tolerance

of those MoO_3/H-ZSM-5 catalysts, while maintaining their enhanced olefin and aromatic yields. And here the balance between the number of active Mo catalytic sites inside zeolite channels, and the zeolite intrinsic Brønsted acidity of course is still the most important.

6.3 Al-incorporated nano H-ZSM-5 zeolites and the amplified MTH reaction

After series of MTH reactions in amplified conditions (catalyst loading increased to 20g vs. 1g commonly used by laboratory investigations), we conclude that the major catalytic activities of shaped Al-incorporated nano H-ZSM-5 catalysts, for an efficient methanol conversion, are still mainly dependent upon the amount of Brønsted acid sites in the zeolite framework, which is somewhat determined by the Si/Al ratio of the parent zeolite. However, the incorporated Al binders have unique impacts on the time-on-stream gas olefin yields. The obtained catalytic properties rely on a delayed H_2 transfer process, which is possibly due to the incorporated Al cations. The protecting effects on the Brønsted acid sites by the incorporated Al binders are attributed to a potentially existed pool of tetrahedrally coordinated Al. The Al binder phases also help to prevent the coke accumulation on catalytic sites by efficient dispersion of coke species, also observed in the TEM pictures. Coke formation over different sample groups are various, but have shown a favourite of aromatics on the parent H-ZSM-5 zeolites, and a preference to olefinic species on the Al-incorporated samples.

The proposed ‘pool of tetrahedrally coordinated Al’, formed as a result of the Al incorporation, is such an interesting phenomenon that firstly leads to the reduction of zeolite Brønsted acid sites due to the neutralization by AlOOH species, but subsequently, plays an important role to ‘complement’ the zeolite Al sites, thus, the Brønsted acid sites, for a sustainable MTH reaction. Although our NMR evidences well illustrated the evolution from γ – Al_2O_3 framework Al (octahedrally coordinated, 12ppm) to zeolite framework Al (tetrahedrally coordinated, 55ppm) via γ – Al_2O_3 extra-framework Al (tetrahedrally coordinated, 70ppm) and zeolite extra-framework Al (tetrahedrally coordinated, showing as broadenings at around 55ppm), a further explanation from the theoretical perspective would ulteriorly upgrade the knowledge. On the other hand, more experiments on other different zeo-types, e.g. H-SAPO-34, are recalled to further confirm the ‘tetrahedrally coordinated Al pool’ hypothesis, and also for a better utilization of the potential catalytic benefits.

Recent investigations have highlighted the importance of nano-sized zeolites for their advantages in reaction mass transfer, anti-coking properties, as well as a better dispersion of catalytic promoters. [238-241] However, the industrial utilization of those nano zeolites, in a scaled-up plant is greatly restricted by the ‘form’ of which they are. For instance, powder nano zeolites easily lead to reactor system blocking even in the laboratory experiments. Therefore, there is no doubt that they should be ‘shaped’ to suit with the more critical industrial requirements. Our investigations have indicated a good combination of Al_2O_3 binder phase with the parent H-ZSM-5 nano particles, with part of their nano properties maintained for the reaction. A direct evidence is the SEM (Fig.

4.8) shows that the inter-crystallite space between nano H-ZSM-5 particles are not fully filled, on the other hand, TEM pictures (Fig. 4.11-4.13) also confirm that the 'incorporation' of Al is visually seen in terms of a thin layer, covering the parent zeolite nano particles. At the current stage, as suggested by our colleagues from Qingdao Lianxin company, the 30wt% of $\gamma - Al_2O_3$ employed is to reserve as many as the original catalytic properties while obtain a maximum mechanical strength of the shaped catalysts. At this incorporating level, although the 'pool of tetrahedrally coordinated Al' may have complemented the zeolite Al sites to a certain extent, there is still unavoidable loss of the zeolite Brønsted acid sites in the early preparation process. Therefore, we would foresee a reduced Al usage may possess better catalytic performance as more original zeolite Brønsted acid sites can be saved. The reaction pressure employed in our experiments is 6bar and therefore the mechanical strength of samples are more important, by contrast, atmospheric reaction condition (~1bar reaction pressure) is also available in many cases, so the mechanical strength governed by incorporated Al species can be reduced to a lower level.

Nevertheless, the customized, amplified catalysis itself also possesses many advantages, such as the experiments employing shaped catalysts rather than powders. Here many potential problems can be pre-exposed before the larger scale applications, thus, benefiting the industry. In fact, the catalyst loading volume can be further enlarged, and this would be put into our future works in a more critical, but closer-factory reaction condition.

6.4 Coke analysis via Microwave based techniques

In this project, we have demonstrated that different coking levels on acid zeolite catalysts can be readily distinguished with their dielectric loss properties, as reflected by their different ε" values detected with the Microwave Resonance Cavity. The contribution of unit coke contents to a complex dielectric loss value obtained by the coked sample, given by ε"/wt%, is entirely characteristic of the coke compositions formed under different experimental conditions. Particularly, we find that at the working frequencies near 2.45GHz, poly-aromatics dominate in the microwave response, with outstanding ε"/wt% values, as compared to those olefin/paraffin cokes. Here the separation of different coke contents is based on the nature of catalytic coke formation which is an evolution from sp^3 carbons to sp^2 carbons that forms graphite structures by progressive dehydrogenation under the reaction conditions.

A lack of information from cokes inside zeolite cavities/channels, due to the technical limitations (the zeolite framework should be melted so as to extract the inner cokes), has been a major challenge of commonly used coke analysis methods. Infrared and Raman spectroscopies, as a surficial technique, are restricted by the electromagnetic energy penetrating depth when beamed onto a sample surface (energy is dissipated when passes through the sample structures). The NMR spectroscopy has somehow completed the gap, as it is also a volumetric technique with full sample body penetration scanning in the configured experiments (here the sample penetration

depth is not a major issue). However, when applied to those deeply-dehydrogenated species, e.g. poly-aromatics as the major coke contents, an extremely poor signal response without ^{13}C exchange (this apparently increases the cost of such analysis) leads to unavoidable restrictions. [12, 225] The microwave cavity perturbation technique has similar volumetric advantages as the NMR (full sample penetration in the set experimental conditions), but has extremely sensitive response to those deeper dehydrogenated species, which has been proved in our results (poly-aromatics exhibited a very high ε"/wt% value). Previous works have quantified the sp^2 carbon contents with observed microwave responses, [68] and this brings us a great confidence to develop the MW based new method for more accurate specification and quantification of different coke species. Here a simple comparison is shown in table 6.1.

Table. 6.1 A comparison between commonly employed coke analysis methods with microwave cavity perturbation analysis [12]

Methods	Scope of measurements	Volumetric measurement	Penetration depth	Specification	Quantification	Extra cost in coke analysis
Infrared	point	no	limited	yes	semi	----------
Raman	point	no	limited	yes	semi	UV
NMR	whole sample	yes	full	yes	semi	^{13}C exchange
TGA	whole sample	yes	----------	no	yes	----------
MW	whole sample	yes	full	yes	In principle	----------

In the future, a most attractive target would be getting the technique patented (already being proceeded), and we will also come back for a larger, amplified

application of the technique. Increase of target sample volume will greatly shorten the distance to a real industrial application, and we have strong confidence to see the technique's future application on a real reaction plant, such a full penetration measurement when adjusted and applied to the whole catalyst bed will more effectively monitor the catalyst coke formation and here an on-line analysis can be better defined.

References

1. Olah, G.A., *Towards Oil Independence Through Renewable Methanol Chemistry.* Angew. Chem., Int. Ed., 2013. **52**(1): p. 104-107.
2. Shafiee, S. and E. Topal, *When will fossil fuel reserves be diminished?* Energy policy, 2009. **37**(1): p. 181-189.
3. Ross, J.R.H., *Heterogenous Catalysis - Frundamentals and Applications*. 2012, Amsterdam, The Netherlands: Elsevier
4. Davis, B.E., R.C. Maxwell, and A.H. Singleton, *Production of Transportation Fuels Using Underground Coal-Gasification and Fisher-Tropsch Technology.* Proceedings of the 17th International Conference on Coal Utilization & Slurry Technologies, 1992: p. 397-408.
5. Chemweekly.com. *Coal Based Energy & Chemicals*. 2012 [cited 2015; Available from: http://www.chemweekly.com/images/ASIACHEM_Products.gif.
6. Hunter, N.R., et al., *Methanol formation at high pressure by the catalyzed oxidation of natural gas and by the sensitized oxidation of methane.* Appl. Catal., 1990. **57**(1): p. 45-54.
7. Hamelinck, C.N. and A.P.C. Faaij, *Future prospects for production of methanol and hydrogen from biomass.* J. Power Sources, 2002. **111**(1): p. 1-22.
8. Zhen, X. and Y. Wang, *An overview of methanol as an internal combustion engine fuel.* Renewable Sustainable Energy Rev., 2015. **52**: p. 477-493.
9. Olsbye, U., et al., *Conversion of Methanol to Hydrocarbons: How Zeolite Cavity and Pore Size Controls Product Selectivity.* Angew. Chem., Int. Ed., 2012. **51**(Copyright (C) 2013 American Chemical Society (ACS). All Rights Reserved.): p. 5810-5831.
10. Mitchell, S., N.-L. Michels, and J. Perez-Ramirez, *From powder to technical body: the undervalued science of catalyst scale up.* Chem. Soc. Rev., 2013. **42**(14): p. 6094-6112.
11. Hargreaves, J.S.J. and A.L. Munnoch, *A survey of the influence of binders in zeolite catalysis.* Catalysis Science & Technology, 2013. **3**(5): p. 1165-1171.
12. Guisnet, M. and R.F. Ribeiro, *Deactivation and Regeneration of Zeolite Catalysts*. CATALYTIC SCIENCE SERIES, ed. H.G. J. Vol. VOL.9. 2011, London: Imperial College Press. 340.
13. Spivey, J.J. and G. Hutchings, *Catalytic aromatization of methane.* Chemical Society Reviews, 2014. **43**(3): p. 792-803.
14. Ilias, S. and A. Bhan, *Mechanism of the Catalytic Conversion of Methanol to Hydrocarbons.* ACS Catalysis, 2013. **3**(1): p. 18-31.
15. Stocker, M., *Methanol-to-hydrocarbons: catalytic materials and their behavior.* Microporous Mesoporous Mater., 1999. **29**(1-2): p. 3-48.
16. Haw, J.F., et al., *The Mechanism of Methanol to Hydrocarbon Catalysis.* Acc. Chem. Res., 2003. **36**(5): p. 317-326.
17. Mikkelsen, Ø., P.O. Rønning, and S. Kolboe, *Use of isotopic labeling for mechanistic studies of the methanol-to-hydrocarbons reaction. Methylation of toluene with methanol over H-ZSM-5, H-mordenite and H-beta.* Microporous and Mesoporous Materials, 2000. **40**(1–3): p. 95-113.
18. Sullivan, R.F., et al., *A New Reaction That Occurs in the Hydrocracking of Certain Aromatic Hydrocarbons.* Journal of the American Chemical Society, 1961. **83**(5): p. 1156-1160.

19. Mole, T., G. Bett, and D. Seddon, *Conversion of methanol to hydrocarbons over ZSM-5 zeolite: An examination of the role of aromatic hydrocarbons using 13carbon- and deuterium-labeled feeds.* Journal of Catalysis, 1983. **84**(2): p. 435-445.
20. Langner, B.E., *Reactions of methanol on zeolites with different pore structures.* Applied Catalysis, 1982. **2**(4): p. 289-302.
21. Dahl, I. and S. Kolboe, *On the reaction mechanism for propene formation in the MTO reaction over SAPO-34.* Catalysis Letters, 1993. **20**(3-4): p. 329-336.
22. Dahl, I.M. and S. Kolboe, *On the Reaction Mechanism for Hydrocarbon Formation from Methanol over SAPO-34: I. Isotopic Labeling Studies of the Co-Reaction of Ethene and Methanol.* Journal of Catalysis, 1994. **149**(2): p. 458-464.
23. Svelle, S., et al., *Conversion of Methanol into Hydrocarbons over Zeolite H-ZSM-5: Ethene Formation Is Mechanistically Separated from the Formation of Higher Alkenes.* Journal of the American Chemical Society, 2006. **128**(46): p. 14770-14771.
24. Bjørgen, M., et al., *Conversion of methanol to hydrocarbons over zeolite H-ZSM-5: On the origin of the olefinic species.* Journal of Catalysis, 2007. **249**(2): p. 195-207.
25. Ilias, S. and A. Bhan, *Tuning the selectivity of methanol-to-hydrocarbons conversion on H-ZSM-5 by co-processing olefin or aromatic compounds.* Journal of Catalysis, 2012. **290**: p. 186-192.
26. Song, W., et al., *An Oft-Studied Reaction That May Never Have Been: Direct Catalytic Conversion of Methanol or Dimethyl Ether to Hydrocarbons on the Solid Acids HZSM-5 or HSAPO-34.* Journal of the American Chemical Society, 2002. **124**(15): p. 3844-3845.
27. Michels, N.-L., S. Mitchell, and J. Perez-Ramirez, *Effects of Binders on the Performance of Shaped Hierarchical MFI Zeolites in Methanol-to-Hydrocarbons.* ACS Catal., 2014. **4**(8): p. 2409-2417.
28. Shihabi, D.S., et al., *Aluminum insertion into high-silica zeolite frameworks.* Journal of Catalysis, 1985. **93**(2): p. 471-474.
29. Han, D.H., O.O. Park, and Y.G. Kim, *Study on the possible existence of multiplicity features in ethene hydrogenation over platinum/boehmite catalysts.* Appl. Catal., A, 1992. **86**(2): p. 71-82.
30. Martin, A., et al., *Effect of silicon-aluminum ratio and type of binder on the catalytic properties of HZSM-5 catalysts.* J. Chem. Soc., Faraday Trans., 1993. **89**(8): p. 1277-82.
31. Mitchell, S., et al., *Visualization of hierarchically structured zeolite bodies from macro to nano length scales.* Nat. Chem., 2012. **4**(10): p. 825-831.
32. Perez-Ramirez, J., et al., *Hierarchical zeolites: enhanced utilisation of microporous crystals in catalysis by advances in materials design.* Chemical Society Reviews, 2008. **37**(11): p. 2530-2542.
33. Ilias, S. and A. Bhan, *Mechanism of the Catalytic Conversion of Methanol to Hydrocarbons.* ACS Catal., 2013. **3**(1): p. 18-31.
34. Bjorgen, M., et al., *Conversion of methanol to hydrocarbons over zeolite H-ZSM-5: On the origin of the olefinic species.* Journal of Catalysis, 2007. **249**(2): p. 195-207.
35. Guisnet, M. and P. Magnoux, *Coking and deactivation of zeolites: Influence of the Pore Structure.* Applied Catalysis, 1989. **54**(1): p. 1-27.
36. Magnoux, P., et al., *New Technique for the Characterization of Carbonaceous Compounds Responsible for Zeolite Deactivation*, in *Studies in Surface Science and Catalysis*, B. Delmon and G.F. Froment, Editors. 1987, Elsevier. p. 317-330.

37. Guisnet, M. and P. Magnoux, *Organic chemistry of coke formation.* Applied Catalysis A: General, 2001. **212**(1–2): p. 83-96.
38. Gallezot, P., et al., *Coking, aging, and regeneration of zeolites. VII. Electron microscopy and EELS studies of external coke deposits on USHY, H-OFF, and H-ZSM-5 zeolites.* J. Catal., 1988. **114**(1): p. 100-11.
39. Bibby, D.M., R.F. Howe, and G.D. McLellan, *Coke formation in high-silica zeolites.* Applied Catalysis A: General, 1992. **93**(1): p. 1-34.
40. Schulz, H., Z. Siwei, and W. Baumgartner, *Coke Forming Reactions During Methanol Conversion on Zeolite Catalysts*, in *Studies in Surface Science and Catalysis*, B. Delmon and G.F. Froment, Editors. 1987, Elsevier. p. 479-492.
41. Li, C. and P.C. Stair, *Ultraviolet Raman spectroscopy characterization of coke formation in zeolites.* Catalysis Today, 1997. **33**(1–3): p. 353-360.
42. Chua, Y.T. and P.C. Stair, *An ultraviolet Raman spectroscopic study of coke formation in methanol to hydrocarbons conversion over zeolite H-MFI.* J. Catal., 2003. **213**(1): p. 39-46.
43. Zhang, W.P., et al., *A high-resolution solid-state NMR study on nano-structured HZSM-5 zeolite.* Catalysis Letters, 1999. **60**(1-2): p. 89-94.
44. Mores, D., et al., *Space- and Time-Resolved In-situ Spectroscopy on the Coke Formation in Molecular Sieves: Methanol-to-Olefin Conversion over H-ZSM-5 and H-SAPO-34.* Chemistry – A European Journal, 2008. **14**(36): p. 11320-11327.
45. Arstad, B. and S. Kolboe, *Methanol-to-hydrocarbons reaction over SAPO-34. Molecules confined in the catalyst cavities at short time on stream.* Catalysis Letters, 2001. **71**(3-4): p. 209-212.
46. Nordvang, E.C., et al., *Effects of Coke Deposits on the Catalytic Performance of Large Zeolite H-ZSM-5 Crystals during Alcohol-to-Hydrocarbon Reactions as Investigated by a Combination of Optical Spectroscopy and Microscopy.* Chemistry – A European Journal, 2015. **21**(48): p. 17324-17335.
47. Norval, G.W., et al., *Olefin conversion over zeolite H-ZSM-5.* Can. J. Chem. Eng., 1989. **67**(3): p. 521-3.
48. Bibby, D.M., et al., *Coke formation in zeolite ZSM-5.* Journal of Catalysis, 1986. **97**(2): p. 493-502.
49. Menéndez, J.A., et al., *Microwave heating processes involving carbon materials.* Fuel Processing Technology, 2010. **91**(1): p. 1-8.
50. Risman, P. *Microwave dielectric properties of foods and some other substances*. 2009. Woodhead Publishing Ltd.
51. Chakraborty, R., et al., *Literature study of microwave-assisted digestion using electrothermal atomic absorption spectrometry.* Fresenius' J. Anal. Chem., 1996. **355**(2): p. 99-111.
52. Matusiewicz, H., *DEVELOPMENT OF A HIGH PRESSURE/TEMPERATURE FOCUSED MICROWAVE HEATED TEFLON BOMB FOR SAMPLE PREPARATION.* Analytical Chemistry, 1994. **66**(5): p. 751-755.
53. Smith, F.E. and E.A. Arsenault, *Microwave-assisted sample preparation in analytical chemistry.* Talanta, 1996. **43**(8): p. 1207-1268.
54. Deaker, M. and W. Maher, *Low volume microwave digestion for the determination of selenium in marine biological tissues by graphite furnace atomic absorption spectroscopy.* Analytica Chimica Acta, 1997. **350**(3): p. 287-294.

55. Beary, E.S., et al., *Determination of Environmental Lead Using Continuous-Flow Microwave Digestion Isotope Dilution Inductively Coupled Plasma Mass Spectrometry.* Anal. Chem., 1997. **69**(4): p. 758-766.
56. Caminati, W. and J.-U. Grabow. *Microwave spectroscopy: molecular systems*. 2009. Elsevier B.V.
57. Barrow, R.F. and P. Crozet, *Gas-phase molecular spectroscopy.* Annu. Rep. Prog. Chem., Sect. C: Phys. Chem., 1997. **93**: p. 187-256.
58. Gabriel, C., et al., *Dielectric parameters relevant to microwave dielectric heating.* Chemical Society Reviews, 1998. **27**(3): p. 213-224.
59. Gabriel, C., et al., *Dielectric parameters relevant to microwave dielectric heating.* Chem. Soc. Rev., 1998. **27**(3): p. 213-224.
60. Kappe, C.O., *Microwave dielectric heating in synthetic organic chemistry.* Chem. Soc. Rev., 2008. **37**(6): p. 1127-1139.
61. Zhang, X. and D.O. Hayward, *Applications of microwave dielectric heating in environment-related heterogeneous gas-phase catalytic systems.* Inorg. Chim. Acta, 2006. **359**(11): p. 3421-3433.
62. Galema, S.A., *Microwave chemistry.* Chemical Society Reviews, 1997. **26**(3): p. 233-238.
63. Thostenson, E.T. and T.W. Chou, *Microwave processing: fundamentals and applications.* Composites Part A: Applied Science and Manufacturing, 1999. **30**(9): p. 1055-1071.
64. Ciacchi, F.T., S.A. Nightingale, and S.P.S. Badwal, *Microwave sintering of zirconia-yttria electrolytes and measurement of their ionic conductivity.* Solid State Ionics, 1996. **86-88**(Pt. 2): p. 1167-1172.
65. Juang, R.-S., et al., *Microwave-assisted synthesis of titania coating onto polymeric separators for improved lithium-ion battery performance.* J. Power Sources, 2015. **286**: p. 526-533.
66. Zlotorzynski, A., *The application of microwave radiation to analytical and environmental chemistry.* Critical Reviews in Analytical Chemistry, 1995. **25**(1): p. 43-76.
67. Zlotorzynski, A., *The application of microwave radiation to analytical and environmental chemistry.* Crit. Rev. Anal. Chem., 1995. **25**(1): p. 43-76.
68. Porch, A., D. Slocombe, and P.P. Edwards, *Microwave absorption in powders of small conducting particles for heating applications.* Physical Chemistry Chemical Physics, 2013. **15**(8): p. 2757-2763.
69. Slocombe, D., et al., *Microwave properties of nanodiamond particles.* Applied Physics Letters, 2013. **102**(24): p. 244102.
70. Cuenca, J.A., et al., *Microwave determination of sp 2 carbon fraction in nanodiamond powders.* Carbon, 2015. **81**: p. 174-178.
71. Summers, J.C. and S.A. Ausen, *Catalyst impregnation: Reactions of noble metal complexes with alumina.* Journal of Catalysis, 1978. **52**(3): p. 445-452.
72. Kazansky, V., et al., *Nature of the sites of dissociative adsorption of dihydrogen and light paraffins in ZnHZSM-5 zeolite prepared by incipient wetness impregnation.* Catalysis letters, 2000. **66**(1-2): p. 39-47.
73. Bowker, M., *THE BASIS AND APPLICATIONS OF HETEROGENEOUS CATALYSIS. Edition en anglais*. 1998: Oxford University Press, Incorporated.
74. Thomas, J.M. and W.J. Thomas, *Principles and practice of heterogeneous catalysis*. 2014: John Wiley & Sons.

75. Dann, S.E., *Reactions and characterization of solids*. Vol. 2. 2000: Royal Society of Chemistry.
76. Karge, H.G. and J. Weitkamp, *Molecular Sieves.* Science and Technology, 1998. **1**.
77. Stefanidis, S.D., et al., *In-situ upgrading of biomass pyrolysis vapors: Catalyst screening on a fixed bed reactor.* Bioresour. Technol., 2011. **102**(17): p. 8261-8267.
78. Ni, J. and F.C. Meunier, *Esterification of free fatty acids in sunflower oil over solid acid catalysts using batch and fixed bed-reactors.* Appl. Catal., A, 2007. **333**(1): p. 122-130.
79. Chica, A., A. Corma, and M.E. Domine, *Catalytic oxidative desulfurization (ODS) of diesel fuel on a continuous fixed-bed reactor.* J. Catal., 2006. **242**(2): p. 299-308.
80. Adam, J., et al., *In situ catalytic upgrading of biomass derived fast pyrolysis vapours in a fixed bed reactor using mesoporous materials.* Microporous Mesoporous Mater., 2006. **96**(1-3): p. 93-101.
81. Benkli, Y.E., et al., *Modification of organo-zeolite surface for the removal of reactive azo dyes in fixed-bed reactors.* Water Res., 2005. **39**(2-3): p. 487-493.
82. Zhang, C.-L., et al., *Aromatization of methane in the absence of oxygen over Mo-based catalysts supported on different types of zeolites.* Catal. Lett., 1999. **56**(4): p. 207-213.
83. Adjaye, J.D. and N.N. Bakhshi, *Production of hydrocarbons by catalytic upgrading of a fast pyrolysis bio-oil. Part I: Conversion over various catalysts.* Fuel Process. Technol., 1995. **45**(3): p. 161-83.
84. Wang, L., et al., *Dehydrogenation and aromatization of methane under non-oxidizing conditions.* Catal. Lett., 1993. **21**(1-2): p. 35-41.
85. Aucejo, A., et al., *Beckmann rearrangement of cyclohexanone-oxime on HNaY zeolites: kinetic and spectroscopic studies.* Appl. Catal., 1986. **22**(2): p. 187-200.
86. Steehler, J.K., *Instant Notes: Analytical Chemistry (Kealey, D.; Haines, P. J.).* Journal of Chemical Education, 2003. **80**(3): p. 267.
87. Dettmer-Wilde, K., Engewald, Werner (Eds.), *Practical Gas Chromatography*. 2014: Springer.
88. Azzouz, I., et al., *Feasibility of the preparation of silica monoliths for gas chromatography: Fast separation of light hydrocarbons.* J. Chromatogr. A, 2015. **1383**: p. 127-133.
89. Carlson, D.A., U.R. Bernier, and B.D. Sutton, *Elution patterns from capillary GC for methyl-branched alkanes.* J. Chem. Ecol., 1998. **24**(11): p. 1845-1865.
90. Deans, D.R. and I. Scott, *Gas chromatographic columns with adjustable separation characteristics.* Anal. Chem., 1973. **45**(7): p. 1137-41.
91. Jennings, W., E. Mittlefehldt, and P. Stremple, *Chapter 4 - The stationary phase*, in *Analytical Gas Chromatography (Second Edition)*, W. Jennings, E. Mittlefehldt, and P. Stremple, Editors. 1997, Academic Press: San Diego. p. 92-113.
92. Sun, J.H., et al., *Micro-fabricated packed gas chromatography column based on laser etching technology.* J. Chromatogr. A, 2016. **1429**: p. 311-316.
93. Zheivot, V.I., et al., *Silica and alumina based functional materials: Substructures, adsorption and gas chromatographic properties.* Microporous Mesoporous Mater., 2015. **202**: p. 57-67.
94. Mahdavifar, A., et al., *Implementation of a Polysilicon Micro Electro-Thermal Detector in Gas Chromatography System with Applications in Portable Environmental Monitoring.* ECS J. Solid State Sci. Technol., 2015. **4**(10): p. S3062-S3066.
95. da Silva, C.G.A. and C.H. Collins, *Super/subcritical fluid chromatography with packed columns: state of the art and applications.* Quim. Nova, 2014. **37**(6): p. 1047-1057.

96. Bjorklund, J., et al., *Influence of the injection technique and the column system on gas chromatographic determination of polybrominated diphenyl ethers.* J. Chromatogr. A, 2004. **1041**(1-2): p. 201-210.
97. Grall, A.J. and R.D. Sacks, *Column performance and stability for high-speed vacuum-outlet GC of volatile organic compounds using atmospheric pressure air as carrier gas.* Anal. Chem., 1999. **71**(22): p. 5199-5205.
98. Burton, W.G., et al., *Separation of proteins by reversed-phase high-performance liquid chromatography. I. Optimizing the column.* J. Chromatogr., 1988. **443**: p. 363-79.
99. Pierce, K.M., J.S. Nadeau, and R.E. Synovec, *Chapter 17 - Data Analysis Methods*, in *Gas Chromatography*, C.F. Poole, Editor. 2012, Elsevier: Amsterdam. p. 415-434.
100. Klee, M.S., *Chapter 12 - Detectors*, in *Gas Chromatography*, C.F. Poole, Editor. 2012, Elsevier: Amsterdam. p. 307-347.
101. Blumberg, L.M., *Chapter 2 - Theory of Gas Chromatography*, in *Gas Chromatography*, C.F. Poole, Editor. 2012, Elsevier: Amsterdam. p. 19-78.
102. Kim, K.-H., et al., *A combined application of thermal desorber and gas chromatography to the analysis of gaseous carbonyls with the aid of two internal standards.* J. Sep. Sci., 2010. **33**(21): p. 3354-3364.
103. Kallio, M. and T. Hyotylainen, *Simple calibration procedure for comprehensive two-dimensional gas chromatography.* J. Chromatogr. A, 2008. **1200**(2): p. 264-267.
104. Kim, K.-H., *The properties of calibration errors in the analysis of reduced sulfur compounds by the combination of a loop injection system and gas chromatography with pulsed flame photometric detection.* Anal. Chim. Acta, 2006. **566**(1): p. 75-80.
105. Hoke, P.B., J.J. McGrath, and P.R. Loconto, *Quantitative analysis by indirect and reactive static headspace GC determination of a thin film of water deposited on an aluminum surface. Calibration considerations.* Am. Lab. (Shelton, CT, U. S.), 2002. **34**(1): p. 13-17.
106. Sheppard, A.J., W.D. Hubbard, and A.R. Prosser, *Comparison of gas chromatographic calibration methods for analysis of menadione and menadione sodium bisulfite content of pharmaceutical products.* J. Ass. Off. Anal. Chem., 1972. **55**(3): p. 660-1.
107. Jennings, W., E. Mittlefehldt, and P. Stremple, *Chapter 9 - Selected applications*, in *Analytical Gas Chromatography (Second Edition)*, W. Jennings, E. Mittlefehldt, and P. Stremple, Editors. 1997, Academic Press: San Diego. p. 285-355.
108. Cruz-Hernandez, C. and F. Destaillats, *Chapter 23 - Analysis of Lipids by Gas Chromatography*, in *Gas Chromatography*, C.F. Poole, Editor. 2012, Elsevier: Amsterdam. p. 529-544.
109. Jennings, W., E. Mittlefehldt, and P. Stremple, *Chapter 8 - Special analytical techniques*, in *Analytical Gas Chromatography (Second Edition)*, W. Jennings, E. Mittlefehldt, and P. Stremple, Editors. 1997, Academic Press: San Diego. p. 265-284.
110. Sparkman, O.D., *GC/MS: A practical user's guide, 2nd edition Marvin McMaster.* Journal of the American Society for Mass Spectrometry, 2011. **19**(8): p. R1-R5.
111. Gross, J.H., *Mass spectrometry: a textbook*. 2004: Springer Science & Business Media.
112. Watson, J.T., *Introduction to mass spectrometry*. 3rd ed. 1997, Philadelphia: Lippincott-Raven. ix, 496 p.
113. Milne, G.W.A., *Mass spectrometry : techniques and applications*. 1979, Huntington, N.Y.: R. E. Krieger Pub. Co. ix, 521 p.

114. Kitson, F.G., B.S. Larsen, and C.N. McEwen, *Gas chromatography and mass spectrometry: a practical guide*. 1996: Academic Press.
115. Hites, R.A., *Gas chromatography mass spectrometry.* Handbook of instrumental techniques for analytical chemistry, 1997: p. 609-626.
116. Downard, K., *Mass spectrometry : a foundation course*. 2004, Cambridge: Royal Society of Chemistry.
117. Sokolova, E.V. and Y.K. Kabalov, *Analysis of structures of new minerals and series of solid solutions by Ritveld method.* Poverkhnost, 1999(4): p. 17-18.
118. Massinga, P.H. and W.W. Focke, *Intercalating Cationic Surfactants in Koppies Bentonite.* Mol. Cryst. Liq. Cryst., 2012. **555**(1): p. 85-93.
119. Data, I.C.f.D. *www.icdd.com/profile/index.htm*. 2016 2016 [cited 2016
120. INTERNATIONAL, A. *www.astm.org*. 2016 [cited 2016.
121. Materialsdata.com. *www.materialsdata.com*. 2014 [cited 2016.
122. Stuart, B., *Infrared spectroscopy*. 2005: Wiley Online Library.
123. Brisdon, A.K., *Inorganic spectroscopic methods.* Oxford Chemistry Primers, 1998. **62**(1): p. ALL-ALL.
124. Dean, J.A., *Lange's handbook of chemistry.* 1985.
125. Lever, A.B.P., *Inorganic electronic spectroscopy.* 1968.
126. Kumar, D., et al., *QUANTUM COMPUTATION IN THE BRAIN, EMERGENCE OF UNPERTURBED MIND AND BEHAVIOURAL PATTERN DUE TO RESISTIVE, INDUCTIVE AND CAPACITATIVE BIS LOAD.*
127. Griffiths, P.R. and J.A. De Haseth, *Fourier transform infrared spectrometry*. Vol. 171. 2007: John Wiley & Sons.
128. VAN DE WEERT, M., J.A. HERING, and P.I. HARIS, *Fourier Transform Infrared.* Methods for Structural Analysis of Protein Pharmaceuticals, 2005. **3**: p. 131.
129. Xu, R., et al., *Chemistry of zeolites and related porous materials: synthesis and structure*. 2009: John Wiley & Sons.
130. Colthup, N., *Introduction to infrared and Raman spectroscopy*. 2012: Elsevier.
131. Cvetanovic, R. and Y. Amenomiya, *Application of a temperature-programmed desorption technique to catalyst studies.* Adv. Catal, 1967. **17**: p. 103-149.
132. Katada, N., et al., *Determination of the acidic properties of zeolite by theoretical analysis of temperature-programmed desorption of ammonia based on adsorption equilibrium.* The Journal of Physical Chemistry B, 1997. **101**(31): p. 5969-5977.
133. Miller, J.T., et al., *The effect of nonframework aluminum on acidity in dealuminated mordenite.* Journal of Catalysis, 1992. **138**(1): p. 115-128.
134. Karge, H.G. and V. Dondur, *Investigation of the distribution of acidity in zeolites by temperature-programmed desorption of probe molecules. I. Dealuminated mordenites.* Journal of Physical Chemistry, 1990. **94**(2): p. 765-772.
135. Cejka, J., A. Corma, and S. Zones, *Zeolites and catalysis: synthesis, reactions and applications*. 2010: John Wiley & Sons.
136. Majano, G., et al., *Seed-Induced Crystallization of Nanosized Na-ZSM-5 Crystals.* Ind. Eng. Chem. Res., 2009. **48**(15): p. 7084-7091.
137. Hay, D.G., H. Jaeger, and K.G. Wilshier, *Systematic intergrowth in crystals of ZSM 5 zeolite*. Zeolites, 1990. **10**(6): p. 571-6.

138. Scholle, K.F.M.G.J., et al., *Characterization of intermediate TPA-ZSM-5 type structures during crystallization.* Appl. Catal., 1985. **17**(2): p. 233-59.
139. Gedemer, T.J., *The Use of Derivative Thermogravimetry to Estimate Degree of Thermal Degradation.* Journal of Macromolecular Science—Chemistry, 1974. **8**(1): p. 95-104.
140. Andrew, E.R., *Nuclear magnetic resonance.* Nuclear Magnetic Resonance, by ER Andrew, Cambridge, UK: Cambridge University Press, 2009, 2009. **1**.
141. Hunger, M., *Bronsted acid sites in zeolites characterized by multinuclear solid-state NMR spectroscopy.* Catal. Rev. - Sci. Eng., 1997. **39**(4): p. 345-393.
142. Hunger, M., *Multinuclear solid-state NMR studies of acidic and non-acidic hydroxyl protons in zeolites.* Solid State Nucl. Magn. Reson., 1996. **6**(1): p. 1-29.
143. Klinowski, J., *Solid-state NMR studies of molecular sieve catalysts.* Chem. Rev., 1991. **91**(7): p. 1459-79.
144. Ernst, R.R., G. Bodenhausen, and A. Wokaun, *Principles of nuclear magnetic resonance in one and two dimensions*. Vol. 14. 1987: Clarendon Press Oxford.
145. Pervushin, K., et al., *Attenuated T2 relaxation by mutual cancellation of dipole–dipole coupling and chemical shift anisotropy indicates an avenue to NMR structures of very large biological macromolecules in solution.* Proceedings of the National Academy of Sciences, 1997. **94**(23): p. 12366-12371.
146. Yannoni, C., et al., *Carbon-13 NMR study of the C60 cluster in the solid state: molecular motion and carbon chemical shift anisotropy.* The Journal of Physical Chemistry, 1991. **95**(1): p. 9-10.
147. Brunauer, S., P.H. Emmett, and E. Teller, *Adsorption of gases in multimolecular layers.* Journal of the American chemical society, 1938. **60**(2): p. 309-319.
148. Dollimore, D., P. Spooner, and A. Turner, *The BET method of analysis of gas adsorption data and its relevance to the calculation of surface areas.* Surface Technology, 1976. **4**(2): p. 121-160.
149. Fagerlund, G., *Determination of specific surface by the BET method.* Matériaux et Construction, 1973. **6**(3): p. 239-245.
150. Bhambhani, M., et al., *Analysis of nitrogen adsorption isotherms on porous and nonporous silicas by the BET and α s methods.* Journal of Colloid and Interface Science, 1972. **38**(1): p. 109-117.
151. Svelle, S., et al., *Conversion of methanol into hydrocarbons over zeolite H-ZSM-5: Ethene formation is mechanistically separated from the formation of higher alkenes.* J Am Chem Soc, 2006. **128**(46): p. 14770-14771.
152. Tessonnier, J.-P., et al., *Methane dehydro-aromatization on Mo/ZSM-5: About the hidden role of Bronsted acid sites.* Appl. Catal., A, 2008. **336**(1-2): p. 79-88.
153. Tessonnier, J.-P., et al., *Quantitative Measurement of the Broensted Acid Sites in Solid Acids: Toward a Single-Site Design of Mo-Modified ZSM-5 Zeolite.* J. Phys. Chem. B, 2006. **110**(21): p. 10390-10395.
154. Li, B., et al., *Structure and acidity of Mo/ZSM-5 synthesized by solid state reaction for methane dehydrogenation and aromatization.* Microporous Mesoporous Mater., 2006. **88**(1-3): p. 244-253.
155. Kim, Y.H., R.W. Borry, and E. Iglesia, *Genesis of methane activation sites in Mo-exchanged H-ZSM-5 catalysts.* Microporous Mesoporous Mater., 2000. **35-36**: p. 495-509.

156. Wang, D., J.H. Lunsford, and M.P. Rosynek, *Characterization of a Mo/ZSM-5 catalyst for the conversion of methane to benzene.* J. Catal., 1997. **169**(1): p. 347-358.
157. Solymosi, F., et al., *Aromatization of methane over supported and unsupported Mo-based catalysts.* J. Catal., 1997. **165**(2): p. 150-161.
158. Holthausen, M.C. and W. Koch, *A Theoretical View on Co+-Mediated C-C and C-H Bond Activations in Ethane.* J. Am. Chem. Soc., 1996. **118**(Copyright (C) 2013 American Chemical Society (ACS). All Rights Reserved.): p. 9932-9940.
159. Borry, R.W., et al., *Structure and density of Mo and acid sites in Mo-exchanged H-ZSM5 catalysts for nonoxidative methane conversion.* Journal of Physical Chemistry B, 1999. **103**(28): p. 5787-5796.
160. Xu, Y.D., et al., *Interaction between Ammonium Heptamolybdate and Nh(4)Zsm-5 Zeolite - the Location of Mo Species and the Acidity of Mo/Hzsm-5.* Catalysis Letters, 1995. **35**(3-4): p. 233-243.
161. Brewer, L., *Molybdenum - Physicochemical Properties of Its Compounds and Alloys - Preface.* Atomic Energy Review, 1980: p. 5-6.
162. Zhang, J.-Z., M.A. Long, and R.F. Howe, *Molybdenum ZSM-5 zeolite catalysts for the conversion of methane to benzene.* Catal. Today, 1998. **44**(Copyright (C) 2013 American Chemical Society (ACS). All Rights Reserved.): p. 293-300.
163. Vora, B.V., et al., *Economic route for natural gas conversion to ethylene and propylene.* Natural Gas Conversion Iv, 1997. **107**: p. 87-98.
164. Groenvold, A., et al., *Conversion of methanol to lower alkenes on molecular sieve type catalysts.* Stud. Surf. Sci. Catal., 1994. **81**(Natural Gas Conversion II): p. 399-404.
165. Socha, R.F., et al., *Fluid-Bed Studies of Olefin Production from Methanol.* Acs Symposium Series, 1987. **328**: p. 34-41.
166. Hellring, S.D., K.D. Schmitt, and C.D. Chang, *Synthesis and Decomposition of Trimethyloxonium Zsm-5, a Purported Intermediate in Methanol Conversion into Gasoline.* Journal of the Chemical Society-Chemical Communications, 1987(17): p. 1320-1322.
167. Li, B., et al., *Structure and acidity of Mo/ZSM-5 synthesized by solid state reaction for methane dehydrogenation and aromatization.* Microporous and Mesoporous Materials, 2006. **88**(1-3): p. 244-253.
168. Zhang, W.P., et al., *Methane dehydro-aromatization over Mo/HZSM-5 in the absence of oxygen: A multinuclear solid-state NMR study of the interaction between supported Mo species and HZSM-5 zeolite with different crystal sizes.* Journal of Catalysis, 1999. **188**(2): p. 393-402.
169. Chen, K., et al., *Structure and properties of oxidative dehydrogenation catalysts based on MoO3/Al2O3.* Journal of Catalysis, 2001. **198**(2): p. 232-242.
170. Kondo, J.N., et al., *Acid property of silanol groups on zeolites assessed by reaction probe IR study.* Journal of Catalysis, 2000. **191**(2): p. 275-281.
171. Hunger, B., *Temperature Programmed Desorption (Tpd) on Zeolites by Means of Non-Linear Temperature Programs.* Journal of Thermal Analysis, 1989. **35**(1): p. 107-112.
172. Song, L.C., Q. Dong, and Q.M. Hu, *Study on Metal-Metal Bond Formation Reactions Synthesis and Characterization of [Eta-5-Ro2cc5h4(Co)3m]2hg (R=Me, Et, M=Cr, Mo, W).* Acta Chimica Sinica, 1992. **50**(2): p. 193-199.
173. Solymosi, F. and A. Szoke, *Conversion of ethane into benzene on Mo2C/ZSM-5 catalyst.* Appl.

Catal., A, 1998. **166**(Copyright (C) 2013 American Chemical Society (ACS). All Rights Reserved.): p. 225-235.

174. Fellah, M.F. and I. Onal, *C-H bond activation of methane on M- and MO-ZSM-5 (M = Ag, Au, Cu, Rh and Ru) clusters: A density functional theory study.* Catal. Today, 2011. **171**(1): p. 52-59.
175. Zhou, D., et al., *Study with density functional theory method on methane C-H bond activation on the MoO2/HZSM-5 active center.* Chem. Phys. Lett., 2003. **373**(1,2): p. 46-51.
176. Weckhuysen, B.M., et al., *Conversion of methane to benzene over transition metal ion ZSM-5 zeolites. I. Catalytic characterization.* J. Catal., 1998. **175**(2): p. 338-346.
177. Ding, W., et al., *Methane Conversion to Aromatics on Mo/H-ZSM5: Structure of Molybdenum Species in Working Catalysts.* J. Phys. Chem. B, 2001. **105**(Copyright (C) 2013 American Chemical Society (ACS). All Rights Reserved.): p. 506-513.
178. Du, X., et al., *Dry reforming of methane over ZrO2-supported Co-Mo carbide catalyst.* Appl. Petrochem. Res., 2014. **4**(1): p. 137-144.
179. Tessonnier, J.P., et al., *Methane dehydro-aromatization on Mo/ZSM-5: About the hidden role of Bronsted acid sites.* Applied Catalysis a-General, 2008. **336**(1-2): p. 79-88.
180. Mores, D., et al., *Coke Formation during the Methanol-to-Olefin Conversion: In Situ Microspectroscopy on Individual H-ZSM-5 Crystals with Different Bronsted Acidity.* Chem. - Eur. J., 2011. **17**: p. 2874-2884, S2874/1-S2874/2.
181. Bleken, F.L., et al., *Conversion of methanol into light olefins over ZSM-5 zeolite: Strategy to enhance propene selectivity.* Applied Catalysis a-General, 2012. **447**: p. 178-185.
182. Liu, H., et al., *The chemical nature of carbonaceous deposits and their role in methane dehydro-aromatization on Mo/MCM-22 catalysts.* Appl. Catal., A, 2002. **236**(Copyright (C) 2013 American Chemical Society (ACS). All Rights Reserved.): p. 263-280.
183. Bi, Y., et al., *Improved Selectivity toward Light Olefins in the Reaction of Toluene with Methanol Over the Modified HZSM-5 Catalyst.* ChemCatChem, 2014. **6**(3): p. 713-718.
184. Bedard, J., D.-Y. Hong, and A. Bhan, *CH4 dehydroaromatization on Mo/H-ZSM-5: 1. Effects of co-processing H2 and CH3COOH.* J. Catal., 2013. **306**: p. 58-67.
185. Vitale, G., et al., *Low temperature synthesis of cubic molybdenum carbide catalysts via pressure induced crystallographic orientation of MoO3 precursor.* Applied Catalysis A: General, 2011. **400**(1–2): p. 221-229.
186. Hanif, A., et al., *Study on the Structure and Formation Mechanism of Molybdenum Carbides.* Chem. Mater., 2002. **14**(3): p. 1009-1015.
187. Vo, D.-V.N., et al., *Evaluation of alumina-supported Mo carbide produced via propane carburization for the Fischer–Tropsch synthesis.* Fuel, 2012. **93**(0): p. 105-116.
188. Xu, Y.D., X.H. Bao, and L.W. Lin, *Direct conversion of methane under nonoxidative conditions.* Journal of Catalysis, 2003. **216**(1-2): p. 386-395.
189. Wang, T., et al., *Conversion of methanol to aromatics in fluidized bed reactor.* Catalysis Today, 2014. **233**: p. 8-13.
190. Al-Jarallah, A.M., U.A. El-Nafaty, and M.M. Abdillahi, *Effects of metal impregnation on the activity, selectivity and deactivation of a high silica MFI zeolite when converting methanol to light alkenes.* Applied Catalysis A: General, 1997. **154**(1): p. 117-127.
191. Aramburo, L.R., et al., *Interplay between nanoscale reactivity and bulk performance of H-ZSM-5 catalysts during the methanol-to-hydrocarbons reaction.* J. Catal., 2013. **307**: p.

185-193.

192. Ni, Y.M., et al., *The preparation of nano-sized H[Zn, Al]ZSM-5 zeolite and its application in the aromatization of methanol.* Microporous and Mesoporous Materials, 2011. **143**(2-3): p. 435-442.
193. Milina, M., et al., *Mesopore quality determines the lifetime of hierarchically structured zeolite catalysts.* Nat Commun, 2014.
194. *New-Zealand Methanol-to-Gasoline Process Can Be Based on Coal.* Oil & Gas Journal, 1980. **78**(2): p. 95-96.
195. Yurchak, S., S.E. Voltz, and J.P. Warner, *Process aging studies in the conversion of methanol to gasoline in a fixed bed reactor.* Ind. Eng. Chem. Process Des. Dev., 1979. **18**(3): p. 527-34.
196. Yu, Z., et al., *Bronsted/Lewis Acid Synergy in H-ZSM-5 and H-MOR Zeolites Studied by 1H and 27Al DQ-MAS Solid-State NMR Spectroscopy.* J. Phys. Chem. C, 2011. **115**(45): p. 22320-22327.
197. Hereijgers, B.P.C., et al., *Product shape selectivity dominates the Methanol-to-Olefins (MTO) reaction over H-SAPO-34 catalysts.* J. Catal., 2009. **264**(1): p. 77-87.
198. Mei, C., et al., *Selective production of propylene from methanol: Mesoporosity development in high silica HZSM-5.* J. Catal., 2008. **258**(1): p. 243-249.
199. Chang, C.D., et al., *Insertion of Aluminum into High-Silica-Content Zeolite Frameworks .3. Hydrothermal Transfer of Aluminum from Al2o3 into [Al]Zsm-5 and [B]Zsm-5.* Journal of the Chemical Society-Faraday Transactions I, 1985. **81**: p. 2215-2224.
200. Shihabi, D.S., et al., *Aluminum Insertion into High-Silica Zeolite Frameworks .2. Binder Activation of High-Silica Zsm-5.* Journal of Catalysis, 1985. **93**(2): p. 471-474.
201. Dahl, I.M. and S. Kolboe, *On the Reaction-Mechanism for Hydrocarbon Formation from Methanol over Sapo-34 .1. Isotopic Labeling Studies of the Co-Reaction of Ethene and Methanol.* Journal of Catalysis, 1994. **149**(2): p. 458-464.
202. Haw, J.F., *Zeolite acid strength and reaction mechanisms in catalysis.* Physical Chemistry Chemical Physics, 2002. **4**(22): p. 5431-5441.
203. Tan, P.L., et al., *The effect of calcination temperature on the catalytic performance of 2 wt.% Mo/HZSM-5 in methane aromatization.* Applied Catalysis a-General, 2002. **228**(1-2): p. 115-125.
204. Pradhan, S., et al., *Multi-functionality of Ga/ZSM-5 catalysts during anaerobic and aerobic aromatisation of n-decane.* Chemical Science, 2012. **3**(10): p. 2958-2964.
205. Duevel, A., et al., *Mechanically Induced Phase Transformation of γ-Al2O3 into α-Al2O3. Access to Structurally Disordered γ-Al2O3 with a Controllable Amount of Pentacoordinated Al Sites.* J. Phys. Chem. C, 2011. **115**(46): p. 22770-22780.
206. Dědeček, J., et al., *Effect of Al−Si−Al and Al−Si−Si−Al Pairs in the ZSM-5 Zeolite Framework on the 27Al NMR Spectra. A Combined High-Resolution 27Al NMR and DFT/MM Study.* The Journal of Physical Chemistry C, 2009. **113**(4): p. 1447-1458.
207. Derouane, E.G., J.-P. Gilson, and J.B. Nagy, *In situ characterization of carbonaceous residues from zeolite-catalysed reactions using high resolution solid state 13C-n.m.r. spectroscopy.* Zeolites, 1982. **2**(1): p. 42-46.
208. Barrage, M.C., et al., *Multinuclear Nmr and Catalytic Investigations of Deactivation of Zeolite H-Zsm-5.* Catalysis Letters, 1990. **6**(2): p. 201-207.
209. Cheng, H., *Carbon-13 NMR characterization of ethylene/1-butene copolymers.*

Macromolecules, 1991. **24**(17): p. 4813-4819.
210. Mirji, S.A., et al., *Adsorption of toluene on Si(1 0 0)/SiO2 substrate and mesoporous SBA-15.* Colloids and Surfaces A: Physicochemical and Engineering Aspects, 2006. **272**(3): p. 220-226.
211. Minejima, C., T. Ebata, and N. Mikami, *C-H stretching vibrations of benzene and toluene in their S1 states observed by double resonance vibrational spectroscopy in supersonic jets.* Phys. Chem. Chem. Phys., 2002. **4**(9): p. 1537-1541.
212. Trombetta, M., et al., *Conversion and hydroconversion of hydrocarbons on zeolite-based catalysts: an FT-IR study.* Catalysis Today, 2001. **65**(2–4): p. 285-292.
213. Lange, J.P., et al., *Coke formation through the reaction of ethene over hydrogen mordenite. III. IR and carbon-13 NMR studies.* Appl. Catal., 1988. **45**(2): p. 345-56.
214. Castano, P., et al., *Insights into the coke deposited on HZSM-5, Hβ and HY zeolites during the cracking of polyethylene.* Appl. Catal., B, 2011. **104**(1-2): p. 91-100.
215. Vandenabeele, P., *Practical Raman Spectroscopy - An introduction*. 1 ed. 2013, Chichester UK: WILEY. 161.
216. Chua, Y.T. and P.C. Stair, *An ultraviolet Raman spectroscopic study of coke formation in methanol to hydrocarbons conversion over zeolite H-MFI.* Journal of Catalysis, 2003. **213**(1): p. 39-46.
217. Li, J., et al., *Coke formation during the methanol conversion to olefins in zeolites studied by UV Raman spectroscopy.* Microporous Mesoporous Mater., 2000. **39**(1-2): p. 275-280.
218. Choi, M., et al., *Stable single-unit-cell nanosheets of zeolite MFI as active and long-lived catalysts.* Nature, 2009. **461**(7261): p. 246-249.
219. Haag, W.O., R.M. Lago, and P.B. Weisz, *The Active-Site of Acidic Aluminosilicate Catalysts.* Nature, 1984. **309**(5969): p. 589-591.
220. BuurmansInge, L.C., et al., *Catalytic activity in individual cracking catalyst particles imaged throughout different life stages by selective staining.* Nat Chem, 2011. **3**(11): p. 862-867.
221. Anderson, M.W. and J. Klinowski, *Direct observation of shape selectivity in zeolite ZSM-5 by magic-angle-spinning NMR.* Nature, 1989. **339**(6221): p. 200-203.
222. Karge, H.G., *Chapter 16 Coke formation on zeolites*, in *Studies in Surface Science and Catalysis*, E.M.F.P.A.J. H. van Bekkum and J.C. Jansen, Editors. 2001, Elsevier. p. 707-746.
223. Sarbak, Z., *Fourier - transform infrared studies on coke formation over alumina silica-alumina and zeolites.* React. Kinet. Catal. Lett., 2000. **69**(1): p. 177-181.
224. Li, C., et al., *In-situ FTIR investigation of coke formation on USY zeolite.* Appl. Surf. Sci., 1994. **81**(4): p. 465-8.
225. Snape, C.E., et al., *Structural characterization of catalytic coke by solid-state 13C-NMR spectroscopy.* Catal. Today, 1997. **37**(3): p. 285-293.
226. Behera, B. and S.S. Ray, *Structural changes of FCC catalyst from fresh to regeneration stages and associated coke in a FCC refining unit: A multinuclear solid state NMR approach.* Catal. Today, 2009. **141**(1-2): p. 195-204.
227. Klein O, D.S., Dressel M, et al., *Microwave cavity perturbation technique*. 1993: International Journal of Infrared and Millimeter Waves.
228. de Paula, A.L., J.J. Barroso, and M.C. Rezende. *Comparative study of the Teflon® electromagnetic parameters (permittivity and permeability) experimentally obtained and numerically simulated*. in *Microwave and Optoelectronics*

Conference (IMOC), 2009 SBMO/IEEE MTT-S International. 2009.

229. Hutcheon, R., M. De Jong, and F. Adams, *A system for rapid measurements of RF and microwave properties up to 1400 C.* Journal of microwave power and electromagnetic energy, 1992. **27**(2): p. 87-92.
230. Metaxas, A.a. and R.J. Meredith, *Industrial microwave heating*. 1983: IET.
231. Peregrinus, P., *On behalf of the Institution of Electrical Engineers*. 1983, London, UK.
232. Vandenabeele, P., *Practical Raman spectroscopy: an introduction*. 2013: John Wiley & Sons.
233. Kim, T., J. Lee, and K.-H. Lee, *Full graphitization of amorphous carbon by microwave heating.* RSC Adv., 2016. **6**(29): p. 24667-24674.
234. Zheng, A.M., et al., *Insight into the activation of light alkanes over surface-modified carbon nanotubes from theoretical calculations.* Carbon, 2014. **77**: p. 122-129.
235. Impeng, S., et al., *Direct oxidation of methane to methanol on Fe-O modified graphene.* Rsc Advances, 2014. **4**(24): p. 12572-12578.
236. Conte, M., et al., *Modified zeolite ZSM-5 for the methanol to aromatics reaction.* Catalysis Science & Technology, 2012. **2**(1): p. 105-112.
237. Mitra, B. and D. Kunzru, *Disproportionation of Toluene on Monoliths Washcoated with Metal Oxide Modified ZSM5.* Catalysis Letters, 2011. **141**(10): p. 1569-1579.
238. Taniguchi, T., et al., *Methanol Conversion Reaction Over MFI Ferroaluminosilicate Nano Crystal.* Catalysis Letters, 2016. **146**(2): p. 442-451.
239. Alipour, S.M., *Recent advances in naphtha catalytic cracking by nano ZSM-5: A review.* Chinese Journal of Catalysis, 2016. **37**(5): p. 671-680.
240. Zhang, H.B., et al., *Nano-crystallite oriented self-assembled ZSM-5 zeolite and its LDPE cracking properties: Effects of accessibility and strength of acid sites (vol 302, pg 115, 2013).* Journal of Catalysis, 2014. **311**: p. 169-169.
241. Zhang, G.Q., et al., *Conversion of Methanol to Light Aromatics on Zn-Modified Nano-HZSM-5 Zeolite Catalysts.* Industrial & Engineering Chemistry Research, 2014. **53**(39): p. 14932-14940.

Appendix of supporting NMR spectra (for Chapter 5)

The supporting NMR spectra were employed to show the coking level and coke compositions achieved by different samples, where special attention is paid to those samples that have shown a higher dielectric loss value (e.g. the coked catalyst bed top samples) measured by our microwave method. The tests were proceeded at the national NMR service at Durham (the University of Durham).

A short description of the measured results from our colleague Dr. David Apperley (the NMR service manager at Durham) is directly quoted: *The results give a signal at 130 ppm from aromatic carbon. There is signal at 51 ppm which is consistent with residual methanol (although as it is visible in this CP spectrum it must be relatively immobile). The third signal is at 22 ppm which is probably aromatic-CH_3. As this is a CP spectrum without exchange of ^{13}C isotope any highly "graphitized" carbon will not be detected.*

The stronger NMR signal of aromatics on those aromatic-poor samples (e.g. the coked SAPO-34 sample) does not show an abundance of the aromatic cokes, however, it is benefited from the less-dehydrogenated coke composition that allows the CP signal to be greatly enhanced (the signal of smaller amount of aromatic cokes can be amplified). [12] The poor aromatics signal is a good evidence, in a 'special way', that proved the rich poly-aromatics abundance (this reflects a deeper dehydrogenated status, further towards a 'graphite carbon' status) in those higher ε"/wt% value samples.

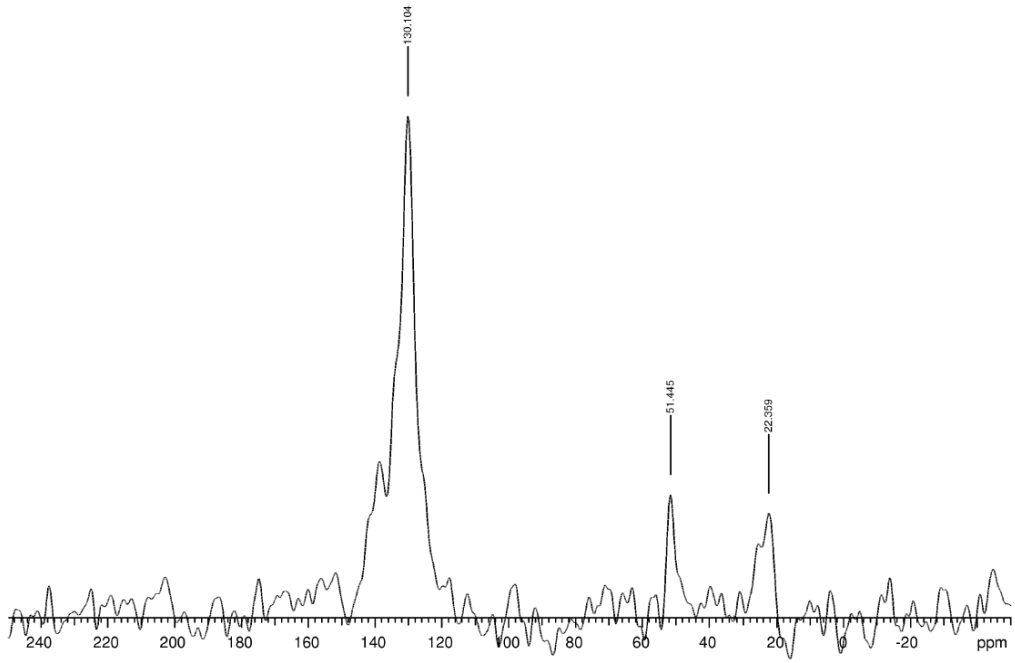

Fig. Ap.1 ^{13}C NMR spectra of 5h reacted MCM-22 (Si/Al=20-30) showing coke composition (130.104, 51.445, and 22.359)

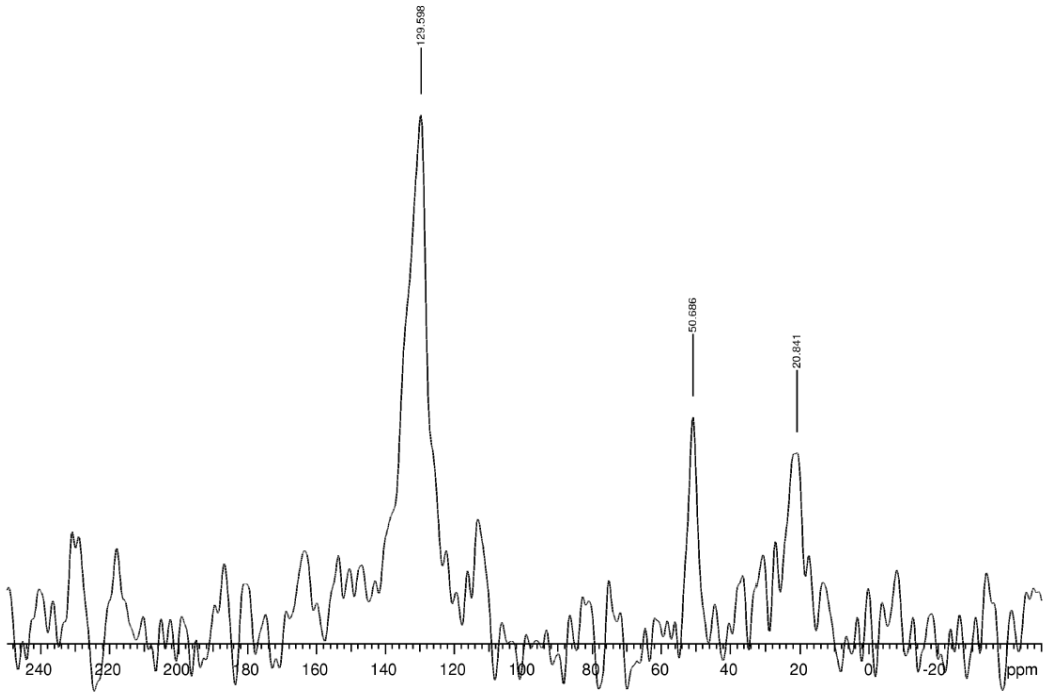

Fig. Ap.2 ^{13}C NMR spectra of 2h reacted MCM-22 (Si/Al=20-30) showing coke composition (129.598, 50.686, 20.841)

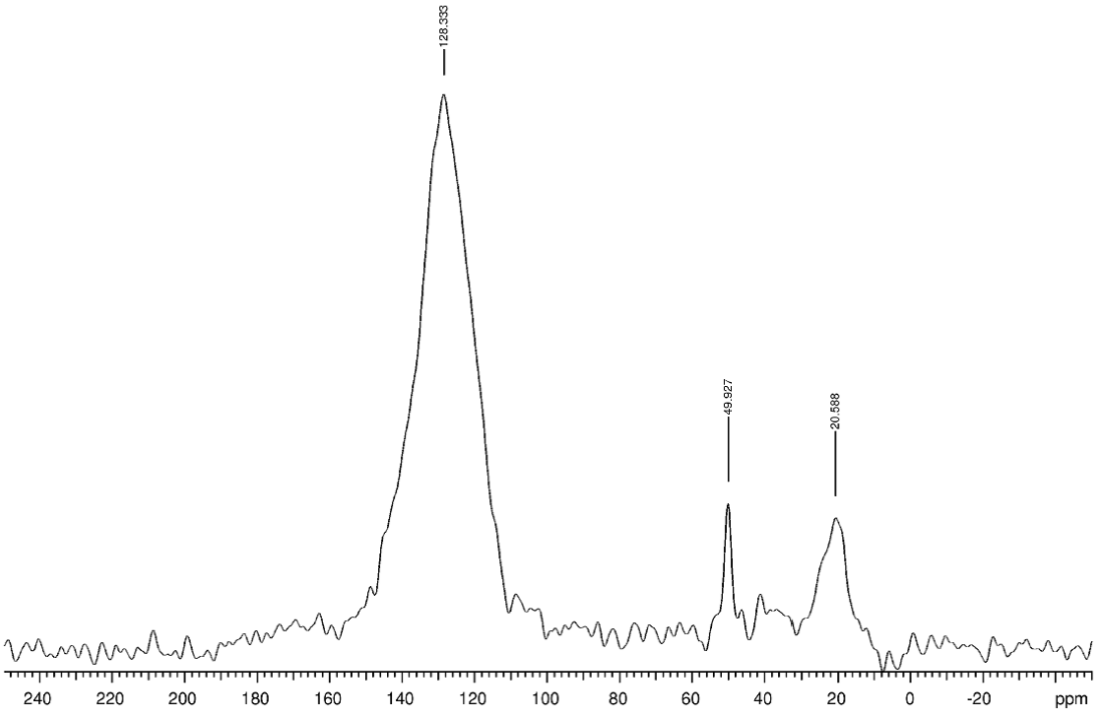

Fig. Ap.3 ^{13}C NMR spectra of 5h reacted mesoporous ZSM-5 (Si/Al=40-60) showing coke composition (128.333, 49.927, 20.588)

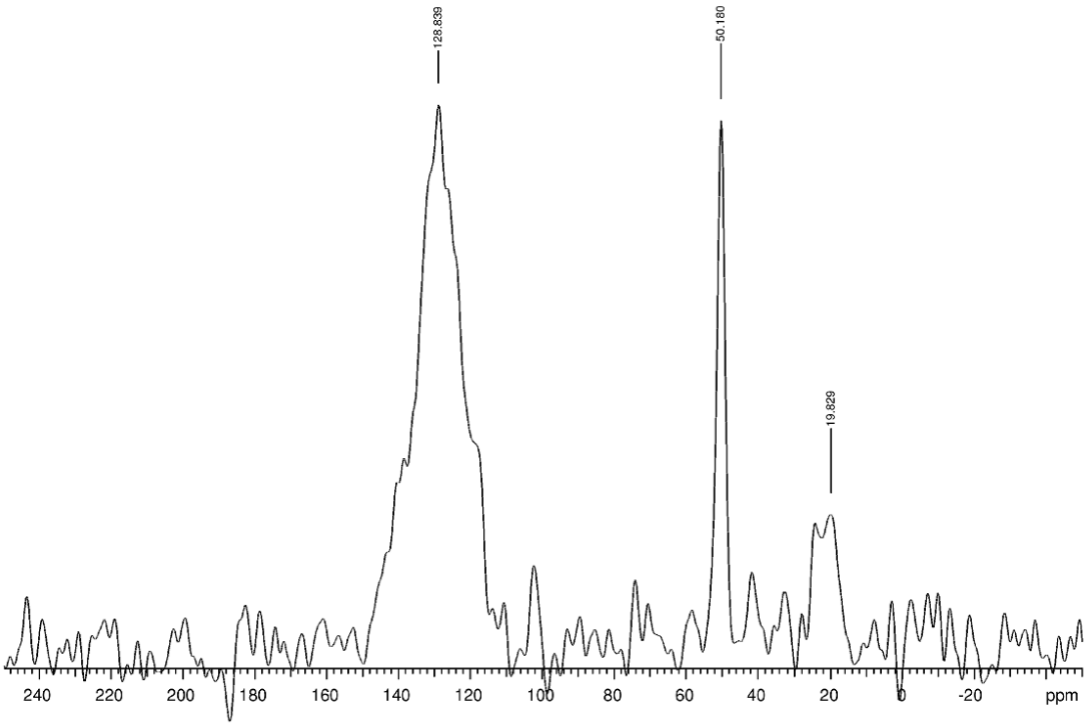

Fig. Ap.4 ^{13}C NMR spectra of 2h reacted mesoporous ZSM-5 (Si/Al=40-60) showing coke composition (128.839, 50.180, 19.829)

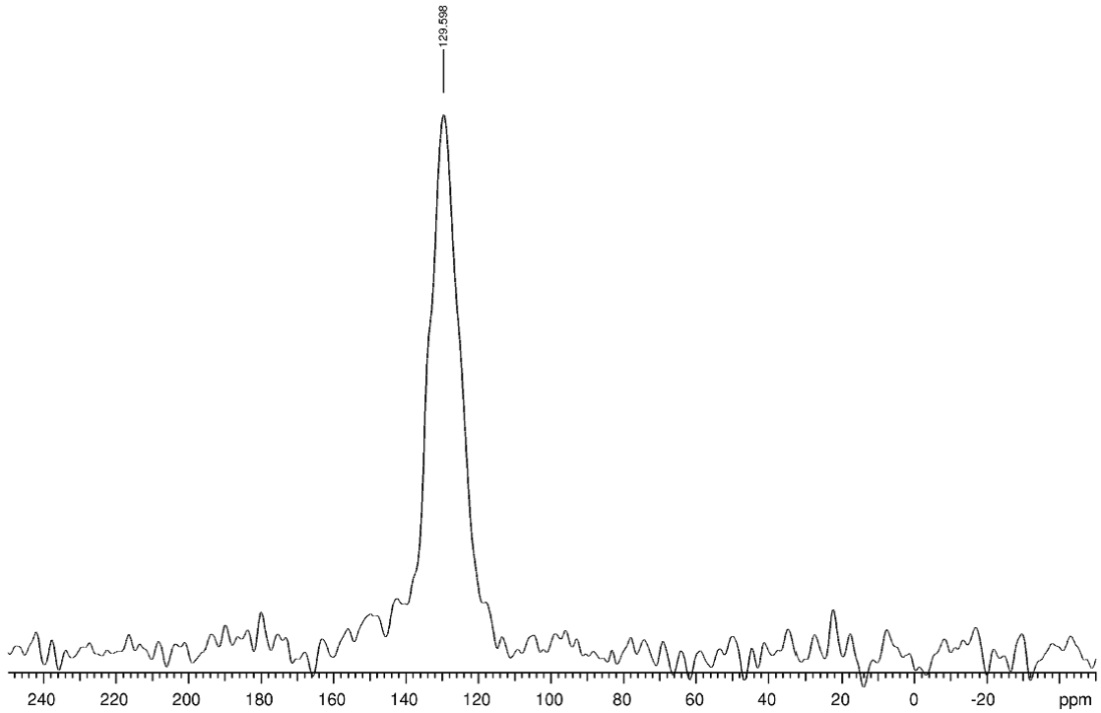

Fig. Ap.5 ^{13}C NMR spectra of 5h reacted SAPO-34 (Si/Al=20-30) showing coke composition (129.598)

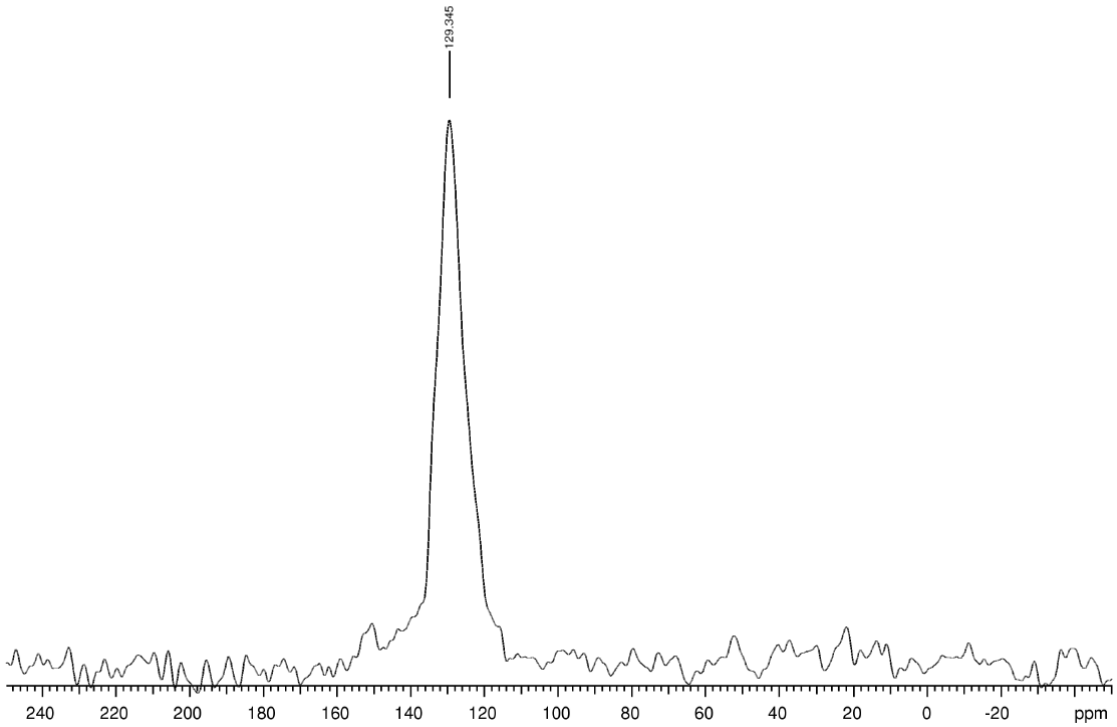

Fig. Ap.6 ^{13}C NMR spectra of 2h reacted SAPO-34 (Si/Al=20-30) showing coke composition (129.345)

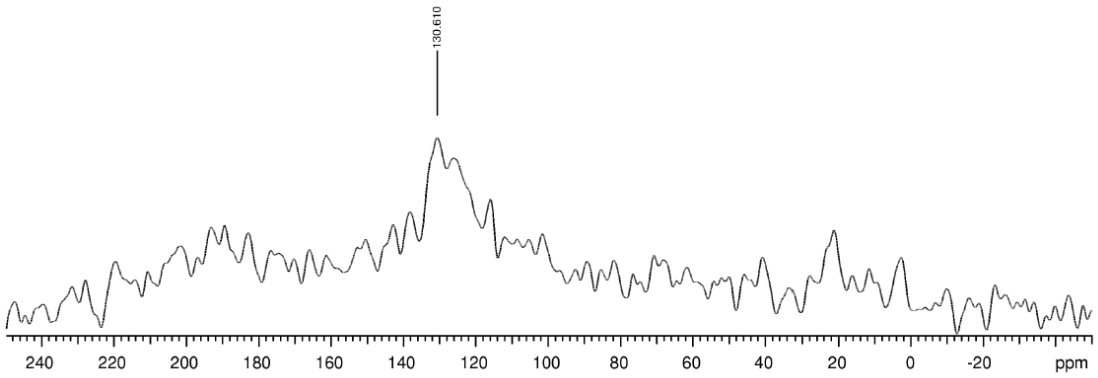

Fig. Ap.7 ^{13}C NMR spectra of 5h reacted industrial ZSM-5 (Si/Al=25) showing coke composition (130.610)

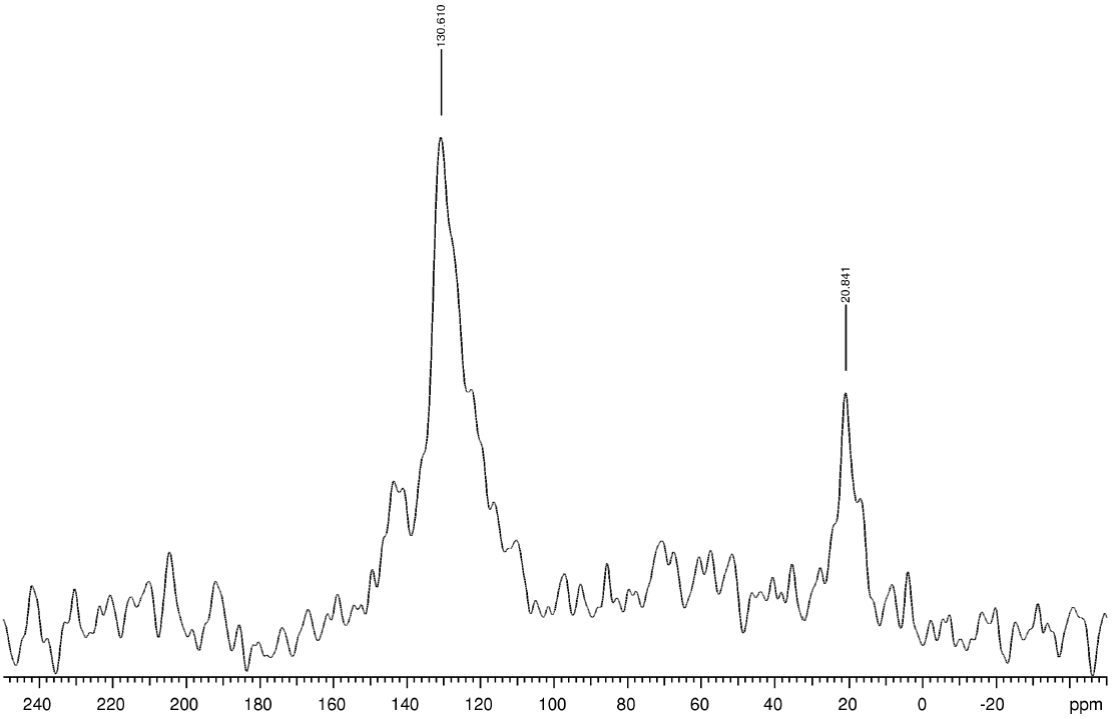

Fig. Ap.8 ^{13}C NMR spectra of 2h reacted industrial ZSM-5 (Si/Al=25) showing coke composition (130.610, 20.841)

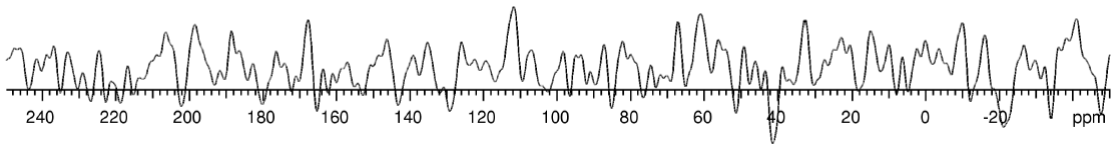

Fig. Ap.9 ^{13}C NMR spectra of top-catalyst-bed coked nano ZSM-5 (Si/Al=160) showing coke composition *(poly-aromatics rich, MW response high, no NMR signal)*

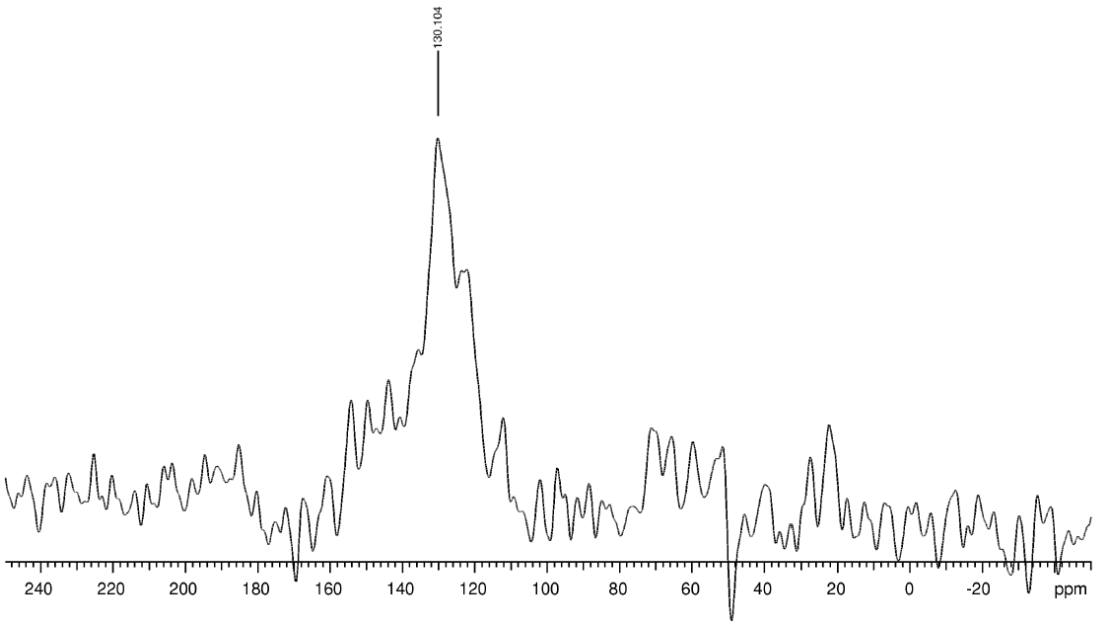

Fig. Ap.10 ^{13}C NMR spectra of bottom-catalyst-bed coked nano ZSM-5 (Si/Al=160) showing coke composition (130.104)

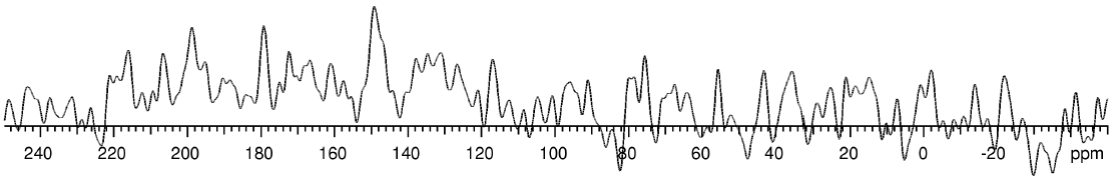

Fig. Ap.11 ^{13}C NMR spectra of top-catalyst-bed coked nano ZSM-5 (Si/Al=60) showing coke composition *(poly-aromatics rich, MW response high, no NMR signal)*

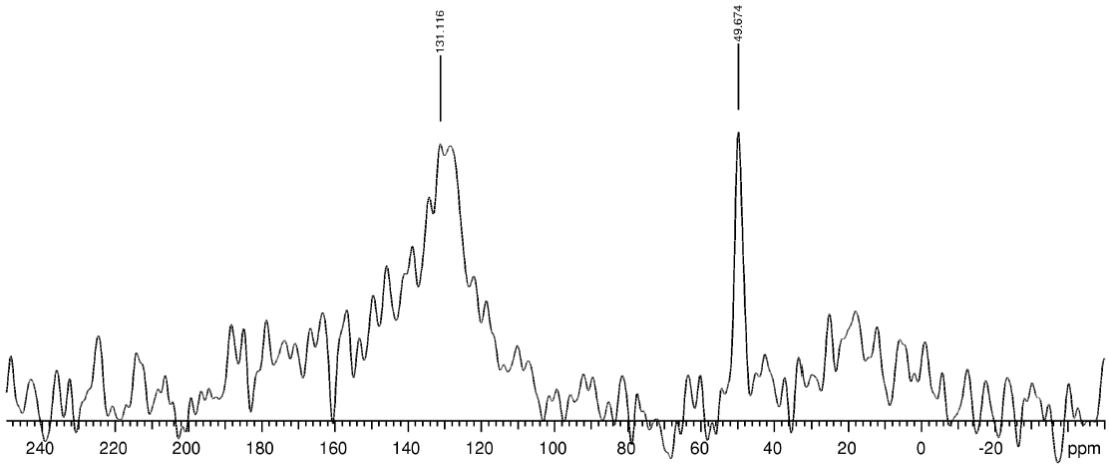

Fig. Ap.12^{13}C NMR spectra of bottom-catalyst-bed coked nano ZSM-5 (Si/Al=60) showing coke composition (131.116, 49.674)

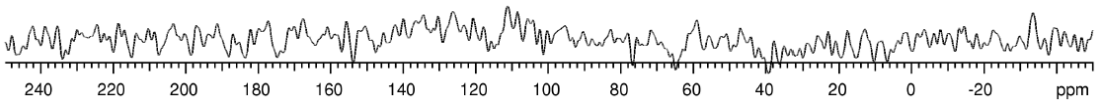

Fig. Ap.13 ^{13}C NMR spectra of top-catalyst-bed coked nano ZSM-5 (Si/Al=46) showing coke composition *(poly-aromatics rich, MW response high, no NMR signal)*

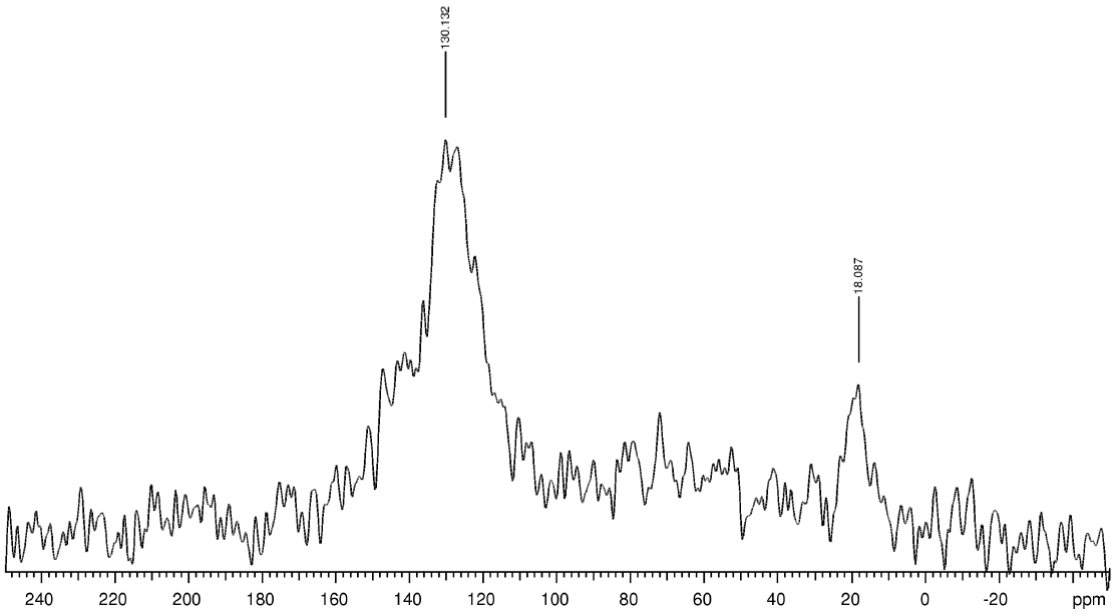

Fig. Ap.14 ^{13}C NMR spectra of bottom-catalyst-bed coked nano ZSM-5 (Si/Al=46) showing coke composition (130.132, 18.087)